Development of an ultrasensitive cavity ring down spectrometer in the 2.10-2.35 μm region : application to water vapor and carbon dioxide

Semen Vasilchenko

Communauté
UNIVERSITÉ Grenoble Alpes

THÈSE

Pour obtenir le grade de

DOCTEUR DE LA COMMUNAUTE UNIVERSITE GRENOBLE ALPES

Spécialité : **Physique de la Matière Condensée et du Rayonnement**

Arrêté ministériel : 25 mai 2016

Présentée par

Semen VASILCHENKO

Thèse dirigée par **Didier MONDELAIN**
codirigée par **Alain CAMPARGUE**

préparée au sein du **Laboratoire Interdisciplinaire de Physique**
dans **l'École Doctorale Physique**

Development of an ultrasensitive cavity ring down spectrometer in the 2.10-2.35 µm region. Application to water vapor and carbon dioxide.

Thèse soutenue publiquement le **8 juin 2017**,
devant le jury composé de :

Madame Muriel LEPÈRE
Professeur, Université de Namur, Rapporteur
Monsieur Robert GEORGES
Professeur, Université Rennes 1, Rapporteur
Monsieur Hugues GUILLET DE CHATELLUS
Chargé de recherche, CNRS LIPhy UMR5588, Examinateur
Monsieur Olivier PIRALI
Chargé de recherche, Institut des Sciences Moléculaires d'Orsay - UMR8214, Examinateur
Monsieur Jean-Michel HARTMANN
Directeur de recherche, Laboratoire de Météorologie Dynamique (UMR 8539), Président
Monsieur Leonid SINITSA
Professeur, V.E. Zuev Institute of Atmospheric Optics SB RAS (IAO SB RAS), Examinateur

Acknowledgments

First and foremost, I would like to express sincere gratitude to my supervisor Didier Mondelain for guidance, patience, and the experience he shared; he handled my professional and personal issues and read, and corrected the manuscripts of the thesis a multitude of times.

I would also like to thank my co-supervisor Alain Campargue, who was always open to discussions and questions and created the perfect working conditions as the head of the scientific group.

I am grateful to Peter Čermák for tutoring me, giving advice, a great many fruitful discussions and being sociable

Heartfelt thanks to all of the LAsers, Molécules et Environnement group for a pleasant atmosphere at work. I am honored to be working with such a strong and productive scientific group. Samir Kassi, Jean-Luc Martin, Serge Béguier, Semen Mikhailenko and Daniele Romanini deserve a special mention in the acknowledgments list for their help, advice, and useful discussions. Special thanks to my fellow PhD students Magdalena Konefal and Ekaterina Karlovets for sharing the same office and becoming good friends with me.

I would like to thank the Université Grenoble Alpes for a 3 years support of my PhD. This support was obtained in the relation of the strong collaboration between our group at LIPhy and my home institute, the Institute of Atmospheric Optics in Tomsk in the frame of the LIA SAMIA (Laboratoire International Associé "Spectroscopie de Molécules d'Intérêt Atmosphérique")

But for the endeavor of Leonid Sinitsa, carrying out this research of mine would have been impossible.

I am grateful to Gleb Lantsman for correcting the style and the language of this manuscript.

Last but not least, I would like to give my warmest thanks to my family and friends for their support, communication, and genuine interest in my research.

Abstract

A cavity ring down spectrometer has been developed in the 2.00–2.35 μm spectral range to achieve highly sensitive absorption spectroscopy of molecules of atmospheric and planetologic interest and at high spectral resolution. This spectral region corresponds to a transparency window for water vapor and carbon dioxide. Atmospheric windows, where absorption is weak, are used to sound the Earth's and Venus' atmospheres where water vapor and carbon dioxide represent the main gaseous absorbers in the infrared, respectively.

The CRDS technique consists in injecting photons inside a high finesse optical cavity and measuring the photon's life time of this cavity. This life-time depends on the mirror reflectivity and on the intra-cavity losses due to the absorbing gas in the cavity. Measuring these losses versus the wavelength allow obtaining the absorption spectrum of the gas. The extreme reflectivity of the mirrors allows reaching, for a 1-meter long cavity, a sensitivity equivalent to the one obtained classically with absorption cells of several thousands of kilometers.

Three DFB laser diodes emitting around 2.35, 2.26, 2.21 μm were used with this spectrometer giving access to the 4249-4257, 4422-4442 and 4516-4534 cm^{-1} interval, respectively. Thanks to optical feedback from an external cavity, two of these diodes were spectrally narrowed leading to a better injection of the high finesse cavity thus reducing the noise level of the spectrometer. In parallel, we tested a VECSEL (Vertical-external-Cavity, Surface Emitting laser) through a collaboration with the Institut d'Electronique (IES, UMR 5214) in Montpellier and the Innoptics firm. This laser source is able to cover a 80 cm^{-1} spectral range centered at 4340 cm^{-1}, equivalent to four DFB laser diodes. In routine the achieved sensitivity with this spectrometer, corresponding to the minimum detectable coefficient is typically of 1×10^{-10} cm^{-1}. The introductive chapter (Chapter 1) makes the point on the different techniques allowing absorption spectra recordings in the studied spectral region and on their sensitivity. The experimental set-up, the characteristics and performances by the CRD spectrometer developed in this work are detailed in Chapter 2. To our knowledge this instrument is the most sensitive in the considered spectral region.

In Chapter 3, detection of quadrupolar electric transitions of HD and N_2 illustrate the level of sensitivity reached: (i) the S(3) transition in the 1–0 band of HD has been recorded for the first time and its intensity measured ($s = 2.5 \times 10^{-27}$ cm/molecule), (ii) the position and intensity of the highly forbidden O(14) quadrupolar electric transition of the 2–0 band of N_2 have also been newly determined.

The two last chapters are devoted to the characterization of the CO_2 absorption, in the centre of the transparency window, and of the water vapor absorption. In both cases, we not only studied the allowed transitions of the monomer, but also

the continuum absorption. This latter correspond to a weak background absorption varying slowly with the wave length. The self-continuum cross-sections of the water vapor continuum were measured in many spectral points through the transparency window with a much better accuracy compared to existing measurements. These CRDS data constitute a valuable data set to validate the reference model (MT_CKD) for the continuum which is implemented in most of the atmospheric radiative transfer codes.

Résumé

Un spectromètre utilisant la technique CRDS a été développé entre 2.00 et 2.35 μm afin de réaliser la spectroscopie en absorption de molécules d'intérêt atmosphérique et planétologique avec une très grande sensibilité et à haute résolution spectrale. Cette région du spectre correspond à une fenêtre de transparence de la vapeur d'eau et du dioxyde de carbone. Ces fenêtres sont des zones de très faible absorption utilisées pour le sondage des atmosphères terrestre et vénusienne dans lesquelles la vapeur d'eau et le dioxyde de carbone représentent respectivement les absorbants gazeux principaux dans l'infrarouge.

La technique CRDS consiste à injecter des photons dans une cavité optique de haute finesse et à mesurer la durée de vie des photons dans cette cavité. Celle-ci est mesurée en interrompant l'injection des photons dans la cavité optique lors du passage en résonance du laser avec l'un des modes longitudinaux. Cette durée de vie dépend de la réflectivité des miroirs et des pertes intra-cavité comme celles induites par un gaz qui absorbe. Mesurer ces pertes en fonction de la longueur d'onde permet d'obtenir le spectre d'absorption du gaz en question. L'extrême réflectivité des miroirs permet d'atteindre dans une cavité d'un peu plus d'1 m de longueur une sensibilité équivalente à celle qui serait obtenue classiquement avec une cellule d'absorption longue de plusieurs milliers de kilomètres.

Trois diodes laser DFB émettant autour de 2.35, 2.26 et 2.21 μm ont été utilisées avec ce spectromètre. Grâce à une rétro-action optique provenant d'une cavité externe, certaines de ces diodes ont pu être affinées, ce qui a permis de mieux injecter la cavité haute finesse et ainsi de réduire le niveau de bruit du spectromètre. Parallèlement grâce à une collaboration avec l'Institut d'Electronique (IES, UMR 5214) à Montpellier et la société Innoptics nous avons pu tester le prototype d'un VECSEL (Vertical-External-Cavity Surface-Emitting-Laser). Ce laser a permis de couvrir une gamme spectrale de 80 cm^{-1}, entre 4300 et 4380 cm^{-1}, équivalente à quatre diodes laser DFB. La sensibilité obtenue en routine avec ce spectromètre, correspondant au coefficient minimum détectable, est typiquement de 1×10^{-10} cm^{-1}. Le chapitre introductif (Chapitre 1) fait le point sur les différentes techniques permettant d'acquérir des spectres en absorption dans la gamme spectrale étudiée et sur les sensibilités atteintes. A notre connaissance l'instrument développé ici est le plus sensible dans cette région du spectre. Le fonctionnement de ce spectromètre CRDS est détaillé dans le chapitre 2.

Pour démontrer les performances obtenues avec notre instrument celui-ci a été utilisé pour enregistrer des transitions quadrupolaires donc de très faible intensité. Ainsi la transition S(3) de la bande 1–0 de HD a été enregistrée pour la première fois et son intensité mesurée ($s = 2.5 \times 10^{-27}$ cm/molecule). La sensibilité obtenue

en routine a encore pu être améliorée en réalisant une moyenne d'une centaine de spectres sur une gamme spectrale réduite pour atteindre 1×10^{-11} cm^{-1}. Grâce à cela nous avons pu mesurer la position et l'intensité de la raie quadrupolaire électrique O(14) de la bande 2–0 de N_2 qui est très fortement interdite avec une intensité de 1.5×10^{-30} cm/molecule. Ces mesures font l'objet du chapitre 3 de cette thèse.

Les deux derniers chapitres sont dédiés à la caractérisation de l'absorption du CO_2, au centre de la fenêtre de transparence, et à celle de la vapeur d'eau. Dans les deux cas, les transitions permises du monomère et la contribution du continuum ont été étudiées. Ce dernier correspond à une absorption variant lentement avec la longueur d'onde. Les sections efficaces du "self-continuum" de la vapeur d'eau ont notamment été mesurées en plusieurs points de la fenêtre de transparence avec une incertitude beaucoup plus faible que les mesures existantes. Elles représentent un jeu de données décisif pour tester les modèles décrivant ce continuum.

List of publications

D. Mondelain, S. Vasilchenko, P. Čermák, S. Kassi, and a. Campargue. The self- and foreign-absorption continua of water vapor by cavity ring-down spectroscopy near 2.35 μm. *Phys. Chem. Chem. Phys.*, pages 1–18, 2015.

A. Campargue, S. Kassi, D. Mondelain, S. Vasilchenko, and D. Romanini. Accurate laboratory determination of the near-infrared water vapor self-continuum: A test of the MT_CKD model. *Journal of Geophysical Research: Atmospheres*, 121(21):13,180–13,203, 2016.

S. Vasilchenko, M. Konefal, D. Mondelain, S. Kassi, P. Čermák, S.A. Tashkun, V.I. Perevalov, and A. Campargue. The CO_2 absorption spectrum in the 2.3 μm transparency window by high sensitivity CRDS: (I) Rovibrational lines. *Journal of Quantitative Spectroscopy and Radiative Transfer*, 184:233–240, 2016.

D. Mondelain, S. Vasilchenko, P. Čermák, and A. Campargue S. Kassi. The CO_2 absorption spectrum in the 2.3 μm transparency window by high sensitivity CRDS: (ii) self absorption continuum. *Journal of Quantitative Spectroscopy and Radiative Transfer*, 2016.

P. Čermák, S. Vasilchenko, D. Mondelain, S. Kassi, and A. Campargue. First laboratory detection of an absorption line of the first overtone electric quadrupolar band of N2 by CRDS near 2.2μm. *Chemical Physics Letters*, 668:90–94, 2017.

P. Čermák, B. Chomet, L. Ferrieres, S. Vasilchenko, D. Mondelain, S. Kassi, A. Campargue, S. Denet, V. Lecocq, M. Myara, L. Cerutti, and A. Garnache. CRDS with a VECSEL for broad-band high sensitivity spectroscopy in the 2.3 μm window. *Review of Scientific Instruments*, 87(8):083109, aug 2016.

A. Campargue, S. N. Mikhailenko, S. Vasilchenko, C. Reynaud, S. Béguier, P. Čermák, D. Mondelain, S. Kassi, and D. Romanini. The absorption spectrum of water vapor in the 2.2–μm transparency window: High sensitivity measurements and spectroscopic database. *Journal of Quantitative Spectroscopy and Radiative Transfer*, 189:407–416, 2017.

S. Vasilchenko, D. Mondelain, S. Kassi, P. Čermák, B. Chomet, A. Garnache, S. Denet, V. Lecocq, and A. Campargue. The HD spectrum near 2.3 μm by CRDS-VECSEL: Electric quadrupole transition and collision-induced absorption, 2016.

Contents

Introduction

Spectroscopy is one of the most important diagnostic tools in science. Despite its more than two-hundred-year history, spectroscopic techniques continue to evolve, supporting scientists in the development of planetary science, astrophysics, and many others applications, for instance, including the refinement of fundamental Boltzmann's constant [1].

This thesis project was realized at *Laboratoire Interdisciplinaire de Physique* of Université Grenoble Alpes under supervision of Didier Mondelain and Alain Campargue. Significant progress in this project was achieved through collaboration with Peter Čermák from Comenius University in Bratislava, and with Innoptics and the Institut d'Électronique et des Systèmes in Montpellier.

The thesis is dedicated to the high sensitivity Cavity Ring-Down Spectroscopy (which is known to be one of the most sensitive spectroscopic techniques) of atmospheric gases like water vapor, carbon dioxide, and their isotopologues. The goal of the project was to build a new CRDS instrument in the 2.3–μm region and carry out a study of these main atmospheric gases with unprecedented sensitivity.

In the first chapter, we will discuss the scientific motivation of the high sensitivity spectroscopy in the 2.3–μm region and remind the reader of some basic physical principles and laws of spectroscopy and optical cavities. A significant part of the chapter will be dedicated to a review of highly sensitive spectroscopic techniques used in the near infrared region; we will describe several of those.

The second chapter describes the CRD-spectrometer developed within the framework of the thesis. We will discuss the different parts of the instrument as well as the laser sources used and their characteristics. We will describe modifications which we implemented during the evolution of the spectrometer, its sensitivity, and performance.

Then, in chapter 3, we will describe a test of sensitivity, i.e. two experiments intended dedicated to the first laboratory detection of electric quadrupole transitions of the HD and N_2 molecules. We will show the limit performance of the spectrometer achieved with mode tracking.

At the beginning of the fourth chapter, we will describe the recordings of rovibrational transitions of water vapor in the 2.2–μm region. Then, we will use our results

to test and validate line lists available in the literature, and more specifically, the intensities provided by *ab initio* calculations and the HITRAN2012 database [2]. After the water vapor rovibrational spectroscopy, we will present the new experimental data on the self-continuum of water vapor along the low frequency slope of the transparency window centered at 2.1 μm and compare them to the existing experimental data and a widespread semi-empirical model called MT_CKD. In addition to our self-continuum measurements we will report experimental results of foreign-continuum recording provided in the narrow spectral range around 4250 cm^{-1}.

The last chapter is devoted to the characterization of CO_2 absorption in the 2.3–μm transparency window. In the first part of the chapter, we will report the high sensitivity recordings of the CO_2 rovibrational spectrum and compare our results to the Ames variational line list [3] and to the CDSD database [4], which is based on the effective Hamiltonian approach. These line lists are used as sources in the frequently used HITRAN spectroscopic database and their verification with valuable experimental results is desirable.

In the second part of the last chapter, we report the accurate measurements of the CO_2 continuum in the center of the 2.3 μm region. To the best of our knowledge, this is the first laboratory detection of the weak collision-induced absorption at sub-atmospheric pressures.

Chapter 1

High sensitivity spectroscopy in 2.3–μm transparency window: Motivations and review of existing techniques in absorption spectroscopy

1.1 Scientific motivations

As shown in Fig. 1.1 for several spectral regions, Earth's atmosphere is quasi- transparent, allowing downgoing solar radiation reaching the surface and upgoing thermal radiation emitted by the surface or the atmosphere to escape into space. These regions of high transmissivity are called transparency windows. These atmospheric windows correspond mainly to spectral intervals of weak absorption of water vapor which is the main absorber in the visible and infrared regions. In this thesis work, the instrument we developed makes it possible to record high sensitivity spectra in the K band corresponding to the 2.0–2.4 μm transparency window. This latter is widely used for remote sensing by means of different instruments onboard satellites (i.e. the SCIAMACHY satellite [5], the future TROPOMI/Sentinel–5 and its precursor [6], and the Geostationary Emission Explorer [7]) and at the ground level [8–10] to retrieve methane, water vapor, carbon dioxide, carbon monoxide, nitrous oxide, and other species.

An accurate characterization of water absorption is a prerequisite for trace detection in the region because there might be interference with absorption lines used to retrieve target trace gases in the Earth's atmosphere. For instance, an insufficient knowledge of the absorption features of water vapor in the 2.3–μm region has been

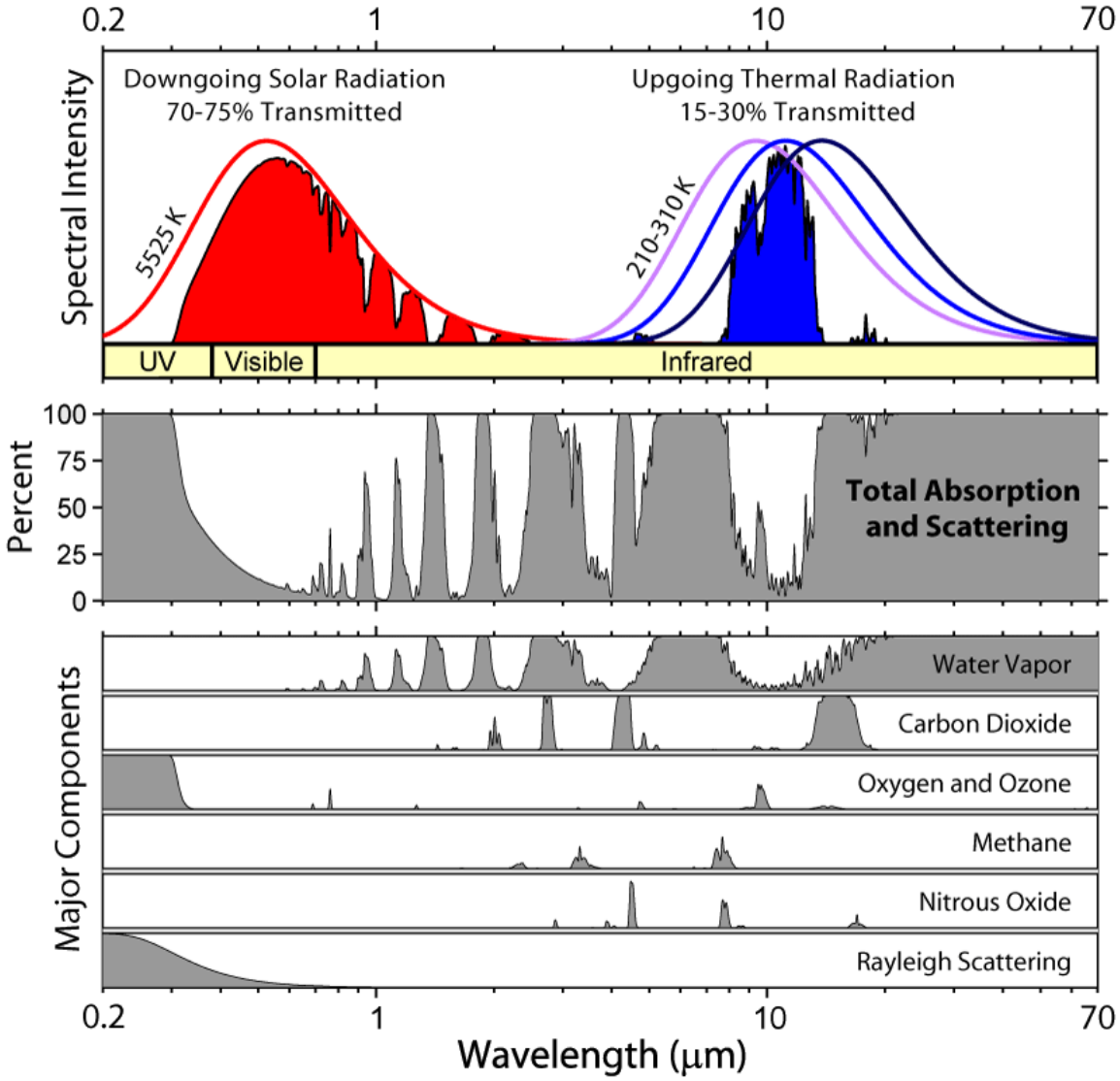

Figure 1.1. Solar and thermal radiation transmitted by the Earth atmosphere. Absorption spectra of major components of the atmosphere are also shown [11].

identified as a significant error source for the TROPOMI/Sentinel–5 precursor ESA mission. Depending on water vapor content, the CO retrieval bias showed differences of up to 15% between the driest and the most humid days [12].

Similarly to the Earth's atmosphere, Venusian atmosphere has transparency windows, yet the main absorber is the carbon dioxide and the windows correspond to regions of weak CO_2 absorption, allowing the thermal radiation emitted by the lower atmospheric layers and Venusian surface to escape into space. One of the windows is centered around 2.1 μm and is used to study the atmosphere at altitudes from 25 to 40 km, which makes it possible to study such minor constituents of the Venusian lower atmosphere as CO, H_2O, OCS, SO_2, and others [13].

In [14] Marcq *et al.* underline that the fit of the night side spectrum of Venus in the 2.3–μm region is poor due to the lack of knowledge of the CO_2 absorption

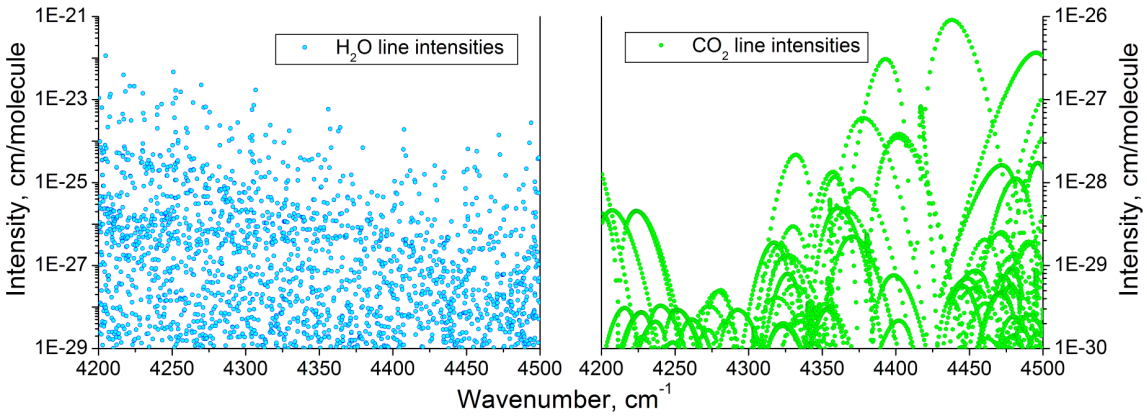

Figure 1.2. Overview of line intensities of water vapor and carbon dioxide in 2.3–μm region from HITRAN database [2].

in the window. Thus, in order to precisely characterize the content of Earth's or Venus's atmosphere, it is necessary to support ground-based observations and satellite missions with reliable and highly–sensitive laboratory measurements in the windows of background absorbers' (i.e. CO_2 and H_2O) contribution.

The laboratory study of the water vapor and carbon dioxide absorption around 2.3 μm supposes a research on two major aspects: rovibrational lines of monomer and broadband continuous absorption. An overview of monomer local lines intensities of water vapor and carbon dioxide in 2.3–μm region is illustrated in Fig. 1.2 [2]. According to the HITRAN2012 database [2], for H_2O, despite the number of relatively strong lines, there is a great number of absorption lines with intensities lower than 1×10^{-26} cm/molecule. Unlike water vapor, all CO_2 local lines have intensities lower than 1×10^{-26} cm/molecule, which requires high sensitivity in detection, and as will be shown in Chapter 5, some absorption bands are completely missing in this spectroscopic database, which is the most widely used.

Continuum of water vapor manifests as broadband slowly changing absorption component which has an important contribution in radiative transfer [15]. As will be shown later in this thesis, the continuous absorption of the water vapor and carbon dioxide in the region around 4350 cm^{-1} have values of $\approx 5 \times 10^{-4}$ and $\approx 2 \times 10^{-8}$ $cm^{-1}amagat^{-2}$ respectively, which reveals in spectrum as the baseline level increasing on the magnitude of the order of 10^{-8} cm^{-1} in absorption coefficient at pressure of 11 and 750 Torr, respectively, for water vapor and carbon dioxide.

All above mentioned features underline the need of using of highly sensitive technique to characterize the absorption of these two molecules in particular 2.3 μm transparency window. In the framework of this PhD research, we investigated this window with unprecedented sensitivity by means of cavity ring-down spectroscopy.

In the following part, some basic concepts of absorption spectroscopy will be

considered. Then we will give an overview of the highly sensitive techniques for absorption spectroscopy available in the 2 to 2.4 μm region; we will describe several of those.

1.2 Review of the high sensitivity absorption spectroscopic techniques used in the 2.3–μm region

1.2.1 Basic concepts of absorption spectroscopy

The Beer-Lambert law

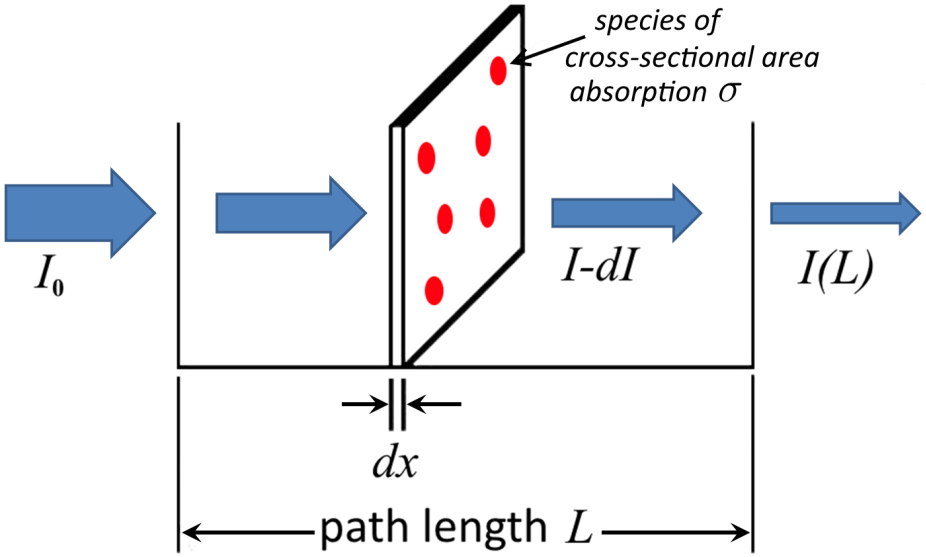

Figure 1.3. Illustration to Beer–lambert's law.

The law of decreasing radiation in an absorbing homogeneous medium of length L is easily derived by integrating the equation:

$$dI = -\alpha I dx \text{ from 0 to } L, \tag{1.1}$$

where the part dI of radiation absorbed by an infinitely small layer of medium of the thickness dx at the intensity I is proportional to the absorption coefficient α (in cm^{-1}). Its integration gives us Bouger-Lambert-Beer's law:

$$I(\nu) = I_0(\nu)e^{-\alpha(\nu)L}, \tag{1.2}$$

assuming that $I(x = 0) = I_0$, and α does not depend on x and I (Fig. 1.3). Value $\alpha(\nu)L$ represents the optical depth or thickness of the medium. The absorption coefficient α is proportional to the density of the absorber N (in molecules/cm^3) and

the absorption cross-section $\sigma(\nu)$ (in cm^2/molecule):

$$\alpha(\nu) = N\sigma(\nu) \tag{1.3}$$

Intensity of transitions

The intensity $S_{a\leftarrow b}(T)$ (cm/molecule) of the vibrational–rotational transition $a \leftarrow b$ can be expressed by the equation:

$$S_{a\leftarrow b}(T) = \frac{1}{4\pi\varepsilon_0}\frac{8\pi^3}{3hc}\frac{I_a g_a \nu_{b\leftarrow a}}{Q(T)} \exp\left(-\frac{hcE_a}{kT}\right)\left[1-\exp(-\frac{hc\nu_{b\leftarrow a}}{kT})\right]W_{b\leftarrow a}, \tag{1.4}$$

where c is the speed of light, h is the Planck's constant and k is the Boltzmann constant. $Q(T)$ is the partition function [16], $1/4\pi\varepsilon_0 = 10^{-36}$ erg·cm^3·D^{-2}, I_a is the isotopic abundance, g_a is nuclear spin statistical weight of the lower state, $\nu_{b\leftarrow a}$ is the wavenumber (in cm^{-1}) of the transition, E_a is the energy of the lower state, $W_{b\leftarrow a}$ is the transition moment squared (in D^2), which represents the transition probability weighted and is independent of both temperature and isotopic abundance.

Knowing the partition function, the lower state energy and intensity $S_{a\leftarrow b}(T_{ref})$ of the transition at temperature T_{ref}, $S_{a\leftarrow b}(T)$ can be found with the following equation:

$$S_{a\leftarrow b}(T) = S_{a\leftarrow b}(T_{ref})\frac{Q(T_{ref})}{Q(T)}\frac{\exp(-C_2E_bT)}{\exp(-C_2E_bT_{ref})}\frac{1-\exp(-C_2\nu_{a\leftarrow b}/T)}{1-\exp(-C_2\nu_{a\leftarrow b}/T_{ref})}, \tag{1.5}$$

with $C_2 = hc/k_b$.

In practice $S(T)$ (cm/molecule) of the line centered at ν_0 can be derived from the integrated absorption coefficient

$$A(T) = \int_{-\infty}^{\infty}\alpha(\nu)d\nu = NS(T) \tag{1.6}$$

knowing that

$$\alpha(\nu) = NS(T)\phi(\nu-\nu_0) \tag{1.7}$$

where $S(T)$ is the integrated absorption cross-section (in cm/molecule):

$$S(T) = \int_{-\infty}^{\infty}\sigma(\nu)d\nu, \tag{1.8}$$

and $\phi(\nu-\nu_0)$ is the normalized absorption profile function:

$$\int_{-\infty}^{\infty}\phi(\nu-\nu_0)d\nu = 1. \tag{1.9}$$

If we plot absorption coefficient α versus wavenumber the integrated absorption coef-

ficient corresponds to the area under the absorption line, which in practice is obtained with a mathematical profile, i.e., the Voigt profile.

1.2.2 Direct absorption techniques

The general idea of direct absorption techniques is to record the intensity $I(\nu)$ of the signal at the output of a singlepass or multipass cell using grating or Fourier-transform spectrometer in the case of broadband light source, or tuning the laser diode across a given spectral range. In this part we will discuss the most widely used of such techniques.

Fourier-transform spectroscopy

Fourier-transform spectroscopy (FTS) is a non-dispersive spectroscopic method based on obtaining the spectrum by means of a Fourier-transform of an interferogram recorded with a Michelson interferometer [17]. This technique became available for practical use in the mid-1960's with the advent of computers and the proposed Cooley-Tukey fast Fourier transform method (FFT) [18]. The typical scheme of a Fourier-transform experiment is shown in Fig. 1.4. The input aperture is illuminated with some light source (a globar, a tungsten lamp, or a Xenon arc-lamp, etc). The diverging beam is made parallel by means of a parabolic mirror. Next, the beam is separated in two arms with a beam splitter (BS). One half of the beam reflected by the beam splitter, goes into a first arm with the fixed mirror at the end and then is reflected back. The other half, transmitted through the BS, falls on the movable mirror and is then also reflected too. These two beams are recombined with the BS. At a given wavelength λ constructive or destructive interference occurs depending on the optical path difference (OPD) between the two arms while the entire recombined beam containing all wavelength represents a superposition of the interfering beams at each wavelength. The integrated intensity of the recombined beam passes through a cell with the absorbing gas to study and falls on the detector. A signal on the detector as a function of the optical path difference x represents an interferogram:

$$F(x) = \int_0^\infty I(\tilde{\nu}) \cos(2\pi\tilde{\nu}x) d\tilde{\nu}, \tag{1.10}$$

where $I(\tilde{\nu})$ is a real spectrum. The interferogram can be transformed into the spectrum in the wavenumber domain by means of an inverse Fourier transformation:

$$I(\tilde{\nu}) = C \int_0^\infty F(x) \cos(2\pi\tilde{\nu}x) dx \tag{1.11}$$

where C can be considered to be a normalization constant.

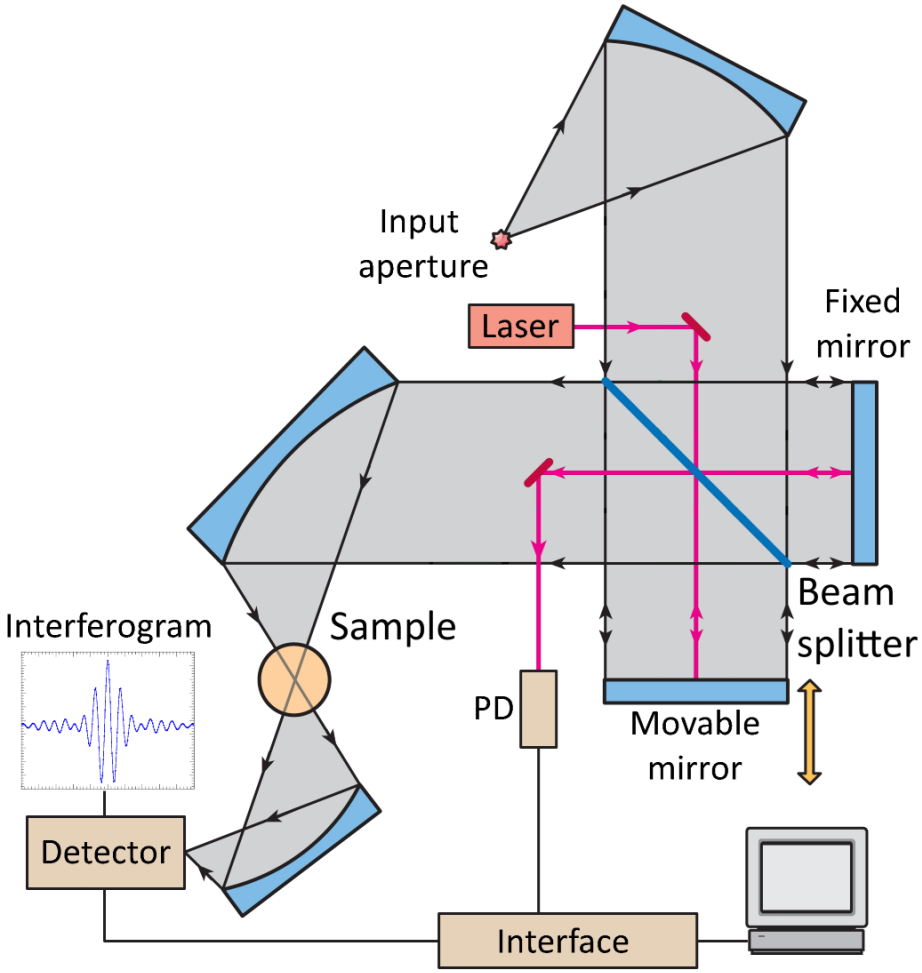

Figure 1.4. Scheme of a Fourier-transform experiment.

Equation 1.10 implies that the interferogram has to be determined with the optical path difference varying from 0 to ∞. It is obvious that in practice there is a limit on the displacement of the movable mirror in an interferometer, and the OPD is from 0 to l_0, where l_0 is the maximum optical path difference (MOPD). This truncation is equivalent to the infinitely long interferogram $F(x)$ multiplied by the rectangular, or boxcar, function Π which in the case of the mirror displacement from $-l_0$ to l_0 is defined as

$$\Pi(x) = \begin{cases} 1, |l| \leq l_0 \\ 0, |l| > l_0 \end{cases} \tag{1.12}$$

$$\widetilde{F}(x) = F(x) \cdot \Pi. \tag{1.13}$$

Therefore, the measured spectrum $\widetilde{I}(\tilde{\nu})$ is a convolution of the real spectrum $I(\tilde{\nu})$ with the sinc function (Fig. 1.5, black curve):

$$\widetilde{I}(\tilde{\nu}) = I(\tilde{\nu}) * 2l_0 \operatorname{sinc}(2\pi\tilde{\nu}l_0), \tag{1.14}$$

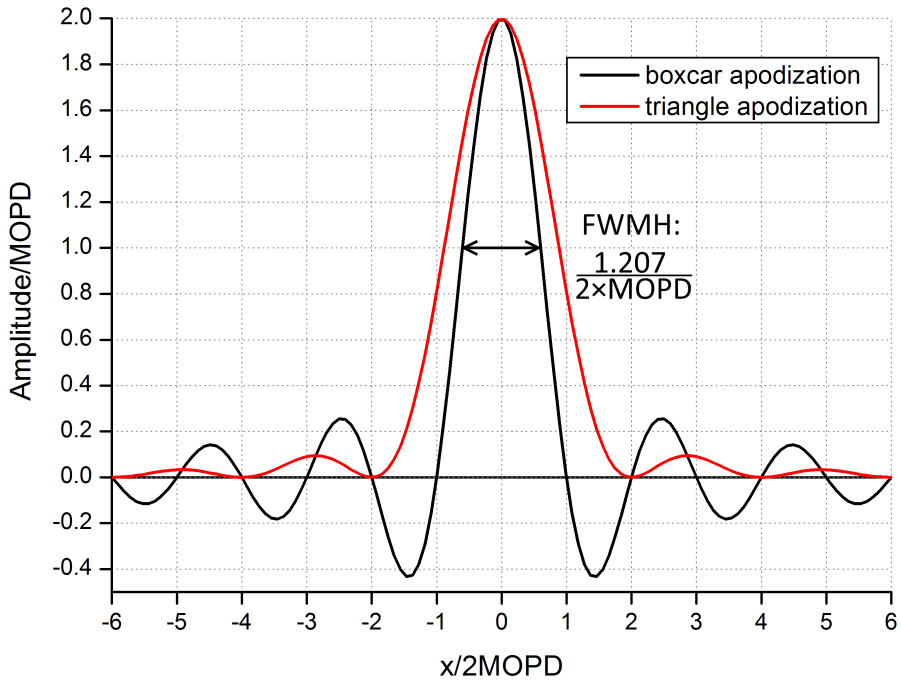

Figure 1.5. Comparison of the instrumental line shape with the 'boxcar' (black line) and the triangle (red line) apodization function.

where

$$\mathrm{sinc}(2\pi\tilde{\nu}l_0) = \frac{\sin(2\pi\tilde{\nu}l_0)}{2\pi\tilde{\nu}l_0}. \tag{1.15}$$

The sinc function is the apparatus function, or instrumental line shape (ILS), of the ideal interferometer with the full width at half maximum (FWHM) equal to $\delta\nu = \frac{1.207}{2\times l_0}$ [19]. This represents the 'unapodized' resolution of an interferometer.

In real instruments, modulation loss broadens the ILS, and phase error makes it asymmetric, which may lead to systematic error in line detection [20]. An exemplary case of the ILS of the FT-spectrometer Bruker IFS-120 HR is described in [21]. In the framework of the study, OCS spectra in the region of 4000-4200 cm^{-1} were recorded at the resolution of 0.0033 cm^{-1}.

The typical resolution for FTS experiments is 0.005 to 0.015 cm^{-1} [21–23], which corresponds to the mirror displacement (0.5×MOPD) of 100 and 33 cm respectively.

The truncation of interferogram by the 'boxcar' function leads to a ringing behavior of the ILS (Fig. 1.5). In order to reduce the amplitude of these lateral lobes, the interferogram can be multiplied by a so called 'apodization' function with a more gradual cutoff i.e. the triangle function:

$$\Lambda(x) = \begin{cases} 1 - |l|, |l| \leq l_0 \\ 0, |l| > l_0 \end{cases} \tag{1.16}$$

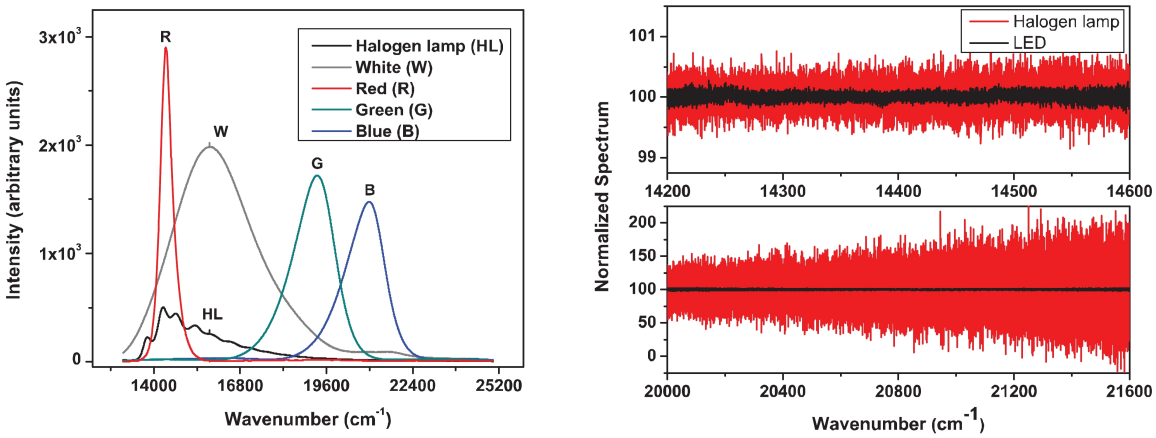

Figure 1.6. *Left panel:* Comparison of LED intensities with respect to that of the halogen lamp. *Right panel:* Comparison of S/N ratios of the normalized spectra of a red LED and a blue one with respect to that of the halogen lamp (figures are taken from [26]).

$$\widetilde{I}(\tilde{\nu}) = a \int_0^{\infty} F(x)\Lambda(x)\cos(2\pi\tilde{\nu}x)dx \tag{1.17}$$

The effect of apodization by the function $\Lambda(X)$ is the convolution of real spectrum with the function $2l_0\,\mathrm{sinc}^2(\pi\tilde{\nu}l_0)$ which damps lobes but at the same time increases the width of the main peak, reducing the resolution (red line in Fig. 1.5).

In order to achieve high sensitivity with FTS technique, two general approaches are used:

- Extension of the beam path length in the gaseous sample
- Using more intense and low noise light sources

With a view to the former, multipass absorption cells are used, i.e.: a 6-meter base multipass White cell [24] is used [23] in Kitt Peak, a 30-meter base [25] in Tomsk, and a 50-meter base [22] in Reims. The absorbing path in long-base multipass cells can reach 1800 m [22]. Such cells are unique and expensive parts of equipment. Because of the considerable volume of the cell (up to 19 m^3 [25]), a large amount of test gas is required for research, it makes it difficult to study expensive gases, e.g. isotopic enriched samples, and toxic and explosive gases.

As for the second approach, commercial bright light emitting diodes (LEDs) are used as radiation sources in FTS [25, 27]. Their spectral brightness and noise characteristics significantly exceed those of the traditional sources for interferometric spectroscopy and have excellent spatial and temporal stability of output radiation [26] (Fig 1.6).

A spectrum in the 2.3–μm region using the 30-meter multipass cell (with a total absorption path length of 1065 m) and a 50W halogen lamp was recorded in IAO,

Tomsk. The 20–hours recording of a signal at a resolution of 0.01 cm^{-1} made it possible to achieve a minimal detectable absorption coefficient of the order of 6.4 $\times$

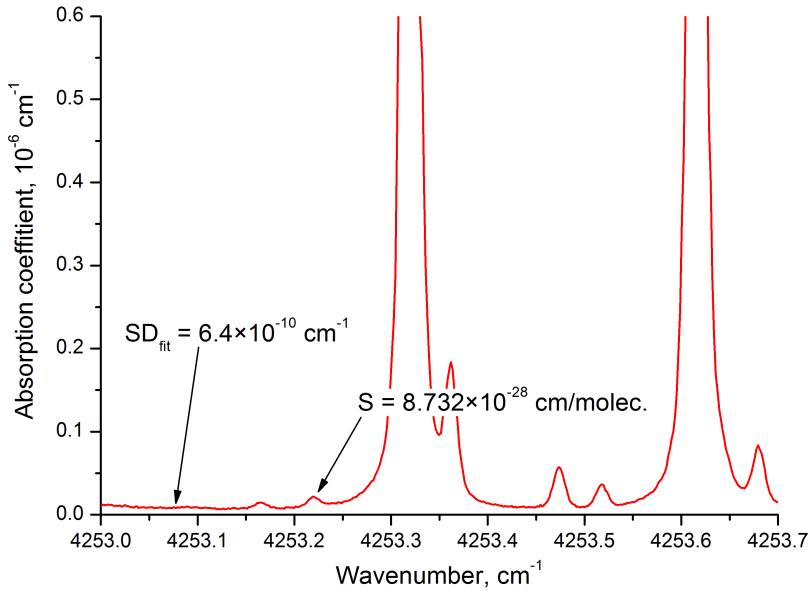

Figure 1.7. FTS sensitivity example when coupled with a multipass absorption cell (30–meter base, 19 m^3 of volume, Tomsk, Russia) and a 50W halogen lamp in 4253–4253.7 cm^{-1} microwindow.

10^{-10} cm^{-1} (Fig 1.7), which is to the best of our knowledge the highest sensitivity achieved with FTS.

Tunable diode laser absorption spectroscopy

The tunable diode laser absorption spectroscopy (TDLAS) is widely used for atmospheric gas monitoring, gas sensing in combustion conditions [28], breath analysis [29] and isotopic ratio determination [30]. Being a direct absorption technique, first performed by Hinkley [31] in 70's, TDLAS possesses a row of advantages for gas monitoring applications:

- The spectrum is directly obtained by scanning the laser across a desired absorption line of the target specie;
- Fast response time is achieved, which is necessary for example in a combustion environment;
- Resistance to misallignment due to severe environment conditions makes it possible to use *in situ* for gas sensing [32];
- Compact instrument and not too expensive;

The simplest scheme of a TDLAS experiment is illustrated on Fig. 1.8. TDLAS is a direct absorption technique based on the detection of the laser radiation transmitted along a given absorption path in a single pass or multipass gas cell. The reference

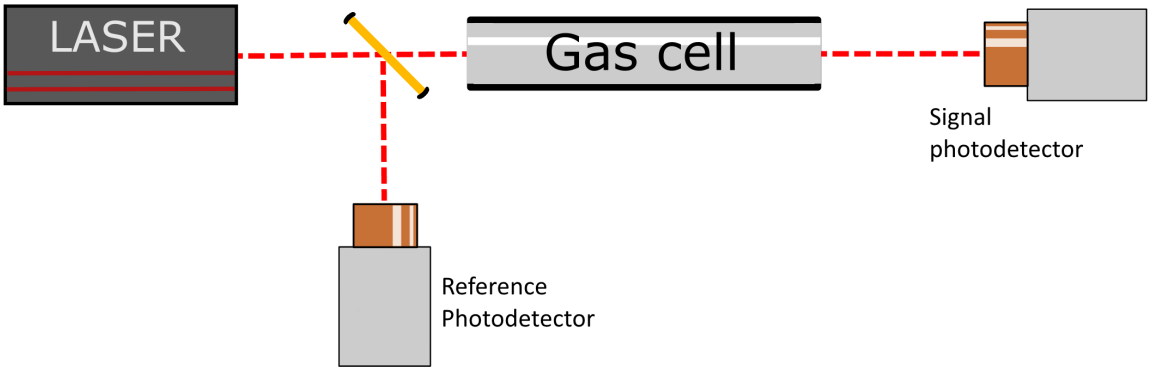

Figure 1.8. Scheme of a tunable diode laser spectroscopy experiment.

photodetector monitors the incident intensity I_0 value while the signal photodetector records the attenuated radiation which has passed through the cell with the absorber. Transmission of the radiation at wavenumber $\tilde{\nu}$ is described by Beer–Lambert law (Eq. 1.2 in Section 1.2.1):

$$T(\tilde{\nu}) = \frac{I(\tilde{\nu})}{I_0(\tilde{\nu})} = e^{-\alpha(\tilde{\nu})L} \tag{1.18}$$

For the case of weak absorption this equation can be simplified to a linear relationship:

$$\alpha(\tilde{\nu}) \approx \frac{1 - I(\tilde{\nu})/I_0(\tilde{\nu})}{L} = \frac{I_0(\tilde{\nu}) - I(\tilde{\nu})}{I_0(\tilde{\nu})L} = \left[\frac{\Delta I(\tilde{\nu})}{I_0}\right]\frac{1}{L} \tag{1.19}$$

It is therefore evident that by means of increasing the path length, we decrease the absorption coefficient which is possible to detect for given radiation attenuation ΔI.

The absorption path length L can be increased by applying a multipass absorption cell i.e. a Herriott cell [33] or a compact astigmatic mirror multipass absorption cell with a base length of about 45 cm and a total absorbing path of up to 240 m [34].

An alternative opportunity to enhance the sensitivity is to use the Wavelength Modulation Spectroscopy (WMS) approach [28]. The signal on the photodetector – called $1f$ signal – obtained from the laser with wavelength modulated at frequency f and scanning a single absorption line manifests itself as the first derivative of the absorption feature (Fig. 1.9). The true derivative is obtained if the modulation amplitude is much smaller than the absorption linewidth.

An additional increase in sensitivity can be achieved by analyzing the detector signal at $2f$ frequency [35] which reaches its maximum in the center of the absorption line and has no or very low signal when there is no absorption. Thanks to the WMS-2f/1f method applied by Chao *et al.* [28] the detection limit of CO concentration in the 2.3 μm region was improved from 140 ppm to <10 ppm (corresponding to 3.4×10^{-6} cm^{-1} in absorption coefficient) compared to the direct absorption technique. Coupling the WMS technique with a commercial 100-meter astigmatic multipass cell [36] made

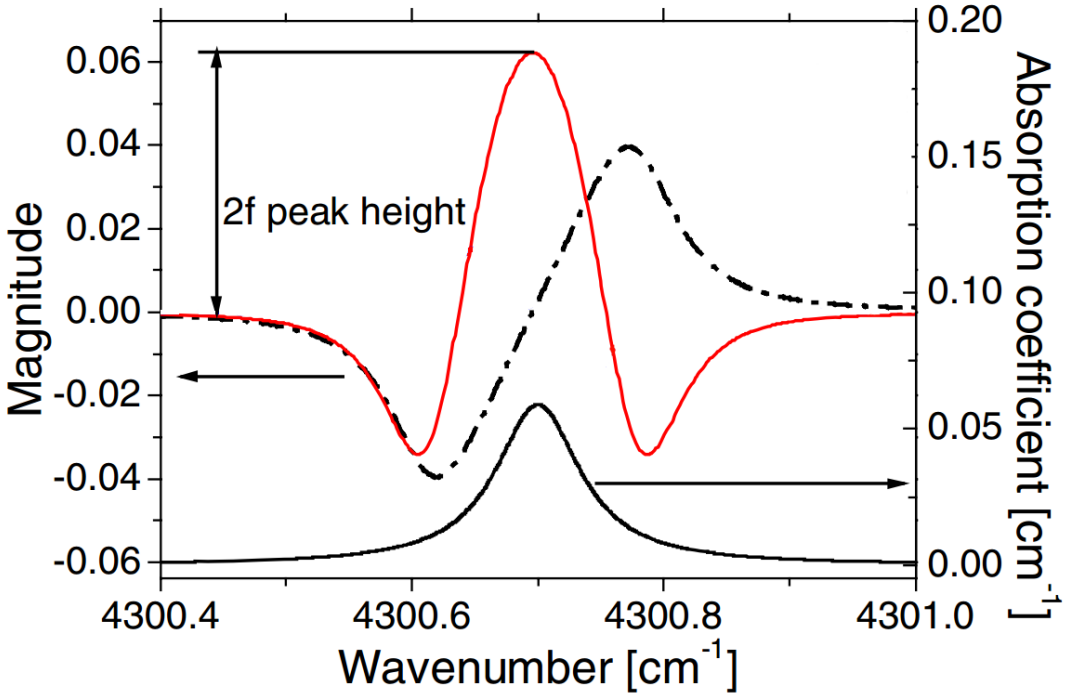

Figure 1.9. Calculated harmonic components of the $1f$ (dash dot curve) normalized transmitted $2f$ (red curve) signal at 500 K with 2% CO in N_2 for the $R(11)$ line at 4300.7 cm^{-1} with a pathlength of 9.9 cm [28]

it possible to measure carbon monoxide mixed with nitrogen with a detection level of 0.3 ppmv (1.2×10^{-7} cm^{-1}) [37].

The TDLAS technique handles gas detection and concentration measurement using strong lines of the target gas, but its scientific application is limited because of the insufficient sensitivity in the retrieval of spectroscopic parameters of weak absorption lines in transparency windows. The sensitivity of cavity–enhanced techniques to be discussed further makes it possible to achieve several orders of magnitude higher sensitivity than the direct laser absorption technique.

1.2.3 Cavity–enhanced absorption techniques

Cavity–enhanced absorption techniques are a group of spectroscopic methods where the absorbing gas is put in a high finesse optical cavity to maximize the time of interaction between the gas of interest and radiation. At the beginning of the section, we will discuss the physics of optical cavities, their eigenmodes and characteristics. After that, we will discuss several cavity–enhanced spectroscopic techniques and their performance in 2.3–μm region.

Optical cavities

Within the framework of problems dedicated to the description of the propagation of laser beams with low divergence close to the optical axis, it is possible to apply the important paraxial approximation. In this approximation, we can write the Maxwell wave equation as [38]:

$$\frac{\partial^2 E}{\partial x} + \frac{\partial^2 E}{\partial y} - 2ki\frac{\partial^2 E}{\partial z} = 0, \tag{1.20}$$

where $E(x, y, z)$ is the field and k is the wave factor. The solution of the equation in a Cartesian coordinate system is a Hermite-Gaussian (HG) beam, which is written as

$$E_{mn} = E_0 \frac{w_0}{w(z)} H_m\left(\sqrt{2}\frac{x}{w(z)}\right) H_n\left(\sqrt{2}\frac{y}{w(z)}\right) \exp\left(-\frac{r^2}{w(z)^2}\right) \times \exp\left(i\frac{kr^2}{2w(z)} - i(m+n+1)\arctan\frac{z}{z_0} + i(kz - \omega t)\right), \tag{1.21}$$

where $r^2 = x^2 + y^2$ and H_i denotes the i-th Hermite polynomial [39]. Functions $w(z)$ and $R_c(z)$ represent the beam size (the radius where the field amplitude drops to $1/e^2$ of the maximum) and the curvature of the wavefront, respectively:

$$w(z) = w_0\sqrt{1 + \left(\frac{\lambda z}{\pi w_0^2}\right)^2} = w_0\sqrt{1 + \left(\frac{z}{z_0}\right)^2}, \tag{1.22}$$

$$R_c(z) = z\left[1 + \left(\frac{\pi w_0^2}{\lambda z}\right)^2\right] = z\left[1 + \left(\frac{z_0}{z}\right)^2\right] \tag{1.23}$$

with the beam waist $w_0 = w(z = 0)$ and the Rayleigh range z_0 indicating the distance from the waist of the beam to the point where the beam diameter is equal to $\sqrt{2}w_0$.

$$z_0 = \frac{\pi w_0^2}{\lambda}. \tag{1.24}$$

The cavity is an optical resonator consisting of two highly reflective mirrors of radii of curvature R_1 and R_2 aligned along an optical axis z (Fig. 1.10). In order to find resonant modes of a cavity formed by two spherical mirrors, we will apply boundary conditions to the HG beam. These are as follows:

- wavefront curvatures coincided with the curvature radii of the resonator's mirrors at the location of mirrors;
- the amplitude of the wave is zero on the mirrors (the standing wave caused in the resonator has a node there);

By applying the boundary conditions to the HG beam, we will obtain the resonant modes denoted TEM_{mn} (TEM here stands for the Transverse Electromagnetic Mode),

which have a different field distribution in the xy–plane (see Fig. 1.10). The principal mode TEM_{00} has the form of a Gaussian peak and most of the field is concentrated along the principal axis of the cavity.

The frequency eigenvalues of the cavity:

$$\nu_{nml} = \frac{lc}{2n_0 L} + \frac{c}{2n_0 \pi L}(n + m + 1) \arccos \sqrt{g_1 g_2}, \tag{1.25}$$

where L is the cavity length, n_0 the refractive index of medium inside the cavity, l is the longitudinal mode index and g_i with $i = 1, 2$ are parameters of geometric configuration equal to:

$$g_1 = 1 - \frac{L}{R_1} \tag{1.26}$$

$$g_2 = 1 - \frac{L}{R_2} \tag{1.27}$$

will be discussed below. According to Eq. 1.25 the frequency spacing – Free spectral range (FSR) – between two adjacent longitudinal modes l and $l + 1$ for equivalent transverse mode TEM_{mn} is

$$f_{FSR} = \frac{c}{2n_0 L}. \tag{1.28}$$

It is worth noting that the wavefront curvature radii of HG beams are the same as that of the fundamental Gaussian beam, and if at least one beam of the family (e.g. the fundamental one when $m = n = 0$) meets the boundary conditions on the mirrors, all the other beams of the family will meet the condition, yet at a different frequency. HG beams can therefore be the resonant modes in a resonator formed by spherical mirrors, although the resonator has no astigmatism [40]. Applying the curvature

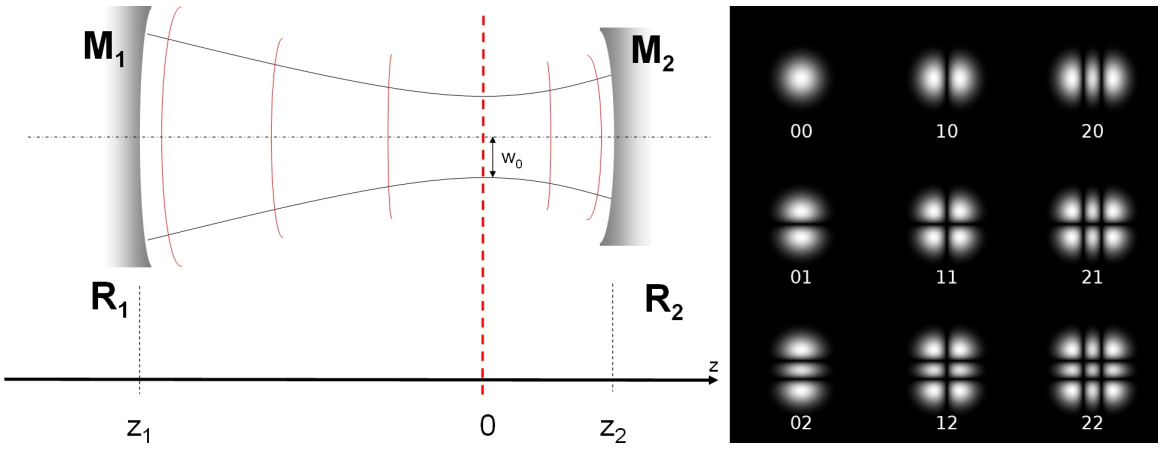

Figure 1.10. Optical resonator formed by two spherical mirrors (left). The field distribution corresponding to different TEM_{mn} (right)

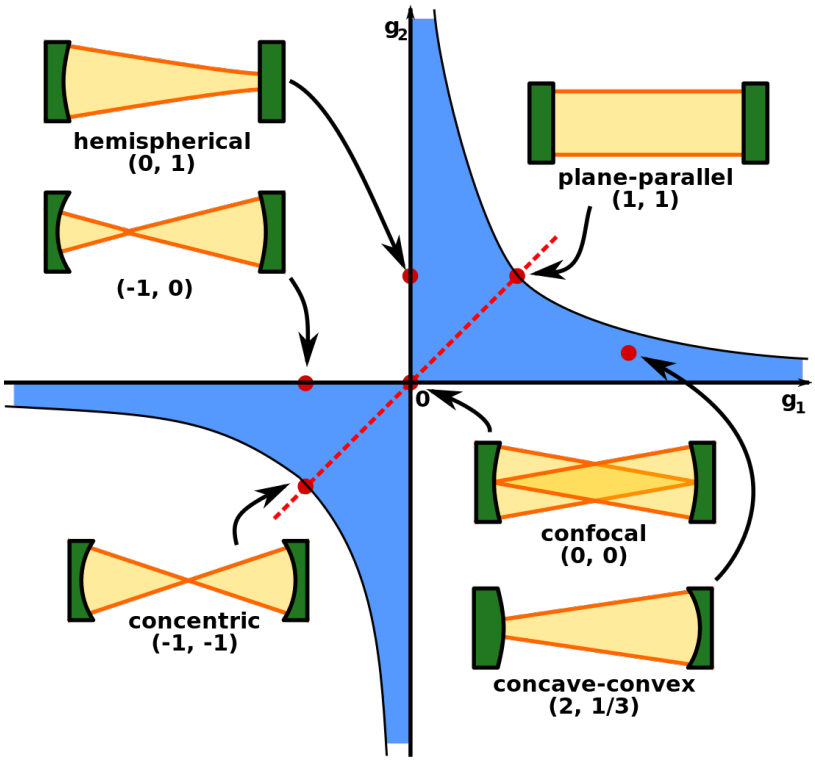

Figure 1.11. A diagram of stability of an optical resonator [41].

conditions on two mirrors we can find the waist of the intracavity beam

$$w_0 = \sqrt{\frac{\lambda L}{\pi}} \frac{(g_1 g_2 (1 - g_1 g_2))^{\frac{1}{4}}}{(g_1 + g_2 - 2 g_1 g_2)^2} \tag{1.29}$$

The above mentioned parameters g_1 and g_2 define the stability of the resonator, the characteristics of ability of the resonator to refocus the intracavity beam after one round trip. In the case of the unstable cavity the beam size grows without a limit and leaves the cavity. The $ABCD$ law for a finite beam size gives the following condition [38]:

$$0 \leq g_1 g_2 \leq 1. \tag{1.30}$$

The stability condition can be illustrated graphically on $g_1 g_2$–plane (Fig. 1.11) blue-shaded areas correspond to stable configurations.

In an optical resonator composed of two mirrors of reflectivity $\mathcal{R}$ and transmittance $\mathcal{T}$, interference between multiple reflected light fields traveling inside the cavity creates frequency-dependent transmission described by the Airy function [38] (Fig. 1.12)

$$T_{cav} = \frac{\mathcal{T}^2}{(1 - \mathcal{R})^2 + 4\mathcal{R} \sin^2 \frac{\Phi}{2}}, \tag{1.31}$$

where Φ is round-trip phase equal $4\pi n_0 L/\lambda$, L is a cavity length. It reads that

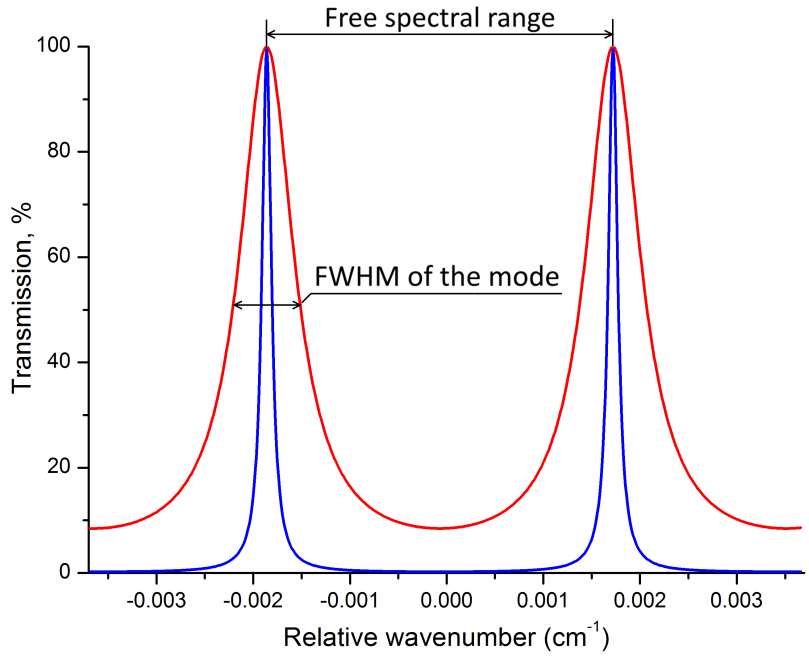

Figure 1.12. Function of optical cavity transmission. Red curve correspond to the 140–cm cavity formed by two mirrors with reflectivity of 55%. Blue curve – to 90% of reflectivity

constructive interference occurs when round trip phase $\Phi \equiv 0 \pmod{2\pi}$. The FSR is equal to $f_{FSR} = c/2n_0L$, and is the inverse of round trip time. Around the resonance, ($\Phi \equiv 0 \pmod{2\pi}$) T_{cav} can be described with a first-order of a Taylor series; hence, T_{cav} can be presented as a Lorentz function:

$$T_{cav} \approx \frac{\frac{(1-\mathcal{R})^2}{\mathcal{R}}}{\Phi^2 + \frac{(1-\mathcal{R})^2}{\mathcal{R}}} \tag{1.32}$$

with its full width at half maximum (FWHM)

$$\Delta\Phi = \frac{2(1-\mathcal{R})}{\sqrt{\mathcal{R}}}. \tag{1.33}$$

The FWHM depends on the reflectivity of the cavity mirrors and for $\mathcal{R} \to 1$ resonance peaks becomes very narrow. As two consecutive longitudinal modes have a phase difference of 2π we can write that the finesse $\mathcal{F}$ is:

$$\mathcal{F} \doteq \frac{f_{FSR}}{\Delta\nu_c} = \frac{2\pi}{\Delta\Phi} = \frac{\pi\sqrt{\mathcal{R}}}{1-\mathcal{R}}, \tag{1.34}$$

where $\Delta\nu_c$ is the FWHM of longitudinal mode in frequency domain. For $R \approx 1$ $\mathcal{F}$ can be approximated by $\pi/(1-\mathcal{R})$. Using highly reflective mirrors makes it possible to increase the effective path of radiation inside the cavity by the factor of $G = 2\mathcal{F}/\pi = 2\sqrt{\mathcal{R}}/(1-\mathcal{R})$ [42]. So, for a 1–meter long cavity with $\mathcal{F} = 50000$, the effective path

length is of the order of 32 km, which drastically increases the sensitivity of the system compared to a multi–pass absorption cell.

Intracavity laser absorption spectroscopy

The broadband Intracavity Laser Absorption Spectroscopy technique (ICLAS) suggested in the 1970ies in [43] consists in extinguishing laser radiation at frequencies of absorption lines of a medium placed inside a broadband laser resonator, whose generation width significantly exceeds the width of the spectral lines under study. Herein, the radiation spectrum of the laser has dips at absorption line frequencies. These dips can be next recorded by means of conventional spectroscopic devices (see Fig. 1.13).

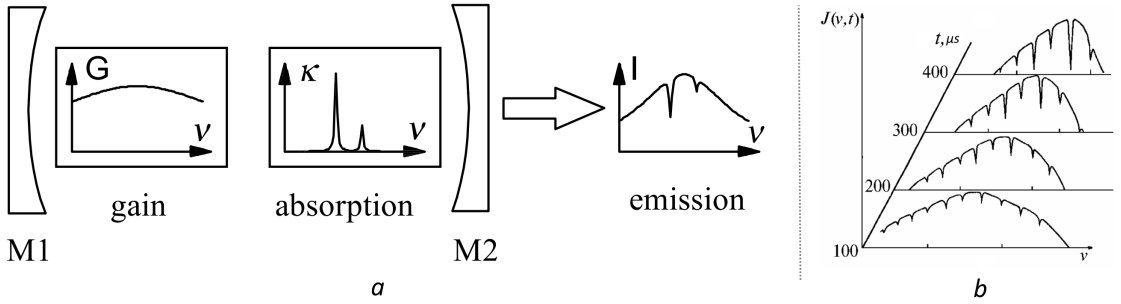

Figure 1.13. *a*: Schematic of the ICLAS technique; *b*: Evolution of an ICLAS spectrum

During the laser generation, absorption lines grow with time in the spectrum according to the Lambert-Beer law:

$$J(\tilde{\nu}, t) = J(\tilde{\nu}, t_0) e^{-\alpha(\tilde{\nu}) L_{eq}}, \tag{1.35}$$

where L_{eq} denotes an equivalent path length equal to continuous generation time t_g multiplied by the speed of light c in the medium. $J(t_0)$ is the normalized laser emission spectrum built up at time t_0 corresponding to the beginning of the generation.

The threshold sensitivity of an ICLAS instrument is generally defined by the equivalent length L_{eq} of the interaction between laser radiation and the medium, which is proportional to continuous generation time near the absorption line under study:

$$L_{eq} = t_g c \mu, \tag{1.36}$$

where $\mu = L_{abs}/L_{cav}$ is the coefficient defining the part which the absorber occupies in the cavity.

The reader can find a more detailed description of the ICLAS technique in [44–46].

In the 2.3–μm region, the ICLAS technique was applied using a Vertical External Cavity Surface Emitting Laser (VECSEL) source [47] leading to a sensitivity of the order of $\alpha_{min} \approx 1.5 \times 10^{-9}$ cm^{-1} with a maximum generation time of 400 μs ($L_{eq} = 54$ km with $\mu = 0.45$). Such a sensitivity made it possible to detect CO_2 lines with intensities down to 2×10^{-28} cm/molecule.

Optical feedback cavity enhanced absorption spectroscopy (OF–CEAS)

The group of CEAS techniques, also known as integrated cavity output spectroscopy (ICOS), is focused on the detection of either the peak amplitude or the time–integrated signal at the output of the cavity [48]. In this approach the optical cavity is a direct analog of a multi–pass absorption cell, which is used to enhance the sensitivity of the system by means of increasing the absorbing path length.

The inefficient injection of laser radiation with a typical bandwidth of 2 MHz (for distributed feedback laser) which is much larger than the width of a cavity mode ($\approx$ 1 kHz) due to high–frequency phase noise produces a very weak and noisy cavity output signal. This problem can be solved by narrowing the laser and locking it to a cavity resonance mode.

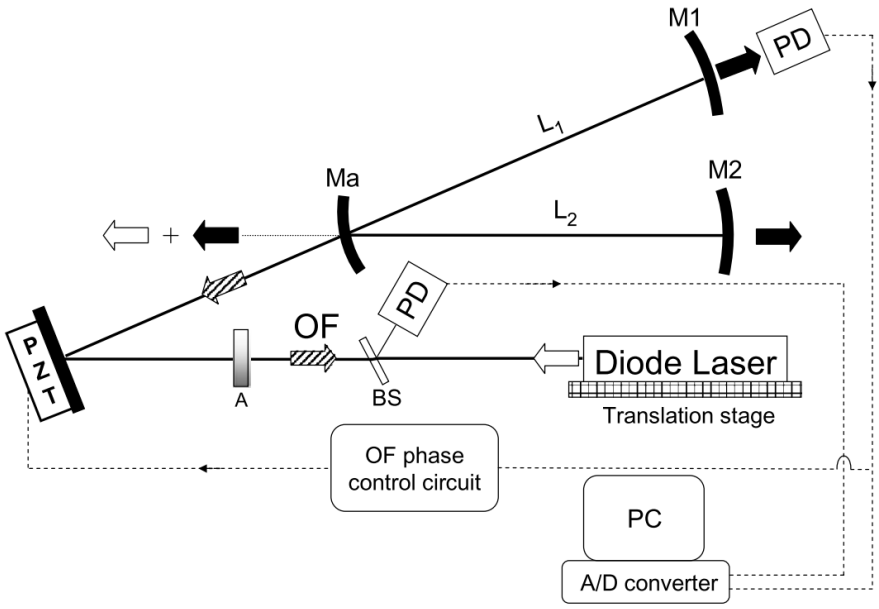

Figure 1.14. Schematic of OF–CEAS experiment [49]. PD is photodiode; BS – beam splitter; PZT – piezoelectric transducer;

In this section we consider Optical Feedback Cavity Enhanced Absorption Spectroscopy when a semiconductor laser producing a broad bandwidth radiation is passively narrowed by means of the optical feedback from the high-finesse cavity and is locked and hence efficiently injected into the cavity. A detailed description of OF–

CEAS is given in [49]. More on the detailed theoretical analysis of optical feedback stabilization of semiconductor lasers can be found in [50].

The spectral narrowing of the laser is a consequence of the sensitivity of semiconductor lasers to optical feedback and the optical cavities feature of filtering injected radiation and return the narrowed filtered signal to the laser. The schematic of a typical OF-CEAS as built in our group experiment is shown in Fig. 1.14. A V–shaped cavity is formed of three identical concave mirrors. Thanks to such a cavity configuration, the optical feedback towards the diode laser source comes only from the high-finesse cavity when the laser frequency matches one of the narrow longitudinal cavity modes. This feedback light from the cavity is not masked by the signal reflected by the input mirror M_a. A diode laser is focused by a single aspheric lens so that its waist is superposed with that of the L_1 arm of the cavity. The reference detector measures the initial laser intensity while the signal detector behind the mirror M_1 records the cavity output. To seed the laser source, the narrow feedback signal from the cavity must have the same phase. This phase of the feedback signal depends on the distance between the laser and the cavity, which is actively controlled by a mirror mounted on a PZT to remain at the optimum value.

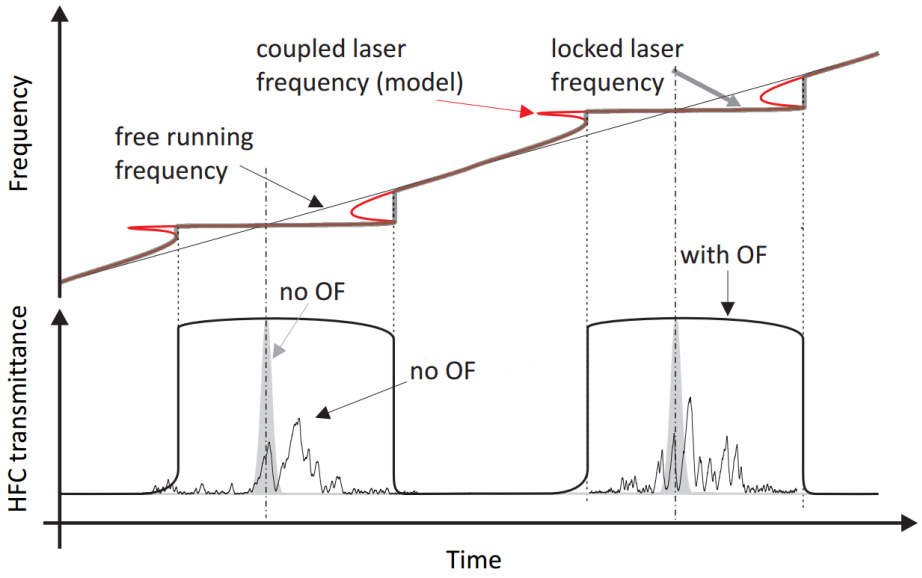

Figure 1.15. Laser frequency tuning and cavity transmission in the case of free tuning and OF locking [51].

When the free running laser being detuned from the high finesse cavity resonance is inside the locking range, there is a feedback phase that forces laser emission back to this resonance frequency [50]. Thus, when the laser is being slowly tuned, optical feedback is keeping it locked to the mode of the cavity long enough to build up the intracavity field, and thus eliminate amplitude noise intrinsic to free–tuning laser injection (Fig. 1.15).

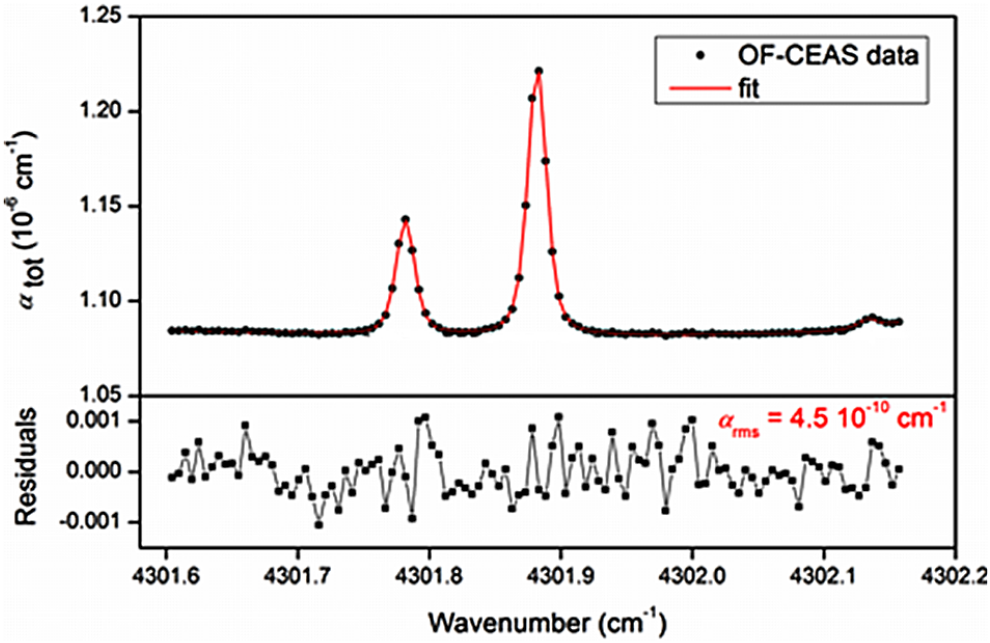

Figure 1.16. *upper panel*: Example of a OF–CEAS spectrum [52] (black dots) of water vapor. Fitted spectrum (red solid line); *lower panel*: Fit residuals.

The OF–CEAS technique measures the maximal signal $\mathcal{H}_{max}$ at the output of the cavity, which, in effect, is the peak transmission to within a factor of k. To calibrate this transmittance and obtain an absolute absorption coefficients, we need a single ring-down measurement with the sample inside the cell. The ring-down decay is obtained by interrupting laser injection while the laser frequency is at resonance with the cavity mode (for more information, see Part 1.2.3). The ring–down decay rate γ_m at mode m can be written as [53]

$$\gamma_m = c\alpha_m - \frac{c}{L}\ln(\mathcal{R}\mathcal{R}_1) \simeq \frac{K}{\sqrt{H_{max(m)}}}, \tag{1.37}$$

where α_m is the absorption coefficient of the mode m, $\mathcal{R}$ and $\mathcal{R}_1$ are the reflectivities of the V–shape cavity and folding mirrors, and K is the factor k multiplied by the other parameters of the system. Therefore, γ_m gives the absorption coefficient α_m. So, having obtained the K factor, which is constant throughout the laser scan, and then measuring the transmission H_{max}, it is possible to deduce the calibrated absorption spectrum.

Such a technique applied to the 2.3–μm region made it possible to achieve the noise level of the order of 4.5×10^{-10} cm^{-1} [52] (see Fig. 1.16). The advantage of this technique is the fast scan rate of up to 50 Hz with a sensitivity to absorption coefficients of the order of 10^{-9} cm^{-1} in [53], which makes it suitable for real–time trace gas detection.

Continuous wave cavity ring-down spectroscopy (CW–CRDS)

Cavity ring-down spectroscopy (CRDS) is based on the temporal measurement of the exponential decay of the radiation inside a high finesse optical cavity after the injection of photons was interrupted.

To find the cavity photon lifetime, we will consider a wave with a Gaussian distribution of the field.

$$E_{in}(x,y,z,t) = E_0(x,y,z)e^{i(\omega t - kz)} \tag{1.38}$$

which is injected in a symmetric linear cavity of length L and is exciting the TEM_{00} mode. Taking into account that the beam is refocused by the cavity mirrors after each round trip and that it has a small intensity loss due to transmission, scattering, and absorption on the mirrors, we can write down the expression for the field at the output of the cavity:

$$E_{out} = E_0(x,y,z)\sum_{p=0}^{\infty} t^2 r^{2p} e^{i\omega(t-2pL/c-L/c)-ikz} = \frac{t^2 e^{-i\omega L/c}}{1-r^2 e^{-i\omega t_r}} E_{in}(x,y,z,t) \tag{1.39}$$

where t and r are the field transmission and the reflection coefficients of both cavity mirrors respectively. Taking the square of those coefficient yields the corresponding coefficients $\mathcal{T}$ and $\mathcal{R}$ for light intensity. Turning from field to intensity by taking the squared absolute value gives the intensity transmitted by the cavity (the Airy function):

$$I_{out} = \frac{\mathcal{T}^2}{|1-\mathcal{R}e^{-i\omega t_r}|^2} I_{in} = \frac{\mathcal{T}^2}{(1-\mathcal{R})^2} \frac{I_{in}}{1+\left(\frac{2\sqrt{\mathcal{R}}}{1-\mathcal{R}}\right)^2 \sin^2(\omega t_r/2)} \tag{1.40}$$

Considering the pulsed excitation of the cavity, we can derive the relation between $\delta\nu_c$ and ring–down time τ_0 which takes place with negligible absorption inside the cell. Mathematically, it can be obtained as a convolution of the pulse time profile and the Fourier transformation of Eq. 1.39 obtained for $r \approx 1$. With the impulse shaped like the delta–function we obtain the exponential decay of the field. Turning to the intensity $I = |E|^2$, the exponential decay is twice faster and is inversely proportional to the FWHM of the cavity mode (Eq. 1.33):

$$\tau_0 = \frac{1}{2\pi\Delta\nu_c} = \frac{L}{c}\frac{\sqrt{\mathcal{R}}}{(1-\mathcal{R})}. \tag{1.41}$$

Allowing for the absorption inside the cavity, we consider that after each passage through the cavity, the field is decreased by the factor of $\exp(-\alpha L/2)$, where α is

the absorption coefficient, defined by the Beer–Lambert law (the factor 1/2 stemming from the field rather than the intensity being considered). We can see that the absorption factor can be associated to the mirror reflectivity and transmittance due to the fact that after each adjacent passage it passes the absorption medium and is reflected by the mirror, and during the first passage the field transmitted by both mirrors is attenuated by the $\exp(-\alpha L/2)$ factor. Hence, it gives us the global multiplication factor, so we can write Eq. 1.39, applying the following substitutions:

$$r \to re^{-\alpha L/2} \quad \text{or} \quad \mathcal{R} \to \mathcal{R}e^{-\alpha L} \tag{1.42}$$

$$t^2 \to t^2 e^{-\alpha L/2} \quad \text{or} \quad \mathcal{T}^2 \to \mathcal{T}^2 e^{-\alpha L}. \tag{1.43}$$

This will result in the photon lifetime in the cavity (the ring-down time) affected by intracavity absorption:

$$\tau_\alpha = \frac{L}{c} \frac{\sqrt{Re^{-\alpha L}}}{1 - Re^{-\alpha L}}. \tag{1.44}$$

In the approximation of $R \to 1$, this equation resolves into

$$\tau_\alpha(\nu) = \frac{L}{c(1 - \mathcal{R} + \alpha(\nu)L)}; \tag{1.45}$$

therefore, in CRDS, the absorption coefficient $\alpha(\nu)$ can be obtained as

$$\alpha(\nu) = \frac{1}{c\tau} - \frac{c(1-\mathcal{R})}{cL}, \tag{1.46}$$

where the value $L/(c(1-\mathcal{R}))$ is the ring-down time τ_0 (to within $\sqrt{\mathcal{R}}$, which is very close to 1) conditioned by losses due to the reflectivity of the mirrors, scattering, etc. in the absence of the absorbing matter and defines the baseline of the spectrum.

Originally, pulsed lasers were used for the first applications of CRDS [54]. Nearly a decade after the pioneering work on pulsed CRDS, continuous wave lasers were applied in CRDS [55–57].

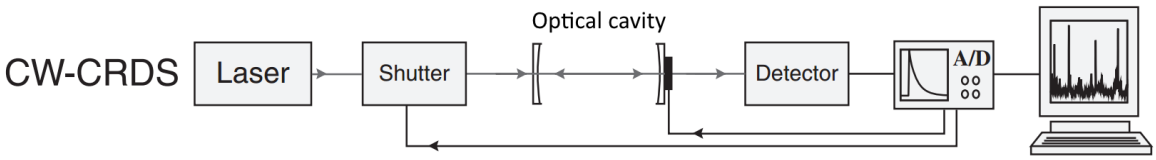

Figure 1.17. Schematic of CW–CRDS experiment [58].

A simplified schematic of a CW-CRDS experiment is presented in Fig. 1.17. The ring-down decay signal in CW–CRDS occurs when the interaction between the cavity mode and the exciting laser is interrupted. There are several ways to achieve fast interruption:

- fast electronic modulation of frequency or amplitude of the laser
- fast modulation of the cavity length; hence, resonance frequency modulation
- using a fast optical switch,

with the latter being the most widespread, and it is mostly done by means of an acousto-optic modulator when the threshold signal level is achieved on the detector.

The CRD technique is one of the most sensitive techniques used in absorption spectroscopy. In the 1.6–μm region over 4.5 days averaging with the Noise Equivalent Absorption of 2.6×10^{-11} cm^{-1}Hz$^{-1/2}$ made it possible to detect the S4 transition of N_2 of the (0–3) band with an intensity of 1.5×10^{-31} cm/molecule, which corresponds to the minimal detectable absorption coefficient 5×10^{-13} cm^{-1} [59]. In the 2.17–μm region, Bray et al. recorded a tritiated water (HTO) spectrum with a noise level of 1×10^{-9} cm^{-1} for about 50 averaged ring–downs at each wavenumber and with limit of detection of 1.2×10^{-10} cm^{-1} (600 ring-downs per spectral point) [60].

During this thesis, we developed a CW–CRDS instrument for the 2.3–μm region using different laser sources with achieved sensitivities down to 1×10^{-10} cm^{-1}. A detailed description of our CRDS set-up in the 2.3–μm region is given in the next Chapter.

Chapter 2

The Cavity ring-down spectrometer developed for the 2.3–μm region

Even though high sensitivity techniques such as ICLAS [47] and OF-CEAS [61] have already been developed in the 2.3–μm region, to the best of our knowledge, only the aforementioned experiment of Bray et al. [60] and a pulsed-CRDS experiment by Zhao et al. [62] with a detection sensitivity of the order of 2.0×10^{-7} cm^{-1} have previously been reported in this region. This restricted number of experimental developments is probably related to technical limitations such as less powerful and non-fibered laser sources, less sensitive detectors and the unavailability of elements adapted for this spectral region.

Designing our setup we aimed to cover a maximal spectral range in 2.3–μm window, and in order to do that, different laser sources (3 units of DFB and 1 VECSEL) were used. The DFB lasers were purchased from Nanoplus and the VECSEL was obtained through a collaboration with Innoptics and the Institut d'Électronique et des Systèmes (IES). The development of the CRDS experiment with each single source introduced a number of specific aspects and tasks, so we separated descriptions of the different setups in individual sections. Moreover, in this chapter we will describe the gain in the performance of the DFB when we narrow it by means of Optical Feedback (OF) and an increase in sensitivity we got thanks to the tracking of the resonance cavity mode in the generation of ring-down (RD) events.

2.1 CW–CRDS with a standard DFB

The first implementation of CRD-spectrometer is presented in Fig. 2.1. The High Finesse Cavity (HFC) consists of a stainless steel tube having the length of 1400±5

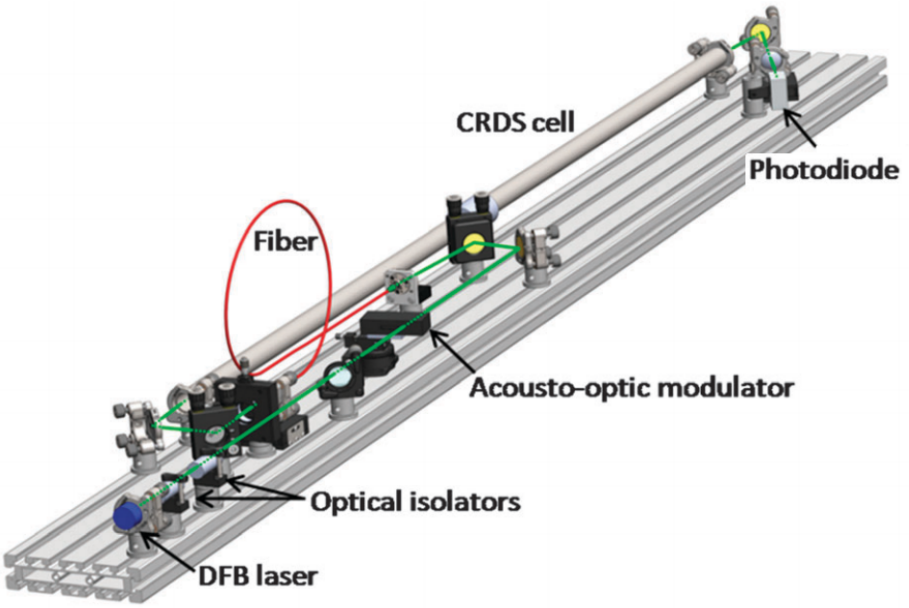

Figure 2.1. General view of CRDS spectrometer. Infrared beam trajectory is marked green.

mm and an inner diameter of 10.5 mm with highly reflective mirrors at both ends. These dielectric mirrors, manufactured by Layertec, have a reflectivity higher than 99.99% from 2170 nm to 2490 nm with a maximum around 2330 nm (Fig. 2.2). Transmittance has the value of ≈0.01% at 2300 nm with normal beam folding. Such mirrors ensure a cavity finesse > 31000 in the region from 2170 to 2490 nm leading to a ring-down time of 46 μs and better (up to 120 μs in the 2330 nm region) with the cavity evacuated. The mirrors have a radius of curvature of 1 m and are wedged by 1 ° to avoid interference fringes. In order to achieve a resonant coupling between the laser and the HFC, the output mirror was mounted on a PZT to change the cavity length and move the longitudinal modes over one FSR.

In its first version, the spectrometer used as a light source a Distributed FeedBack (DFB) Nanoplus laser diode (DFB 2351 nm) driven by home-made temperature and current boards. The diode was frequency tuned between 4248.8 and 4257.3 cm^{-1} by stepping up its temperature from 18 °C to 40 °C with a constant laser current of 136 mA. The emitted power of this laser was typically 5.5 mW at the maximal operational current (140 mA).

Each time resonance occurs, the light transmitted through the HFC is detected by a Hamamatsu G12183–203K InGaAs PIN photodiode followed by a transimpedance amplifier. When the photodiode signal (in volts) is higher than the threshold value set by the user a RD event is generated by switching off the beam with an anti-reflection coated acousto-optic modulator (AOM, IntraAction Corp. ACM–1002AA1) placed before the fiber injection optics. The frequency driving the AOM was generated by a

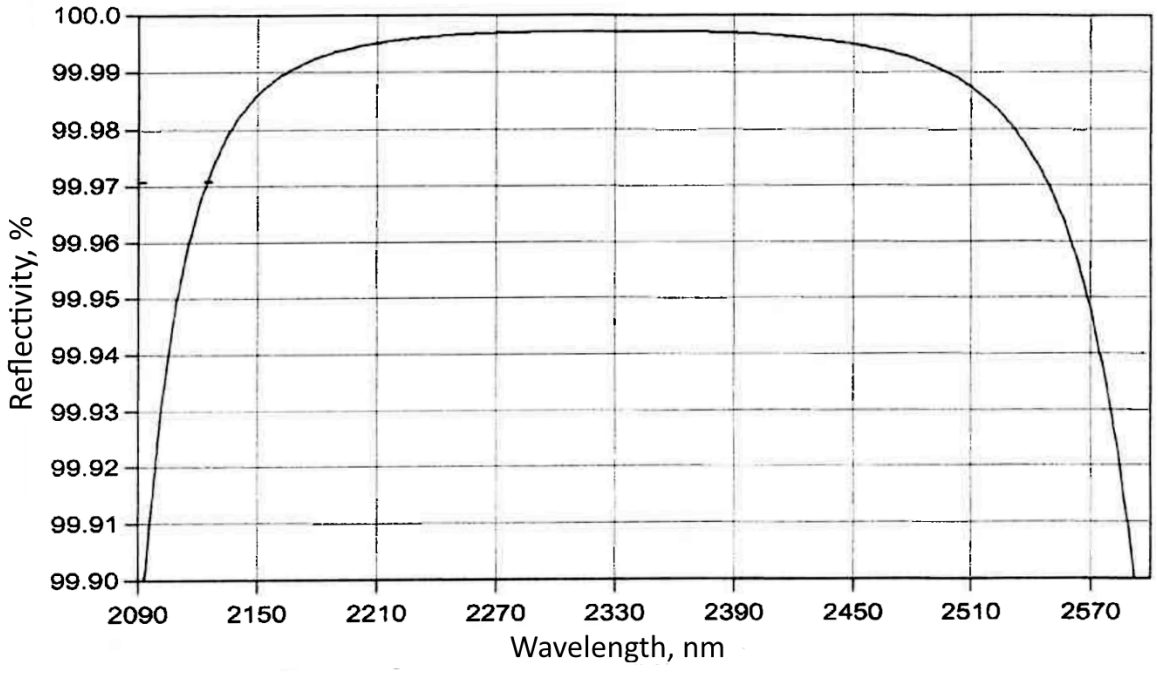

Figure 2.2. Reflection coefficient of the mirrors used in our high finesse cavity. The curve is extracted from the datasheet provided by Layertec.

Rohde&Schwartz SMC100A radio frequency generator, and it was optimized at 98.9 MHz to get the maximal power in the first order of diffraction. Efficiency of the AOM was about 25%.

To eliminate beam distortions caused by the AOM and get a Gaussian beam before injection into the HFC, the first order of the laser beam diffracted inside the AOM was sent into a Thorlabs P3–23Z–FC–1 monomode fiber with a 9 μm core made of ZrF_4 fluoride fiber. The injection efficiency was 50%, which gave about 0.3 mW of power at the output of the fiber. This corresponds to 5.5% of the laser output power, and most of it (about 75%) was lost in the AOM. A lens with a focal length of 11 mm was placed at the distance of 9.88 mm from the fiber output. This distance and the distance between the fiber output and the input mirror of the high finesse cavity (256 mm) are critical to obtain a good overlap between the TEM_{00} of the cavity and the laser waist and excite only the TEM_{00} mode of the HFC (mode matching).

To avoid perturbation of the laser due to optical feedback, two Isowave I–21B–4 optical isolators, with a typical isolation of 35 dB per isolator, were used after the laser. About 10% of the emitted light was sent into a Bristol 621-A IR wavelength meter with a measurement repetition rate of 2.5 Hz. The Standard Deviation (SD) of measurements is given to be 0.06 ppm in the wavelength meter datasheet which corresponds to 2.5×10^{-4} cm^{-1} at 4250 cm^{-1} and was confirmed by our measurements. The manufacturer claims accuracy at the level of ± 0.2 ppm, but it is highly dependent on the injection of the measured beam and can lead to a systematic shift

of measurements.

The temperature of the cavity was monitored by a TSic 501 sensor from IST-AG with accuracy of ±0.1 K. The sensor was fixed on the surface of the cell covered by thermal insulation foam material. Pressure and temperature were monitored while the recording of spectra. The main characteristics of the critical components of the CRDS setup are summarized in Table 2.1 in the end of this Section.

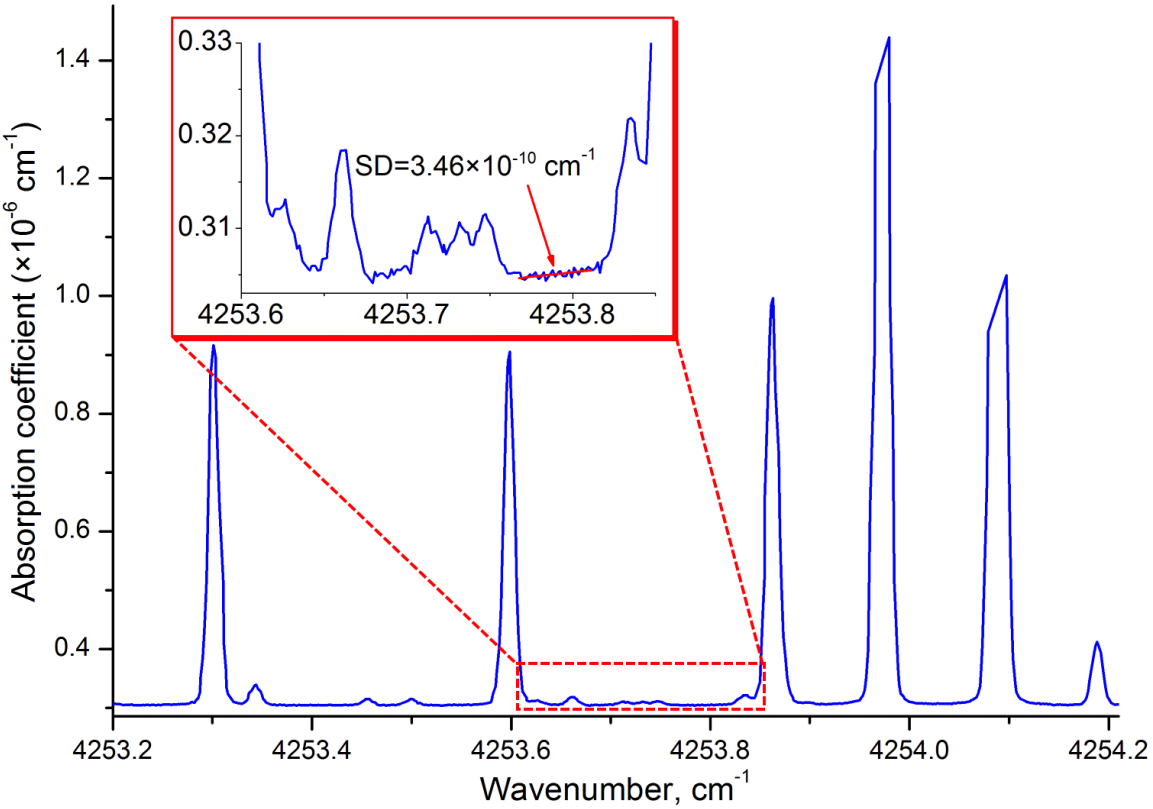

Figure 2.3. Sample spectrum of water vapor recorded with the first implementation of CW-CRDS setup at 2.3 μm. The noise level is illustrated in insert.

Signals coming from all channels like RDs, the temperature and pressure monitoring in the CRDS cell, and others were acquired through a dedicated LabView routine using two multifunction boards from National Instrument. The program also allows to completely control temperature and pump current of the laser source or, additionally, optical pump current and PZT voltage in the case of the VECSEL source (see Section 2.2.4), and the AOM operation through dedicated tailored electronic boards.

A part of one of the first spectra recorded with this setup is shown in Fig. 2.3. The threshold sensitivity achieved for the recording time of 400 ms per spectral point was 3.46×10^{-10} cm^{-1}. It is also necessary that the laser frequency drift during the single point averaging be negligible compared to the spectral features being analyzed (e.g., for absorption lines with widths of the order of 100 MHz, frequency excursion

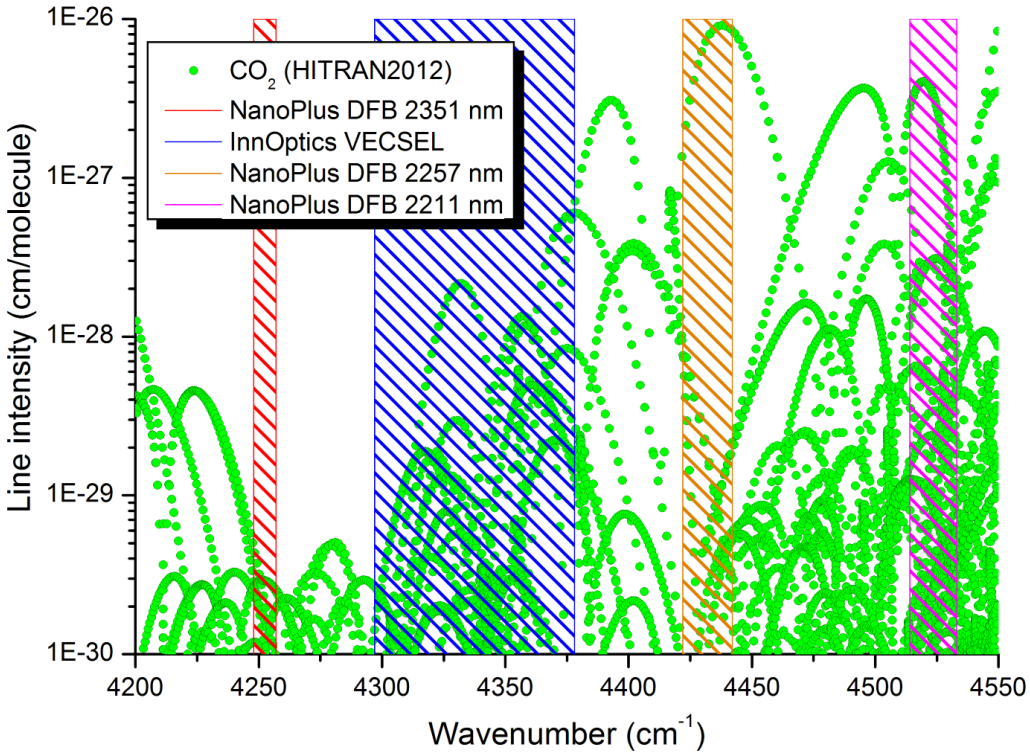

Figure 2.4. Total spectral range covered using different laser sources coupled with the CW–CRDS setup developed in the framework of the thesis. CO_2 absorption lines (green circles) from the HITRAN2012 database [2] are presented for illustration purposes.

below 1 MHz/s is suitable). This usually limits the single point acquisition times to 1 s.

In the framework of this PhD thesis, 3 different laser sources were coupled with this developed CW–CRDS setup in addition to the DFB laser already mentioned. These sources (2 DFB and the VECSEL) cover different parts of the spectral region from 2.2 to 2.35 μm as illustrated in Fig. 2.4. In following parts of this chapter we will describe these sources and the performance achieved by using them in the CRDS setup. In the case of the DFB lasers, an OF from an external reference cavity was used to narrow the laser emission.

Table 2.1. List of the critical components used in the CRDS experimental set-up.

Component	Supplier	Characteristics
DFB laser diode	Nanoplus	FWHM line width ≈2 MHz Power : 5.5 mW Spectral range : 4248.5–4257.0 cm^{-1}
Wavemeter Model 621–A IR	Bristol	Range: 1 to 5 μm Abs. Accuracy ±0.2 ppm Repeatability: ±0.06 ppm
Single mode ZrF_4 Fiber (Ref: P3–23Z–FC–1)	Thorlabs	Core dia. 9 μm Cut-off freq.: 2.3 μm
High-reflectivity mirrors (Batch #C213K031)	Layertec Gmbh	Reflection curve at 0 centered at 2330 nm, R>99.99% between 2170 nm and 2495 nm
Optical isolators I–21B–4	Isowave	Typical isolation: 35 dB Typical Insertion losses: 1dB
AOM Model ACM–1002AA1	IntraAction Corp	ARC 1500–2400 nm Center RF freq.: 100 MHz Rise time: 255 ns
InGaAs PIN photodiode Ref: G12183–203K	Hamamatsu	Photosensitive area: dia. 0.3 mm Spectral response range: 0.9 to 2.55 μm Detectivity (at λ_p) : 4.5×10^{11} $cmHz^{1/2}/W$ NEP (at λ_p) : 7×10^{-14} $W/Hz^{1/2}$
Temperature sensor Tsic–501F	Innovative Sensor Technology	Accuracy: ±0.1 °C in the range of 5 °C to 45 °C
1 bar pressure sensor Ref: ATM.1ST	STS AG	Accuracy: ±0.04% of reading down to 10 mbar
100 Torr pressure sensor Model 626–BX	MKS	Accuracy: ±0.25% of reading
1 Torr pressure sensor Model 626–BX	MKS	Accuracy: ±0.25% of reading

2.2 CW-CRDS with InnOptics vertical–external–cavity surface–emitting-laser (VECSEL–CRDS)

2.2.1 VECSEL OPScan–2300

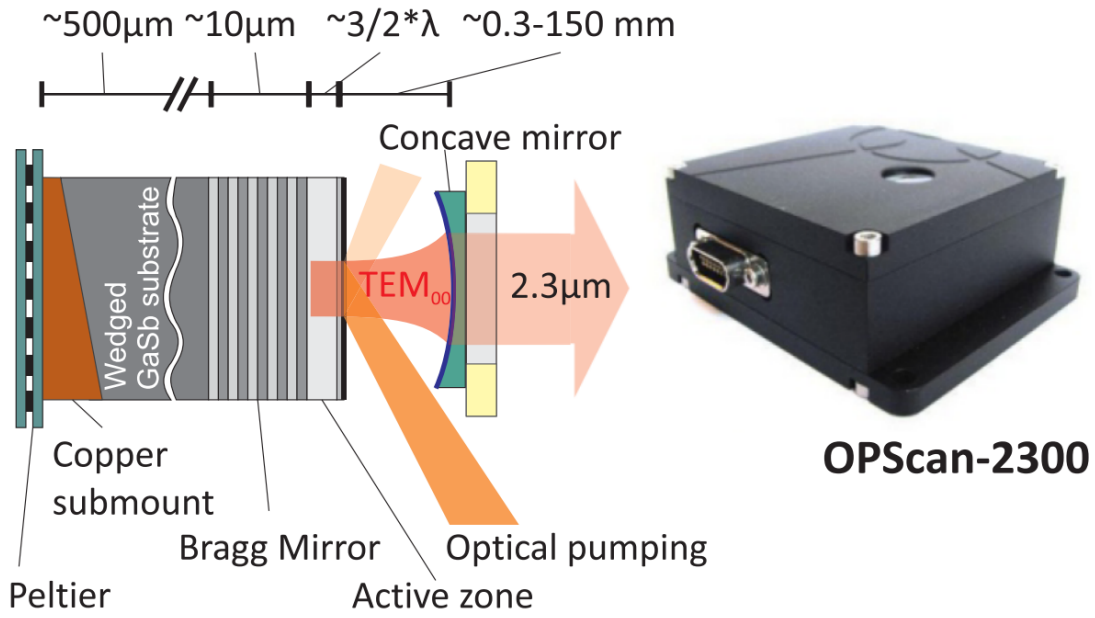

Figure 2.5. Scheme of the VECSEL setup with the external cavity and optical pumping (left) and packaged VECSEL OPScan–2300 (right).

To extend our accessible spectral range we used a Vertical External Cavity Surface–Emitting Laser, or VECSEL, source developed by A. Garnache from IES (Montpellier) and Innoptics. This work was done in collaboration with P. Čermák from Comenius University (Bratislava).

The VECSEL sources belong to a group of surface–emitting lasers originally designed by K. Iga [63]. In the region of 2.3 μm, this source represents a good alternative to DFB laser sources [64]. In a relatively compact setup, the VECSEL offers continuous-wave performance at room temperature with a total tunability of the order of 100 cm^{-1}, which is equivalent to 4–5 DFB diodes typically, and a mode hop–free tuning range of 10–12 cm^{-1}. The emission linewidth is fundamentally limited to 1 kHz. The output beam has a diffraction–limited Gaussian beam profile and low divergence of 1° [51]. The VECSEL consists of a 1/2–VCSEL semiconductor structure with an external mirror and an optical pumping system (Fig. 2.5). The temperature stabilized 1/2–VCSEL structure contains the active laser layer atop a highly reflective Bragg mirror. Because of the shortness of the gain region in comparison with edge–emitting lasers, the overall gain per pass ratio is relatively low. A high finesse resonator is necessary to achieve the conditions of laser generation; thus,

Table 2.2. Typical OPScan–2300 VECSEL properties in comparison to standard DFB.

Parameters	Unit	OPScan-2300	DFB
Max. operation temperature	K	298	323
Min. operation temperature	K	268	253
Typical output power	mW	~ 5	$5 - 13$
Beam divergence (SA/FA)[a]	deg	2.6	20/40
SMSR[b]	dB	> 25	> 32
Free running laser linewidth[c]	MHz	4.5	< 3
Temperature tuning coefficient[d]	GHz/K	-102	-13
Current tuning coefficient[d]	GHz/mA	-10.5	-1
Piezo tuning coefficient	GHz/V	-12	–
Total spectral coverage[e]	cm^{-1}	≈ 100	20
Fast MHF tuning range[f]	cm^{-1}	11.26	2

[a] Full width at half-maximum, SA – slow axis, FA – fast axis.
[b] SMSR – side mode suppression ratio.
[c] Full width at half-maximum, over a 1 ms integration time.
[d] For VECSEL this corresponds to the quantum well gain wavelength (see Fig. 2.6)
[e] Measured value for VECSEL, for the DFB, the value was calculated as a product of temperature tuning coefficient and the operational temperature interval.
[f] MHF – Mode-hop free, PZT tuning in case of VECSEL (0-30 V, 3 kHz bandwidth), current tuning for DFB (60-120 mA).

a highly reflective ($R > 99\%$) dielectric mirror is located at the other side of the open air cavity. The optical pumping is placed independently of the laser resonator with its beam directly focused on the active zone of the 1/2-VCSEL.

The industry-ready packaged GaSb based VECSEL source emitting around 2.3 μm (OPScan–2300, see Fig. 2.5) was developed, manufactured and packaged into a compact module by Innoptics in collaboration with IES.

The OPScan-2300 includes a laser cavity as shown in Fig. 2.5. formed by the gain mirror (called 1/2–VCSEL structure), a 440–μm air gap, and a commercial mirror. The GaSb–based 1/2–VCSEL emitting at 2.3 μm was grown using molecular beam epitaxy [65]. The laser cavity is closed by the mirror with a transmittance of 0.7% and a curvature radius of 10 mm. This mirror mounted on a low-voltage piezoelectric transducer (PZT) allows to continuously tune the laser. The 1/2–VCSEL chip is optically pumped with a commercial multimode diode laser emitting at 975 nm with power of up to 300 mW. Thanks to its compact integration, the device keeps dimensions of 74×58×32 mm. In addition, the compact design without any movable intracavity elements ensures a robust single frequency regime with long-term optical frequency stability better than a few GHz/hour. The characteristics and performances

of the OPScan-2300 device are detailed in Table 2.2 where they are also compared with those of a standard DFB diode.

2.2.2 VECSEL tunability

Because of VECSELs long "free space" cavity, the longitudinal cavity modes and spectral behavior of the gain are not expected to be coupled with thermal effects.

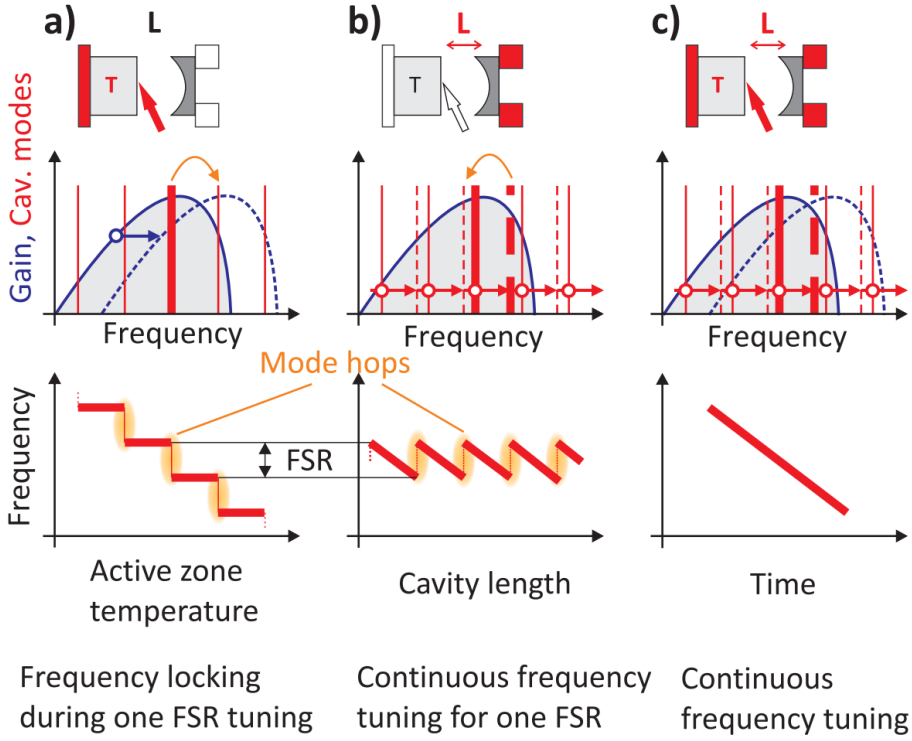

Figure 2.6. Laser frequency tuning principle. (a) Tuning of the gain curve with pump power or temperature. (b) Continuous tuning of the cavity mode with PZT. (c) Cavity mode tuned in phase with the gain curve for broad continuous laser wavelength tuning.

The gain curvature itself acts as an efficient spectral filter through regular mode competition dynamics, to select only one mode within 1 μs [66]. Thus, large tuning of the gain emission wavelength with quantum well (QW) temperature can be exploited for wide tuning of the laser wavelength. This can be controlled either with a Peltier cooler or optical pump power (case (a) in Fig. 2.6). The fine mode-hop free tuning is performed by the cavity length modulation over one FSR (case (b)) using a piezo electric transducer (PZT). Finally, as the two operation modes are independent, they can be combined to achieve a mode-hop free tuning throughout the whole laser emission spectrum (case (c)) (see details in Ref. [67]).

To characterize the OPScan tunability range, transmission spectra through a 6–cm long cell filled with pure methane at 1 atm were recorded by changing the PZT voltage for different conditions of temperature and pumping current. The frequency

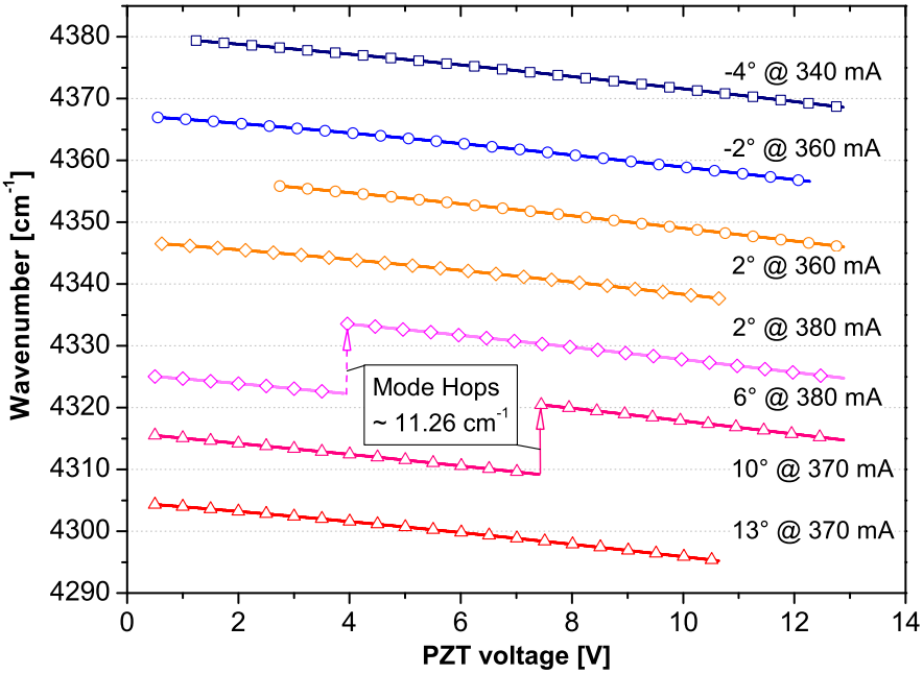

Figure 2.7. An example of the OPScan–2300 tuning map with seven PZT scans for different laser temperatures and currents. The scans at 6 °C and 10 °C were selected to show the FSR determination of the laser cavity from the mode-hop frequency positions.

scale of these spectra was calibrated using the CH_4 reference lines provided by the HITRAN2012 database [2]. A tuning map of the laser is presented in Fig. 2.7; the tuning rates are -0.4 cm^{-1}/V, -3.4 cm^{-1}/K and -0.35 cm^{-1}/mW for the PZT voltage, 1/2-VCSEL temperature, and pumping power respectively.

From the measurements of the mode-hop frequency range, the OPScan FSR was found to be 11.26 cm^{-1} (see Fig 2.7) corresponding to a 440–μm laser cavity. In total, spectral range covered by the OPScan was found to be larger than 100 cm^{-1}. Because of lack of power for high temperature regimes, the CRDS implementation was possible only for a more limited spectral range of 81 cm^{-1}. This spectral coverage has to be compared to the 20 cm^{-1} spectral coverage of a standard DFB laser (see Table 2.2). For the latter, spectral filtering is carried out by a grating embedded in the laser chip, which limits the temperature tunability of the structure, leading to typical tuning rates of about -0.4 cm^{-1}/K compared to -3.4 cm^{-1}/K in the OPScan.

2.2.3 Temporal coherence and frequency stability

Frequency noise characteristics of the OPScan plotted in Fig. 2.8 was provided by B. Chomet from Innoptics. Fundamentally, in continuous wave regime, the laser linewidth is limited by the spontaneous emission noise, described by the modified Schawlow-Townes formula [68]. For the OPScan, this value is around 1 kHz for 2 mW output power [69]. The fundamental linewidth for a DFB was found in [69] to

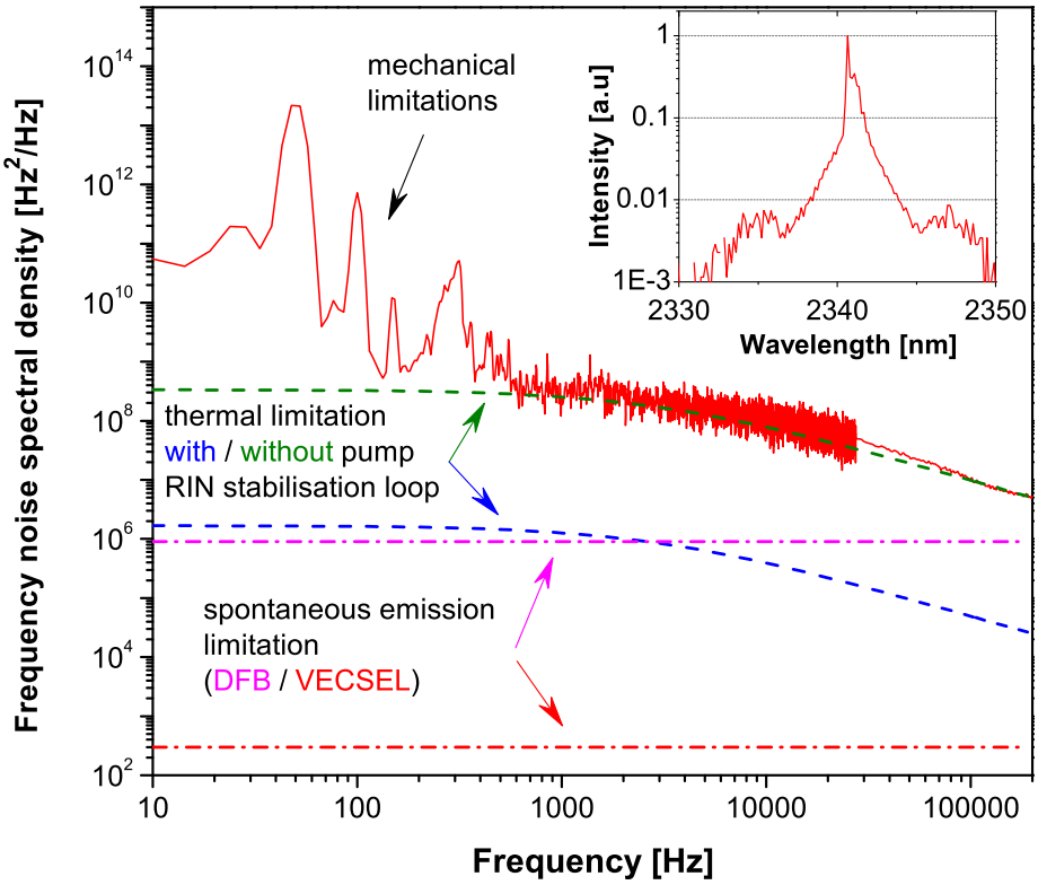

Figure 2.8. Frequency noise of the OPScan-2300 for P_{out} = 2 mW. Further reduction of the VECSEL frequency noise could be achieved by implementing pump noise reduction or pumping with a less noisy pump. Inset plot: Single frequency spectrum of the OPScan-2300 for I= 380 mA and T= 279 K.

be typically 2 MHz for 3 mW output power using parameters in Ref. [70]. In practice, various technical frequency fluctuations lead to an increase of the laser linewidth for longer integration times. To evaluate these contributions, the optical frequency noise spectral density measurements were carried at IES out for the free running VECSEL using an ultra-stable plano-concave Fabry-Pérot interferometer with 100 MHz mode width. The Fabry-Pérot (FP) etalon acted as a frequency discriminator converting the laser frequency fluctuations to intensity fluctuations at the output of the Fabry-Pérot interferometer. The spectral density of this signal, recorded with a low-noise photodiode, is plotted in Fig. 2.8 along with the fundamental limit due to spontaneous emission of both the VECSEL and a typical DFB [71].

Above 1 kHz the optical frequency noise is dominated by frequency fluctuations induced by the optical pump intensity noise. The use of a pump diode with much lower noise (< 140 dB/Hz) or a pump intensity stabilization loop can reduce the laser frequency noise down to 100 kHz for Integration Time (IT) of 100 μs, below typical DFB fundamental limits [69]. For frequencies lower than 1 kHz, the mechanical noise

presents an important contribution to the optical frequency noise due to the free space architecture of the laser.

For CRDS, it is important to have the laser bandwidth comparable to the width of the HFC mode ($\sim$ 1 kHz) at the time scale of the cavity response time for the intracavity field build-up process. The frequency noise of the source larger then 1 kHz thus leads to a reduced output signal on the photodiode. As for the low frequency mechanical noise, it does not introduce additional cavity injection noise but in the case of the modulation of the HFC length manifests itself as displacement of the resonance frequency from RD to RD and leads to additional noise on the slopes of an absorption line. This latter noise could be strongly reduced by optimizing the module packaging. It is also worth noting that good grounding of the OPScan–2300 was critical for achieving its low jitter.

2.2.4 CRDS setup with VECSEL OPScan–2300

The CRDS setup with the OPScan VECSEL is presented in Fig. 2.9. The same experimental setup as the one for the DFB described in Section 2.1 was used here for the VECSEL–CRDS spectrometer. The main difference is the use of FP etalon and a reference cell channels instead of the wavelength meter. More precisely, to implement the frequency scale and to calibrate the recorded spectra, about 10% of the light emitted by the VECSEL was deflected into two reference channels composed of the FP etalon (free spectral range = 0.051 cm^{-1}, $\mathcal{F} = 2$) and of a 6–cm reference cell filled with pure CH_4 at atmospheric pressure. The fringes of the FP signal were used as a ruler to correct the nonlinearity of piezo scanning. After the linearization of the frequency axis, rough absolute spectral calibration was performed using the spectrum of a methane reference cell and then refined using some well-known positions of impurity lines present in the CRDS spectra from the HITRAN2012 database [2] or predicted using the effective Hamiltonian [72, 73] approach.

Typically, only about 20% - 0.4 mW of 2.2 mW - of the VECSEL output power was fed into the cavity, mainly due to the low efficiency of the AOM and losses due to the coupling into the fiber. Because of these losses, the minimum VECSEL power to operate the CRDS instrument was around 2 mW leading to spectral coverage of 81 cm^{-1} from 4297 to 4378 cm^{-1}, which corresponds to 4 times the spectral region of a typical DFB.

In this setup we also added the gas flow system to flush the sample gas through the HFC and remove impurities outgasing from the walls of the cavity. For that the input valve of the cavity was fed with excessive pressure while the flow of sample gas is regulated with a downstream proportional electro-valve controlled by a proportional-integral loop to maintain a constant pressure inside the CRDS cell (Fig. 2.9).

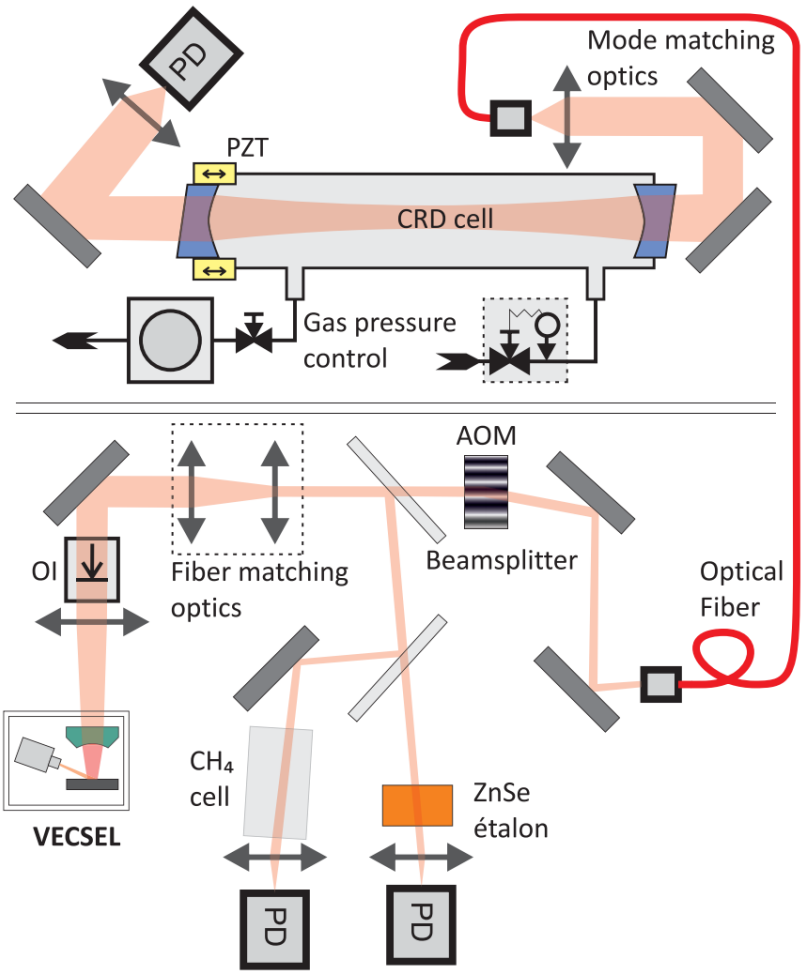

Figure 2.9. The experimental setup of the VECSEL–CRDS instrument.

The same acquisition and home–made control boards were used in this setup. We only added a low noise voltage board supplying the PZT of the VECSEL with the voltage from 0 to 30 V.

Routine VECSEL–CRDS setup performance

To record a spectrum in a chosen spectral interval, the spectral range was selected by the OPScan temperature and pump current. The absorption signal was then recorded by scanning PZT voltage, and thus the laser frequency throughout one FSR of the VECSEL cavity (about 11 cm^{-1}), with a typical step of 0.003 cm^{-1}. Repetitive RD measurements at each spectral point are generally averaged to reduce noise. The problem of averaging in the CRDS scheme under consideration is that since the CRDS cavity length is modulated, the position of a spectral point as a frequency match between the HFC varied from ring-down to ring-down because of the laser frequency jitter. So, typically, 30 to 40 RD events were averaged every second and fitted to an

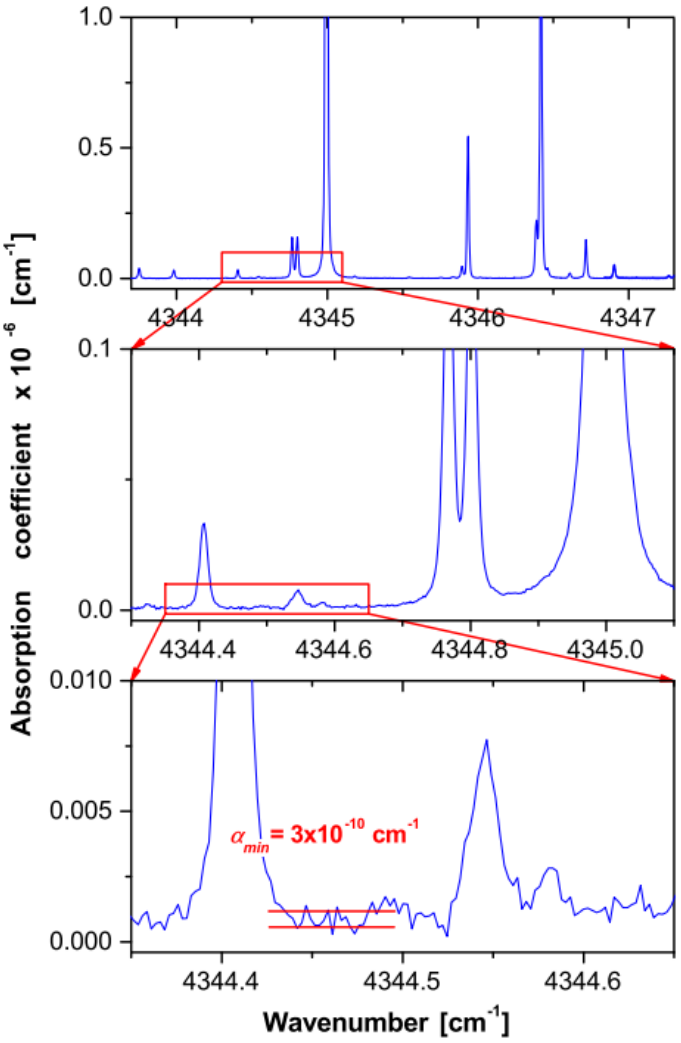

Figure 2.10. Example of CRDS water vapor spectra at 7 Torr showing the dynamical range of the instrument spanning four orders of magnitudes from 1×10^{-5} cm^{-1} to a noise level of around 3×10^{-10} cm^{-1}.

exponential decay to obtain an average RD time for a single spectral point. In these conditions, about 1 h was necessary to record an 11 cm^{-1} spectrum interval.

An example of a CRDS water vapor spectrum is presented in Fig. 2.10. A dynamical range spanning more than four orders of magnitude and a minimum detectable absorption coefficient of $\alpha_{min} \approx 3 \times 10^{-10}$ cm^{-1} are demonstrated. This noise level is comparable to the noise level achieved with the DFB laser source at 4250 cm^{-1}.

Ultimate performance of the VECSEL–CRDS setup

To evaluate the ultimate performances of the instrument, a series of 99 spectra of the same narrow spectral region (Fig. 2.11 upper panel) was recorded and calibrated. Typically, the noise level of a single spectrum in this spectral region is $\alpha_{min} \approx 4 \times 10^{-10}$ cm^{-1}. As shown in Fig. 2.11 lower panel, this noise level decreases with the square root of the number of the averaged spectra. Nevertheless, above a few tens of averaged spectra, parasitic interference limits the noise level to 9×10^{-11} cm^{-1}. Averaging spectra thus allows for a reduction in the noise level, but this has to be restricted to

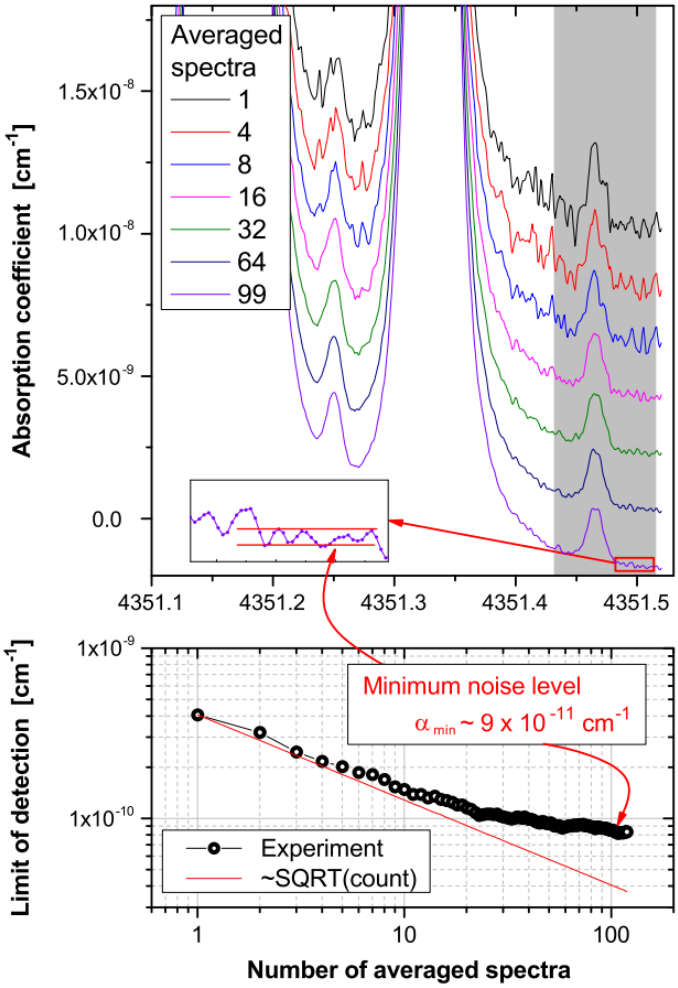

Figure 2.11. Upper panel: Reaching the limiting performance with the VECSEL–CRDS setup by averaging spectra. Lower panel: SD of fit residual shows that the limiting sensitivity of 9×10^{-11} cm^{-1} is achieved after averaging 99 spectra.

a narrow spectral region to keep a reasonable acquisition time.

In Fig. 2.12, we present a fit of the averaged spectrum applying a Voigt profile for the line shape. The line centers and intensities were determined using an interactive least squares multi line fitting program assuming a Voigt profile. The Half-Width at Half-Maximum (HWHM) of the Gaussian component γ_D was fixed for each line to its calculated value knowing the temperature T and the molar mass M of the isotopologue for a given transition of wavenumber $\delta_{f\leftarrow i}$:

$$\gamma_D = \omega_{f\leftarrow i}\sqrt{\frac{\ln(2)k_bT}{2\pi^2mc^2}} = 3.58 \times 10^{-7}\delta_{f\leftarrow i}\sqrt{\frac{T}{M}} \tag{2.1}$$

The integrated line absorption coefficient, line position, Lorentzian widths, and the corresponding local baseline (assumed to be a linear function of the wavenumber) were obtained from the multi line fit. The residuals displayed on the lower panel of Fig. 2.12 show the typical W–shape signature for each line fitted with a Voigt profile showing that additional effects like speed dependence and narrowing have to be considered with more complex profiles. Finally, the precision of the line centers and intensity

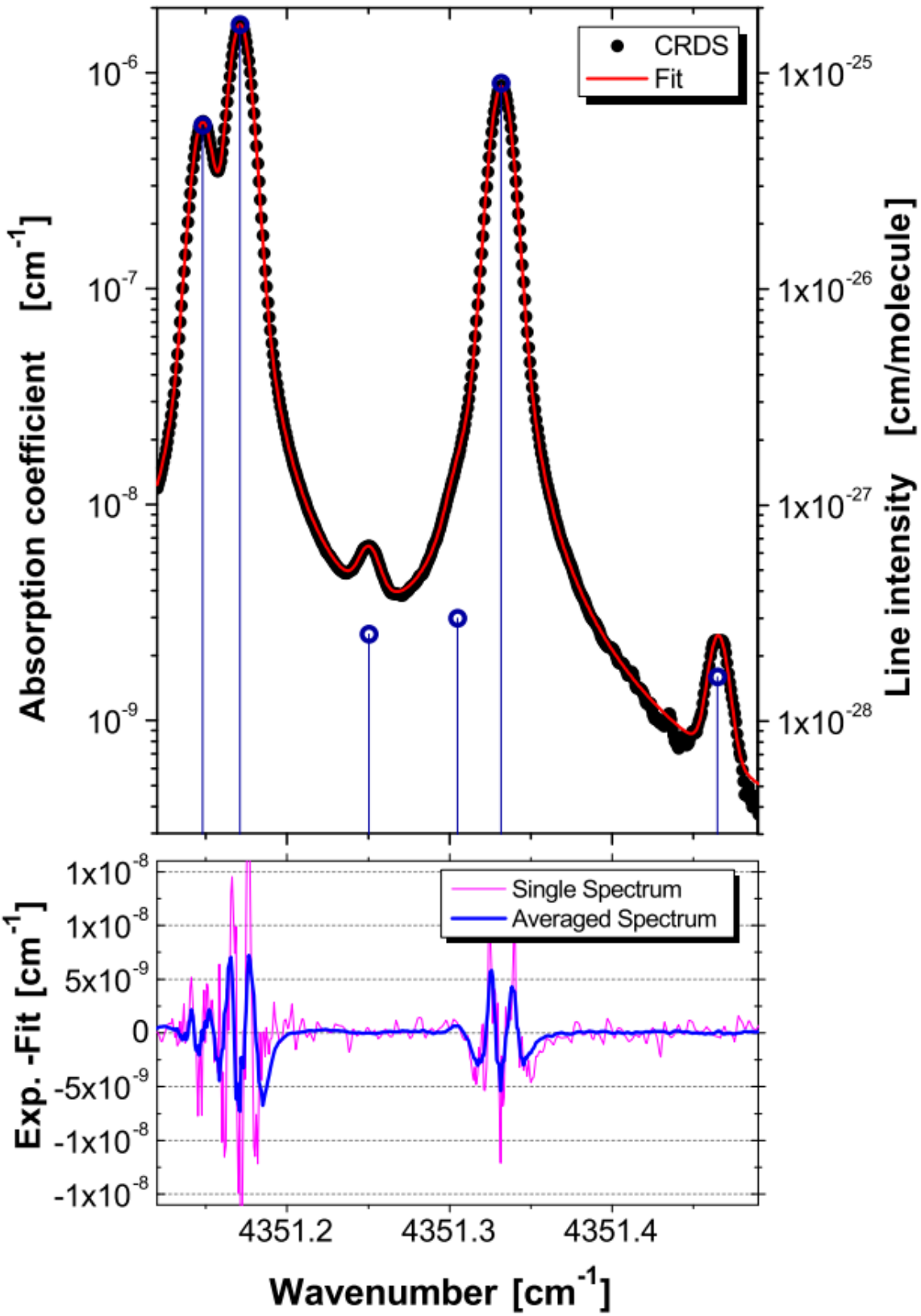

Figure 2.12. The Voigt fit (red) of the averaged spectra (black). The position of fitted transition is marked by violet sticks. The bottom panel shows comparison of two residual signals: for the averaged spectrum fit (blue) and for a single spectrum fit (magenta).

measurements was estimated by comparing the line centers and intensities retrieved from the individual fits to the values obtained from the fit of the averaged spectrum for a well–isolated water vapor line near 4351.33 cm^{-1}. The obtained uncertainty for the line center of this line was 0.00017 cm^{-1} and 2% for the line intensity (peak surface).

2.3 CRDS with DFB source narrowed by optical feedback from an external reference cavity (EC–CRDS)

2.3.1 Setup description

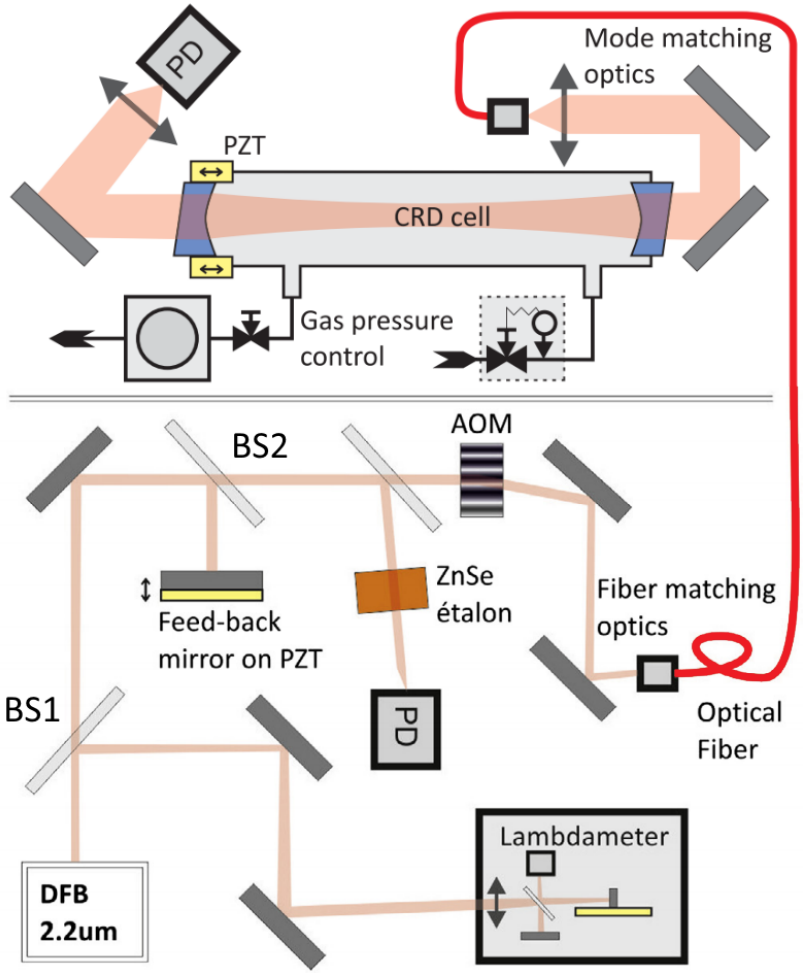

Figure 2.13. The experimental setup of the EC–CRDS instrument.

An extension of the spectral region closer to 2.2 μm was realized using two Nanoplus DFB lasers emitting around 2210 and 2257 nm which covered the 4514–

4533 cm^{-1} and 4422–4442 cm^{-1} spectral ranges, respectively, by temperature tuning from 18 to 60°C. Both lasers had relatively high emission power from 9 to 13 mW depending on temperature. Because of the large laser bandwidth of 5 MHz for IT of 1 ms free running laser was not suitable for CRDS leading to a small transmitted signal insufficient for RD generation. To narrow the laser and have a higher transmitted intensity we applied the technique described by Lin et al. [74] which consists in using the OF from an external cavity (EC) to strongly reduce the laser frequency noise. A 87–cm long external cavity was formed by the DFB semiconductor facet and a plane silver mirror mounted on a PZT. A beamsplitter (BS2) deflected about 3% of the emitted radiation to the external cavity mirror (see Fig. 2.13). The OF rate was thus estimated to -30 dB at maximum. In these conditions the narrowing of the laser with OF is clearly visible during the passage through resonance with a mode of the HFC as shown on Fig. 2.14. The transmitted signal is thus much higher than that with the free running DFB laser.

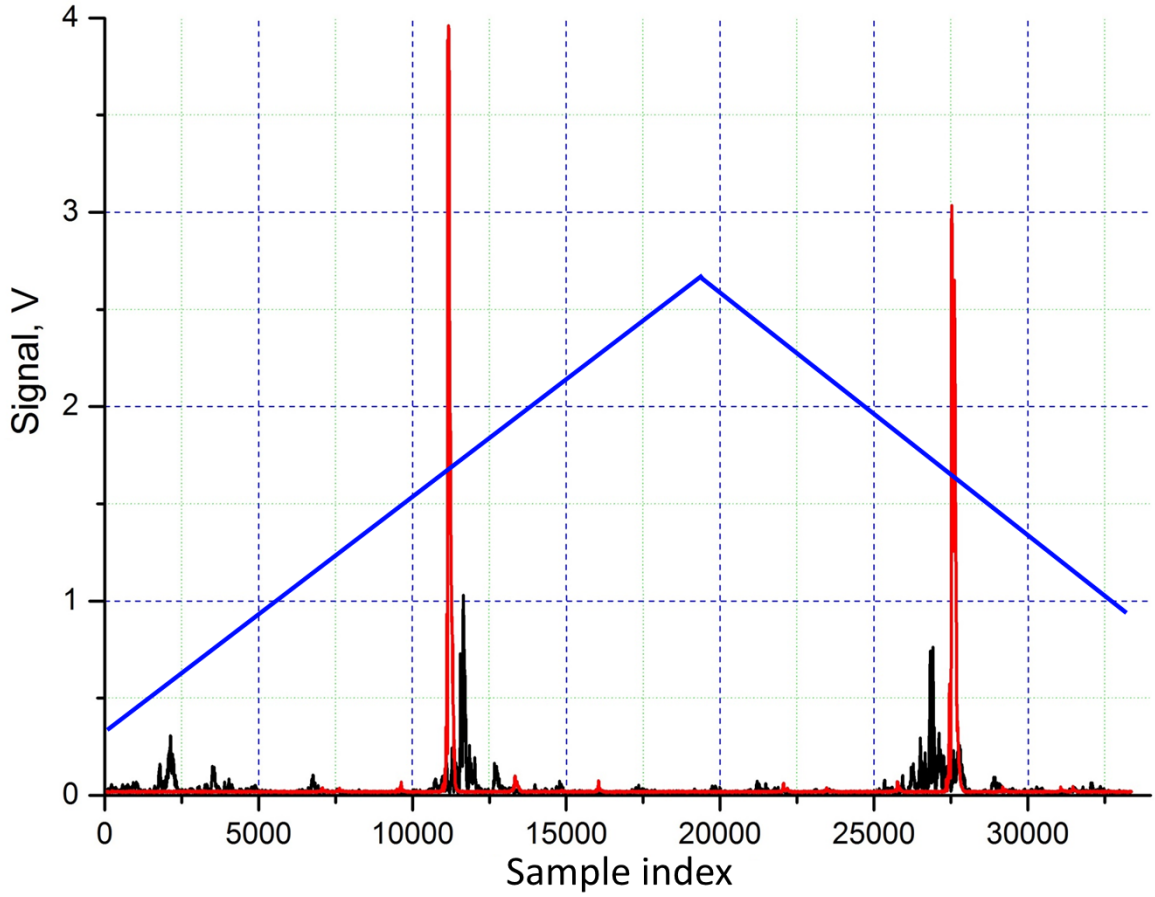

Figure 2.14. Transmitted signal through the HFC for free running DFB (black line) and for the DFB narrowed by OF (red line). Blue line – voltage ramp of the CRDS cavity PZT.

Since the DFB laser is locked, it emits on the dominant external cavity longitudinal mode. As shown in Fig. 2.15, when the laser temperature is tuned, the laser

jumps from one longitudinal mode of the EC to the next one with the FSR of the EC corresponding to ~ 0.005 cm^{-1}. This gap between two laser frequencies is filled

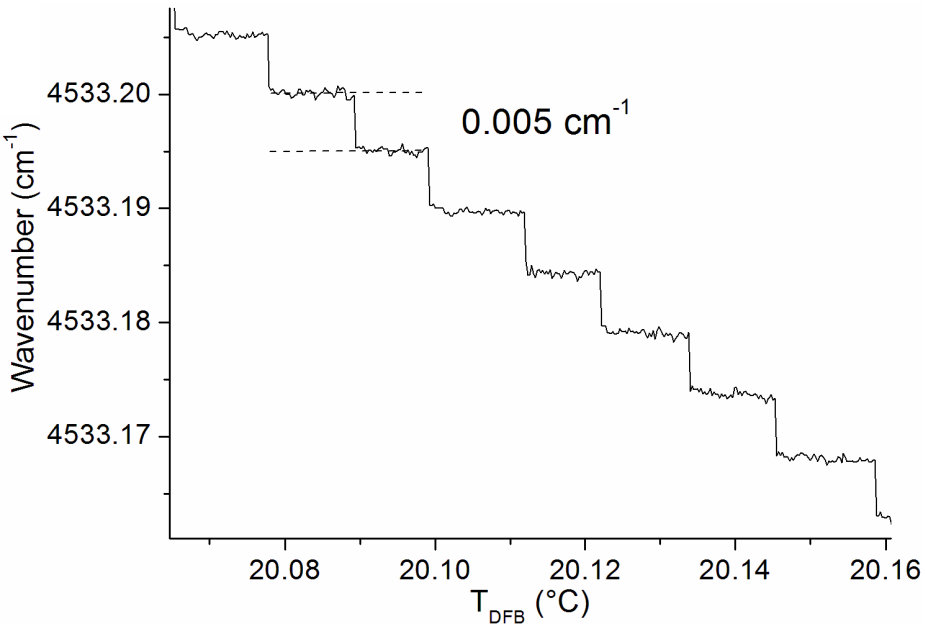

Figure 2.15. Example of temperature scanning of the laser locked to the external cavity. Steps denote adjacent longitudinal modes of the EC.

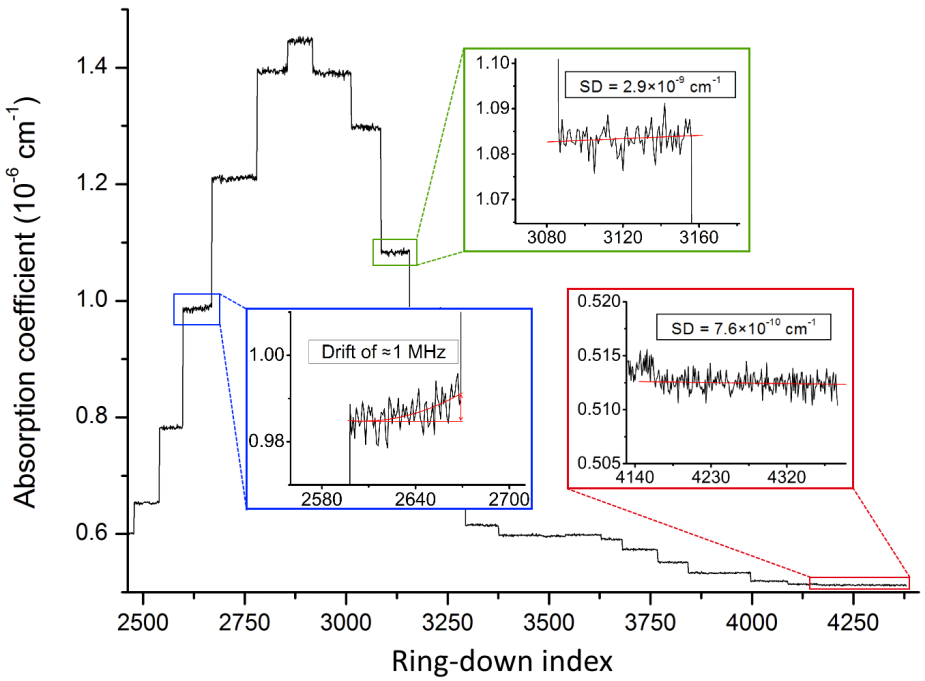

Figure 2.16. All ring-downs obtained during a scan across an absorption line. Each "step" is a group of RDs acquired during $\approx$ 1 s for a single spectral point. Green insert: noise level on the slope of the line; Red insert: noise level on the baseline; Blue insert: laser drift during $\approx$ 1 s.

by changing the voltage of the PZT on which the external cavity mirror is mounted. So, spectrum recordings over the entire spectral range of the DFB were provided by combination of temperature and PZT voltage scan leading to a final spectral sampling of 0.001–0.002 cm^{-1}.

We estimated the narrowed laser drift and jitter from series of RD recorded at the slope of an absorption line (Fig. 2.16) which was used as a frequency discriminator. Every spectral step was recorded for about 1 s. As seen in the blue insert of Fig. 2.16, the 1-second laser drift did not exceed 1 MHz. The difference between the noise level on the slope of the line and on the baseline (the green and red inserts, respectively) gives an idea of the laser frequency noise, which is approximately of the order of 1 MHz as well. Note that the drift is related to the change in the length of the EC which should be stabilized.

In addition to this narrowing of the laser source we have implemented a mode tracking procedure that will be discussed in the following section.

2.3.2 Mode tracking principle and performance

A way to increase sensitivity is to adjust the CRDS cavity length to keep it at resonance with the laser wavelength instead of applying of full amplitude voltage ramp over the cavity FSR. A RD tracking loop combined with a variable PZT waveform offset was implemented allowing for a reduction of the amplitude of the triangular ramp by a factor of about 30. This leads to:

- An increasing of the repetition rate of RD events due to the fact that cavity is always in resonance with the laser;
- A better injection of the cavity and in turn to a higher voltage threshold at which the RD are triggered because of slowing down the passage through resonance. The highest this threshold is, the best the RD time can be determined, leading to a reduced noise on the retrieved absorption coefficients.

The strong improvement due to this tracking procedure is illustrated on Fig. 2.17. This figure shows the evolution of the limit of detection, corresponding to the standard deviation measured on a section of the baseline free of absorption lines, as a function of the number of ring-downs (N). The noise level is decreasing from 3×10^{-10} cm^{-1} to 1.2×10^{-11} cm^{-1} when N increases from 2 to 6500. This variation is a little bit slower than the ideal case of $1/\sqrt{N}$. For comparison, a series of recordings performed without RD tracking during 9 days led to 3×10^{-11} cm^{-1} noise level but RD tracking made it possible to achieve 1.2×10^{-11} cm^{-1} in 1 day of recording. The higher noise level observed without RD tracking for a given number of RD is due to the lower threshold voltage used in that case.

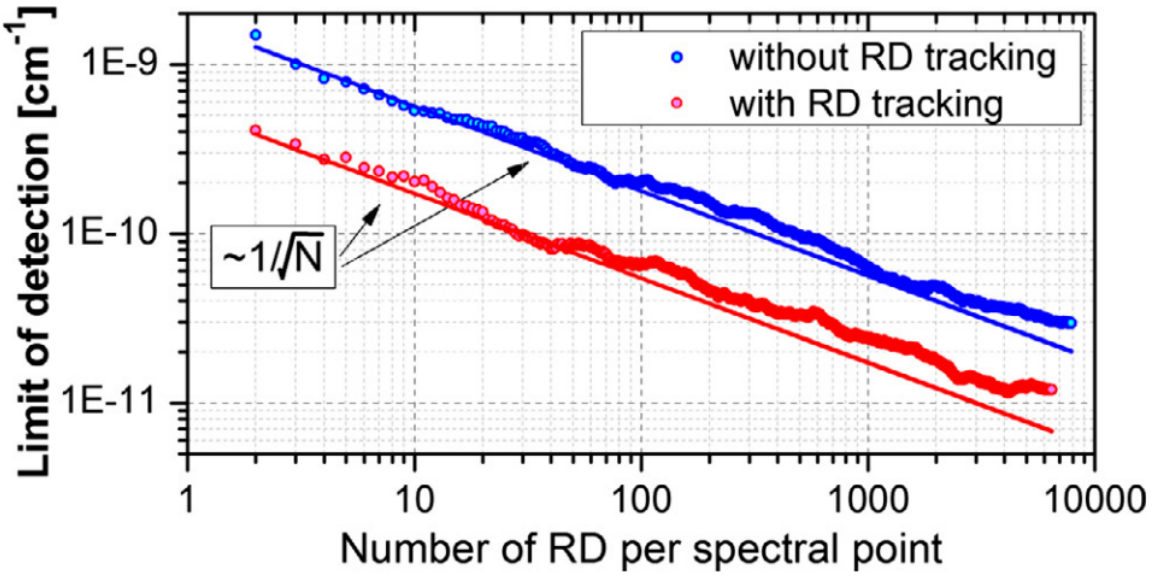

Figure 2.17. Limit of detection in function of the number of RD events per 0.001 cm^{-1} spectral step used for averaging with and without the tracking method.

2.4 Conclusion

The developed VECSEL–CRDS and EC–CRDS setups give access to the important 2.3 μm transparency window, which is of major interest for various atmospheric applications.

An important advantage of VECSEL light sources is their wide tunability allowing for significantly wider spectral coverage than that provided by commercial DFB diode lasers. For instance, the VECSEL used in our experiments allowed for continuous coverage of the 4295–4380 cm^{-1} spectral interval with the sensitivity of 3×10^{-10} cm^{-1} for 1 s of acquisition per spectral point. Such a high sensitivity made it possible to detect the weak S(3) quadrupole transition of the HD molecule, as will be shown it in the next chapter.

New CRDS setup based on narrowing of the DFB laser with optical feedback from an external cavity and the mode tracking procedure made it possible to record highly sensitive spectra in the regions near 2210 and 2257 nm with sensitivity of 1×10^{-10} cm^{-1} obtained for 100 averaged RDs per spectral point acquired for 1 s. Increased averaging allowed us to reduce the noise level by a factor of 5, leading to the noise level of 1.2×10^{-11} cm^{-1} sufficient to detect the highly forbidden quadrupole transition of N_2 (also described in the next chapter).

Chapter 3

The highly sensitive CRD spectrometer applied to the detection of very weak quadrupole transitions of HD and N_2

3.1 Introduction

To test the sensitivity achieved with VECSEL–CRDS and EC–CRDS configurations we recorded at first the weak S(3) 1–0 quadrupole transition of HD and the O(14) 2–0 highly forbidden transition of N_2 near 2.3 and 2.2 μm, respectively.

The N_2 and H_2 absorption spectra consist of very weak electric quadrupole bands following the $\Delta J = 0, \pm 2$ selection rules (where J is the rotational quantum number) because of the absence of allowed dipole transitions. Contrary to its symmetric isotopologues (H_2 and D_2), the HD molecule possesses a weak permanent dipole moment resulting from non-adiabatic effects due to the difference in the masses of the proton and the deuteron. Thus the HD absorption spectrum exhibits electric dipole rovibrational transitions in addition to the weaker electric quadrupole (E2) transitions. The quadrupolar transitions of N_2 and HD under study are challenging for experimental detection because of intensities of the order of 10^{-31} and 10^{-27} cm/molecule and are of importance for validation of *ab initio* calculations.

Additionally to the HD line position and intensity we discuss the first detection of broad HD Collision–Induced Absorption (CIA) which manifests as a quadratic increase of the spectrum baseline level with density.

3.2 First detection of S(3) quadrupole electric transition of the HD fundamental band and collision-induced absorption near 2.3 μm

For approximately a century, the hydrogen molecule and its isotopologues have been a challenge both for theoretical calculations and high sensitivity absorption techniques (see Refs. [75–77] for some pioneering works). As a result of the significant progress of the theory (e.g. Refs. [78–81]) and experiment (e.g. Refs. [82–88]), this interest has recently been renewed and concerns different aspects including transition frequencies and line strengths [82–88], the line profile [89, 90] and collision–induced absorption [91, 92].

Experimentally, the main difficulty is related to the weakness of the absorption lines to be detected. The absorption spectrum of molecular hydrogen and deuterium, H_2 and D_2, consists of vibrational bands of very weak electric quadrupole (E2) transitions. As a result of the large values of the vibrational frequency (about 4160 and 2993 cm^{-1}, respectively) and of the rotational constant (about 60 and 30 cm^{-1}, respectively), the H_2 and D_2 spectra are extremely sparse. For instance, less than fifty H_2 absorption lines have been reported so far in relevant literature, up to the fourth overtone band near 19,000 cm^{-1} [82, 87, 93].

The existence of weak electric dipole (E1) transitions in HD was predicted by Wick in 1935 [75]. The electric dipole transitions form P and R branches corresponding to $\Delta J = -1$ and $+1$, respectively while the electric quadrupole transitions form O, Q and S branches corresponding to $\Delta J = 2$, 0 and $+2$, respectively. Fig. 3.1 shows an overview of the calculated stick spectrum of HD [2, 79, 80] in the 0–20,000 cm^{-1} range covering the rotational spectrum, the fundamental and vibrational overtone bands of up to 6–0. Note that in the 1–0 fundamental band, the E2 transitions are typically two orders of magnitude weaker than the E1 transitions. A complete review of the HD absorption lines reported in the literature is presented in Ref. [100]. In the overview spectrum of Fig. 3.1, the transitions detected so far are highlighted. In total, the seventy–three detected transitions, from the pure rotational spectrum to the (6–0) vibrational band near 520 nm, are reported so far, which were recorded using a variety of experimental techniques. The traditional detection scheme based on a long-path multipass cells associated with grating spectrographs or FTS gives access to lines with minimum intensity values in the $10^{-27} - 10^{-26}$ cm/molecule range [94, 95, 101].

Modern laser spectroscopic techniques like Cavity Ring-down spectroscopy provide a much higher sensitivity and require a small quantity of gas. A CRDS study of the first overtone band of HD between 6900 and 7900 cm^{-1} [101] allowed for accurate measurements of nine E2 and eleven E1 transitions, including the weakest HD line

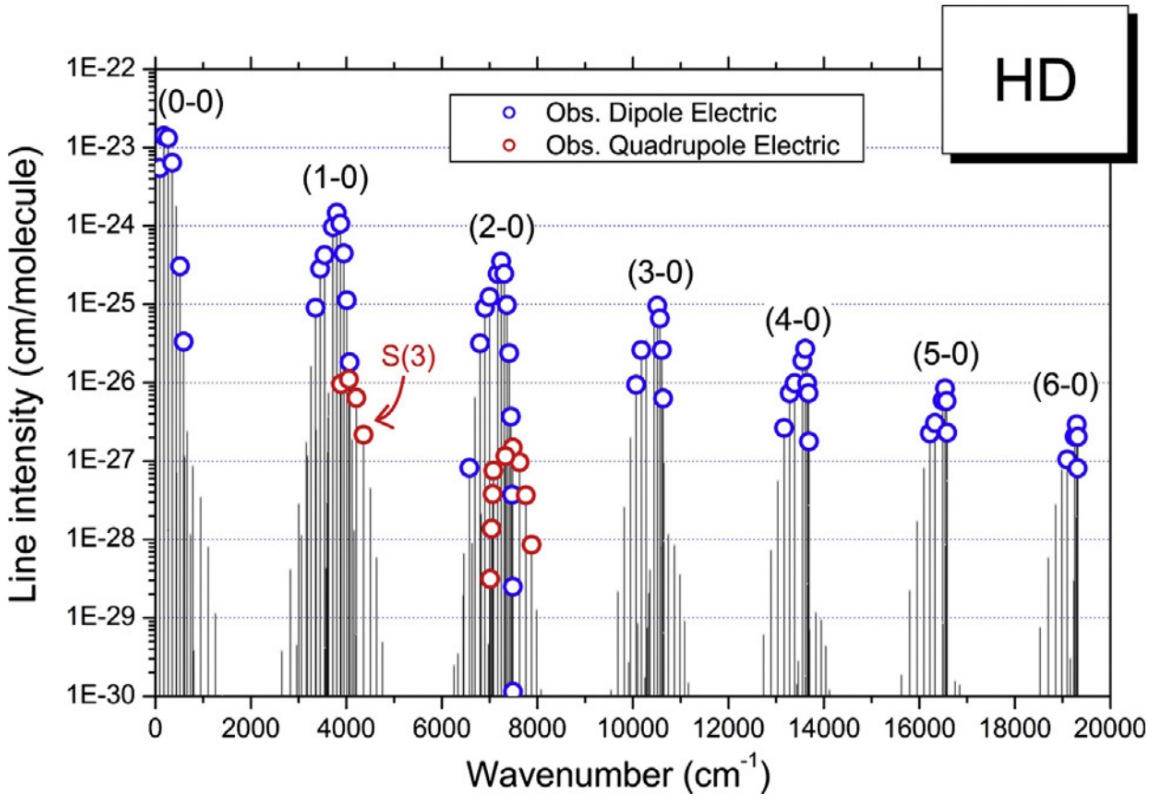

Figure 3.1. Overview of the (pure) HD spectrum between 0 and 20,000 cm^{-1} as provided by the HITRAN2012 database [2]. The line positions and line intensities are calculated values from Refs. [79, 80]. The electric dipole and electric quadrupole transitions which were previously detected by absorption spectroscopy [77, 94–99] are highlighted with blue and red circles respectively. The newly detected S(3) transition is indicated.

detected so far, the R(8) 2–0 line with an intensity of 1.04×10^{-30} cm/molecule at 296 K [101] (see Fig. 3.1). The noise equivalent absorption of the spectra was of the order of $\alpha_{min} = 5 \times 10^{-11}$ cm^{-1}, i.e. about three orders of magnitude better than FTS sensitivity. Other laser detections of HD transitions include photoacoustic studies of high overtone transitions and the P(5) 2–0 line reported by Lin et al. using frequency-modulated difference spectroscopy [102].

The broad CIA bands of molecular hydrogen have also been of interest for a long time. Considerable experimental efforts were undertaken to measure the H_2 bands in a wide range of pressure and temperature conditions relevant for planetary atmospheres and cool stellar objects [91, 103–106]. Due to the weakness of the CIAs, most of the measurements reported in literature were performed at very high gas pressure ranging between a few tens and more than 100 atm. As shown by recent measurements of the H_2 CIA in the region of the first overtone band near 8075 cm^{-1} [87], the CRDS technique provides sufficient sensitivity and baseline stability to derive the hydrogen CIA with pressure values limited to 1 atm. This is an important advantage to make negligible three-body collision effects which may make a significant contribution to

higher pressure. In the case of HD, to the best of our knowledge, no study was dedicated to the CIA measurements. The only result we found in the literature is the CIA spectrum between 3300 and 4000 cm^{-1} displayed in Fig. 1 of Ref. [92] dedicated to the study of interference effects between the allowed HD dipole transition moments and the dipoles induced during collisions.

In the present study, the spectra were recorded at different pressures up to 650 Torr, allowing to study the CIA of HD in addition to S(3) line parameters. This CIA results in a quadratic increase of the baseline with pressure.

3.2.1 Experiment description

The study was performed with the VECSEL–CRDS setup which was described in details in Section 2.2.

In this experiment, the recording was performed at the temperature of the VECSEL of 2°C. At this temperature, a spectral region of about 3 cm^{-1} around the predicted position of the S(3) 1–0 HD line at 4359.94 cm^{-1} [79] was recorded by means of changing PZT voltage. The CRDS cell was filled with HD at room temperature. The cell temperature ($T = 297.5 \pm 0.5K$) measured by a sensor was monitored while recording. The pressure was measured by an STS ATM.1ST capacitive transducer (1000 mbar full range; accuracy of ±0.1% of the full range). A total of 10 spectra were recorded with a typical spectral step of 0.002 cm^{-1}, at pressures ranging between 50 and 650 Torr. About 35 ring-down events were averaged for each spectral point leading to a minimum detectable absorption coefficient, $\alpha_{min} = 5 \times 10^{-10}$ cm^{-1}.

The HD sample (from Sigma–Aldrich) had a chemical purity of 99.3% and an isotopic purity of 98.5%. Fig. 3.2 shows a sample of the recorded spectra at 100, 200, 450, and 600 Torr. From the figure, we observe strong absorption due to methane lines. On the basis of spectral fits and of the HITRAN2012 [2] line intensities, the relative concentration of CH_4 in our sample was found to be between 14 and 23 ppm, depending on the spectrum. But despite a low concentration, methane transitions having intensities larger than 1×10^{-21} cm/molecule i.e. six orders of magnitude larger than the intensity of the line under study led to its partial overlapping. In addition, the different spectra show strong CH_3D lines as a result of considerable deuterium enrichment, most probably resulting from HD synthesis: the CH_3D relative concentration was found to be mostly identical in the different spectra at 28.5 ppm i.e. larger than the CH_4 concentration.

Each spectrum was linearized using the etalon signal, the absolute frequency calibration was achieved using the CH_4 impurity lines present in the CRDS spectrum and CH_4 position values from the HITRAN2012 database. The HITRAN CH_4 reference line positions are given with an uncertainty lower than 0.001 cm^{-1}. In order

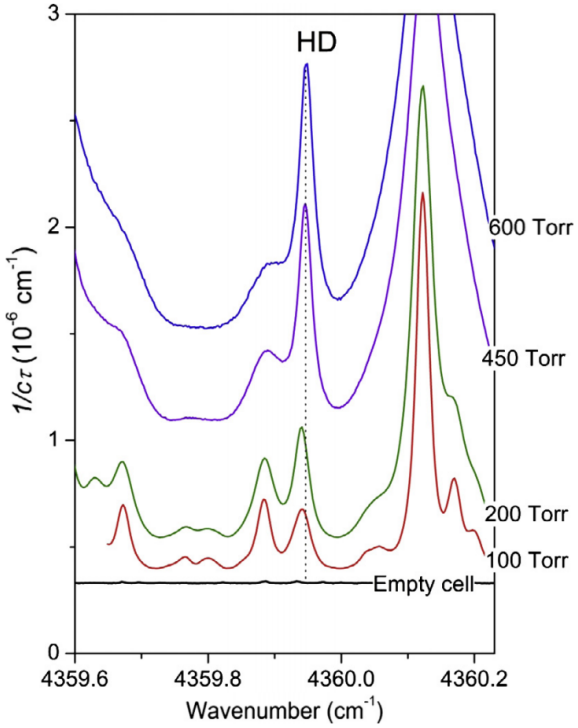

Figure 3.2. Pressure dependence of the cavity loss rates, $1/c\tau$, in the region of the S(3) 1–0 line of HD at different pressures varying from 0 Torr (empty cell) to 600 Torr of HD.

to minimize the uncertainty related to unknown pressure shifts of the CH_4 and HD line centers, the S(3) line position was determined using the recording at the lowest pressure (i.e. 100 Torr). At this pressure, pressure shifts are expected to be smaller than 2×10^{-4} cm^{-1} [107].

It is worth noting that the relative height of the HD and nearby methane lines varies markedly with pressure. The HD peak maximum increases much faster than the CH_4 peak maxima. This is due to a strong Dicke narrowing of the HD line with increasing pressure values [101, 108]. Unlike the methane lines, the width of the HD line decreases with pressure up to 650 Torr.

Another interesting observation from Fig. 3.2 is a strong increase in the spectra baseline level with pressure. This increase, which largely exceeds the cumulative effect of methane lines broadened by pressure, is caused by the CIA band of HD.

3.2.2 Results

The S(3) 1–0 line position

To accurately derive the HD line parameters it is first necessary to correctly take into account the methane absorption which partially blend the HD line. The comparison of the CRDS spectra to spectra simulations based on HITRAN positions and CH_4 and CH_3D intensities scaled to their concentrations revealed significant deviations which may be attributed to some inaccuracies in the HITRAN methane line list and/or possible contribution of additional impurities because the certificate analysis of our

HD sample indicates that the total amount of CH_4 and C_2H_6 should be less than 30 ppm. In those circumstances, we decided to perform our own fit of the methane contribution using an interactive least squares multi-line fitting program assuming a Voigt profile [109]. The Half Width at Half Maximum (HWHM) of the Gaussian component was fixed to the theoretical value of the Doppler width of the considered molecule and isotopologue. In the simulation displayed in Fig. 3.3, the HD line was also fitted using a Voigt-type line shape, but contrary to methane lines, a W–shape residual is observed. To reduce this residual, the HD line was fitted with a Nelkin–Ghatak profile [110] (see Fig. 3.4) taking into account the Dicke narrrowing effect [111].

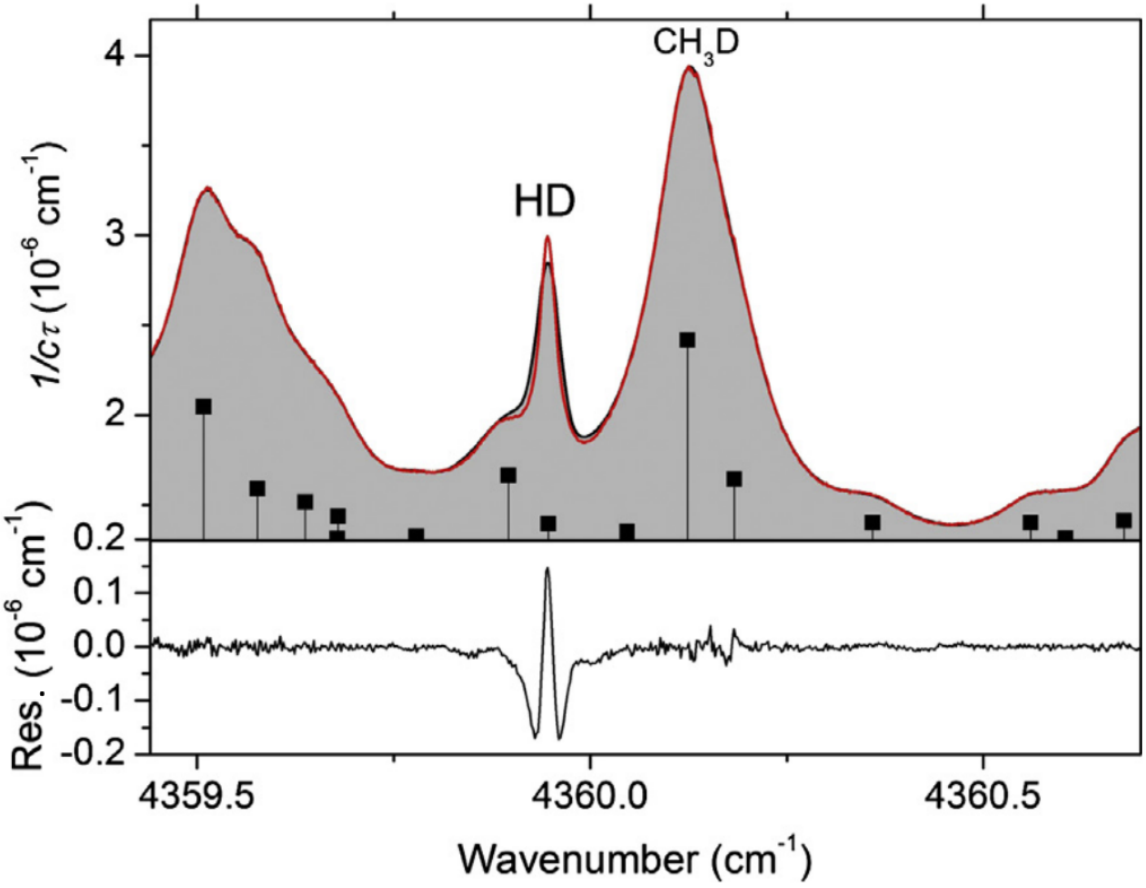

Figure 3.3. Comparison of the CRDS spectrum of HD at 650 Torr with a spectrum fit in the vicinity of the S(3) 1–0 line. All the lines belong to CH_4 except the HD and CH_3D lines which are indicated. A Voigt profile was used to fit all the lines (see text). *Upper panel:* Experimental (red solid line) and fitted (dashed line with gray under the curve) spectra. *Lower panel:* Residuals between the experimental spectra and the simulation.

For each pressure value, the line center (ν_0), the integrated line absorption coefficient, A_{ν_0} (cm^{-2}), and the corresponding local baseline (assumed to be constant over the fitted spectral interval) were provided by the multi-line fit of the spectra. The fitted center of the HD line was provided by the fit procedure with a 1σ stan-

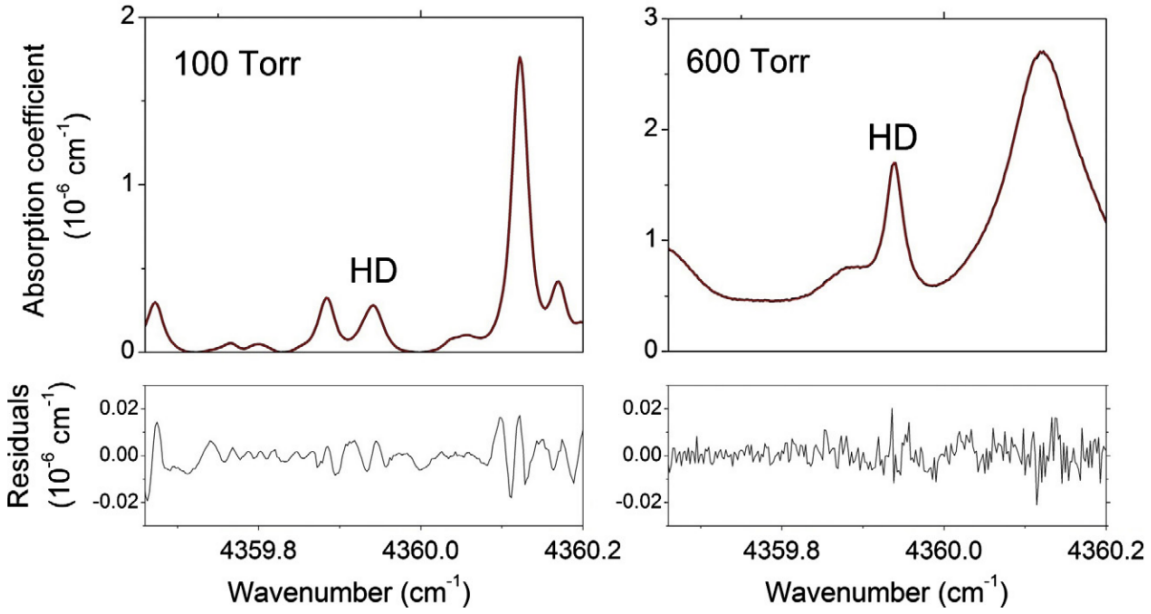

Figure 3.4. Line profile simulations of the CRDS spectrum of HD in the region of the S(3) 1–0 line. Note that the baseline is adjusted for the collision-induced absorption contribution. *Upper panels:* Experimental spectra at 100 and 600 Torr, Lower panels: Corresponding residuals between the experimental spectra and the simulations using a Nelkin–Ghatak profile for the HD line and a Voigt profile for the superimposed methane lines (see text).

dard deviation equal to 2.4×10^{-4} cm^{-1}. As a result, the uncertainty budget on our wavenumber scale leads to an overall error bar of about 0.002 cm^{-1}, mainly dominated by errors related to the linearization of the frequency axis and by the uncertainty due to the pressure shift of the methane lines used as reference lines. The resulting value of the HD S(3) 1–0 position at null pressure was determined to be 4359.9402(20) cm^{-1}. Our line center value at zero pressure was determined to be in very good agreement with its *ab initio* value [79] – 4359.9398(6) cm^{-1}, but the uncertainty of our determination (about 0.002 cm^{-1}) did not allow us to reduce the error bar of calculations or estimate the pressure shift.

The S(3) 1–0 line intensity

Fig. 3.5 shows the pressure dependence of the integrated line absorption coefficient. The line intensity S_{ν_0} (cm/molecule) was derived from the fitted value of the proportionality factor:

$$S_{\nu_0} = A(T)/N \tag{3.1}$$

where $A(T)$ is the integrated absorption coefficient in cm^{-2}, and N is the HD concentration in molecule/cm^3 obtained from the partial pressure and temperature values: $N = 0.978P/kT$ (0.978 is the stated relative concentration of HD in our sample).

We obtained an intensity of $2.54(6) \times 10^{-27}$ cm/molecule at 297.5 K, which leads

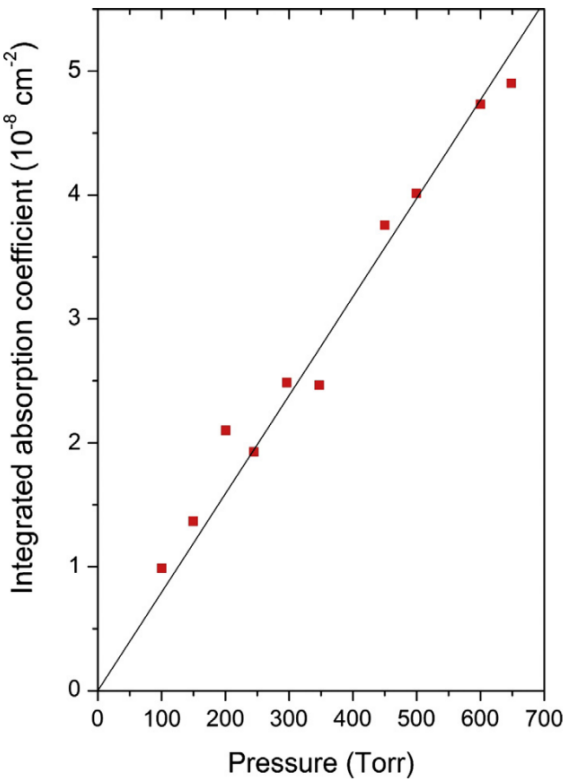

Figure 3.5. Variation of the integrated absorption coefficient of the S(3) 1–0 line versus the HD pressure. The line intensity was derived from the fitted slope (black solid line)

to a value of 2.52(6) $\times$ 10^{-27} cm/molecule at the 296 K HITRAN reference temperature (see eq. 1.5 in Section 1.2.1). The error bar of about 3% corresponds to the fit error and does not include systematic errors (see below). The HITRAN intensity value – 2.166×10^{-27} cm/molecule – is given with a 10–20% error bar, which is consistent with our value. In fact, the most recent theoretical calculations by Komasa and Pachucki [80] provided electric dipole and electric quadrupole moments with a much higher accuracy (<1%), which is probably out of reach by experiment. The quality of these *ab initio* intensity (and position) values was validated by recent state–of–the–art experimental studies of H_2 [86], HD [101] and D_2 [88] transitions of both E1 and E2 types. At the final stage of the analysis, Komasa and Pachucki provided us with their complete HD line list. The agreement with HITRAN intensity values calculated using the electric quadrupole moment of H_2 [112] was excellent (better than 0.1%) in both E1 and E2 transitions. Consequently, the approximation used for the calculation of HITRAN intensities of E2 transitions has no impact on the obtained values and HITRAN error bars are believed to be significantly overestimated. As a result of possible error related to the Born-Oppenheimer breakdown, a conservative uncertainty value between 10% and 20% was attached to the HITRAN E2 intensities of HD. In fact, the comparison to HITRAN values of the E2 HD intensities measured by the CRDS in the first overtone band [101] indicates that HITRAN error bars are overestimated. This comparison leads to an intensity ratio of 1.031(38) for nine E2 lines, what is a remarkable result considering that the considered E2 transitions include

line intensities spanning five orders of magnitude down to 3×10^{-29} cm/molecule.

In our case a 12% difference is observed. The main part of this deviation is believed to have an experimental origin related to nearby CH_4 lines not fully processed by the multiline fit or to underlying weak lines due to methane or other impurities not included in the fit.

3.2.3 Collision-induced HD absorption near 4360 cm^{-1}

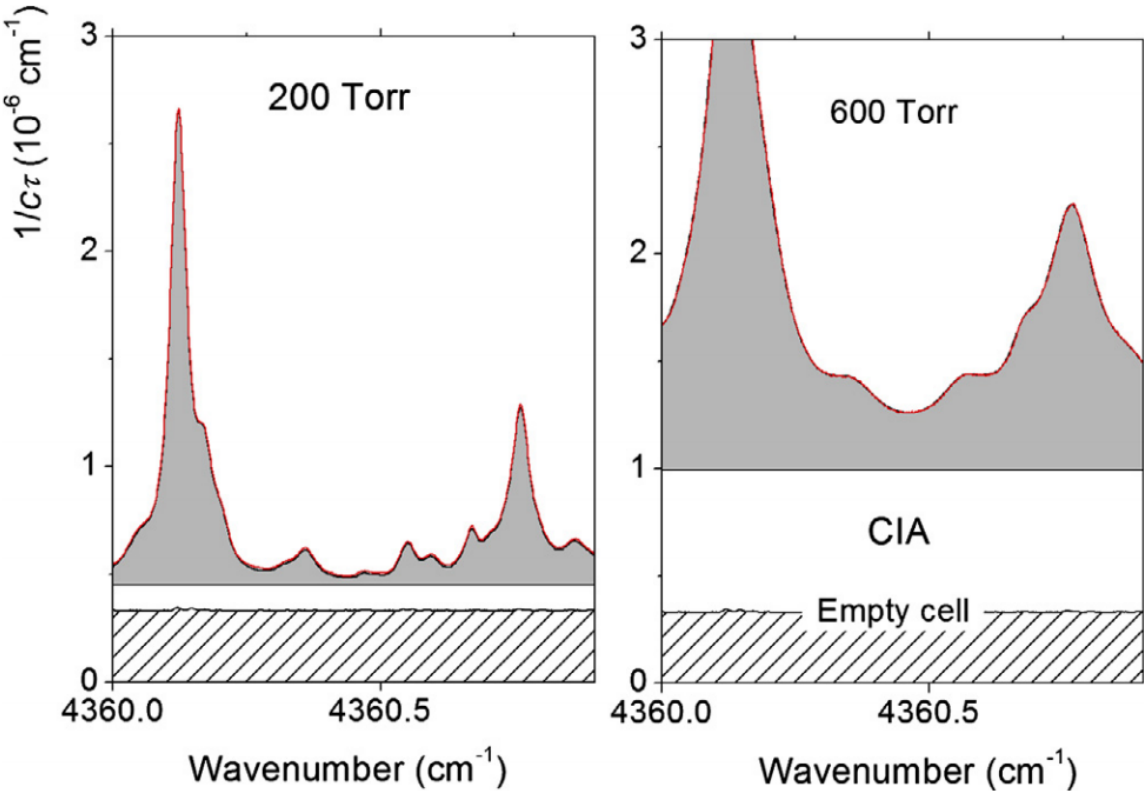

Figure 3.6. Retrievals of HD CIA at 4360 cm^{-1} from VECSEL–CRDS spectra at 200 and 600 Torr. The loss rate, $1c/\tau$, of the CRDS cell (red solid line) is superimposed to the spectrum simulation of methane lines broadened by HD (black line with gray under the curve). The HD CIA is the difference between the baseline of the spectrum simulation and the loss rate of the evacuated cell.

In a CRDS experiment, the CIA is expected to manifest itself as an increase in the baseline level of the spectra when the cell is filled by the gas. In the present case, as illustrated by Fig. 3.6, part of the increase of the baseline level is due to the contribution of the methane lines which are pressure-broadened by HD. This contribution has to be estimated from a spectra fit and subtracted to get the CIA value. Note that losses due to Rayleigh scattering are negligible (see. Section 4.4.2) at the considered wavelength. We chose a spectral interval showing weak methane absorption near 4360.4 cm^{-1} in order to minimize the uncertainty regarding the contribution of

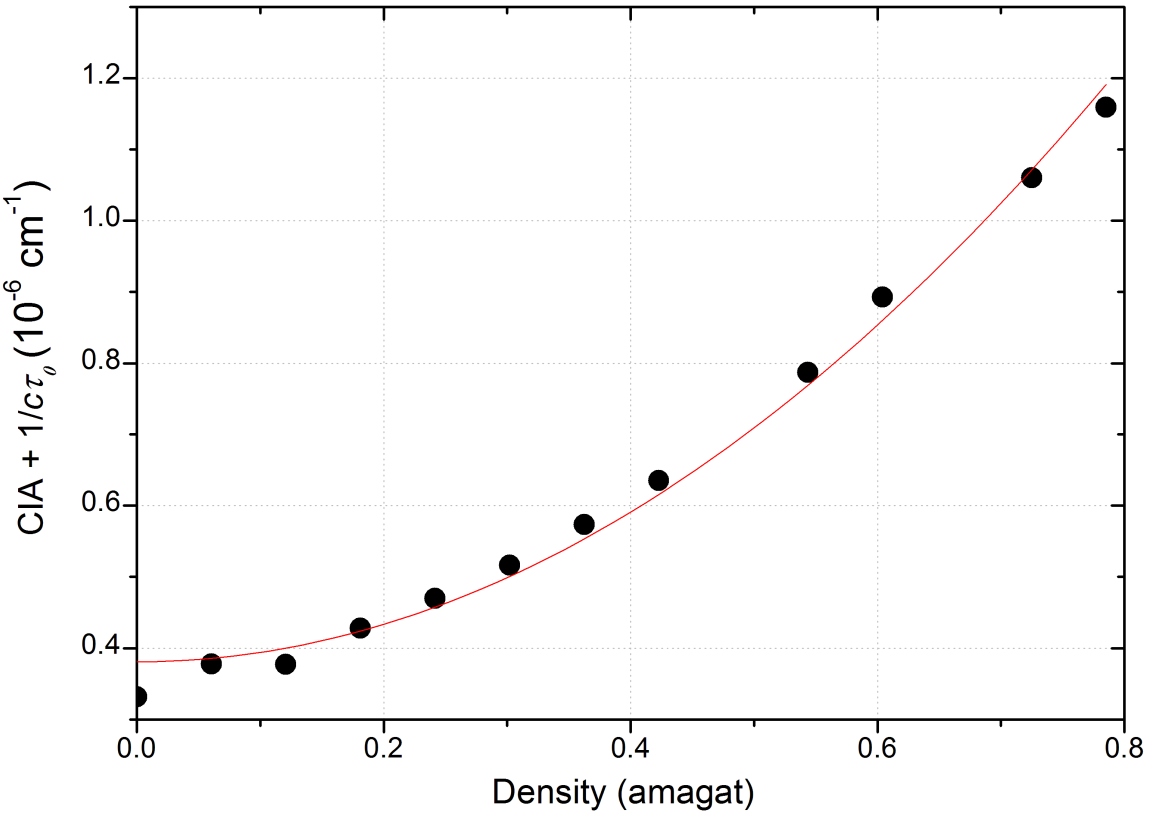

Figure 3.7. Density dependence of HD CIA at 4360.4 cm^{-1} for pressure values up to 650 Torr.

methane. The multiline fit of the methane lines located in the considered spectral interval gave the local baseline corresponding to the sum of the loss rate at zero pressure, the CIA and a weak contribution of the wings of the strong methane lines located outside the fitted spectral interval (see Fig. 3.6).

The latter, estimated in a spectrum simulation was found to be small (4% of the CIA at most) and subtracted. In this way, the CIA could be derived at different pressures which can be converted in density knowing the temperature. The resulting density dependence presented in Fig. 3.7 is near-quadratic. The amagat is a unit of number density and 1 amagat corresponds to the number of ideal gas molecules per unit of volume at 1 atm and 0 °C. The pure quadratic fit of the CIA values leads to an absorption coefficient normalized by the gas density squared, and is equal to 1.17(4) $\times$ 10^{-6} $cm^{-1}amagat^{-2}$. For comparison, we estimated this normalized coefficient using absorption coefficients measured at 35 amagat as per Fig. 1 of Ref. [92]. The CIA frequency dependence displayed in the 3300–4000 cm^{-1} interval in this figure corresponds at maximum to a value of about 2.6 $\times$ 10^{-6} $cm^{-1}amagat^{-2}$ near 3650 cm^{-1} decreasing to 1.6 $\times$ 10^{-6} $cm^{-1}amagat^{-2}$ at 4000 cm^{-1}; which is consistent with our value of 1.17(4) $\times$ 10^{-6} $cm^{-1}amagat^{-2}$ at 4360 cm^{-1}.

In the case of H_2, *ab initio* calculations have made it possible to account for the

measured CIA bands of H_2 with remarkable precision [91]. For instance, an agreement of under 10% was obtained between the *ab initio* and CRDS values in the 2–0 H_2 band near 8075 cm^{-1}. Unfortunately, similar calculations have not yet been reported for HD, probably because of the insufficient interest for astrophysics. Nevertheless, the H→D substitution may provide valuable tests for the theoretical models used for H_2.

3.3 First laboratory detection of an absorption line of the first overtone electric quadrupole band of N_2 by CRDS near 2.2 μm

In the present section we demonstrate the limit sensitivity performance of our spectrometer used with the EC–CRDS configuration accomplishing the first laboratory detection of the extremely weak ($S \approx 1.3 \times 10^{-30}$ cm/molecule) O(14) quadrupole transition of N_2 in the first overtone band centered at 4631 cm^{-1}. An overview of the fundamental and two first overtone bands as provided by the HITRAN2012 database [2] is presented in Fig. 3.8. The HITRAN line positions were derived from the semi-empirical potential energy function of Le Roy et al. [113] while the quadrupole line intensities were converted from the *ab initio* quadrupole moment function of Li and Le Roy [114].

As a consequence of their weakness, previous detections of N_2 quadrupole transitions are very scarce (see Fig. 3.8) and mostly limited to the 1–0 fundamental band centered near 2330 cm^{-1}. Fundamental band transitions were first detected in the atmosphere from ground by Goldman et al. [117] and Camy–Peyret et al. [118] or from stratospheric solar spectra by Rinsland et al. [119]. To the best of our knowledge, the only laboratory detection of 10 transitions was reported by Reuter, Jennings and Brault [115] from spectra recorded at Kitt Peak by FTS with a 434.0 m absorption path length. The weaker 2–0 transitions are observed in the long path atmospheric spectra recorded by FTS in the frame of the Total Carbon Column Observing Network (TCCON). It is important to include them in retrievals as they interfere with the CO_2 bands. 2–0 and 3–0 overtone transitions of N_2 have intensities below 7×10^{-30} and 2×10^{-31} cm/molecule, respectively, making their laboratory detection very challenging and providing difficult tests for ultrasensitive laser spectrometers. Recently, laboratory detection of the S(4) and S(6) transitions in the 3–0 band by very high sensitivity CRDS near 6950 cm^{-1} was reported [116]. A limit of detection determined as the root mean square of the baseline signal, on the order of $\alpha_{min} \approx 5 \times 10^{-13}$ cm^{-1} was achieved by averaging several thousand 0.5 cm^{-1} wide spectra recorded successively over several days [59]. Such a record sensitivity was necessary to detect the 3–0

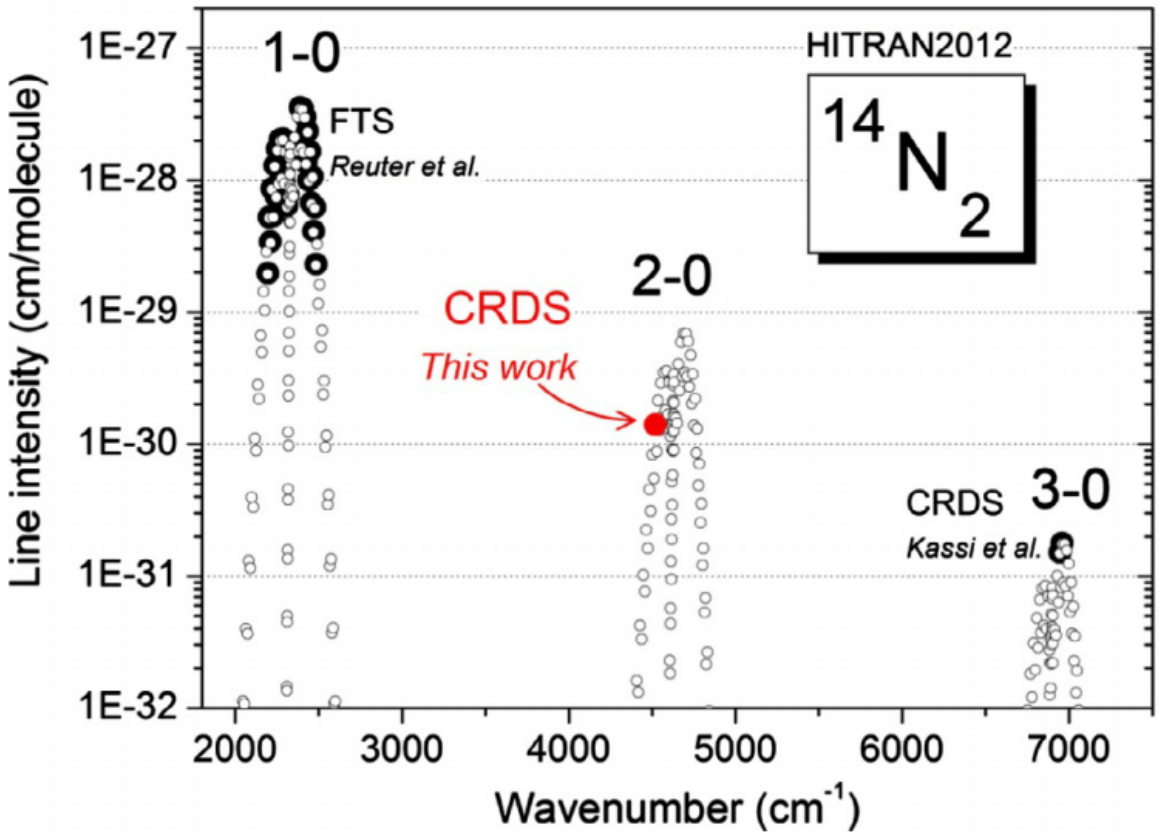

Figure 3.8. Overview of the $^{14}N_2$ calculated line list as provided in the HITRAN2012 database (open black). The highlighted transitions correspond to previous detections from laboratory absorption spectra by FTS in the 1–0 band [115] and by CRDS in the 3–0 second overtone [116]. The presently detected O(14) line in the 2–0 band is indicated.

S(4) and S(6) lines which are among the weakest lines ever measured in the laboratory (intensity on the order of 1.5×10^{-31} cm^{-1} cm/molecule).

3.3.1 Measurements

The EC–CRDS setup is described in detail in Section 2.3. Here we define some of specific details of the experiment. Measurements of the O(14) transition with $\nu_0 = 4518.4128$ cm^{-1} were performed by recording 27 and 32 spectra from 4518.35 to 4518.55 cm^{-1} at 100 Torr and 200 Torr, respectively. In the present experiment, a nitrogen gas flow was used instead of a static cell in order to minimize the impact of impurities (mostly water) out gassing from the walls of the CRDS cell.

As shown later, traces of water vapor and ammonia were nevertheless observed in the spectra. The level of NH_3 impurity is especially crucial here as a transition of this species with an intensity 4×10^9 times stronger than the studied N_2 transition is located at only 0.025 cm^{-1} from the N_2 line. To reduce the NH_3 concentration, the N_2 gas flow was sent through a spiral tube plunged into a bath of liquid nitrogen to

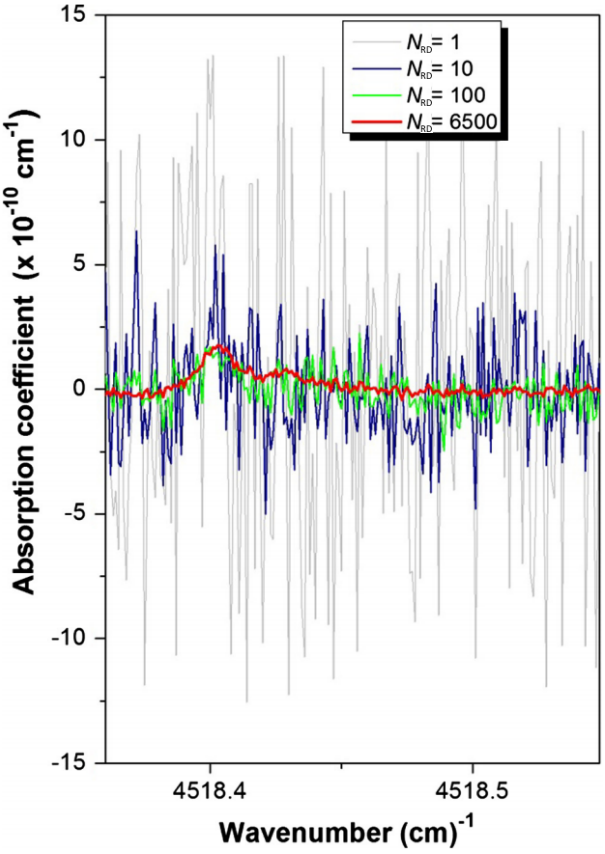

Figure 3.9. Spectra of N_2 recorded at 100 Torr and averaged for different number, N, of RD events per spectral step.

condensate NH_3 (and water vapor). The level of NH_3 measured in the final spectra was then around 180 ppt and 130 ppt for the 100 Torr and 200 Torr series, respectively. As it will be shown below, at this level of concentration the NH_3 transition only partially blended the N_2 line. No water vapor was observed in the spectra of the 100 Torr series but a water line at 4518.5431 cm^{-1} was detected in the 200 Torr series at a level of 20 ppm probably coming from the out gassing of the cell walls.

For each of the recorded spectra, about 250 RDs were acquired using the mode tracking during 10 s per spectral step separated by about 0.001 cm^{-1}. Nevertheless, in these conditions, the limit of detection was of the order of 5×10^{-11} cm^{-1} which was insufficient to detect the N_2 transition under study. Further averaging was then required to statistically decrease the noise level (Fig. 3.9). Based on the wavelength value of the laser attached to each RD event, provided by the wavelength meter at a refresh rate of 2.5 Hz and 1σ of measurements of 2.4×10^{-4} cm^{-1}, all the RD values were gathered and averaged over each 0.001 cm^{-1} bin. Fig. 3.9 shows that the N_2 line (partly overlapping with the nearby NH_3 line) clearly shows up when the number, N_{RD}, of RD events averaged per spectral step is increased up to 6500.

In the following, we analyze the two averaged spectra recorded at 100 and 200 Torr with the tracking method.

3.3.2 Analysis and results

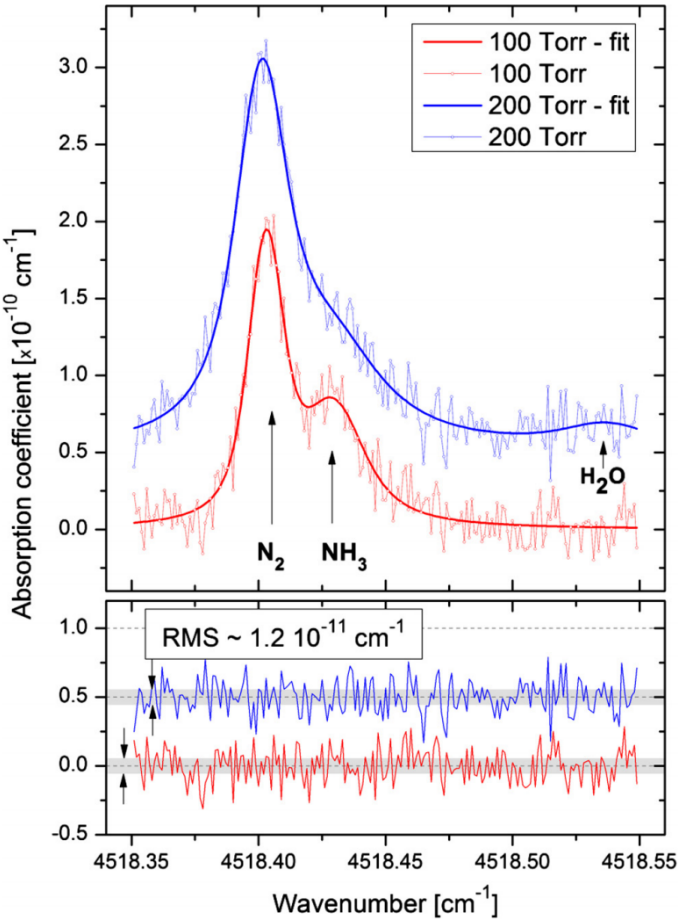

Figure 3.10. CRDS and fitted spectra at 100 and 200 Torr after the averaging process (upper panel). The fit residuals are shown on the lower panel.

The 2–0 O(14) line of N_2, the nearby line of ammonia and a water line (at 200 Torr) were included in a multiline fitting program. From the HITRAN2012 database [2] no other H_2O or NH_3 lines are expected to reveal above the noise level in the considered spectral interval. The three lines were fitted using a Voigt profile, sufficient at this level of signal to noise ratio. The Doppler widths were fixed to the calculated value. The collision width was obtained from the broadening coefficients reported in HITRAN2012. The result of the fitting procedure, where positions and areas are freed, is displayed in Fig. 3.10. The averaged spectra at 100 and 200 Torr are reproduced to the noise level of about 1.2×10^{-11} cm^{-1}.

Line center

The center of the NH_3 line at 4518.437832 cm^{-1} assigned to the $^{R}R(5,3)$ transition of the $\nu_2 + \nu_3$ band [2] was used as reference to fix the absolute value of the frequency scale provided by the wavelength meter. This transition is reported in HITRAN2012 with an uncertainty on the position between 0.0001 and 0.001 cm^{-1}. The air pressure shift of the considered NH_3 transition (not provided in the HITRAN database), is in

fact not needed to derive the zero pressure value of the N_2 line center: the wavenumber difference, δ, of the NH_3 and N_2 line centers varies linearly with pressure: $\delta = \delta_0 + aP$, and from the δ values measured at 100 and 200 Torr, the wavenumber difference at null pressure, δ_0 is obtained. Using the HITRAN NH_3 reference position at null pressure, we obtained a value equal to 4518.4115(23) cm^{-1} for the N_2 line center at null pressure. This value is 1.4×10^{-3} cm^{-1} lower than the position reported in HITRAN2012, well below HITRAN error bar of 0.01 cm^{-1}. Taking into account the uncertainties on the position of the NH_3 reference line, of its pressure shift and of the line positions determination by the multiline fit, we estimate the total error bar on the obtained N_2 line position to be 0.003 cm^{-1}.

Line intensity

The intensity, $S(T)$, of the 2–0 O(14) nitrogen line was determined from the linear fit (weighted by the fit error) of the line surfaces measured at 100 and 200 Torr as a function of the pressure. The fit was constrained to pass through zero at null pressure. The resulting value for S(298 K) is 1.27×10^{-30} cm/molecule, which leads to $S(296\text{K}) = 1.265 \times 10^{-30}$ cm/molecule. The uncertainty given by the fit was around 5%. During the measurements, the total pressure in the HFC was stabilized at the 0.2% level. The total pressure was measured with an uncertainty of 0.4 mbar leading to an error of 0.3% and 0.15% for 100 Torr and 200 Torr, respectively, which has to be added to the previous error source. Nitrogen used in this work was obtained from the vapor phase in the liquid nitrogen tank of our laboratory and is believed to have a purity much better than 99%.

During all the recordings reported here, the cell temperature varied between 296.5 and 298.5 K leading to an uncertainty below 1%. Considering all these uncertainties and the fact that a systematic error of a few % on the determination of the area is possible when using a Voigt profile instead of more complex profiles [120], we estimate the accuracy of the line strength to be 10%. Our value of $S(296\text{K}) = 1.26(13) \times 10^{-30}$ cm/molecule is 10% lower than the intensity reported in HITRAN2012 with an uncertainty between 10 and 20% (see Table 3.1).

Table 3.1. Line center and line position measured in this work and reported in HITRAN2012 [2] for the O(14) transition of the 2–0 band of N_2

	Line center (cm^{-1})	Line intensity at 296 K (cm/molec.)
HITRAN2012	4518.4128 ± 0.01	$1.405 \times 10^{-30} \pm 20\%$
This work	4518.4115 ± 0.003	$1.265 \times 10^{-30} \pm 10\%$

3.4 Conclusion

The study of the HD in 2.3–μm region was the first spectroscopic application of a VECSEL for Cavity Ring Down Spectroscopy in this region. As an illustration of the capabilities of the VECSEL–CRDS setup, the first detection of the S(3) quadrupole electric transition of the fundamental band of HD was realized. The mechanical stability of the setup allowed us to derive the CIA absorption coefficient from the increase of the spectra baseline from its value at zero pressure, after subtraction of the methane contribution.

We have improved the performances of our developed CW–CRD spectrometer by using optical feedback to drastically narrow the DFB laser diode line width (from 10 down to 1 MHz). This narrowing of the laser source and the implementation of a tracking method allowed for a much better injection into the high finesse cavity. Thanks to these improvements and to the fact that we averaged a high number of spectra, we achieved a sensitivity of $\approx 1.2 \times 10^{-11}$ cm^{-1}, sufficient to detect for the first time a very weak quadrupolar transition in the first overtone band of N_2.

In the remaining chapters we will discuss a series of experimental studies of rovibrational transitions and continuum absorption for both CO_2 and H_2O performed using the described highly sensitive cavity ring-down spectrometers.

Chapter 4

Water vapor spectroscopy in 2.3–μm transparency window

4.1 Introduction

The important role of water vapor in the atmosphere of the Earth, especially in radiative balance and minor components monitoring was discussed in Section 1.1. In the present Chapter, we will discuss studies of the water vapor spectrum in the 2.2–2.3 μm range carried out using the various laser sources at disposal.

During the study dedicated to recording of rovibrational transitions of water vapor, the achieved sensitivity allowed us to detect transitions with intensity values down to 1×10^{-28} cm/molecule, more than one order of magnitude better than previous studies performed using FTS. We used our results to test and validate line lists available in the literature and more specifically the intensities provided by *ab initio* calculations and the HITRAN2012 database [2].

We also applied our experimental setup to the measurements of the water vapor self-continuum. We obtained new experimental data along the entire transparency window centered at 2.1 μm. These experiments compensated for the lack of highly sensitive measurements and show the trend across the window.

In addition to our self-continuum measurements, we will report the experimental results of foreign-continuum recording carried out in a narrow spectral range around 4250 cm^{-1}. Despite the uncertainty of 30% on foreign-continuum cross-sections, they are worth discussing for perspective developments.

This extensive study has led to 3 publications dedicated to both rovibrational transitions and continuum absorption published between 2015 and 2017 [121–123].

4.2 The high sensitivity recording of absorption spectrum of water vapor in the 2.2–μm region

4.2.1 Experimental details and recordings

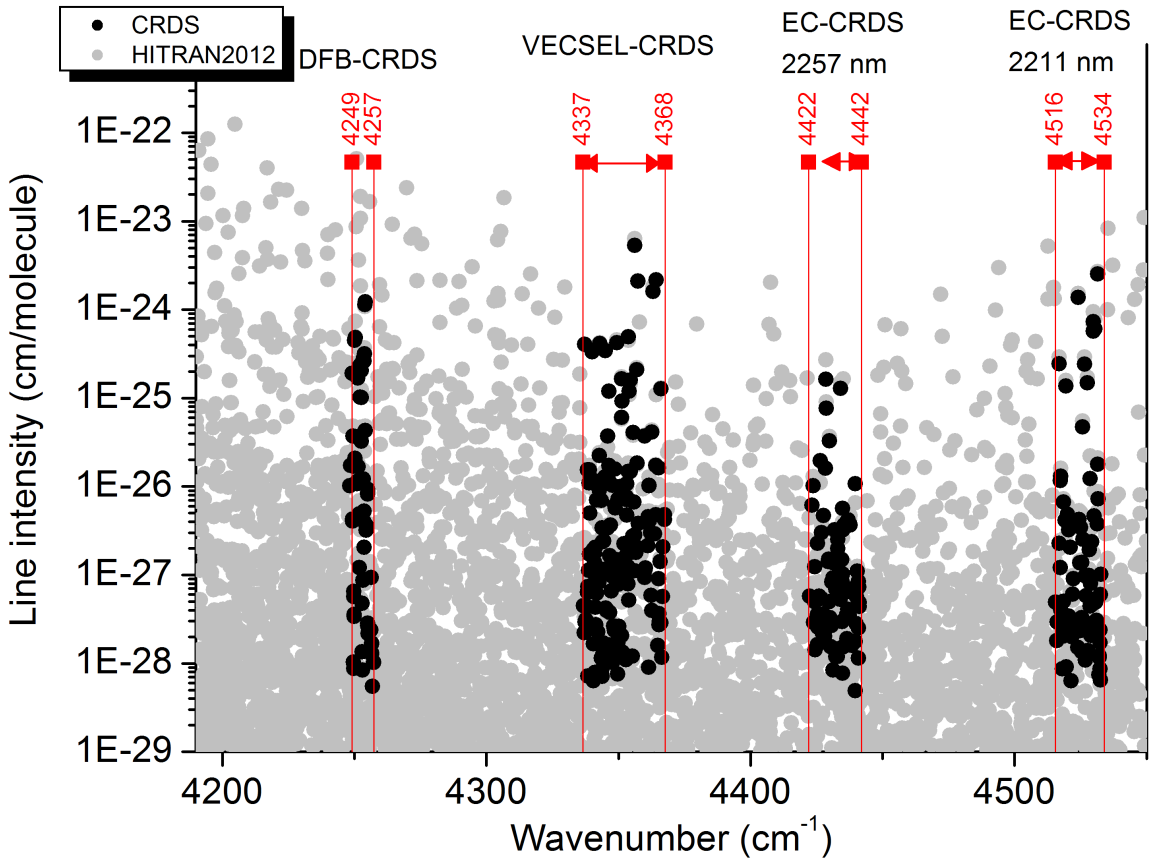

Figure 4.1. Overview of spectral regions accessible with our four laser sources at disposal and recorded transitions.

In the present work, we recorded spectra of pure water vapor in the spectral range between 2.20 and 2.35 μm using our high sensitivity CRDS setup. The laser sources, which were at disposal, i.e. three DFB laser diodes and the VECSEL, allowed us to access four spectral intervals as shown in Fig 4.1. Table 4.1 lists the four spectral intervals of the spectra recordings together with the corresponding laser source. The typical LOD of the spectra varied between 1 and 6×10^{-10} cm^{-1} for both DFB and VECSEL light sources. As described in Chapter 2, the frequency calibration of the DFB based CRDS spectra relied on the frequency measurements provided by the wavelength meter. To refine the calibration, some accurate reference lines (water, methane or carbon dioxide) from the HITRAN database [2] were used to correct the wavelength meter offset (up to 0.006 cm^{-1}), leading to an accuracy of $\pm$0.001 cm^{-1}.

The VECSEL–CRDS spectra were calibrated using the double reference channel

Table 4.1. Summary of CRDS measurements dedicated to the absorption spectrum of water vapor in 2.2 μm window.

Interval, cm^{-1}	Method	Regime/Pressure	Main impurities	N. of lines
4248.2–4257.3	DFB–CRDS	Static/1, 4, 8.5 Torr	NH_3, CH_4	55
4336.8–4367.5	VECSEL–CRDS	Flow/7–8 Torr	NH_3	150
4422.4–4441.2	EC–CRDS	Flow/7–8 Torr	NH_3, CH_2O, CH_4	82
4514.8–4533.7	EC–CRDS	Flow/8 Torr	NH_3, CH_2O	81

(FP etalon + CH_4 reference cell) instead of the wavelength meter and then the calibration was refined using accurate water reference lines from the HITRAN database. Position uncertainty for these spectra is estimated to be of 0.002 cm^{-1} mostly because of uncertainty due to spectrum linearization using the FP-etalon.

The measurements were performed either in a static cell or in flow with a water sample purified by being cooled down to temperature below the freezing point of water using liquid nitrogen and then pumping out impurities in the gaseous phase with a turbo pump. In both the static and flow modes, the water vapor pressure in the cell was continuously monitored with the 1000-mbar STS ATM.1ST capacitive transducer with accuracy of $\pm 0.1\%$ of the full range. In calculating line intensities, we used the corresponding pressure value for each line.

In spite of our attempts to minimize concentration of impurities, ammonia (coming from the water sample itself) and methane (believed to desorb from the stainless steel tubes of the setup), contribute significantly to the spectra because their strongest lines have an intensity on the order of 10^{-20} cm/molecule, i.e. eight orders of magnitude larger than our detection threshold for water lines. The mixing ratios of ammonia and methane were found to be a few ppm.

Formaldehyde is another interfering species that we found in our spectra. To limit its presence in our sample, its origin was investigated. For that we first recorded a CH_2O line during 14 hours with the cell closed after filling it with 8 Torr of water vapor. We observed a continuous increase of the CH_2O concentration with time as plotted in Fig. 4.2. Note that the formaldehyde line partly overlaps with NH_3 impurity line, which reveals no noticeable growth during this time. Formaldehyde was only observed in the presence of water vapor: no formaldehyde lines were detected with the cell filled with dry air or CO_2. Thus, it seems that a part of CH_2O can be produced inside the HFC in presence of water vapor because of chemical reaction.

In addition, the concentration of formaldehyde was also significantly minimized by pouring the purified water, produced by Purelab Classic purification unit by Elga, directly into the metallic water tank instead of using a plastic reservoir for the transfer. This minimizes the initial concentration of CH_2O in the sample. Nevertheless, many

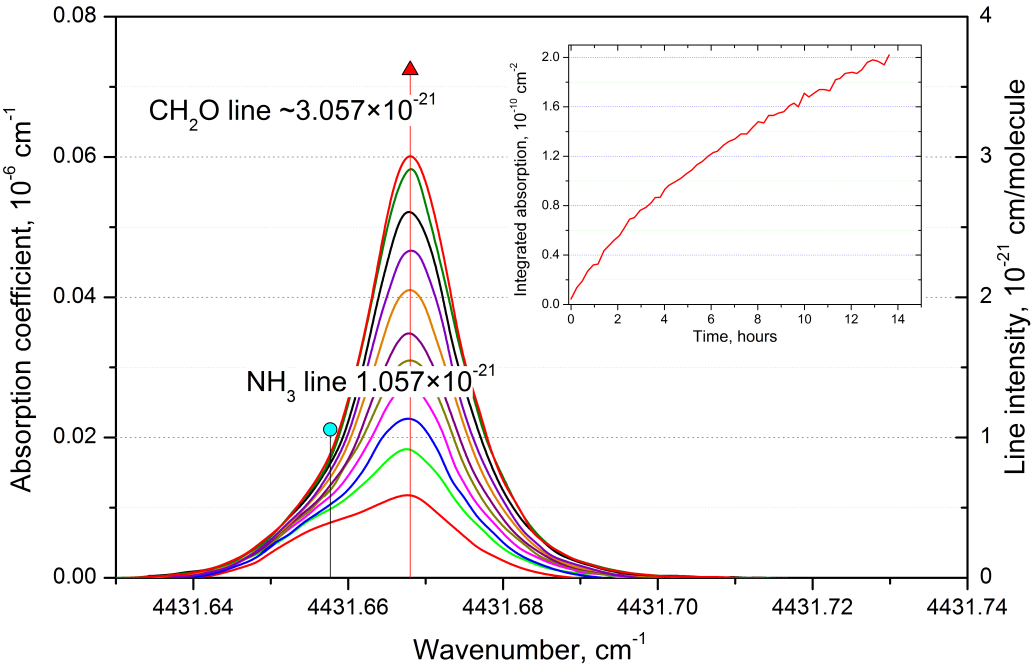

Figure 4.2. Increase of a formaldehyde line with time inside the cell filled with 8 Torr of water vapor. Red triangle denotes the intensity of the line obtained from the FTS spectrum from Ref. [124]. Insert: the normalized integrated absorption of the line versus time. Note that the NH_3 line which stays almost constant during the time of recording.

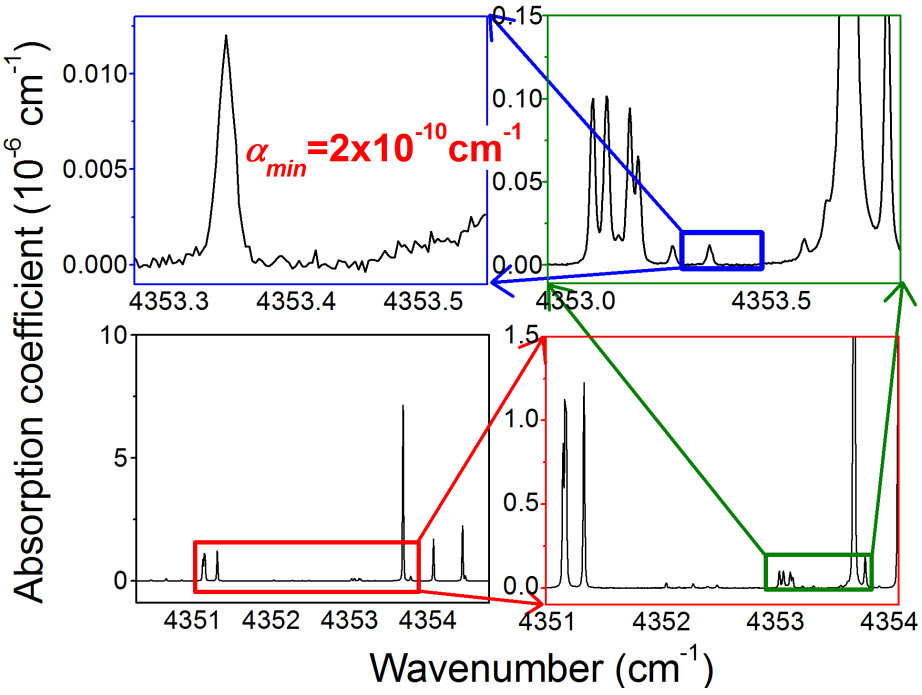

Figure 4.3. CW–CRDS spectrum of water vapor near 4353 cm^{-1} recorded with the VECSEL source. Sample pressure was about 7.6 Torr. Three successive enlargements illustrate sensitivity and high dynamical range of recordings, making it possible to measure absorption coefficients spanning more than four orders of magnitude.

lines were identified in the high frequency part of the spectrum, where formaldehyde absorption is very strong.

As no data is provided for CH_2O by the HITRAN database in the studied region, the lines of this species were identified by comparison with an FTS spectrum, which is in open access at the Kitt Peak data center (Ref. 840109R003). Note that the formaldehyde spectrum in the 2.3 μm range was investigated in refs. [124, 125] (some lines are rovibrationnally assigned). A rough estimation using the FTS spectrum displayed in ref. [124] indicates that the CH_2O relative concentration in our sample was 5 ppm at most.

The CRDS spectrum recorded with the VECSEL presented in Fig. 4.3 illustrates the performance in terms of sensitivity and dynamical range. It is worth mentioning that this VECSEL experiment was conducted later than the one described in Chapter 5 dedicated to CO_2. During this period of time, the spectral range covered by the VECSEL reduced from 85 cm^{-1} to 30 cm^{-1} due to the deposition of matter on the VCSEL semiconductor structure leading to a higher lasing threshold.

The number of water lines measured from the recorded spectra is included in Table 4.1 for each spectral interval. Overall, a total of 368 absorption lines were measured with intensities as weak as 1×10^{-28} cm/molecule. Let us mention that due to impurity lines and a few narrow gaps in the recordings, a number of water lines are missing in our experimental list.

4.2.2 Building of the water vapor line list

Vibrational modes, notation of rovibrational transitions used in HITRAN and selection rules for H_2O molecule are given in Appendix A.

The first experimental line list, including line centers and intensities was established using an interactive least squares multi-line fitting program assuming a Voigt profile, the HWHM of the Gaussian component being fixed to the theoretical value of the Doppler width.

The first step of the analysis consisted in "cleaning" the recorded spectra to remove impurity lines. Indeed, lines of NH_3, CH_4 and CH_2O (formaldehyde) were found superimposed to the weak water vapor lines of interest. Lines due to ammonia and methane were identified by comparison with the HITRAN2012 database [2].

The rovibrational assignment of the remaining water lines and resulting line list was provided by S. Mikhailenko from IAO Tomsk. To do that, the variational calculation results by Schwenke and Partridge (SP) [126, 127] and the values of empirical energy levels of the six most abundant isotopologues ($H_2{}^{16}O$, $H_2{}^{18}O$, $H_2{}^{17}O$, $HD^{16}O$, $HD^{18}O$ and $HD^{17}O$) recommended by an IUPAC-task group [120, 128–130] were taken as a starting point.

Finally, overall in the 4 recorded regtions (Table 4.1) 368 lines were assigned to 424 transitions of six water isotopologues ($H_2{}^{16}O$ – 177 transitions, $H_2{}^{18}O$ – 38 transitions, $H_2{}^{17}O$ – 18 transitions, $HD^{16}O$ – 185 transitions, $HD^{18}O$ – 4 transitions, and $HD^{17}O$ – 2 transitions). Among the 368 measured lines, 184 were detected for the first time. Note that the detection of lines of $HD^{18}O$ and $HD^{17}O$ with natural abundance of 6.23×10^{-7} and of 1.16×10^{-7}, respectively, illustrates the sensitivity of the recordings [12].

It is difficult to give an average uncertainty value for CRDS line intensities. Comparisons with literature values and between various determinations from different CRDS spectra indicate that a value of 2–5% is a reasonable estimate for well-isolated $H_2{}^{16}O$ lines of intermediate intensity. Larger error bars should be attached to blended lines and the relative abundance of the minor isotopologues adds uncertainty to the line intensities of these species. Our experimental list including CRDS line positions and intensities, corresponding SP values [126, 127] and full rovibrational assignment is provided in supplementary material of the paper [123].

4.2.3 Comparison with existing literature data

In the spectral range studied in this work, three previous experimental data sets are available all recorded with FTS technique. These datasets, are plotted in Fig. 4.4. The first one which is the most complete is provided by Jenouvrier *et al.*, who measured lines with intensities down to about 1×10^{-27} cm/molecule from FTS spectra with path lengths up to 1203 m [22]. The second dataset was obtained at the DLR (the national aeronautics and space research centre of Germany) for the strongest water lines in the 4190–4350 cm^{-1} region. This dataset, hereafter called DLR, is provided within the framework of the ESA project SEOM–Improved Atmospheric Spectroscopy Databases (IAS) [131]. The last dataset is reported by Mikhailenko *et al.* and derived from FTS spectra recorded at Giessen with a path length of 288.5 m and pressure up to 24 Torr [132].

An overview comparison to the HITRAN2012 water line list [2] between 4190 and 4550 cm^{-1} is presented in Fig. 4.4. The HITRAN2012 list includes lines of the $H_2{}^{16}O$, $H_2{}^{18}O$, $H_2{}^{17}O$ and $HD^{16}O$ isotopologues with intensities larger than 1×10^{-29} cm/molecule. HITRAN line parameters have experimental or theoretical origins. For instance, among the 2303 transitions included in HITRAN between 4190 and 4550 cm^{-1}, less than 700 are provided with experimental intensities. These experimental intensity values, all belonging to $H_2{}^{16}O$ and $HD^{16}O$, were retrieved by Toth from FTS spectra recorded at Kitt Peak with absorption path lengths of up to 433 m [133]. The minimum intensity values reported by Toth are on the order of 1×10^{-26} cm/molecule, about two orders of magnitude above our detection threshold.

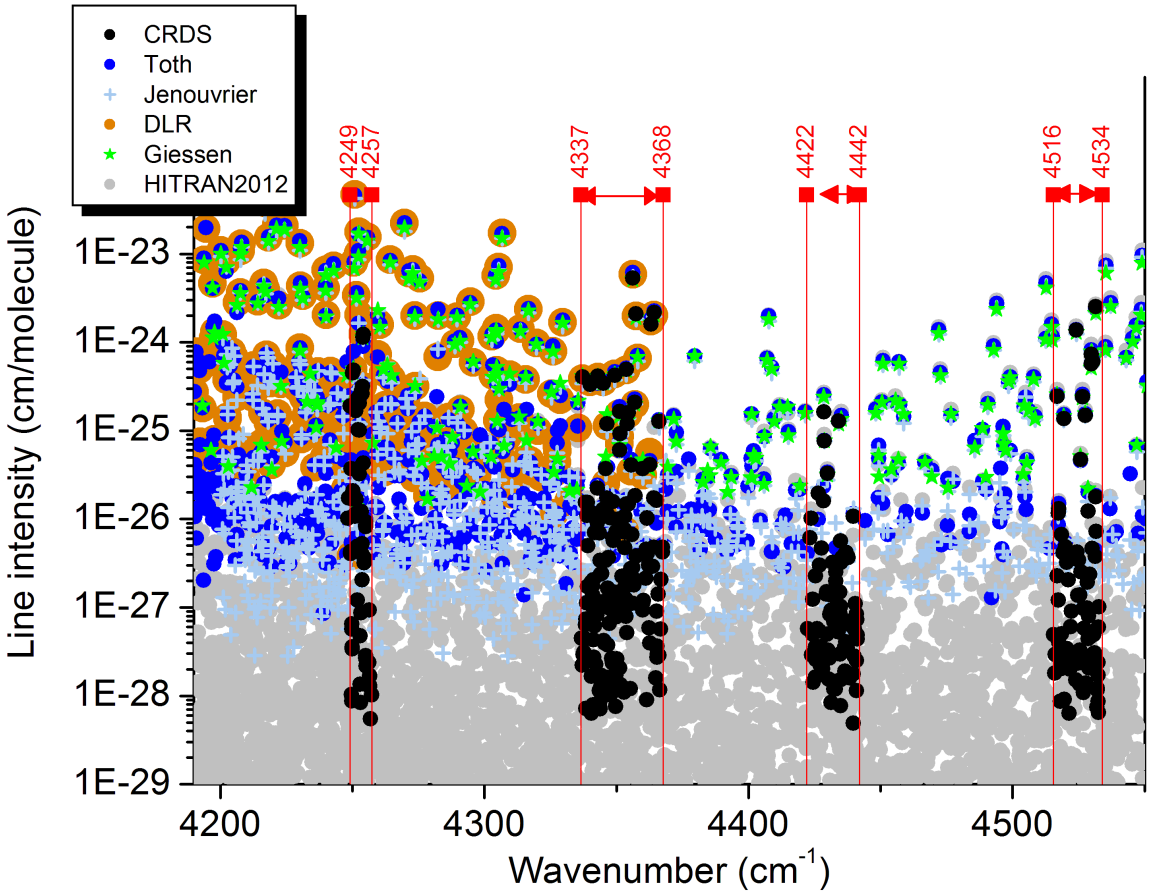

Figure 4.4. Comparison of the main experimental studies of water absorption in the 2.2 μm window to the line list provided by the HITRAN2012 database [2]. The four spectral intervals presently studied by CRDS and OF-CEAS are highlighted. Previous studies were performed by FTS by Toth [133] [35] (blue circles), Jenouvrier *et al.* [22] (light blue cross), Loos *et al.* [131] ("DLR", orange circles) and Mikhailenko *et al.* [135] "Giessen", green stars).

The HITRAN2012 line list contains transition frequencies that are experimental values for some of the $H_2{}^{16}O$ lines and all the $HD^{16}O$ lines as measured by Toth, values derived from the IUPAC-task group energy levels [120,128–130], and variational values [134] for several dozens $H_2{}^{16}O$ and $H_2{}^{18}O$ transitions.

A variational line list (hereafter referred to as UCL2016) for natural water vapor was compiled using the most recent line lists calculated for the various water isotopologues in collaboration between University College London and the Institute of Applied Physics in Nizhny Novgorod [136–141]. We will compare our line intensities and those obtained by DLR for the main isotopologue, on the one hand, to these calculations providing test and validation for the most recent complete variational line list, on the other hand. The UCL2016 will be used as a source of variational intensities for the 2017 version of the HITRAN database. It is expected to significantly improve the overall accuracy of Schwenke–Partridge (SP) variational intensities [126, 127], which

are more than fifteen years old.

Line positions

As illustrated by the histograms of the differences between positions measured in this work and the positions found in the literature displayed in Fig. 4.5, the coincidence with FTS data is not completely congruent: excluding outliers with deviations greater than 0.1 cm^{-1}, standard deviations are 2.09×10^{-3} cm^{-1} for Giessen data, 2.85×10^{-3} cm^{-1} for Jenouvrier and 2.58×10^{-3} cm^{-1} for Toth. Good agreement is achieved with DLR data: except for a few high intensity outliers saturated in CRDS spectra, we have a standard deviation and an average difference of 1×10^{-3} and 0.1×10^{-3} cm^{-1} respectively. The larger standard deviation for Jenouvrier *et al.* measurements can be explained by the fact that the comparison includes lines with intensity down to 10^{-27} cm/molecule, while the comparison with DLR is restricted to stronger lines ($S >\sim 10^{-25}$ cm/molecule). These results are in agreement with our claimed uncertainty of 0.001–0.002 cm^{-1}, but taking into account that in all the aforementioned experimental datasets authors claim the uncertainty of the line positions not worse than 1×10^{-4} cm^{-1}, discrepancy in the line positions is too large. Considering this issue, we can assume that the accuracy of the positions of the weak lines with intensities of less than 1×10^{-26} cm/molecule is more confident for CRDS measurements because of the sensitivity of the technique.

We also added a comparison of our line positions with those from a database compiled in Ref. [123] using empirically determined energy levels from CRDS measurements presented here, OF–CEAS measurements and energy levels adopted from available datasets (see details in Ref. [123]). The comparison gives a standard deviation of 2.02×10^{-3} cm^{-1} for lines with intensities down to 5×10^{-29} cm/molecule.

Line Intensities

In the framework of the ESA project, the goal was to test and validate a complete and accurate line list for the weak lines, which cannot be all measured. In order to do that, the intensities obtained experimentally by CRDS in Grenoble and by FTS by DLR were compared to available *ab initio* calculations. These calculations have the advantage of being complete and are thought to be accurate in terms of the intensities.

In Fig. 4.6, we plotted the ratios of the DLR and CRDS intensities to the UCL2016 values (the upper panel) and to the SP variational calculations [126, 127] (the lower panel) for the main isotopologue in the 4190–4550 cm^{-1} region versus the UCL2016 line intensities. The FTS values recently measured at DLR [131] in the 4190–4365 cm^{-1} region show excellent agreement with UCL2016 values. For intensity values higher than 1×10^{-24} cm/molecule, the agreement is at 1% level, and no sys-

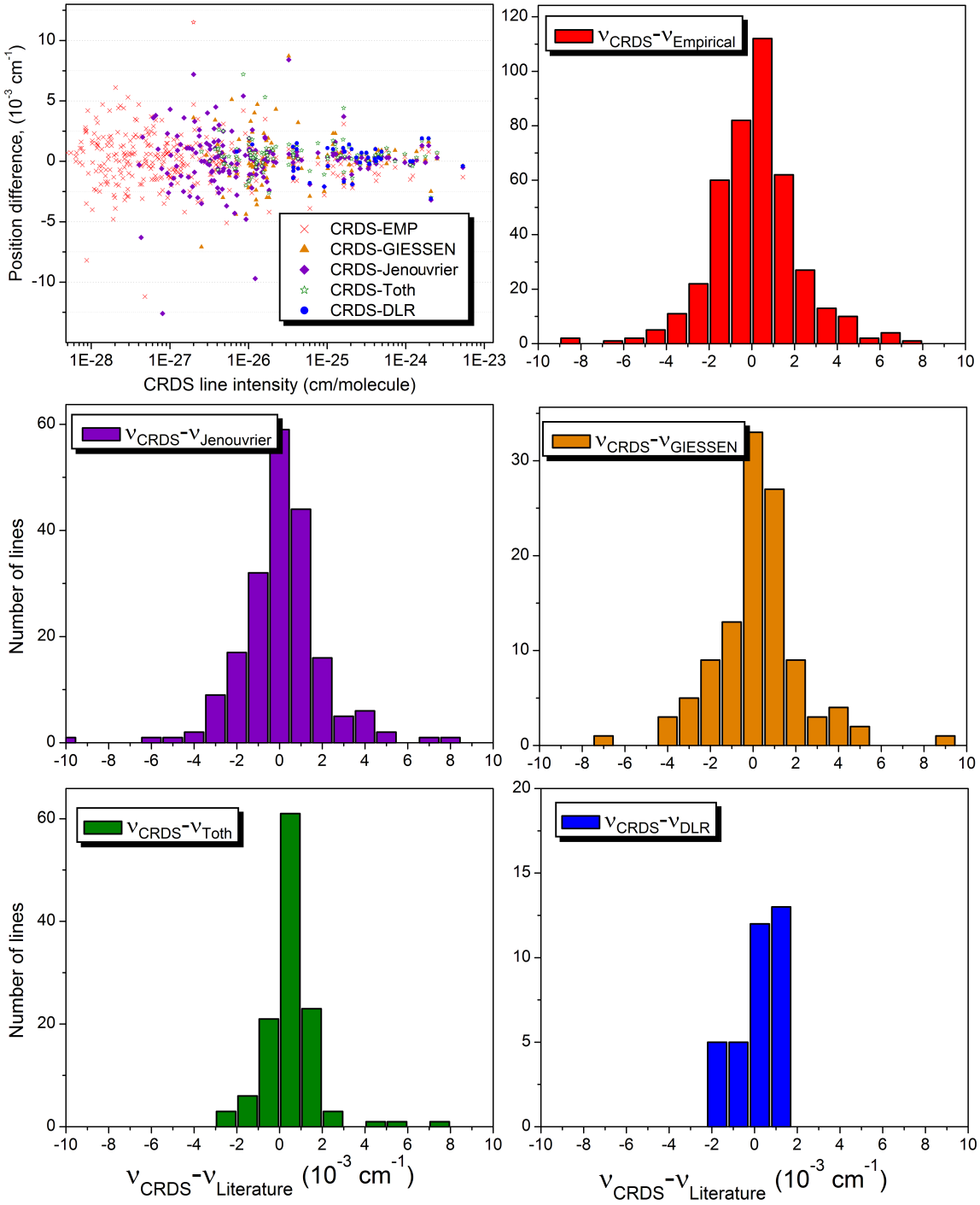

Figure 4.5. Differences between CRDS line positions and those from the literature (top left). Histograms of the differences between CRDS line positions and their corresponding FTS measurements [131, 133, 135], and line positions obtained from empirical energy levels [123].

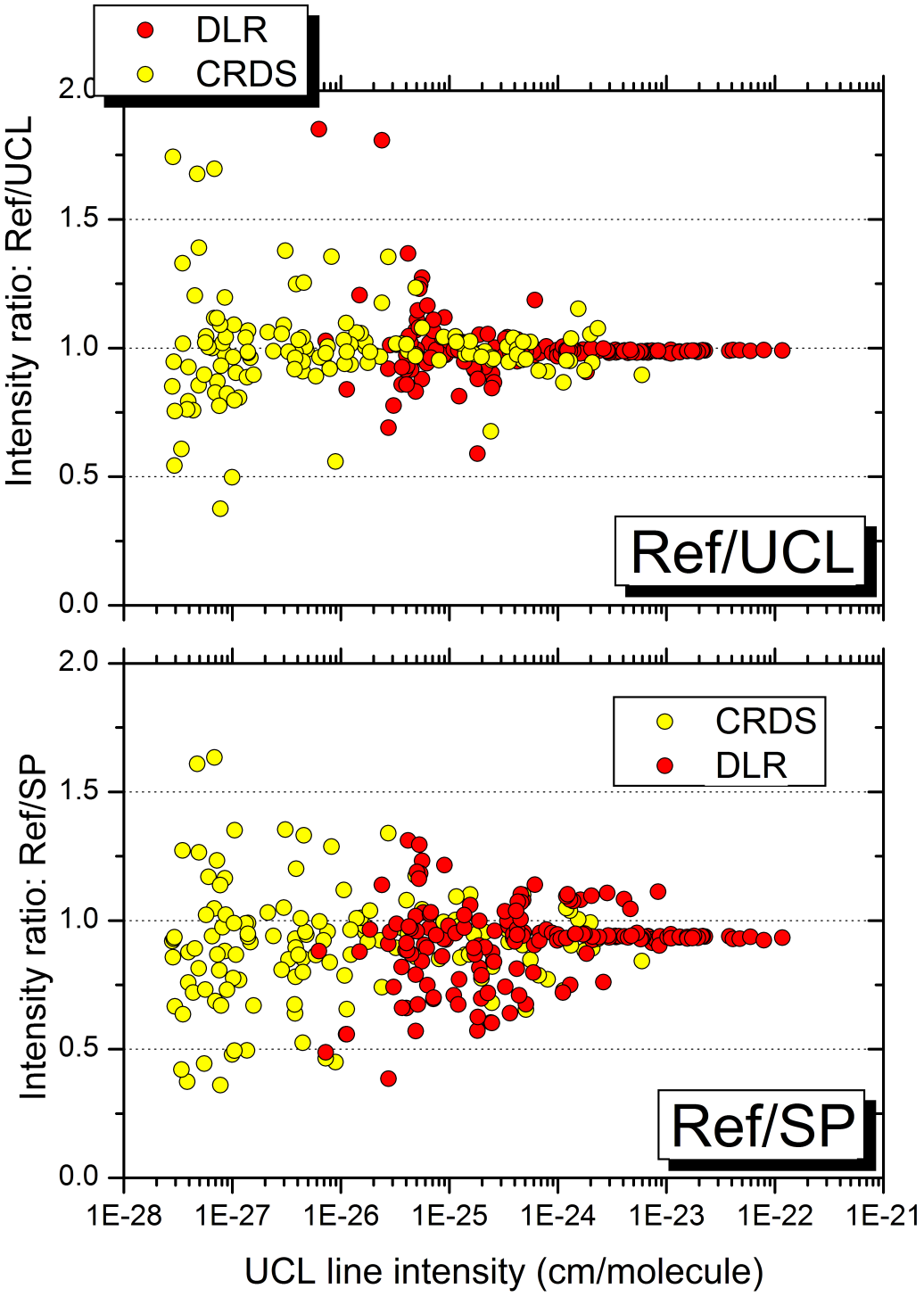

Figure 4.6. Comparison of the DLR [131] and CRDS sets of intensity data between 4190 and 4550 cm^{-1} to recent UCL2016 intensity values (upper panel) and to SP variational values (lower panel)

Table 4.2. General statistics on main isotopologue intensity ratios.

	UCL	SP
DLR	1.00/0.12[a]	0.92/0.14
CRDS	0.99/0.18	0.93/0.29

[a] Mean/SD.

tematic shift of the UCL2016 values with respect to those of DLR is detected. These observations are confirmed for the weaker lines with intensities down to 2×10^{-28} cm/molecule by comparison of the CRDS line intensities with those calculated (see Table 4.2). This shows that UCL calculations notably improve the accuracy of intensities of the water vapor lines compared to SP. The obtained accuracy is of the order of 1% or better when compared to experimental data obtained with the same level of accuracy. This UCL2016 line list will be used as the source of variational intensities in the 2017 version of the HITRAN database and will also be adopted in the line list provided for the ESA project for the weak lines. Note that the larger dispersion observed for the CRDS dataset for intensities higher than 1×10^{-24} is due to the saturation of those in CRDS spectra. We call a line "saturated" in a CRDS spectrum when no ring-downs are acquired for several spectral points due to too strong absorption. This typically occurs when the absorption coefficient is greater then a few 10^{-6} cm^{-1}.

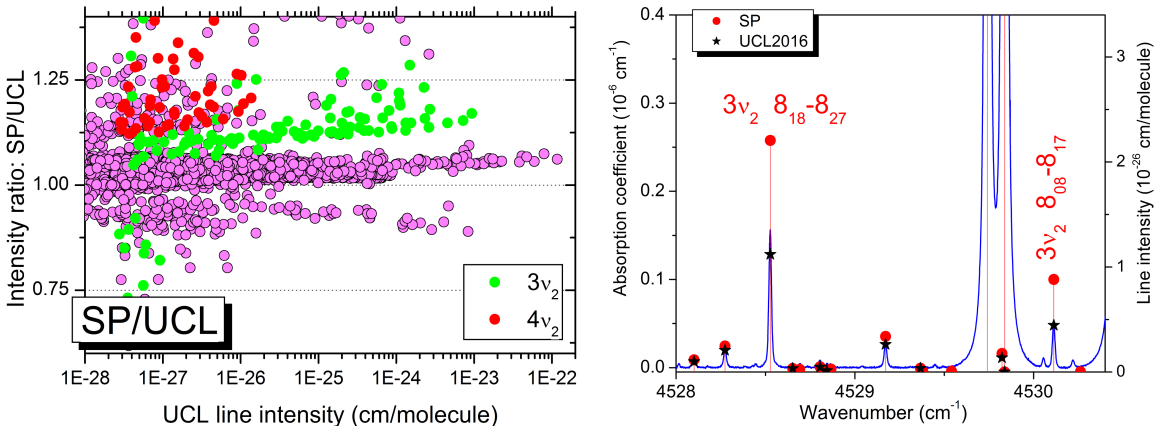

Figure 4.7. Left panel:Intensity ratios of SP variational intensity values to the UCL2016 values. Transitions corresponding to the $3\nu_2$ and $4\nu_2$ bands are highlighted. Right panel: EC–CRDS spectrum of water vapor at 8 Torr near 4530 cm^{-1} compared to variational calculations by Schwenke and Partridge (SP, red circles) [126] and by the UCL group (black stars) [142]. Two $3\nu_2$ transitions of $H_2{}^{16}O$ fall in the displayed interval. The transition frequencies were fixed to their experimental values.

Compared to UCL2016, SP intensities are overall overestimated by 5% and show larger deviations for the transitions of the $3\nu_2$ and $4\nu_2$ bands (see left panel of Fig. 4.7). The overestimation of the variational intensities of the purely bending bands

has already been evidenced in Ref. [143] for SP and previous UCL calculations (see Figs. 6 and 7 of Ref. [143]). As illustrated in Fig. 4.7, which shows our EC–CRDS spectrum in an interval with two $3\nu_2$ transitions, the new UCL calculations agree satisfactorily with the measurements.

New energy levels determination and connection of existing ones

The rovibrational assignment which was provided by S. Mikhalenko allowed us to determine 12 new energy levels of three isotopologues ($H_2{}^{17}O$, $H_2{}^{18}O$ and $HD^{18}O$) in natural abundance. Nine of them correspond to transitions of the ν_1, ν_3 and $3\nu_2$ bands of H^{17}_2O. Note that the (001) $12\ _{3\ 10}$ level was obtained from the ν_1 $12\ _{3\ 10}$ – $11\ _{1\ 11}$ transition at 4348.9409 cm^{-1}. This line was measured and assigned by Jenouvrier *et al.* [22] but not included in the IUPAC database [128].

The (110) $7\ _{6\ 2}$ and (110) $7\ _{6\ 1}$ levels of $HD^{18}O$ were previously determined by Liu *et al.* with an isotopically enriched sample [144], but their energy value relied on an erroneous assignment of the $\nu_1+\nu_2$ $7\ _{6\ 1}$ – $7\ _{6\ 2}$ and $\nu_1+\nu_2$ $7\ _{6\ 2}$ – $7\ _{6\ 1}$ transitions at 4144.596 cm^{-1}. This data was included in the IUPAC database [129]. The difference between our values (5115.108 cm^{-1}) and those of refs. [129, 144] (5114.496 cm^{-1}) is larger than 0.6 cm^{-1}.

4.2.4 Comparison to HITRAN2012

When compare the CRDS spectra with HITRAN2012 we clearly observe the absence of many $HD^{16}O$ lines which are included to the database from the measurements of Toth [133] and are limited to intensities of the order of 10^{-26}. $HD^{16}O$ contribute importantly to the absorption in the considered transparency window due to isotopic shift, similarly to the situation found in the 1.58 and 1.25 μm windows [143,145–147]. Fig. 4.8(a) presents a sample of the CRDS spectrum in a spectral interval where HDO lines are missing from the HITRAN list. In Ref. [123], the complete line list for the region from 4190 to 4550 cm^{-1} and intensities down to 1×10^{-29} cm/molecule was constructed for the 6 most abundant isotopologues including $HD^{16}O$.

In the HITRAN2012 list a number of line positions have a variational origin and thus show large discrepancy compared to experimental spectra. This concerns mainly weak transitions with position offset values of up to 0.2 cm^{-1}. These transitions can now be improved by replacing them with empirical values.

The HITRAN2012 [2] list includes both variational intensities from UCL [136, 137] for the weak lines and FTS intensities for the strongest lines from Toth [133] (see Fig. 4.4). In a number of cases, mostly for lines with intensity on the order of 10^{-26} cm/molecule corresponding to the FTS detection limit, strong discrepancies with our measurements were evidenced. Examples of strong overestimation and underestima-

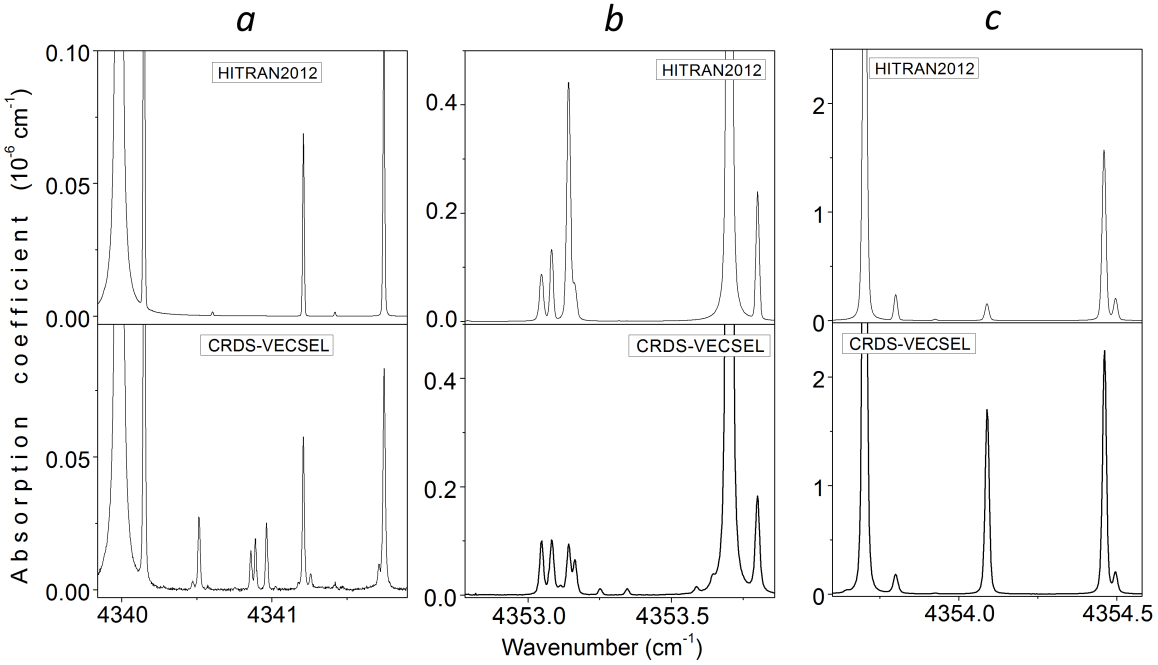

Figure 4.8. Comparison of the CRDS–VECSEL spectrum of water vapor ($P \approx 7.5$ Torr) (lower panels) to simulations based on the HITRAN2012 list (upper panels).

tion are presented in Fig. 4.8 (b) and (c). The HITRAN intensity of the $H_2{}^{16}O$ line at 4353.1425 cm^{-1} ($11\ _{7\ 4} - 10\ _{4\ 7}$ transition of the ν_1 band) is strongly overestimated (left panels). The HITRAN intensity (3.37×10^{-26} cm/molecule) is the experimental value by Toth [133].

The $15\ _{3\ 12} - 14\ _{2\ 13}$ transition of the ν_1 band of $H_2{}^{16}O$ at 4354.0908 cm^{-1} has a strongly underestimated value in HITRAN2012 (1.21×10^{-26} versus 1.19×10^{-25} cm/molecule by CRDS) (right panels). The HITRAN intensity is the experimental value by Toth [133]; interestingly, Toth reported the correct measured value of 1.19×10^{-25} cm/molecule but suggested a 10 times smaller value for HITRAN.

4.2.5 Conclusion

With the CRD spectrometer, developed during this thesis, the spectrum of water vapor was recorded with unprecedented sensitivity in four selected spectral intervals of the 2.2–μm region. About 400 absorption lines of water vapor were measured and rovibrationnally assigned, about half of them has been detected for the first time. Twelve energy levels were first determined for $H_2{}^{17}O$, $H_2{}^{18}O$ and $HD^{18}O$ minor isotopologues in natural isotopic abundance.

Using these experimental results and adopting available empirical energy levels, S. Mikhailenko compiled a complete and accurate database for water vapor between 4190 and 4550 cm^{-1}, which contains 4309 transitions with empirical line positions for six isotopologues and a 1×10^{-29} cm/molecule intensity cut-off. It is believed to be

the most accurate and complete line list in the region. More details on the database can be found in ref. [123].

The comparison of the line intensities of very recent FTS measurements at DLR [131] and obtained in present work to the variational line list UCL2016 evidenced a significant improvement compared to previous variational intensity by Schwenke and Partridge [126, 127] values in the region. The agreement is at 1% level with DLR for a set of about one hundred lines with intensities larger than 1×10^{-24} cm/molecule.

The comparison of our spectra to the HITRAN2012 [2] list indicates that the list obtained in this work and the future HITRAN2017 list will lead to a significant improvement in terms of completeness (the absence of a large fraction of HDO lines being the major deficiency of the present HITRAN2012 list) and in terms of the accuracy of line intensities (some of the intensities with experimental origin in HITRAN2012 are not accurate).

The next Section will be dedicated to high-sensitivity measurements of a water vapor continuum in the transparency window centered at 2.1 μm.

4.3 Water vapor continuum absorption in 2.1–μm transparency window

4.3.1 Introduction

Atmospheric transparency windows, which correspond mainly to spectral intervals of weak water vapor absorption, are used for atmospheric remote sensing [111] and for quantifying the contribution of geophysical elements with a spectrally large optical signature like surface albedoes [111], clouds [148], and aerosols. In the near-infrared atmospheric windows, between 2000 and 9000 cm^{-1}, absorption is believed to be dominated by the water vapor continuum contribution [149], which thus has to be accurately determined for atmospheric applications. The water vapor continuum and its large uncertainty also impact radiative transfer calculations, leading to a larger uncertainty compared to the uncertainty due to the rest of the spectral data used in the calculations [150].

After more than one century from its experimental discovery [151, 152], the strength and physical origin of the absorption continuum of water vapor remain an open question with direct implications for the radiative budget and climate change of the Earth through feedback effects [150, 153–157] and on the estimated boundaries and extension of the habitable zone of stars [158–160].

Two main physical processes are believed to contribute to the water vapor absorption continuum:

- Far-wings of the absorption lines of the monomer and more generally the monomer line shape perturbations due to binary collisional interactions;

- The bimolecular contribution including dimeric and collision induced absorption corresponding to two molecules simultaneously interacting with the field.

A brief history of the water vapor continuum since its discovery, attributed to Rubens and Aschkinass [151] is reported in Ref. [161]. Herein, we will just mention the main stages in this history as was summarized by Ptashnik [162] and then discuss the models and measurements available.

The first explanation was proposed by Elsasser in 1938 [163], 4 decades after the first observation of the continuum. He assumed that the continuum was due to the accumulation of far wings of strong water monomer lines in the region. This hypothesis was generally recognized till 60ies when the quadratic pressure dependence [164] and negative temperature dependence [165] of self-continuum were observed. These two effects could not be explained with a simple Voigt line shape of monomer lines due to collisional broadening. So, in 1967 Penner and Varanasi [165,166] assumed that the water dimer (clusters of two water molecules interacting through a weak hydrogen bound) was the main contributor to self-continuum. The continuum model based on water dimers well explained the pressure and temperature dependencies discovered in many studies [166–168].

In the other hand, later, new approaches in far-wing theory were developed by Ma *et al.* [169], which has an *ab initio* basis but still requires experimental adjustment. Semi-empirical semi-classical model by Tvorogov *et al.* was also presented. [170]. The work of Ma *et al.* was developed later (see Ref. [171]) and aligned well with aforementioned pressure and temperature dependencies of the water continuum in 800–1200 cm^{-1}. Authors concluded that far-wing theory has moderately strong negative T dependence but it can vary with frequency region under the study. Nevertheless, thanks to this fact, far-wing contribution may still be considered relevant.

In the present work, we sidestep the physical causes of water vapor continuum absorption, which remains an actively debated area, and focus on new high-sensitivity measurements performed between 4250 and 4520 cm^{-1} and compare with the previous measurements and existing semi-empirical MT_CKD model [172] (will be discussed later). Our accurate continuum measurements by CRDS in the transparency window centered at 2.1 μm are part of an extensive water vapor continuum investigation by CRDS and OF–CEAS in the transparency windows centered around 4.0, 2.1 and 1.25 μm provided in LIPhy [122].

4.3.2 Water vapor continuum definition

Since the study from the Ref. [168] two different contributions to the continuum are distinguished. The first one is due to interactions between water molecules (self-continuum), and the second one is a result of interaction between water molecules and other atmospheric molecules (foreign-), mainly nitrogen and oxygen. The former's strength reveals a quadratic dependence on water vapor pressure while the latter grows linearly with water vapor partial pressure P_{H_2O} and with the partial pressure of the foreign gas P_f:

$$\alpha_{WC}(\nu,T) = \alpha_{WCS}(\nu,T) + \alpha_{WCF}(\nu,T) = \frac{1}{k_B T} C_s(\nu,T) P_{H_20}^2 + \frac{1}{k_B T} C_f(\nu,T) P_{H_20} P_f, \tag{4.1}$$

where k_B is the Boltzmann constant, T is the temperature in K. C_S and C_F represent the self- and foreign-continuum cross-sections, respectively. In this work we adopted the definition of Burch and Alt [173] where the cross-sections are expressed in $\mathrm{cm^2 molecule^{-1} atm^{-1}}$ for given temperature T. Note that in the MT_CKD and in some publications of experimental results the cross-sections are normalized to the reference number density N_0 at 1 atm and 296 K, following the definition of Clough *et al.* [174]. In this definition the cross-section have to be multiplied by $296/T$ to obtain the cross-section in the definition of Burch [175].

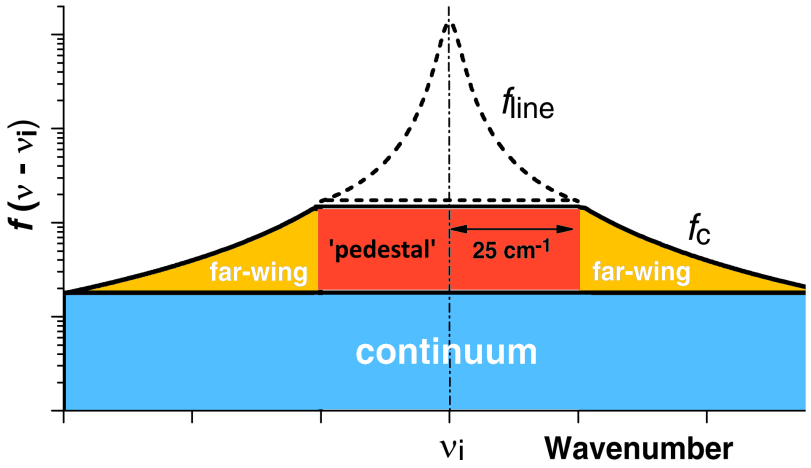

Figure 4.9. Dashed line denotes local monomer line contribution. Solid black line presents components of far-wing continuum of single line including ± 25 $\mathrm{cm^{-1}}$ "pedestal term" according to the definition of the MT_CKD model. Picture is taken from [149].

Nearly all measurements of the self-continuum cross-section available exhibit a marked negative temperature dependence. Conversely, within the available measurements and analysis uncertainties, the foreign-continuum seems independent of temperature between about 300 to 430 K [176].

Because there is no unambiguous way to separate water continuum absorption

from local monomer line absorption, the water continuum is usually defined as proposed first in the Clough–Kneizys–Davies (CKD) model [174] and then in its more recent version called MT_CKD (is for Mlawer–Tobin–CKD) [172]. In these models the water continuum is defined as the difference between the measured absorption spectrum and the sum of absorption due to local lines of water monomer (WML). The WML contribution is obtained by summing the Voigt profiles of the different absorption lines calculated within ± 25 cm^{-1} from the line center but without the "pedestal term" that corresponds to the absorption of the line at 25 cm^{-1} from the line center, which is considered as a part of the continuum [149] (Fig. 4.9). The HITRAN line list [2] is generally used as a reference for these local monomer calculations. The reported continuum values are then dependent on the version and the quality of the chosen line list used (including the data for all the isotopologues). This aspect should be kept in mind in particular in the near-infrared transparency windows, for which the HITRAN line list may contain deficiencies [123].

4.3.3 Review of available measurements and models

Due to a pragmatic approach, the description of the water vapor continuum proposed in the MT_CKD model [172] is widely adopted in most of the radiative transfer codes. This model is a semi-empirical formulation of the continuum with *ad hoc* line profile parameters, adjusted to fit the experimental absorption coefficients. As a consequence of the difficulty of measuring weak broadband absorption signals, up to recently the available experimental information was scarce and consisted mainly of laboratory [173, 175, 177] and field measurements in the microwave and mid-infrared regions [178] which have the strongest impact on radiative fluxes [15, 179]. The major constraint of the MT_CKD self-continuum in the 10–μm window is an analysis of field measurements [180]. In the 4–μm window the values of the MT_CKD 2.5 version are due to a combined analysis of AERI, IASI, and AIRS observations as described in [172]. In the near-infrared region, the MT_CKD continuum is then mostly an extrapolation yet to be validated. This applies in particular to the atmospheric windows corresponding to spectral regions of low opacity between strong absorbing rovibrational bands of water vapor, where water continuum absorption has been found to be the major contributor [149, 150]. The latest version MT_CKD2.8 includes MT_CKD2.5 [172] with modified values for the self-continuum in the 4 μm region based on the analysis of Alvarado *et al.* [181] from 2050-2180 cm^{-1}. Foreign-continuum values were modified in the region from 1800 to 3000 cm^{-1} due to an increase in the foreign-continuum and in N_2–H_2O collision-induced absorption motivated by the measurements of Baranov and Lafferty [182]. In addition, the foreign-continuum values for wavenumbers higher than 4000 cm^{-1} were modified based on

Baranov and Lafferty [182] and our first measurements in the 2.1–μm window [121] described in the end of this chapter.

The mid-infrared window centred at 2500 cm^{-1} (4.0 μm) has been the subject of several studies [168, 173, 182] but until recently there were only a few measurements of the water continuum in the near-infrared windows (see Ref. [183,184]). A few years ago, the CAVIAR (Continuum Absorption at Visible and Infrared wavelengths and its Atmospheric Relevance) consortium reported the first broadband measurements using FTSs coupled with different multi-pass absorption cells with path lengths of 512.7 and 17.7 m for room and high temperature measurements respectively [149,155]. The self- and foreign-continuum cross-sections were retrieved in the 4.0, 2.1, 1.6 and 1.25 μm windows at various temperatures between 293 and 472 K. To detect the weak continuum in the 1.6 and 1.25 μm windows, high temperatures were used to allow for an increase in the water vapor pressure (up to more than 1 atm); no measurements were reported at room temperature in these windows.

In Fig. 4.10, the CAVIAR FTS room-temperature self-continuum cross-sections, C_s are compared to the MT_CKD2.8 model. In the center of the 4.0–μm window, the CAVIAR cross-section was found to be larger than MT_CKD2.8 by a factor ranging from 3 to 5, depending of the wavelength, while a disagreement by more than one order of magnitude was reported in the 2.1–μm window [149]. These results from CAVIAR in the 4.0 and 2.1 μm windows were substantially confirmed by room temperature spectra recorded at IAO–Tomsk [185] using a similar method (FTS with a 612-meter absorption path length). In addition, the IAO-Tomsk spectra (Tomsk2013 hereafter) made it possible to extend the room temperature measurements to the 1.6–μm window, where larger disagreements compared to the MT_CKD2.5 (and thus MT_CKD2.8) model were reported (Fig. 4.10). This discrepancy was found to be even larger – up to two orders of magnitude – for the foreign-continuum cross-sections [155].

To quantify the impact of the much larger self-continuum cross-sections measured using the FTS technique upon solar radiation absorbed by the atmosphere, simulations were performed either with the CAVIAR or MT_CKD2.5 self-continuum cross-sections (the MT_CKD2.5 cross-sections being adopted for the foreign-continuum [155]). For clear sky conditions, a significant additional global mean absorption of $\sim$ 0.74 Wm^{-2} relative to the MT_CKD2.5 continuum is obtained after integration over the 2000 to 10000 cm^{-1} range. This value represents $\sim$ 1% of the total solar radiation absorbed by the atmosphere. Paynter and Ramaswamy [150] estimated that the globally averaged uncertainty due to the (self- and foreign-) continuum uncertainty to be 1.3 Wm^{-2} for absorbed solar radiation. This number has to be compared to the 17 Wm^{-2} range of values (from 74 to 91 Wm^{-2}), over which the solar radiation absorbed by the atmosphere is estimated [187].

Note that very recently Ptashnik *et al.* [186] reported new FTS measurements

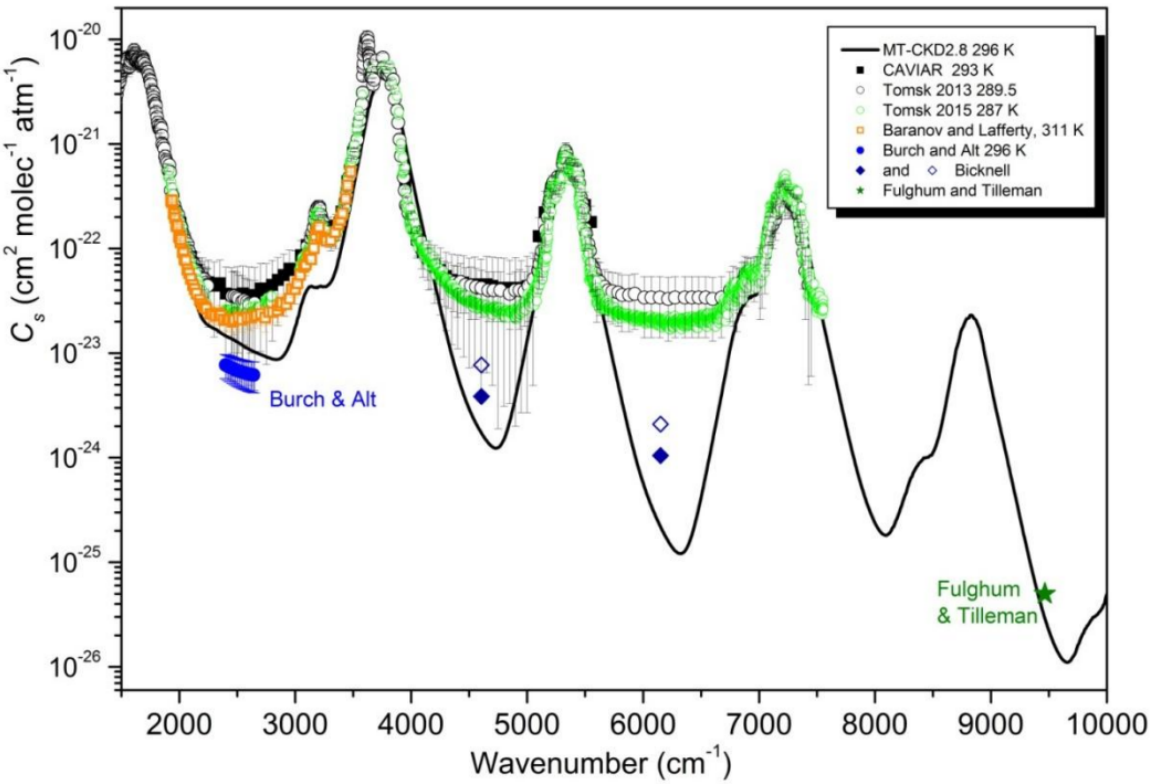

Figure 4.10. Comparison of the MT_CKD2.8 model (black solid line) in the 1500-10000 cm^{-1} range to the FTS values reported by Baranov and Lafferty [182] (orange open squares), the CAVIAR consortium [149] (black full squares), from Tomsk2013 experiments [185] (black open circles) and from Tomsk2015 experiments [186] (green open circles). The 30–50% error bars on Tomsk2015 FTS values are not plotted for clarity. The results reported by Bicknell *et al.* [183] and Fulghum and Tilleman [184] by calorimetric-interferometry in air are also presented (blue diamonds and green star, respectively) together with the results by Burch and Alt [173] (solid blue circles).

at Tomsk using a longer optical path-length and scaled their measurements to the MT_CKD2.5 strength in the 4–μm window. This procedure led to a decrease in their continuum values by 30-50% compared to Ref. [185]. The (relative) continuum values reported in [186] indicate that the continuum absorption in the four near-infrared windows differ by no more than 20%, in strong contradiction with the MT_CKD model.

In Fig. 4.10, we have also included the C_s values deduced from the work of Bicknell *et al.* [183]. Authors reported the total (self- plus foreign-) water vapor continuum cross-sections in nitrogen at atmospheric pressure near 4600 cm^{-1} and 6140 cm^{-1} measured using calorimetric interferometry (CI) technique [188]. In CI the signal is obtained from the shift of interference fringes when the gas sample in one of the arms of the interferometer is being heated by pulsed excitation laser aligned with the reference laser of the interferometer. CI technique is not a direct absorption technique and has to be calibrated on well known absorption lines. Bicknell *et al.* [183]

calibrated their measurements using methane absorption lines at 1.63 and 2.17 μm. It supposes no changes in the alignment of the excitation and the probe beam between the calibration procedure and measurement, and the same shape of the excitation beam at different wavelengths. This issue was not mentioned in the original paper, and thus it is not clear whether it was taken into account or not.

In the framework of the investigations done in our group to accurately measure the continuum cross-sections in different NIR windows, we have done a series of high sensitivity CRDS measurements using the instrument developed in this work. The recordings were provided across the entire spectral region (4250-4520 cm^{-1}) corresponding to the low frequency edge of the broad 2.1–μm window. Hereafter, we will describe these measurements in detail.

4.3.4 Experimental study of water vapor self-continuum

Data acquisition

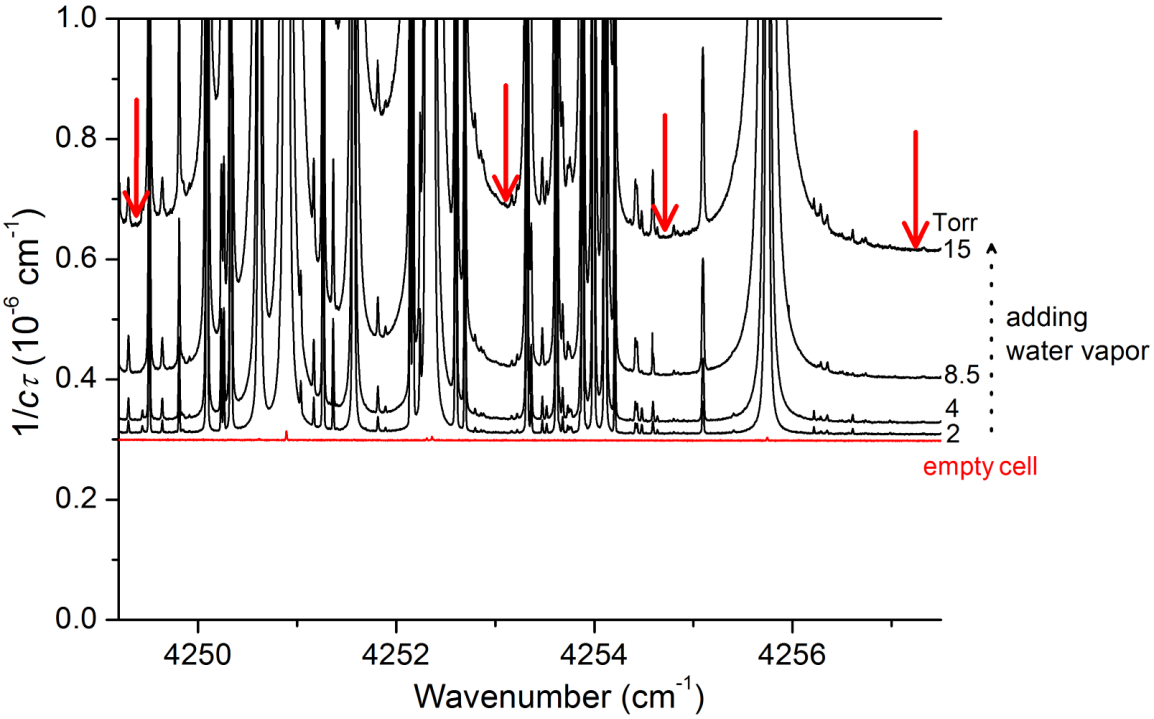

Figure 4.11. Series of CRDS spectra recorded with the first DFB based-CRD spectrometer developed in this work for different pressures of pure water vapor up to 15 Torr. The red arrows indicate the spectral points where the self-continuum measurements were performed.

The spectrometer was used with the different laser sources available (see Table 4.3) to study the self-continuum across the 2.1–μm window. The continuum absorption was derived either from the baseline variation of water vapor spectra recorded for a series of pressure values over a small spectral interval (Fig. 4.11) or from baseline

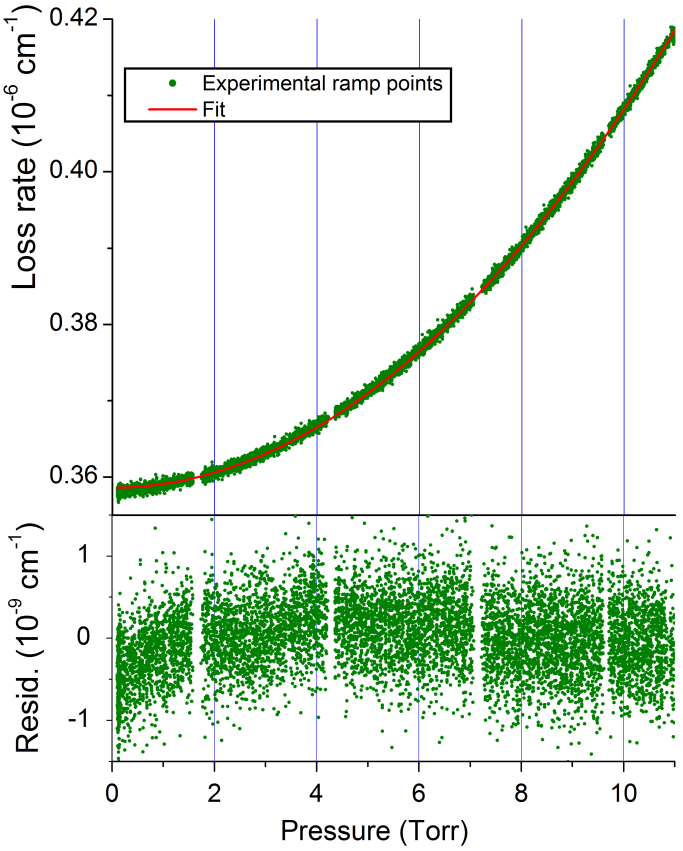

Figure 4.12. Upper panel: Extinction coefficient measured during a pressure ramp from 0 to 11 Torr for the selected spectral point at 4438.85 cm^{-1}. Each green point corresponds to a single ring-down event. The purely quadratic fit (red solid line) is also shown. Lower panel: Residuals between the measured ring-downs and corresponding fit values.

monitoring at fixed laser frequencies during pressure ramps (Fig. 4.12). Further we will specify the recording conditions and the technique of continuum detection.

The **4248–4257** cm^{-1} series of measurements was performed with our first CRDS setup described in Section 2.1. Fig. 4.11 shows spectra recorded in this spectral interval. For the determination of the self-continuum cross-section, several dozen spectra were recorded with the CRDS cell filled with pure water vapor at different pressures from 2 to 15 Torr. We limited the maximal pressure by value of about 71% of the saturation pressure at 296 K to avoid condensation of the water on the cavity mirrors.

The self-continuum cross-sections in the **4341-4367** cm^{-1} range were retrieved from VECSEL–CRDS spectra recorded for a series of pressure values, using the flow of water vapor through the CRDS cell. Two series of water vapor spectra were recorded in the 4341.7-4349 and 4360-4367.5 cm^{-1} spectral intervals for several pressure values between 5 and 11 Torr (i.e. 52 % of maximum humidity rate at 297 K). For all these spectra, the noise level was $\sim 5 \times 10^{-10}$ cm^{-1} or below.

The self-continuum cross-sections in **4427–4439** and **4516–4532** cm^{-1} spectral regions were retrieved using the EC–CRDS setup from pressure ramps recorded between 0 and 12 Torr (and vice versa) at fixed spectral points located in a region free of absorption lines. Fig. 4.12 shows a quadratic character of loss rate dependence on

Table 4.3. Summary of the self- and foreign- continuum retrievals of water vapor performed with our CRDS spectrometer.

Spectral range, cm^{-1}	Instrument	N. of points	Method
4248–4257	DFB–CRDS	4/2[a]	Spectra
4341–4367	VECSEL–CRDS	5	Spectra
4427–4439	EC–CRDS	3	Pressure ramp
4516–4532	EC–CRDS	8	Pressure ramp

[a] For self- and foreign-continuum, respectively.

pressure growing from 0 to 11 Torr at 4438.85 cm^{-1} spectral point. On average, each pressure ramp was being recorded for 1.5 minutes. Every ramp recording consists of about 7000 single ring-downs with peak-to-peak noise of 1.6×10^{-9} cm^{-1}.

Table 4.3 lists spectral intervals of the data recordings together with the corresponding laser source and method of continuum detection.

Continuum retrieval

When the CRDS cell is filled with water vapor, the extinction coefficient can be expressed as a sum of three terms:

$$\alpha(\nu) = \alpha_{WML} + \alpha_{WC} + \alpha_{Ray}, \tag{4.2}$$

where α_{WML}, α_{WC}, and α_{Ray} are the contributions due to water vapor: monomer local lines (WML) and continuum (WC), and Rayleigh scattering, respectively.

a. Rayleigh scattering

The Rayleigh scattering cross section ($cm^2 molecule^{-1}$) was calculated from the refractive indexes using the equation from Thalman *et al.* [189]:

$$\sigma = \frac{24\pi^3\nu^4}{N_S^2}\left(\frac{n_\nu^2 - 1}{n_\nu^2 + 2}\right)^2 F_k(\nu), \tag{4.3}$$

where ν is wavenumber in cm^{-1}, N_S is the number density (in molecule·cm^{-3}) for which the refractive index n_ν at wavenumber ν is measured at temperature T_s and pressure P_s. F_k represents the King correction factor which accounts for the depolarization and equals to 1 in our case. The extinction due to Rayleigh scattering is then given by

$$\alpha_{Ray} = \sigma N_S \frac{P_{meas}}{P_S}\frac{T_S}{P_{meas}}. \tag{4.4}$$

In the present work, we used the scrolling of longitudinal modes due to changes in pressure, to accurately measure the value of the refractive index (n) at 4257 cm^{-1}

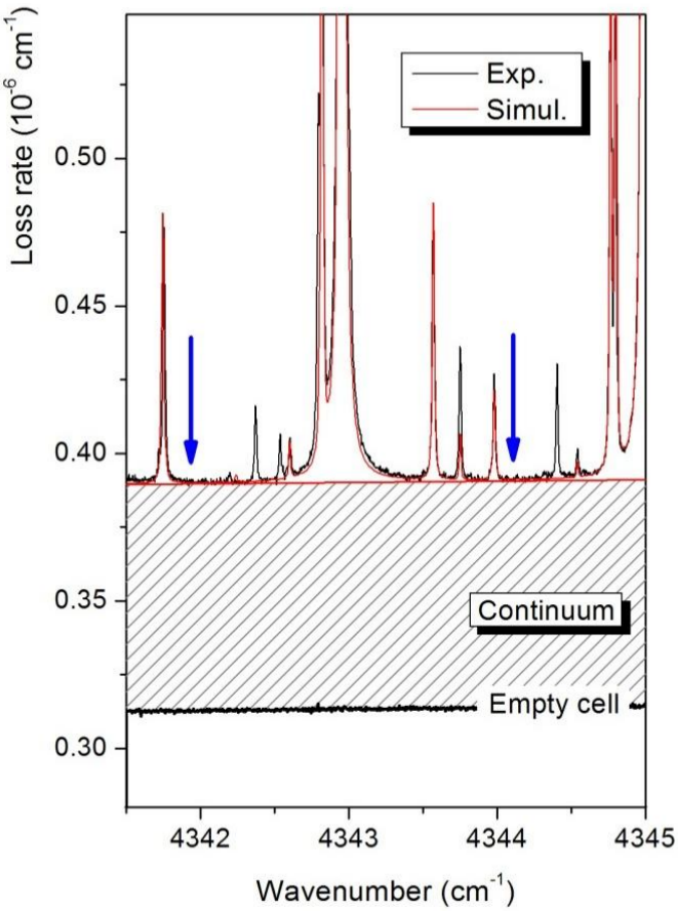

Figure 4.13. The water monomer local line contribution calculated using the HITRAN2012 database (red) is superimposed simulation and the baseline level obtained with the cell evacuated corresponds to the self-continuum absorption. Three additional weak lines due to NH3 present as an impurity are observed in the experimental spectrum. Note also the large difference of the intensity of the $H_2{}^{18}O$ line at 4343.75 cm^{-1} for which the HITRAN2012 database provides a calculated intensity value. The two blue arrows mark selected wavenumbers for which the continuum is measured.

for pure water and air. We obtained $n = 1.000005$ for 15 Torr of water vapor and $n = 1.000296$ for 760 Torr of air at 296.6 K, leading to Rayleigh scattering contributions equal to $\alpha_{Ray} = 5 \times 10^{-12}$ cm^{-1} and 3×10^{-10} cm^{-1}, respectively. Note that our measured value of the refractive index of water vapor at 4257 cm^{-1} is consistent with the value of 1.000006 given in ref. [190] at 4300 cm^{-1} (298.15 K; 24 Torr). Considering that under our experimental conditions the water continuum induces variation of the spectrum baseline on the order of 10^{-8}–10^{-7} cm^{-1}, we conclude that the contribution of Rayleigh scattering can be neglected.

b. Water monomer local line contribution

To retrieve the continuum it is necessary to subtract the contribution of the water monomer local lines to the recorded CRDS spectra. This contribution was simulated for the different experimental conditions using the line list provided in the HITRAN2012 database [2] Following Ref. [172], for each line a Voigt profile is calculated over a ± 25 cm^{-1} interval from the line center and reduced by the value of the "25 cm^{-1} pedestal". In the simulation, the line intensities were calculated at the measured temperature, knowing the lower state energy value of each transition. An illustration of the retrieved continuum after subtraction of the monomer contribution from the recorded spectrum is shown in Fig. 4.13.

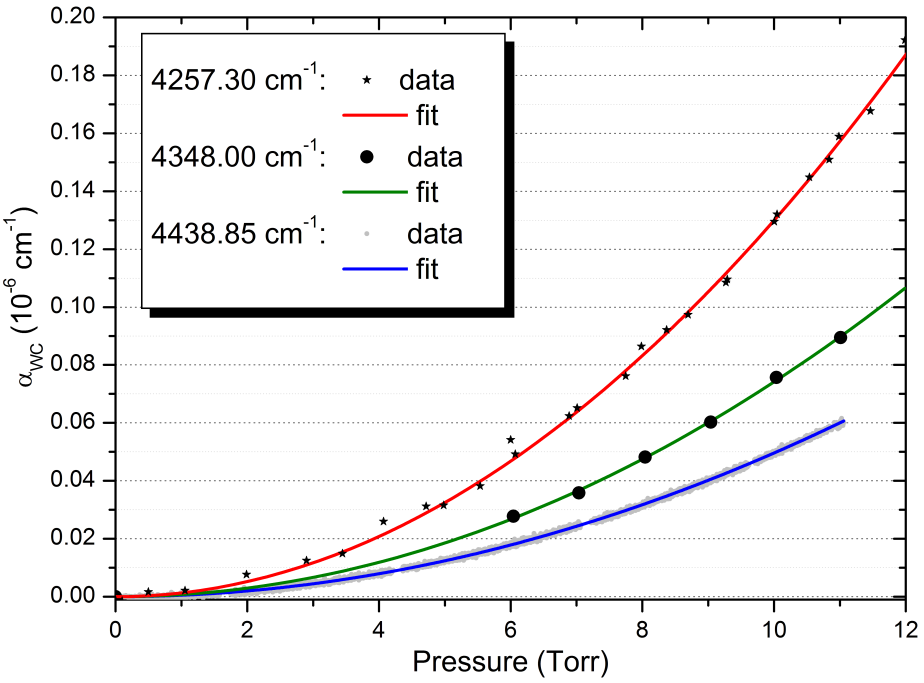

Figure 4.14. Pressure dependence of the water self-continuum absorption in different spectral points taken from three spectral regions. Black stars and circles denote the measured values for DFB–CRDS (4257.30 cm^{-1}) and VECSEL–CRDS (4348.00 cm^{-1}), respectively. Colorful lines corresponds to a purely quadratic polynomial fit of the CRDS data in different regions. Experimental points for the EC–CRDS measurements (4438.85 cm^{-1}) represent single ring-downs and are plotted in light gray.

To subtract α_{WML} from ramp measurements, monomer line contributions were simulated for each selected spectral point of the continuum at several different pressures. Then these $\alpha_{WML}(\nu, P)$ were fitted with a purely quadratic fit and the resulting water monomer absorption contribution were subtracted from extinction coefficient values obtained directly from experimental ramps.

For all spectral ranges we selected spectral points (marked by red arrows on Fig. 4.13) for which the WML contribution has the minimal impact. The pressure dependence of the retrieved continuum was then fitted with a purely quadratic function. This behavior expected from Eq. 4.1 is observed for all our selected spectral points in the 2.1 μm window as shown on Fig. 4.14. The self-continuum cross-section at a selected spectral point is derived from the fitted quadratic coefficient b_2 by: $C_s = b_2 k_b T$.

The resulting experimental values of self-continuum cross-sections are plotted on Fig. 4.15 and are reported in Table 4.4 together with the relative WML contributions. Note that in the spectral regions measured by VECSEL–CRDS and EC–CRDS, the WML contribution is comparably small.

Table 4.4. Self-continuum absorption cross-sections of water vapor at 298 K and relative contribution of the monomer local lines for the different selected spectral points

ν (cm^{-1})	C_s (10^{-23} cm^2 $molecule^{-1}atm^{-1}$)	$\alpha_{WML}/(\alpha_{WML}+\alpha_{WC})$, (×100%)
DFB–CRDS		
4249.36	3.26(3)	13
4253.12	3.21(3)	20
4254.66	3.12(3)	10
4257.30	3.04(2)	5
VECSEL–CRDS		
4341.90	1.793(19)	0.6
4344.15	1.783(21)	0.6
4348.00	1.739(16)	0.4
4360.50	1.667(15)	0.7
4367.13	1.630(28)	0.5
EC–CRDS 2257 nm		
4427.14	1.221(1)	0.3
4432.64	1.181(1)	0.2
4438.85	1.156(1)	
EC–CRDS 2211 nm		
4516.36	0.915(15)	4
4518.18	0.907(8)	
4520.72	0.904(15)	
4521.86	0.933(25)	
4525.82	0.898(28)	5
4527.02	0.880(20)	
4528.93	0.868(23)	
4533.07	0.885(22)	

Note. The error bar is given in parenthesis in unit of the last quoted digit. It corresponds to the statistical uncertainty on the quadratic coefficient of the fit of the continuum versus the water vapor pressure.

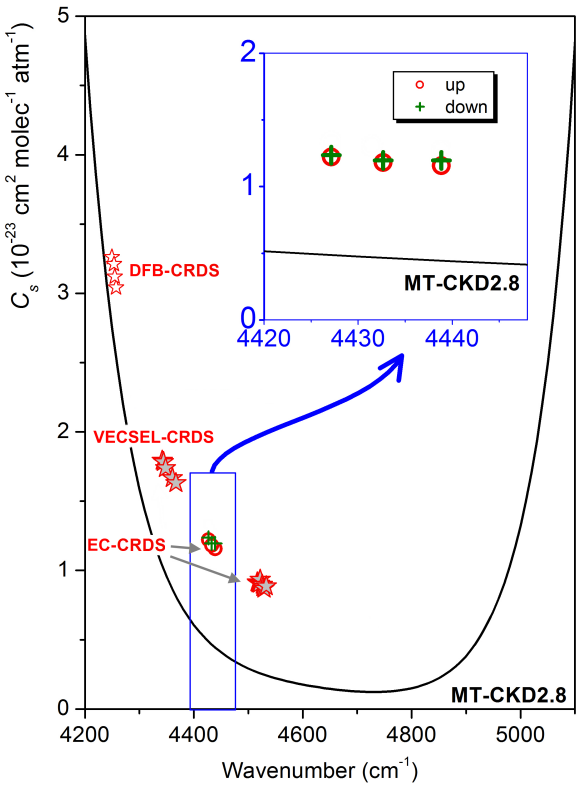

Figure 4.15. Overview of resulting C_s values with comparison to MT_CKD2.8 model. In blue inset the difference between C_s values obtained from upward pressure ramps (red circles) and downward pressure ramps (green crosses)

Self-continuum uncertainties

We have included in Tables 4.4 the statistical error given by the quadratic fit of α_{WC} versus $P^2_{H_2O}$. As illustrated in Figs. 4.14, the quality of the reproduction of the pressure dependence is very good, we obtained less than 1% error bar for all the chosen spectral points. The quality of our C_s values is also confirmed by the frequency dependence included as an insert in Fig. 4.15: although the three EC–CRDS points span no more than 11 cm^{-1}, a clear frequency dependence is evidenced, the C_s values decreasing by about 5% between the two extreme spectral points.

The abovementioned statistical error of the fits represents only a part of the real error bar. Experimental and data treatment biases or errors may also contribute to the uncertainty budget on our continuum values. Among the additional error sources, we identified those related to the following: (i) the stability of the spectrum baseline, (ii) the uncertainty on the calculated contribution of the monomer local lines, (iii) uncertainty on the pressure value and (iv) additional loss rate due to water adsorbed on the mirror surface.

The most critical parameter in continuum recordings is the baseline stability. All our cross-section retrievals rely on the assumption that the optical alignment of the CRDS cavity and then the baseline of the spectra are stable with time and are not affected by pressure changes accompanying the cell filling. In order to estimate to which extent the cavity is mechanically stable, we recorded a series of spectra with Ar

or dry synthetic air at a pressure of up to 700 Torr. Up to 200 Torr (in particular, in pressure conditions similar to those of the self-continuum measurements), the baseline variations were found at the noise level ($\sim 10^{-9}$ cm^{-1}) and then negligible compared to the typical changes induced by the injection of water on the order of 10^{-8}–10^{-7} cm^{-1}.

Note that we observed the difference between upward and downward pressure ramps resulted in a difference of 1–3% for different spectral points with systematically higher downward values. We assume that the difference occurs due to water vapor adsorbed on the surface of the HFC mirrors leading to additional loss rate (see blue insert in Fig. 4.15).

Recently, Serdyukov *et al.* [191] measured an increasing reflectivity (in the blue range) of their mirrors with water vapor pressure. Such an effect may lead to a significant underestimation of the measured CRDS continuum absorption. The evaporated coatings used by Serdyukov *et al.* are more porous than ours, so filling the pores with water changes the refracting index. Thus, the coating reflectivity may show a spectral shift leading to an increase (or a decrease) in the reflectivity coefficient. In our case, we are using sputtered coatings known to be dense and minimize this type of effects. Moreover, a change of reflectivity would result in a non-quadratic behavior of the continuum absorption versus the water vapor pressure which is not observed. An additional argument indicating that such effects are negligible in our measurements is that the typical time scale of the reflectivity change reported by Serdyukov *et al.* is on the order of hours or days, much longer than the time scale of our pressure cycles (a few minutes).

It is also worth mentioning that the exclusion of the ± 25 cm^{-1} pedestal from the continuum has a negligible impact on the self-continuum due to the low water vapor pressures used and a limited impact on the derived foreign-continuum (under a few percent of the total continuum).

In the case of the self-continuum cross-section, taking into account the high consistency of the various measurements performed and the smaller (or negligible in the case of VECSEL– and EC–CRDS measurements) impact of the baseline and α_{WML} uncertainties, 0.2 °C uncertainty on the temperature, uncertainty on the pressure value which was measured to be stable within 1% during the recording time, a 3% uncertainty due to water absorption on the mirrors and a fit error, a 5% error bar seems to be a conservative estimate.

Comparison with literature

In the 2.1–μm window, room temperature measurements were performed by OF–CEAS [52] towards the low energy edge of the window (4302 cm^{-1}) and near the centre (4723 cm^{-1}). The OF–CEAS measurements at 4302 and 4723 cm^{-1} were also

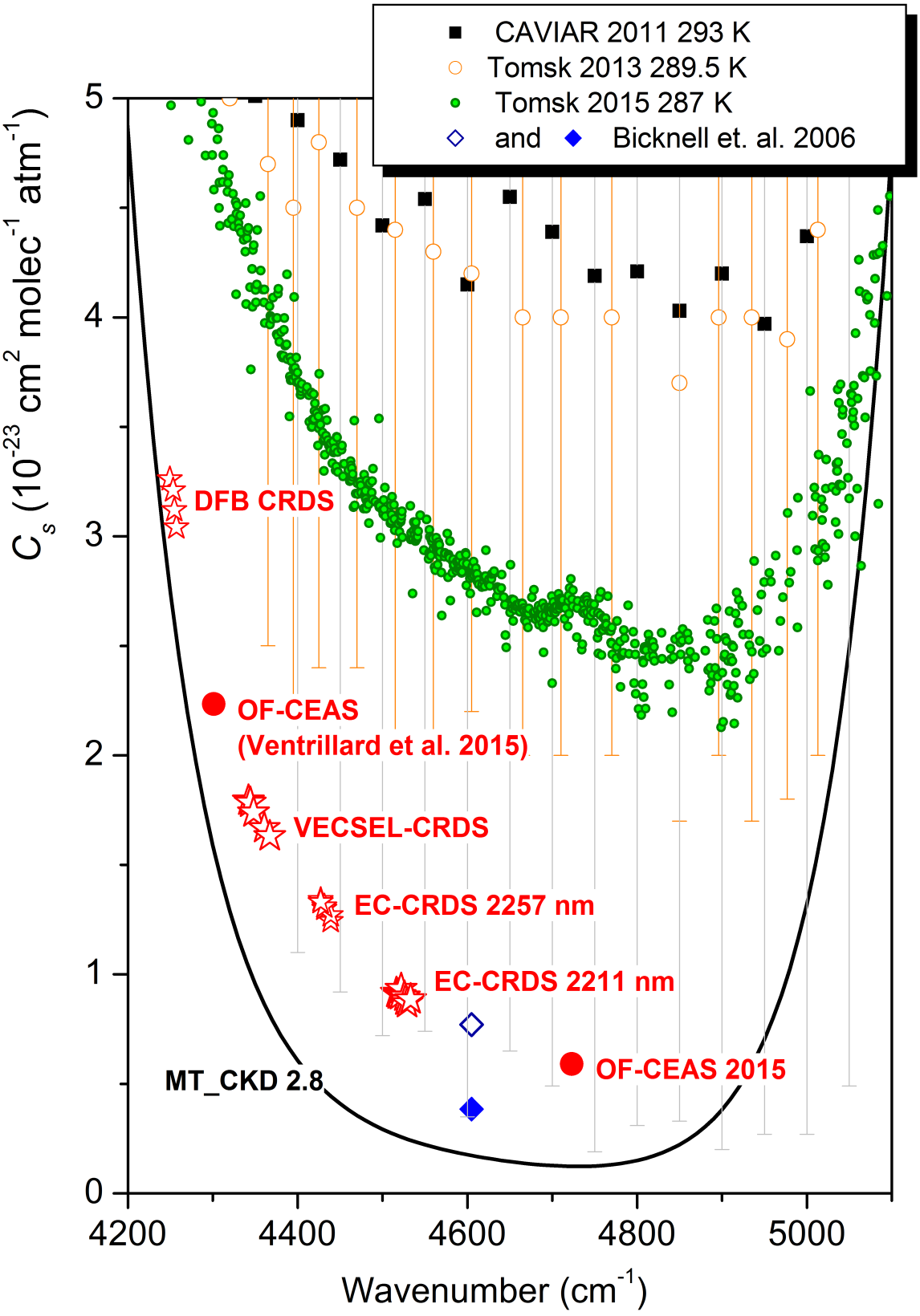

Figure 4.16. MT_CKD2.8 model (black solid line) is compared to: CAVIAR FTS data [149], Tomsk2013 FTS data [185], Tomsk2015 FTS data [186]; calorimetric–interferometry data [183] for which the blue open diamond corresponds to the self plus foreign cross-sections while blue full diamond is an approximated estimation of resulting self-continuum cross-section value); OF-CEAS data reported in [52] and this work. The 30–50% error bars on Tomsk2015 FTS values and the small error bars (< 5 %) on the laser method values are not plotted for clarity

performed at 5 further temperatures up to 323 K [52]. The variation of the derived continuum absorption with water vapour pressure was found purely quadratic and cross-section values were derived with an accuracy of 3–5%. At the centre of the window, the MT_CKD2.8 continuum is about four times weaker than measured by OF–CEAS and about 30 times smaller than the CAVIAR/Tomsk FTS values.

Fig. 4.16 shows the different experimental determinations of the self-continuum cross-section available in the 2.1–μm window and compared them to the MT_CKD2.8 model. They include OF–CEAS continuum determinations near 4300 cm^{-1} and at the center of the window near 4700 cm^{-1} [52] done in Grenoble by other members of our group. All our measurements are fully consistent with each other and the highly sensitive OF–CEAS measurements. The overall frequency dependence is similar to that predicted by the MT_CKD2.8 model, but our measured values are larger, the deviation increasing from a few % at the low energy edge of the window to a factor of 4 at the center of the window.

In Fig. 4.16 we also reported the self-continuum cross-section deduced from the measurements of Bicknell *et al.* [183] assuming the foreign-continuum cross-section measured in [155]. Although not at the same wavenumber and noting the large uncertainty in separating the self- and foreign-continuum components [176], those measurements are roughly consistent with our laser-based results.

Three sets of FTS values measured by Ptashnik *et al.* are reported on the same figure with very large error bars and are all significantly overestimated. For instance, for the 4350 cm^{-1} spectral point of the VECSEL–CRDS measurements, the 1-σ uncertainty range of the CAVIAR value is between 1.2×10^{-23} and 8.8×10^{-23} cm^{2}molecule^{-1}atm^{-1}, which makes it in agreement with our value of 1.73(9).

Grenoble measurements

In the recent years, several members of LAME group to which I belong have made important experimental efforts to solve this conflicting situation by implementing the highly sensitive CRDS and OF–CEAS techniques to measure the self- and foreign-absorption continuum of water vapor in the near-infrared windows. This techniques are inherently much more sensitive and have much better baseline stability than FTS coupled with long path absorption cells.

The first measurements of the room temperature self-continuum of water vapor using CRDS in the 1.6–μm window [192, 193] were found in better agreement with the MT_CKD2.8 model than with the Tomsk2013 FTS results: in the center of the window, Mondelain *et al.* cross section values agree within 50% with MT_CKD2.8 but differ from Tomsk2013 values by nearly two orders of magnitude.

The evidence of contribution due to the water adsorbed on the CRDS mirrors leading to a pressure dependence departing from the expected purely quadratic law

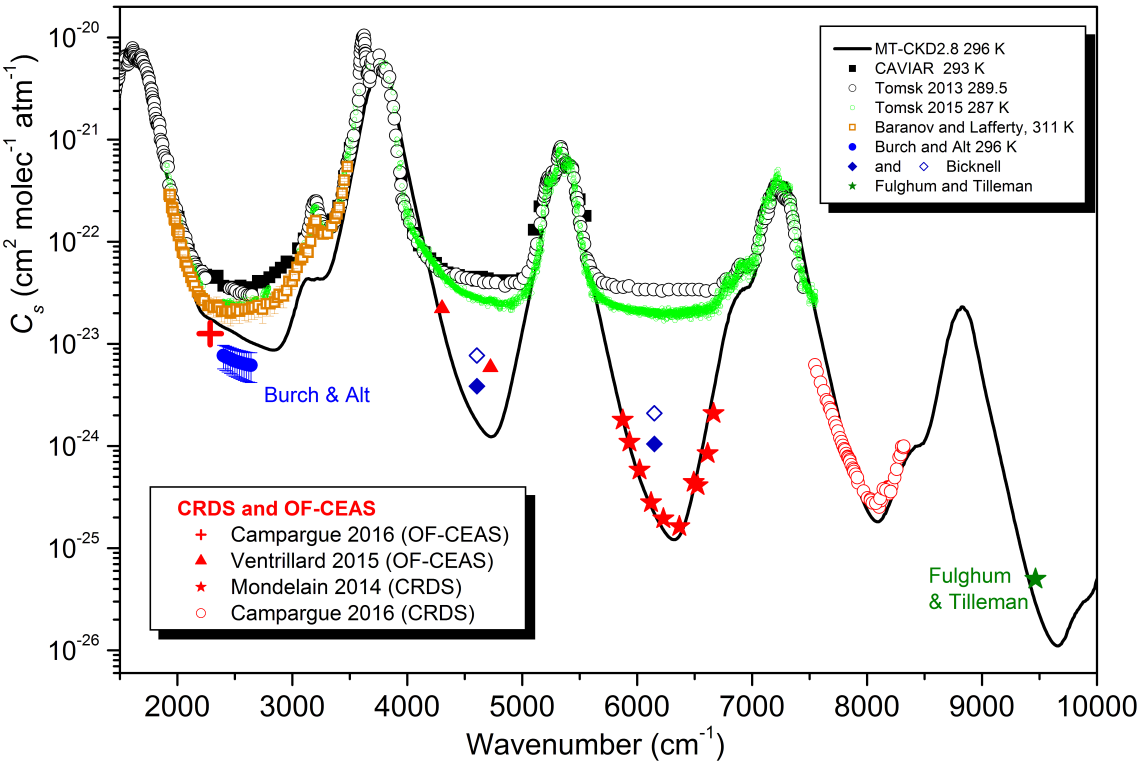

Figure 4.17. Comparison of the experiment determinations of self-continuum cross-sections of water vapor near room temperature to the MT_CKD2.8 model.

added some uncertainty to the CRDS results in this window [192, 193]. Nevertheless, gas phase absorption at the level reported by FTS (a roughly 10^{-7} cm^{-1} constant value over the entire 1.6–μm window) was totally excluded by the CRDS experiment.

The results obtained by CRDS and OF–CEAS in the transparency windows centered at 1.25, 1.6 and, 4 μm were reported in Ref. [122] and are shown in Fig. 4.17. They provide a general validation of the frequency dependence of the MT_CKD2.8 model. The agreement in the 1.25–μm window where room temperature measurements are reported for the first time is quite satisfactory in the center of the window but increasing deviation is observed towards the low energy edge near 7500 cm^{-1}. We note that, in the 4 μm region, the decrease of the MT_CKD model self-continuum value by about 33% compared to the version 2.5, has led to a significantly better agreement with OF-CEAS determination at 2283 cm^{-1}.

This large disagreement evidenced between FTS and CRDS/OF–CEAS measurements across all transparency windows may be explained by the lack of baseline stability and the sensitivity of FTS technique. Notably, the Tomsk and CAVIAR C_s values at room temperature in the different measured windows are frequency independent with an almost identical value of about 4×10^{-23} cm^{2}molecule^{-1}atm^{-1}. This C_s value corresponds to an absorption coefficient α_{WC} of about 10^{-7} cm^{-1} at 10 Torr pressure (about two orders of magnitude larger than the values measured in the

center of the 1.6 and 1.25 μm windows by CRDS) and represents an optical depth of 0.006 for a 612 path length used in Tomsk. Such variation of the transmittance is difficult to measure by FTS (the baseline systematic error estimated in Ref. [185] is 0.004) and we believe that the constant FTS C_s value reported in the windows should have been reported as an upper limit instead of a measurement result with large error bars.

4.3.5 Experimental study of the foreign-continuum absorption

Data acquisition

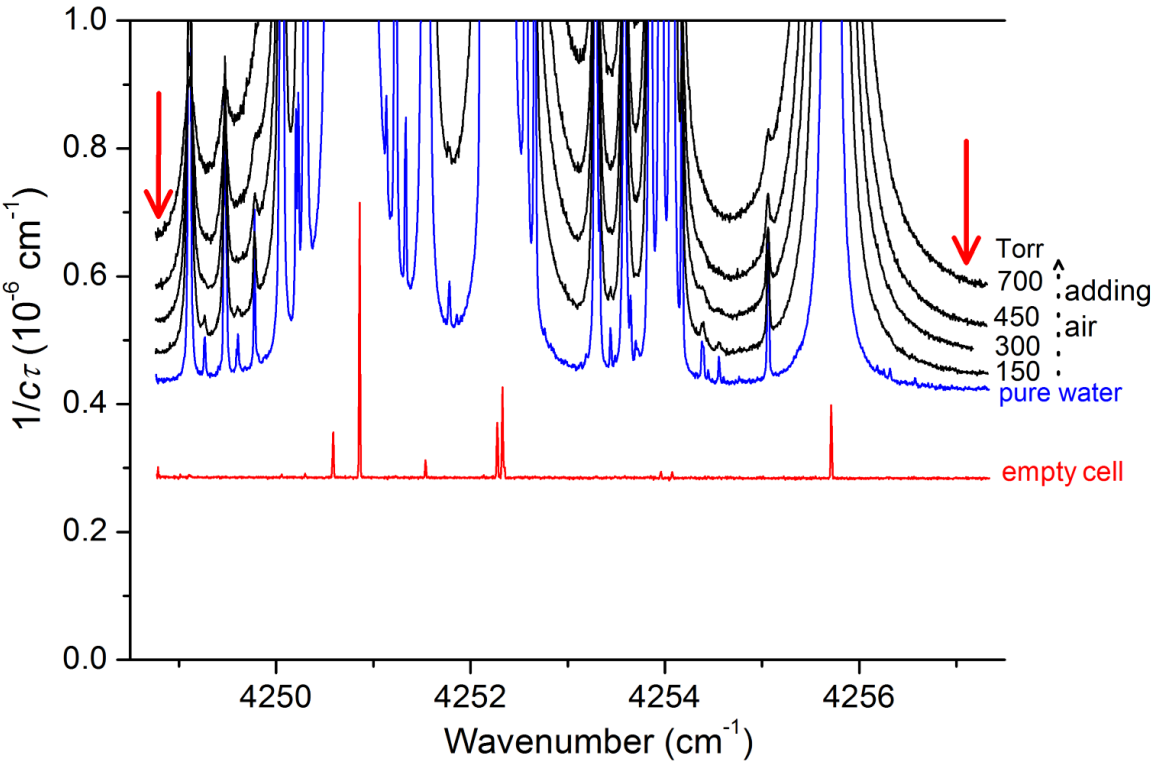

Figure 4.18. Series of CRDS spectra recorded by adding air into the CRDS cell containing water at a partial pressure of 9.65 Torr. The total pressure is increased up to 700 Torr. The red arrows indicate the two spectral points where the foreign-continuum measurements were performed.

The foreign-continuum was measured in the region of 4248–4257 cm^{-1}. For that, the cell was first filled at a certain pressure of pure water vapor and, once stabilized, synthetic air (Alphagaz 2 by Air Liquide) was added into the cell to reach the desired total pressure. As illustrated in Fig. 4.18 for a given value of the partial pressure of water, several spectra were recorded with increasing amounts of air added, corresponding to 4 or 5 pressure values between 150 and 700 Torr. This procedure

was repeated for five different partial pressure of water vapor (see Table 4.5).

Fig. 4.18 shows one of the series of the recordings performed to determine the foreign-continuum. Various amounts of synthetic air are successively injected into the CRDS cell initially filled with water vapor at a pressure of $P_{H_2O} = 9.65$ Torr, leading to total pressure values of $P_{H_2O} + P_f = 150$, 300, 450, and 700 Torr. The injection of air is accompanied by an additional increase in the spectrum baseline due to both water monomer local lines having been broadened by air (α_{WML}) and the foreign-continuum contribution (α_{WCF}).

Foreign-continuum retrieval

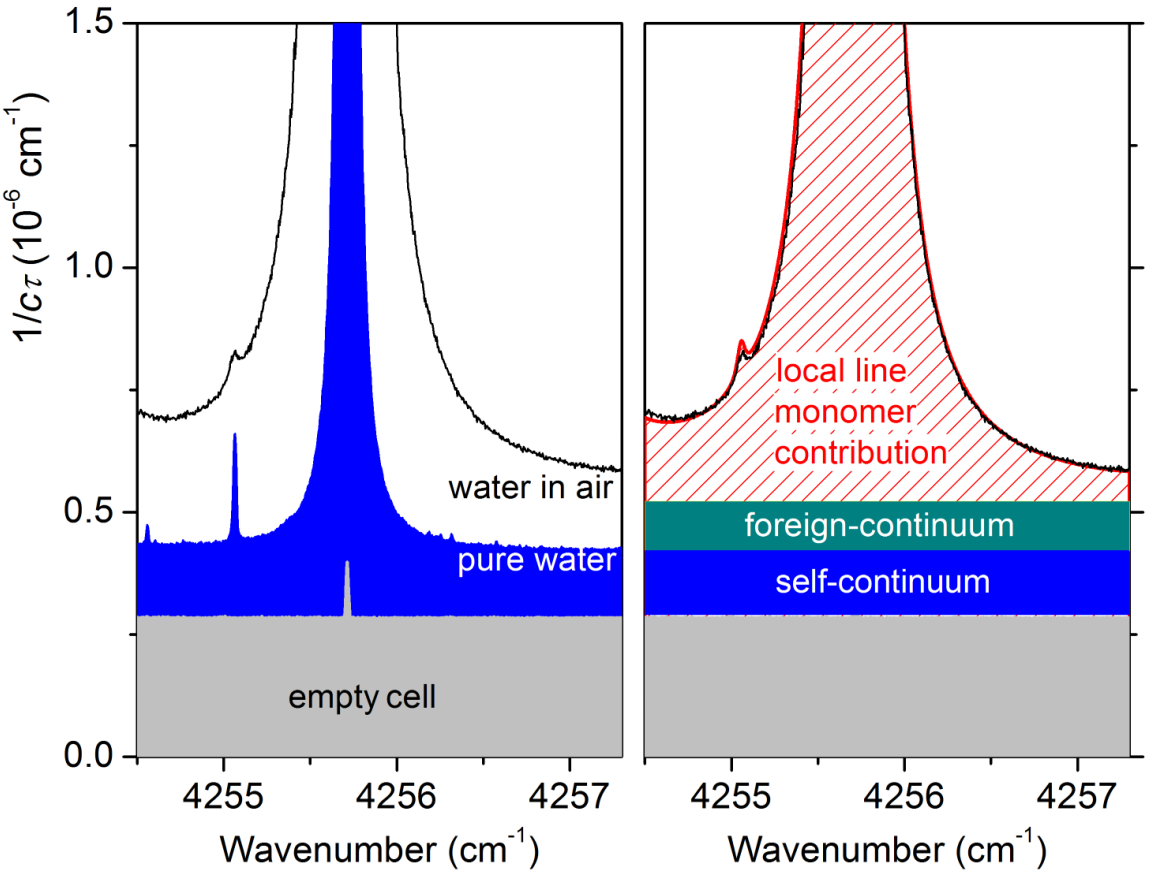

Figure 4.19. Illustration of the procedure used to derive the foreign-continuum contribution near 4256 cm^{-1}. Left panel: evolution of the CRDS spectrum by adding 9.65 Torr of water vapor and then air up to a total pressure of 700 Torr. Right panel: evaluation of the foreign-continuum contribution (dark cyan) as the difference between the absorption signal and the sum of the water monomer local line contribution (dashed) and self-continuum contribution (blue).

Similarly to the self-continuum, in order to remove the WML contribution, we simulated spectra for different experimental conditions using the linelist provided by HITRAN2012. For each line, the profile was calculated using a Voigt profile in the

Table 4.5. Foreign-continuum cross-sections measured by CRDS at 297 K and relative contribution of the monomer local lines for the different selected spectral points. For a given spectral point, the cross section value was derived for several values of the water partial pressure

ν (cm^{-1})	P_{H_2O} (Torr)	C_f (10^{-25} cm^2 molecule^{-1}atm^{-1})		$\alpha_{WML}/(\alpha_{WML}+\alpha_{WC})$
4248.83	4.0	4.42(23)	3.91(40)[a]	50
	6.2	4.24(10)		53
	9.7	3.57(11)		55
	9.8	3.80(11)		55
	10.9	3.75(16)		56
4257.30	4.0	4.26(19)	3.93(30)[a]	31
	6.2	3.93(9)		33
	9.7	3.82(20)		34
	9.8	3.60(23)		34

Note. The error bar is given in parenthesis in unit of the last quoted digit. It corresponds to the statistical uncertainty on the coefficient of the linear fit of the continuum versus the air pressure.

[a] Weighted average.

range of ± 25 cm^{-1}, excluding the "± 25 pedestal" from the WML contribution. Fig. 4.19 illustrates good agreement between the local line simulation and the measured spectrum in the case of 9.65 Torr partial pressure of water in air at a total pressure of 700 Torr: the experimental spectrum coincides with the local line monomer spectrum shifted up by a constant value corresponding to the continuum (which includes in that case both a self- and a foreign- contribution). The α_{WML} contribution subtracted represents the more important part of the measured absorption (see Table 4.5) compared to the self-continuum case.

Note that far from the line center, α_{WML} is roughly proportional to the air partial pressure. The value of the foreign-continuum absorption coefficient (α_{WML}) is then the spectrum baseline shift of the air-water mixture from its level measured with the cell evacuated, decreased by the α_{WML} and self-continuum contributions at the given water partial pressure (Fig. 4.19). Fig. 4.20 shows the pressure dependence of the foreign and local line contributions at 4257.3 cm^{-1}. As expected from Eq. 4.1, α_{WML} is proportional to P_f. The foreign-continuum cross-sections were obtained at 4248.83 and 4257.30 cm^{-1} from the fitted value of the proportionality factor $\frac{1}{k_B T} C_F(\nu, T) P_{H_20}$. The C_f values derived from a series of recordings performed with different partial pressures of water are listed in Table 4.5.

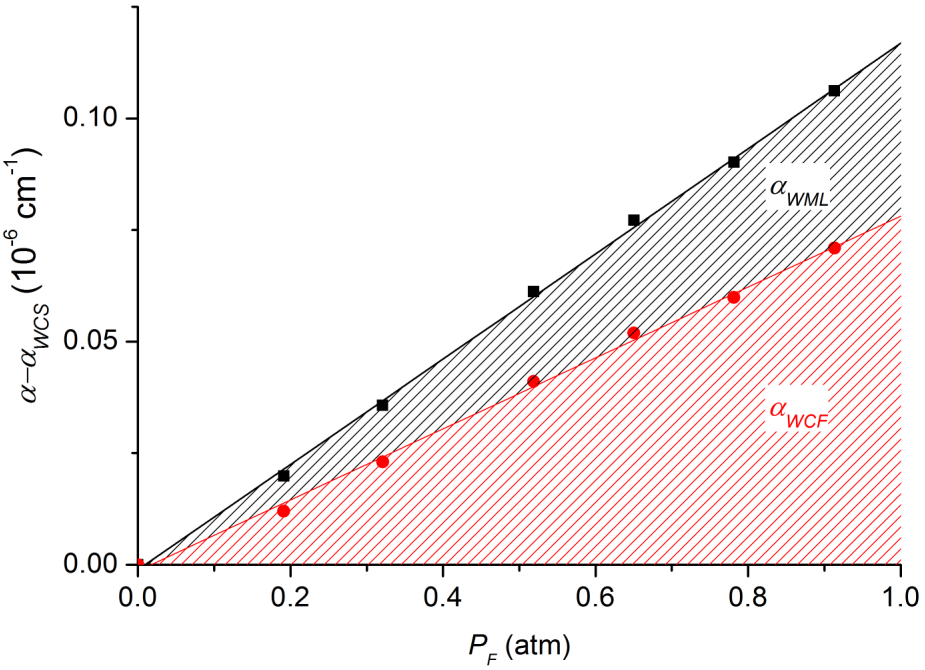

Figure 4.20. Pressure dependence of total minus self-continuum contribution (α_{WCS}) (black squares) measured in this work by CRDS at 4257.3 cm^{-1}. Respective contributions of foreign-continuum (red circles), α_{WCF}, and of calculated monomer local lines, α_{WML}, are also shown. Lines correspond to linear fit of CRDS data.

Foreign-continuum uncertainties

Our C_f values rely on a series of spectra of water vapor in air recorded for various partial pressures of water vapor at 4248.83 and 4257.30 cm^{-1} (Table 4.5). Additional error introduced in foreign-continuum measurements is the uncertainty on the partial pressure of water vapor in the mixture. In order to insure that the partial pressure of water was not affected during air injection, the pressure of the synthetic air admission line was kept at a high value. So as to check that the partial pressure of water was not impacted by a variation in the amount of water adsorbed on the CRDS cell, we determined the partial pressure of water vapor from the fitted value of the profile area of three lines. For the given series, the water pressure values were found to be constant within ±7%.

As for uncertainty on the baseline determination, it was mentioned in Section 4.3.4 that we measured the series of the spectra with Ar or dry air to check the mechanical stability of the HFC and, consequently, stability of the baseline. At higher pressures needed for foreign-continuum measurements, a small misalignment of the mirrors was noted, resulting, after realignment, in an increase in the baseline level never exceeding 7×10^{-9} cm^{-1} at 700 Torr compared to the empty cell level.

Taking into account the various sources of error (baseline stability, HITRAN line parameters, a 7% dispersion of the partial pressure of water vapor in a series

of recordings, statistical dispersion of the measurements) we give a 30% error bar on our foreign-continuum cross-section values as an estimate of our real uncertainty. This value may be reduced after the drawing up an improved line list for water in the region with particular attention to the pressure broadening coefficients and to the lines due to the minor water isotopologues making an important contribution in the region.

Comparison with literature

Our cross-sections are approximately 4.5 times higher than the MT_CKD2.5 values at 296 K, and about 1.7 times lower than the only numerical value reported by the CAVIAR consortium, which is for $T = 402$ K [155] (Fig. 4.21). Note that according to Fig. 4 of Ref. [155], the temperature dependence of the foreign-continuum cross-sections between 350 and 431 K was found very weak in the windows, especially in our spectral region. This is consistent with the fact that our room temperature value and CAVIAR value at 402 K [155] agree within their 30% error bars.

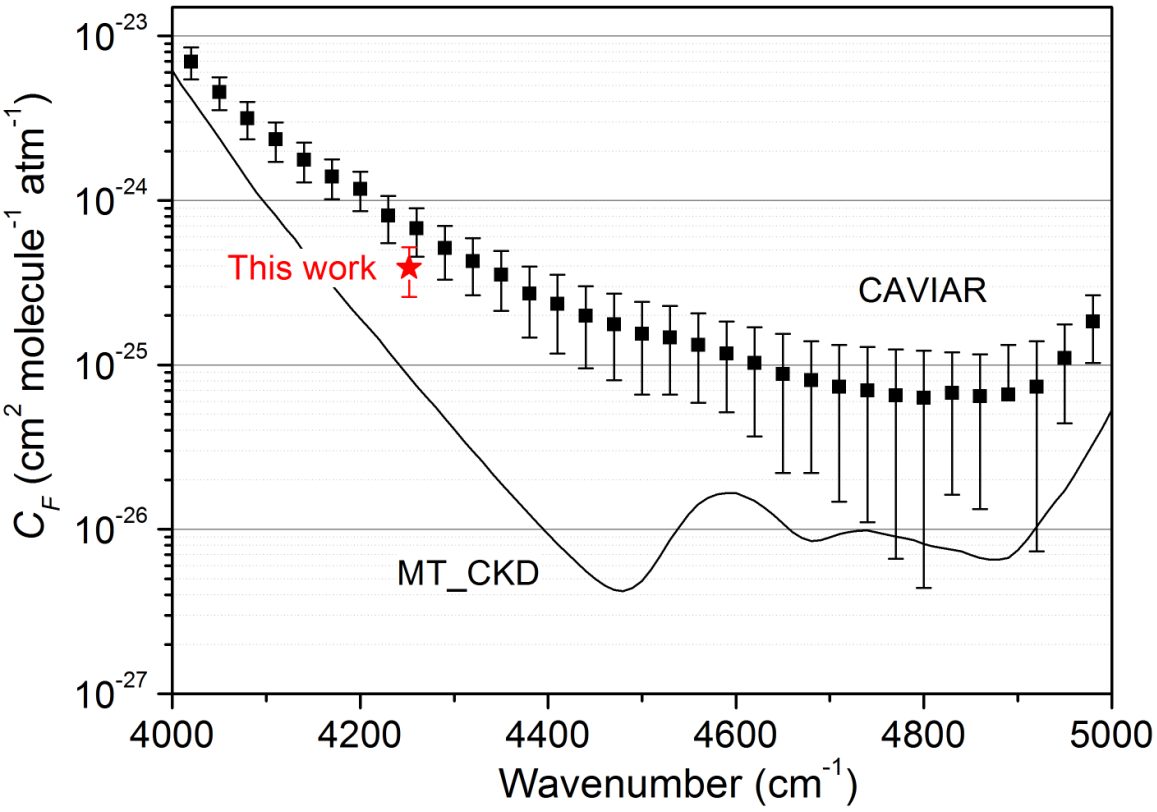

Figure 4.21. Spectral dependence of the foreign-continuum cross-section, CF, derived from the MT_CKD V2.5 model [172] at 296 K (black solid line), measured in this work (red star) at room temperature and in ref. [155] (black squares) at 402 K. Note the logarithmic scale adopted for the ordinate axis.

4.3.6 Conclusion

A newly developed cavity ring down spectrometer was used to accurately determine the self- and foreign-continuum cross-sections of water vapor at room temperature in the 2.1–μm transparency window. The cross-section values were retrieved from a fit of the pressure dependence of the continuum absorption coefficients after the subtraction of the local water monomer lines contribution calculated using HITRAN2012 [2]. As expected, the self-continuum was found to vary quadratically with the water vapor pressure and the foreign-continuum linearly with the pressure of air added into the CRDS cell containing water vapor at a constant partial pressure. The derived C_s values provided for 4 spectral regions in the range from 4250 to 4532 cm^{-1} and C_f for the region of 4250 cm^{-1} have error bars of 5 and 30% respectively.

The presented studies, together with OF–CEAS measurements in 2.1–μm transparency window [52] and previous CRDS results in the 1.25, 1.6 and 4 μm windows [122,192,193], are consistent with the MT_CKD 2.8 self-continuum values. This agreement provides a validation of the standard model widely used to implement the water continuum absorption in atmospheric radiative transfer codes. The performance of our CRDS setup made it possible to measure a 5% decrease in C_s values over a 11 cm^{-1} spectral interval of our measurements, providing a further test of the MT_CKD model, which predicts a 7% variation. In contrast, it seems to indicate that FTS measurements of refs. [149] and [185] largely overestimate the self-continuum cross-section at room temperature in the 2.1–μm window.

The observed differences between our self and foreign values and the FTS data are within the error bars. Nevertheless, we note that the self-continuum cross-sections reported by FTS in ref. [149] and [185] at room temperature are mostly identical in the 2.1, 1.6 and 1.25 μm windows ($C_s \approx 4 \times 10^{-23}$ cm^{2}molecule^{-1}atm^{-1}) and do not show a significant frequency dependence across each window. This almost constant C_s value corresponds to a 1% shift of the baseline of the FTS spectrum when the long multipass cell is filled with 10 Torr of water. Meanwhile, the accuracy of high temperature measurements benefits from increased water vapor pressure values (up to 1.6 atm) [149]. The FTS measurements of the foreign-continuum at high temperature reported in Ref. [155] are also expected to be more accurate because the optical depth and corresponding uncertainty of the continuum were about 0.1 and 0.003, respectively. Even if the discrepancies between the FTS and CRDS measurements remain largely unexplained, we believe that the higher sensitivity of the CRDS technique and the small size of our CRDS setup (the CRDS cell has a volume of about 150 cm^3) make our experimental approach more suitable than FTS for continua absorption measurements in windows where small variations of the spectra baseline have to be detected.

The room temperature contributions of the self- and foreign-absorption of water

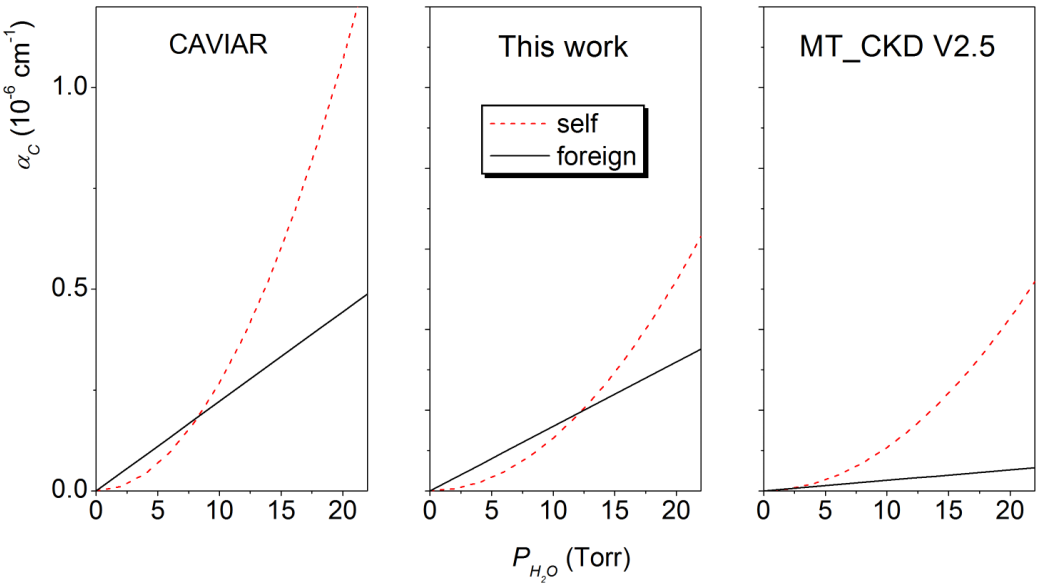

Figure 4.22. Self- (red dashed line) and foreign- (black solid line) water vapor continuum contributions calculated at 4250 cm^{-1} from the cross-sections reported in ref. [149] and [155] (left panel), in this work (center panel) and in ref. [172] (right panel). The different contributions are calculated versus the water vapor partial pressure and for a foreign pressure of 1 atm at room temperature.

in air at an air pressure of 1 atm are plotted in Fig. 4.22 versus the partial pressure of water vapor. In this plot, the absorption coefficients at 4250 cm^{-1}, calculated using the cross section values obtained in this work are compared to the corresponding CAVIAR [149, 155] and MT_CKD2.5 [172] values. For a partial pressure of water of 21 Torr at 296 K, the CAVIAR total (self- plus foreign-) continuum reaches a value of 16.4×10^{-7} cm^{-1}, which is significantly larger than our and MT_CKD2.5 values of 9.1×10^{-7} and 5.3×10^{-7} cm^{-1} respectively. The main difference between our results and the MT_CKD2.5 model concerns the larger foreign-continuum contribution, which represents about one third of our total continuum, but only 10% of the total MT_CKD continuum. In Ref. [121] we noted this important difference for the foreign-continuum values. Such a disagreement largely exceeded our error bar, which is estimated to be on the order of 30%. Considering that there is almost no temperature dependence of the foreign-continuum near 4250 cm^{-1}, as observed in ref. [155], our foreign-continuum value is compatible with the CAVIAR value reported at 402 K within the 30% error bars. In these circumstances, in the MT_CKD2.8 model, released in 2016, foreign-continuum cross-sections were modified based on our foreign-continuum measurements together with results of Baranov and Laferty [194]. Up to date the MT_CKD2.8 foreign-continuum cross-section at 4250 cm^{-1} which is of 3.9015×10^{-25} cm^{2}molecule^{-1}atm^{-1} coincides with our value of 3.91×10^{-25} cm^{2}molecule^{-1}atm^{-1}.

The calculations reported in Fig. 4.22 also show that in the 2.1-μm transparency

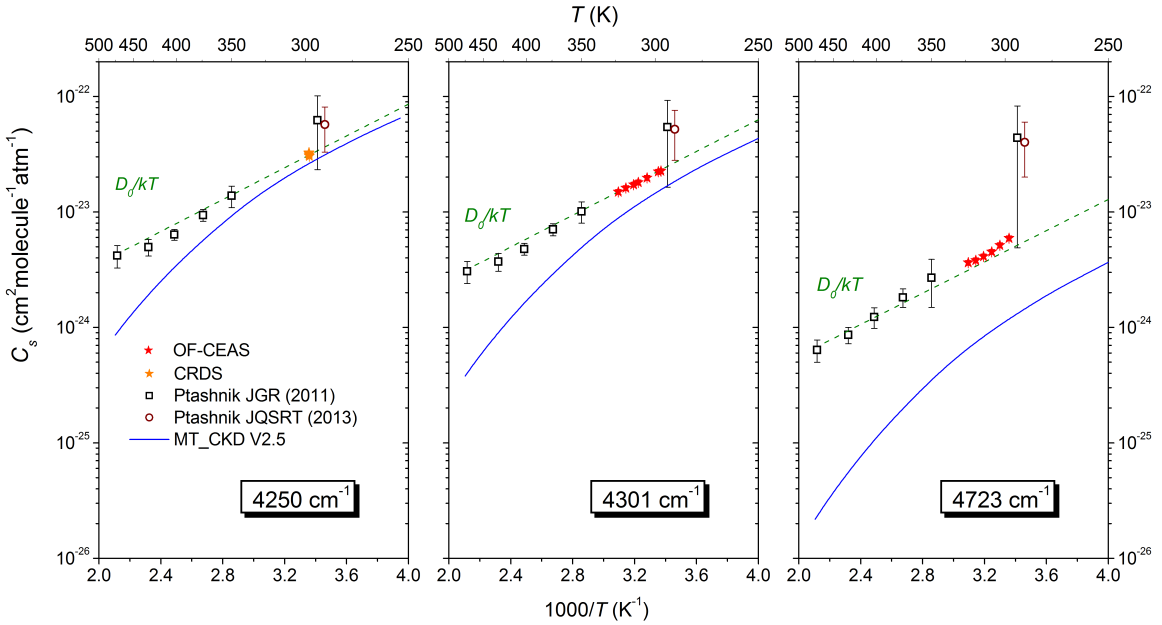

Figure 4.23. Temperature dependence of the water vapor self-continuum cross sections, C_s, obtained by CRDS (orange star) and OF-CEAS at 297 K (red stars) from CAVIAR [149] (black squares) and from the MT_CKD V2.5 model (blue solid line) at 4250, 4302, and 4723 cm^{-1}. The MT_CKD V2.5 values take into account of the 296/T correction factor. Figure from [52].

window, the foreign-continuum contribution in atmospheric conditions is similar to that of the self-continuum. Thus, in order to precisely characterize the absorption of solar radiation in the atmosphere in the 2.1–μm transparency window, more accurate and extensive measurements of the foreign-continuum are required. In order to reduce the large foreign-continuum uncertainty, which is mainly due to the uncertainty of partial pressure of water and baseline stability, we are currently developing an instrument allowing to deliver a flow of humidified air where the humidity level can be well controlled and changed.

The temperature dependence of the self-continuum is another important point to study due to its role in the real atmosphere calculations and to the fact that it can give crucial elements to understand the origin of the continuum. Previously, the temperature dependence of the self-continuum cross-section in the 2.1–μm window was measured using FTS in the temperature range between 350 and 472 K [149] and using OF–CEAS technique for temperatures between 296 and 323 K [52]. Fig. 4.23 taken from Ref. [52] shows the temperature dependence of C_s for three spectral points compared to the one provided by the MT_CKD2.5 model. The CRDS and OF–CEAS measurements are found in very good agreement with the linear extrapolation of high-temperature measurements of CAVIAR leaving the CAVIAR 293 K value significantly apart with too large values. This discrepancy confirms the difficulty to measure weak continuum at RT by FTS technique.

The slopes of the linear dependence of $\log C_s$ versus $1/T$ obtained in [52] were found to be close to the $D_0 = 1105(10)$ cm^{-1} – value corresponding to the dissociation energy of the water dimer measured in [195]. This fact means that C_s temperature dependence can be approximately given by $\exp(\frac{D_0}{kT})$ over the wide temperature range between 296 and 472 K. Despite the clarity of the results, which may be interpreted in support of the water dimer origin of the water self-continuum in the 2.1–μm window, authors of Ref. [52] avoid draw a firm conclusion because of the insufficient knowledge of the spectroscopy of the water dimer in this spectral region.

The observed disagreement of the continuum temperature dependence provided by MT_CKD with experimental data is probably due to the absence of any experimental data in the near-infrared region behind the model and values for the temperature dependence of the self-continuum cross-section in the region were extrapolated using mid-infrared data from [173, 175] carried out in the temperature range between 269 and 338 K. In these circumstances, we can conclude that higher sensitivity measurements of the temperature dependence using our CRDS setup are required to confirm these observations across the entire window.

Chapter 5

The CO_2 spectroscopy in the 2.3–μm transparency window

5.1 Introduction

The present chapter is devoted to the characterization of the CO_2 absorption in the 2.3–μm transparency window and is based on two papers [196,197] published recently.

Carbon dioxide is the main constituent of the atmosphere of Venus (96.5%). A significant greenhouse effect due to this gas, the layer of sulfuric acid clouds, and other greenhouse species with a significant contribution, for instance, H_2O [198] prevent the thermal radiation emitted by the lower atmosphere from escaping into space, and thus heats the atmosphere. The temperature near the surface of the planet can reach 735 K (Fig. 5.1). Nitrogen with a small amount of noble gases and chemically active species like H_2O, CO, OCS, SO_2, HCl, HF constitute the other 3.5% of the Venusian atmosphere.

Sulfuric acid cloud layers reflect most of the incoming (visible) sunlight and absorb IR thermal radiations at wavelength above 2.5 μm. This allows sounding the deep atmosphere and the surface of Venus only through a restricted number of narrow transparency windows between the strong absorption bands of carbon dioxide and water vapor. These windows are centered at 2.3, 1.74, 1.31, 1.27, 1.18, 1.1, 1.0, 0.90 and 0.85 μm [200].

Figure 5.2 illustrates synthetic and observed spectra of windows at 1.7 and 2.3–μm with species identified [13]. Among the mentioned windows, the 2.3–μm one was used to study the lower atmosphere in the 25 to 40 km altitude range and measure abundances of carbon monoxide, carbonyl sulfide, water vapor, sulfur dioxide, and hydrofluoric acid from spectra recorded by the Visible and Infrared Thermal Spectrometer (VIRTIS) aboard the Venus Express spacecraft [14, 201] or from the Earth [10, 202].

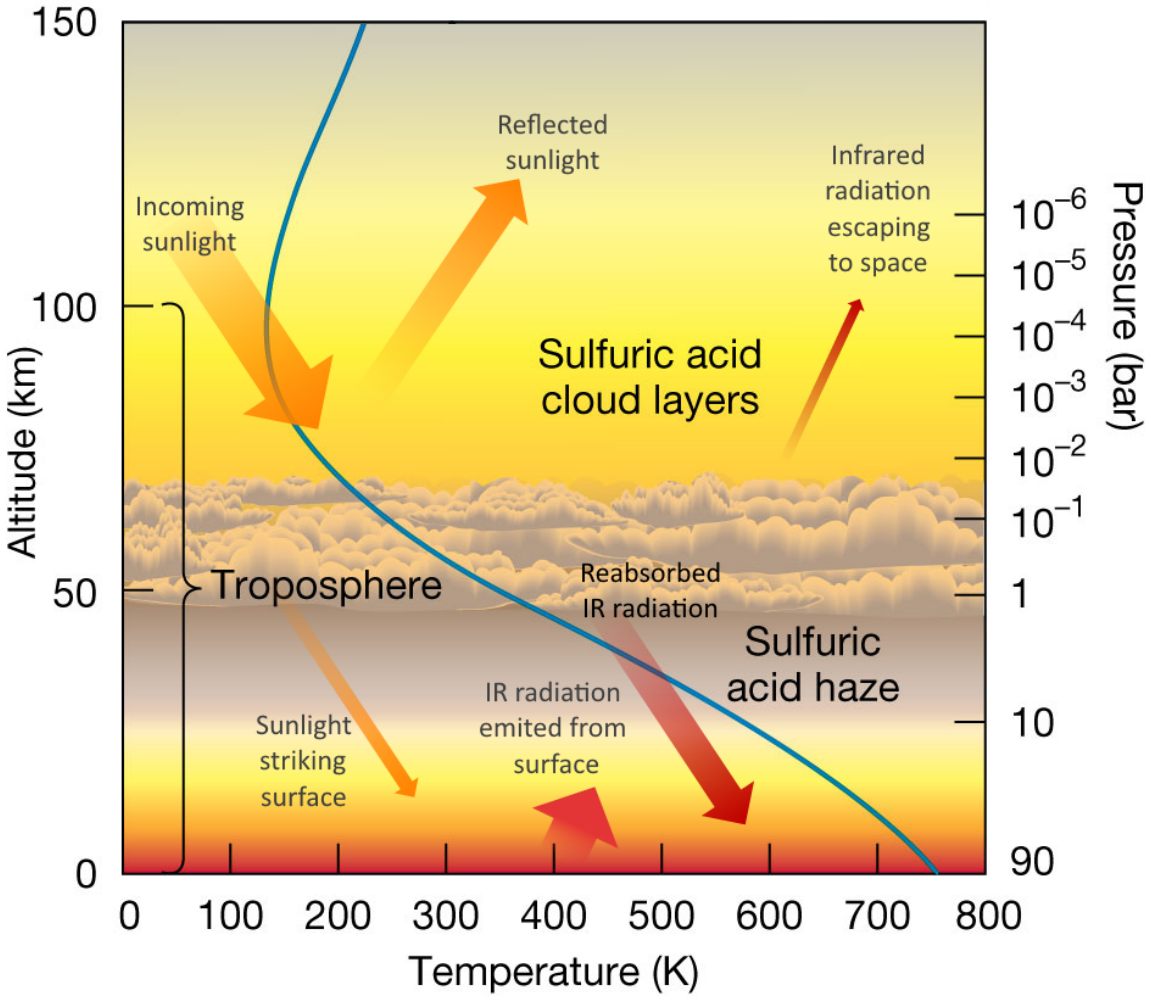

Figure 5.1. Schematic view and greenhouse effect of the Venusian atmosphere [199]

The carbon dioxide absorption in the spectral region under study results from the following contributions:

- local absorption lines corresponding to narrow and sharp peaks occurring because of rovibrational transitions of the monomer.
- broad yet relatively weak continua that result either from the cumulative effects of the pressure-broadened far wings of the rovibrational lines or from absorption by molecular pairs.

This absorption due to molecular pairs includes contributions of dimers but mainly results from the transient dipole induced during inter-molecular collisions (Collision-Induced Absorption, CIA). In the forward synthetic models used to reproduce the spectra of the Venusian atmosphere, the opacity of the CO_2 continuum is taken as a constant value of 3.5×10^{-8} $cm^{-1}amagat^{-2}$ [14, 203] in the 2.3–μm window transparency windows. Due to the lack of laboratory measurements, the adopted continuum values are directly derived from the Venus spectra in order to achieve

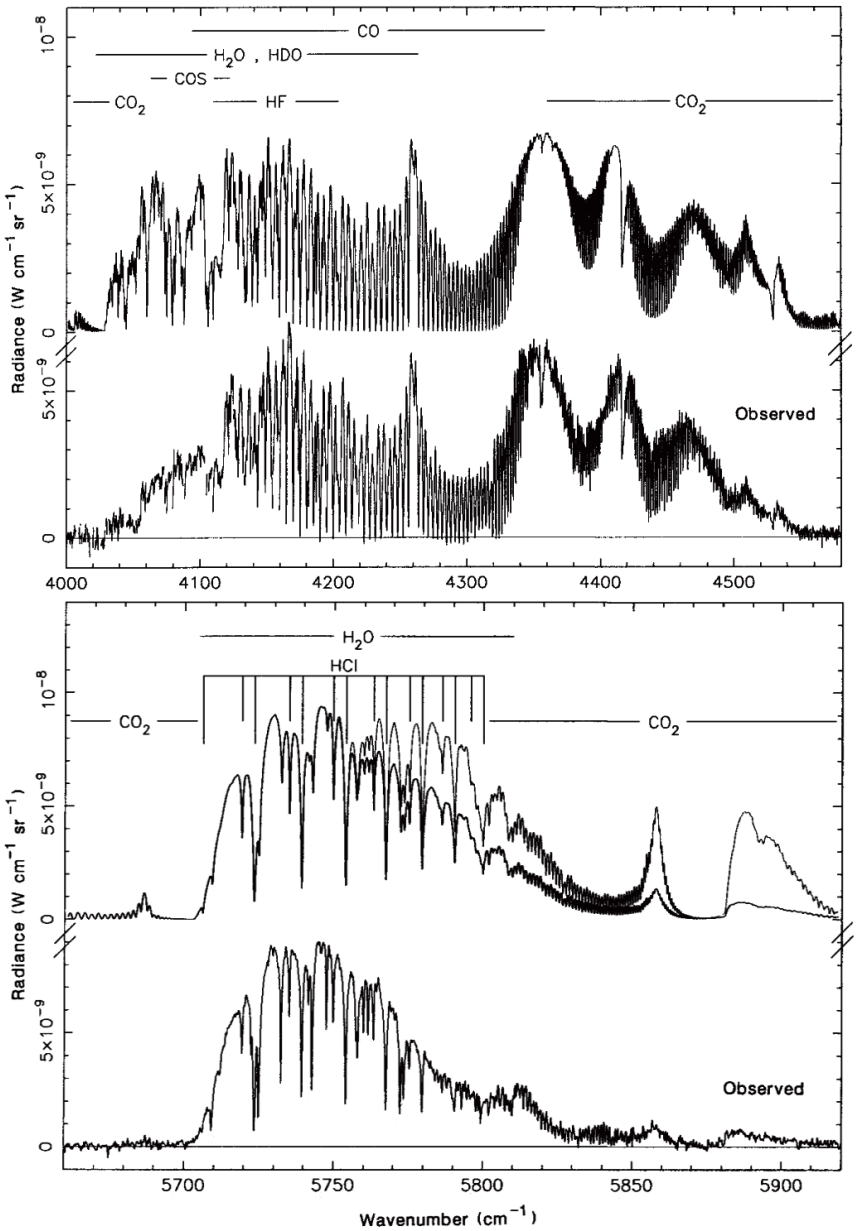

Figure 5.2. Synthetic and observed high resolution spectra of night side of Venus in 2.3–μm (*Higher panel*) and 1.7 μm (*Lower panel*) transparency windows recorded by Bézard *et al.* [13]

the best possible fit of the recorded spectra but without laboratory measurement as a support. As mentioned in Refs. [14, 202], these empirical constraints of the CO_2 continuum absorption underline the critical need for laboratory measurements at the temperature and pressure conditions met in Venus troposphere. In fact, in the 2.3–μm window only a few laboratory measurements almost exclusively at room temperature have been reported so far [204–211] with significant differences between some of them [203].

Spectroscopic databases are generally used in order to precisely simulate the

CO_2 monomer absorption. They include either line positions and intensities calculated with the effective operator method like the Carbon Dioxide Spectral Database (CDSD) [4] or a mix of experimental and calculated parameters obtained from the effective operator, like the HITRAN database [2]. Reliable experimental data must thus verify, validate and complete these databases.

In part 1 we will present the vibrational modes of the CO_2 molecule and the usual spectroscopic notation. In part 2 we will detail the high sensitivity laboratory study carried out with CO_2 samples in natural abundance and enriched with ^{18}O, using the CRDS technique. Part 3 will be dedicated to the experimental measurements of the CO_2 continuum absorption in the 2.3–μm region.

5.2 Rovibrational spectrum of $^{12}C^{16}O_2$ and $^{16}O^{12}C^{18}O$ in 2.3 μm region

5.2.1 Review of experimental data available in 2.3 μm

Description of vibrational modes of CO_2 and spectroscopic notation are given in Appendix B. The review of the literature shows the scarceness of previous observations because of the weakness of the CO_2 transitions in the region. According to the HITRAN [2] database, CO_2 lines in the considered spectral range from 4200 to 4400 cm^{-1} have intensities smaller than 3×10^{-26} cm/molecule at room temperature (Fig. 5.3), which makes it challenging to detect them using traditional methods like Fourier Transform Spectroscopy (FTS) coupled with multi-pass cells.

For the main isotopologue, the only previous FTS observations in the region concern a few P lines of the 31104–00001 band near 4400 cm^{-1} with the line positions in Venus spectra reported by Mandin [213] and intensities measured in the laboratory by Giver and Chackerian [214] with path lengths of up to 1307 m. The same 31104–00001 transitions were also detected as an illustration of the sensitivity of the ICLAS technique with a VECSEL [47]. In addition, this ICLAS-VECSEL study made it possible to detect the R branch of the 40005–01101 hot band centered near 4355 cm^{-1}. Other observations in the region concern a few transitions due to minor isotopologues detected with highly isotopically enriched samples: a few lines of the 31104–00001 band of $^{13}C^{16}O_2$ were reported by ICLAS-VECSEL [47] while the 30001–00001 band of $^{16}O^{12}C^{18}O$ centered at 4194.475 cm^{-1} has recently been reported by means of FTS [215]. Taking into account that no intensities were provided by ICLAS-VECSEL and that Venus line positions were reported with 0.01 cm^{-1} uncertainty, the amount and quality of experimental data available for the validation of the calculated CO_2 line lists is very limited in the region (see Fig. 5.3).

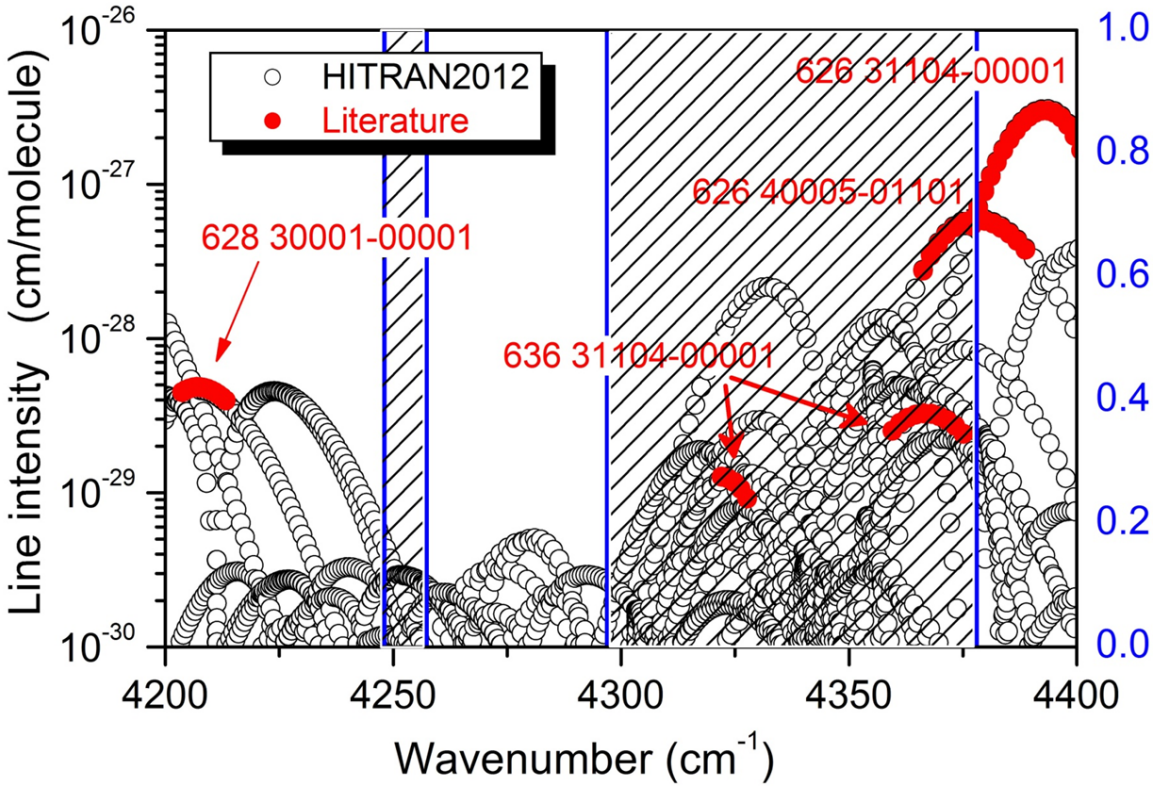

Figure 5.3. The HITRAN2012 line list [2] of natural carbon dioxide between 4200 and 4400 cm^{-1}. The HITRAN2012 list is calculated using the effective operator approach [212]. The transitions highlighted red correspond to the few previous observations available in the region [47, 213–215] (see text). The two spectral intervals corresponding to the present CRDS recordings are indicated and correspond to 4248–4257.3 cm^{-1} and 4297–4378 cm^{-1} spectral ranges.

The experiments described in this chapter were performed with the CRDS experimental set-up described in Chapter 2. coupled with the VECSEL source covering the region from 4297 to 4378 cm^{-1} for CO_2 sample in natural abundance and enriched with ^{18}O. Additionally a spectrum of the ^{18}O enriched sample was recorded with a DFB diode in the region from 4248 to 4257 cm^{-1}. The VECSEL light source makes it possible to record high sensitivity spectra with a minimum detectable absorption $\alpha_{min} = 2 \times 10^{-10}$ cm^{-1}. As a result, CO_2 lines with intensities of less than 10^{-29} cm/molecule could be measured and assigned, providing a valuable data set for testing and validating the most commonly used spectroscopic CO_2 databases.

5.2.2 Experiment with CO_2 in natural abundance

CRDS spectra of natural carbon dioxide (sample from Sigma-Aldrich, stated purity 99.998%) were recorded with a typical spectral step of 0.002 cm^{-1} at a pressure of 100 Torr. The pressure was measured with the 1 bar pressure gauge. Sample gas was slowly flowing through the cell at the rate of ≈0.6 sccm to reduce the content of

impurities.

As explained in Chapter 2, for VECSEL, the spectra were recorded at fixed pumping current and VCSEL temperature over 11 cm^{-1} by tuning the length of the external resonator of the VECSEL. The whole spectral region (4297–4378 cm^{-1}) was covered with different combinations of pumping current and VCSEL temperature.

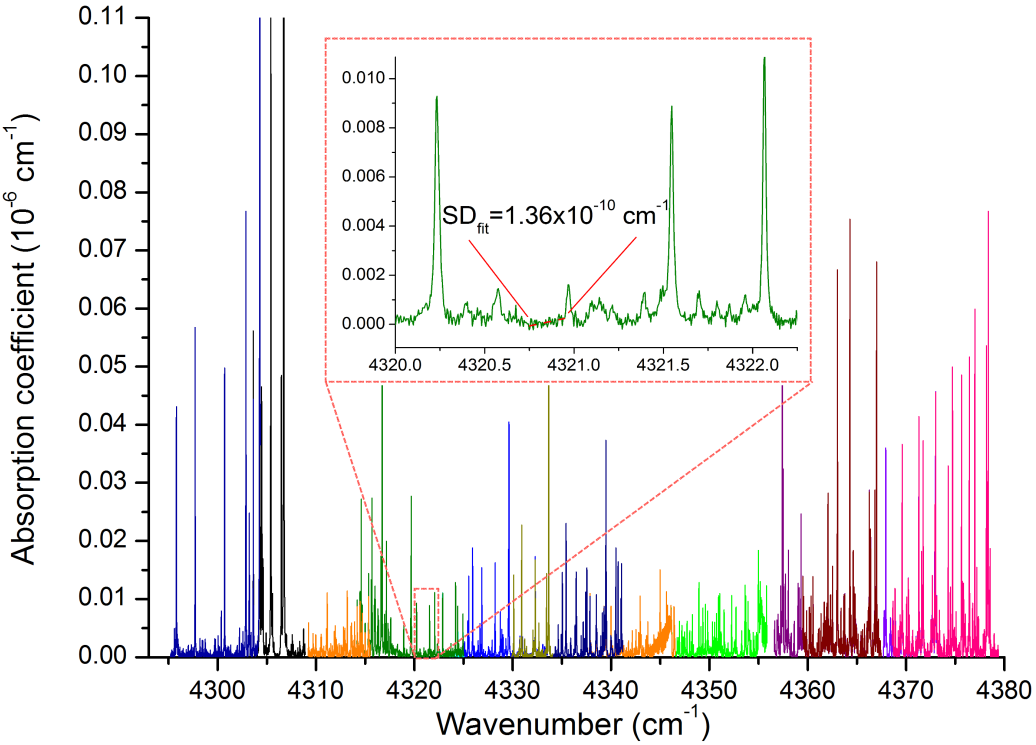

Figure 5.4. Overview of the CRDS spectra of a CO_2 sample in natural abundance. The different colors indicate spectra recorded at different temperature and pumping current conditions of the VECSEL source. Minimum detectable absorption coefficient of $\sim 1.4 \times 10^{-10}$ cm^{-1} is achieved (see insert).

The calibration performed with the FP etalon and the methane-filled reference cell (see more details in Section 2.2.4) was refined using accurate CO_2 lines from the HITRAN2012 [2] database or calculated using the effective Hamiltonian [72,73] (EH) approach. We estimate the error on the reported line positions to be about $\pm 2 \times 10^{-3}$ cm^{-1}, mostly limited by the error related to the linearization of the frequency axis using the etalon fringes.

About 65 ring-down events were averaged for each spectral point leading to a minimum detectable absorption coefficient $\alpha_{min} = 1.4 \times 10^{-10}$ cm^{-1}. Overview of resulting spectra and noise level are illustrated on Figure 5.4. All the recorded spectra were fitted by means of software developed in the LAME group by Serge Béguier, Grenoble. A Voigt profile was used to fit spectral lines with the Gaussian width fixed to its calculated value. Position, area and the Lorentzian width were

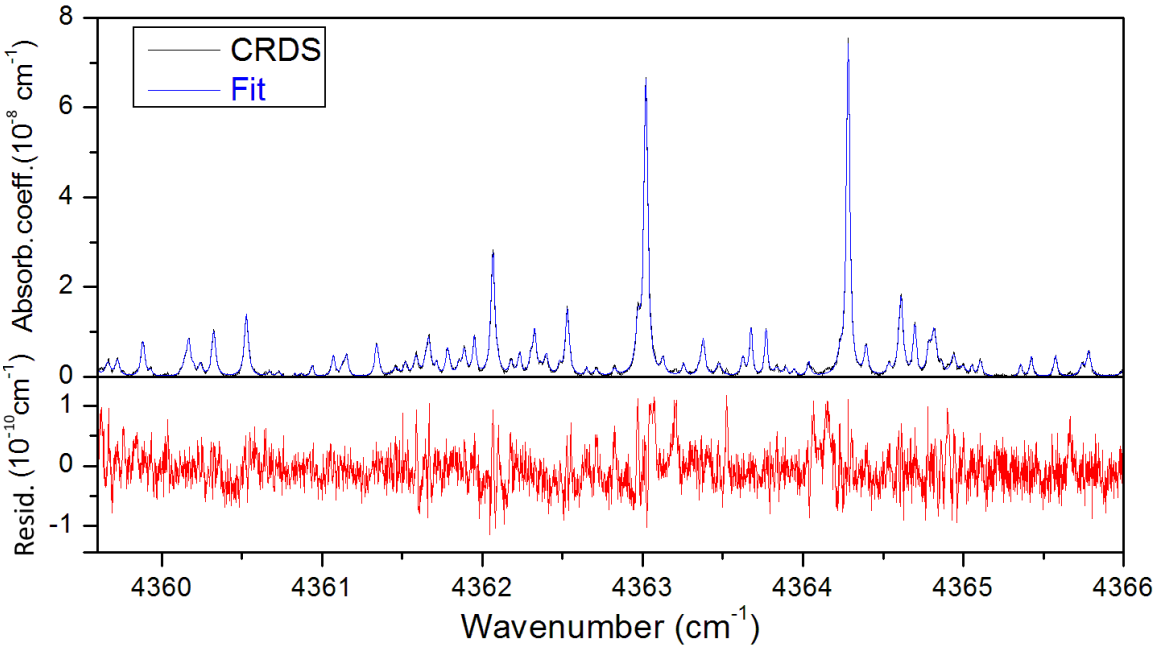

Figure 5.5. Experimental and fitted CO_2 spectra (*Higher panel*) and fit residual (*Lower panel*)

fitted for the different transitions. An example of a fitted spectrum and fit residual is given in the Fig. 5.5.

The line list resulting from the fit included a total of about 660 lines. About half of them were identified as due to methane transitions which are very intense, in particular in the region of the Q branch of the $\nu_3 + \nu_4$ band of $^{12}CH_4$ near 4318 cm^{-1} (intensities of up to 5×10^{-21} cm/molecule i.e. eight orders of magnitude stronger than the weakest CO_2 lines detected in the region). The relative concentration of methane in our sample retrieved from the fitted areas of $^{12}CH_4$ was estimated to be about 4 ppm. About 90 additional lines were assigned to H_2O, CO and N_2O, leaving 246 lines assigned to the first three CO_2 isotopologues: $^{12}C^{16}O_2$, $^{13}C^{16}O_2$, and $^{16}O^{12}C^{18}O$. The fit and assignment were performed by M. Konefal from LIPhy, Grenoble. The resulting CO_2 line list including rovibrational assignments is provided in the supplementary materials of the paper [197].

5.2.3 Comparison to the HITRAN2012 database

A comparative overview with the HITRAN2012 [2] line list is presented in Fig. 5.6. The CO_2 lines belong to a total of nine bands listed in Table 5.1, six of them being newly observed. All but two bands are included in the HITRAN list and correspond to a $\Delta P = 7$ series of transitions. An excellent agreement is noted between the HITRAN line positions which are values calculated using the EH approach and our

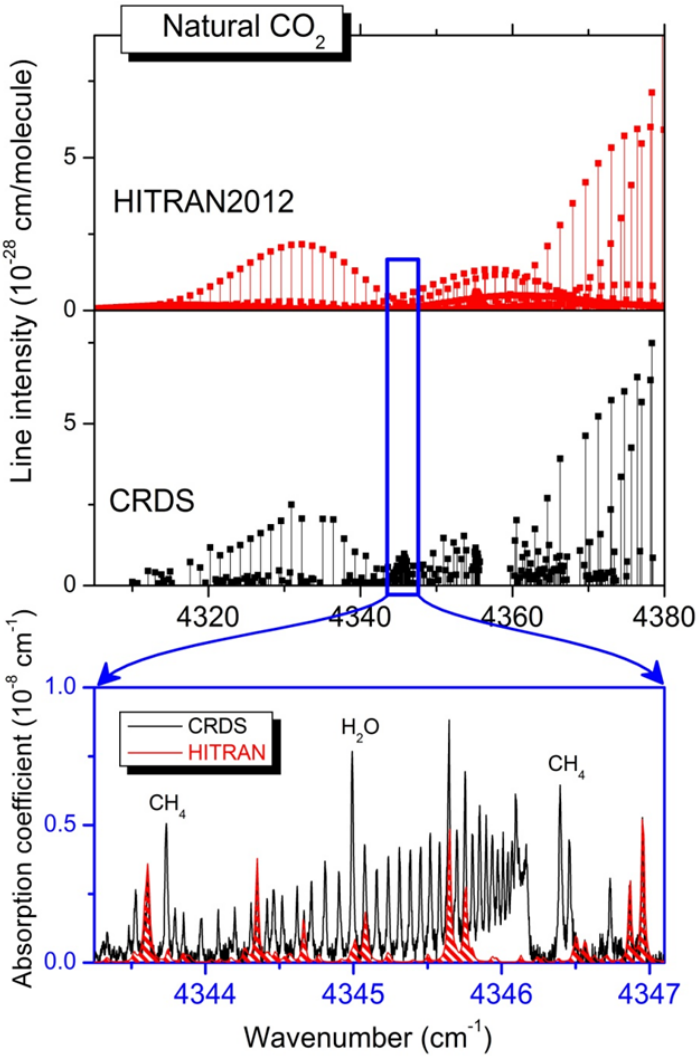

Figure 5.6. Comparison of the CRDS spectrum of carbon dioxide in natural abundance near 4350 cm^{-1} to the HITRAN database. The two upper panels compare the stick spectra between 4305 and 4380 cm^{-1} while the lowest panel compares the CRDS absorption spectrum in the region of the Q branch of 11111-00001 band of $^{16}O^{12}C^{18}O$ to a spectrum simulation using the HITRAN database (red).

Table 5.1. Summary of the assignments of the CO_2 spectrum recorded by CRDS between 4297 and 4378 cm^{-1}.

Isot. [2]	Nat. abund.	Band	ΔP	Center (cm^{-1})	Numb. of lines
$^{12}C^{16}O_2$	0.9842	00031-20002	5	4302.20	4
		31104-00001	7	4416.15	12
		32204-01101	7	4379.88	29
		33304-02201	7	4348.52	12
		40005-01101	7	4354.97	41
		41105-10002	7	4354.89	35
$^{13}C^{16}O_2$	0.0111	31104-00001	7	4344.03	10
$^{16}O^{12}C^{18}O$	0.00395	11111-00001	6	4346.18	73
		31104-00001	7	4339.82	30

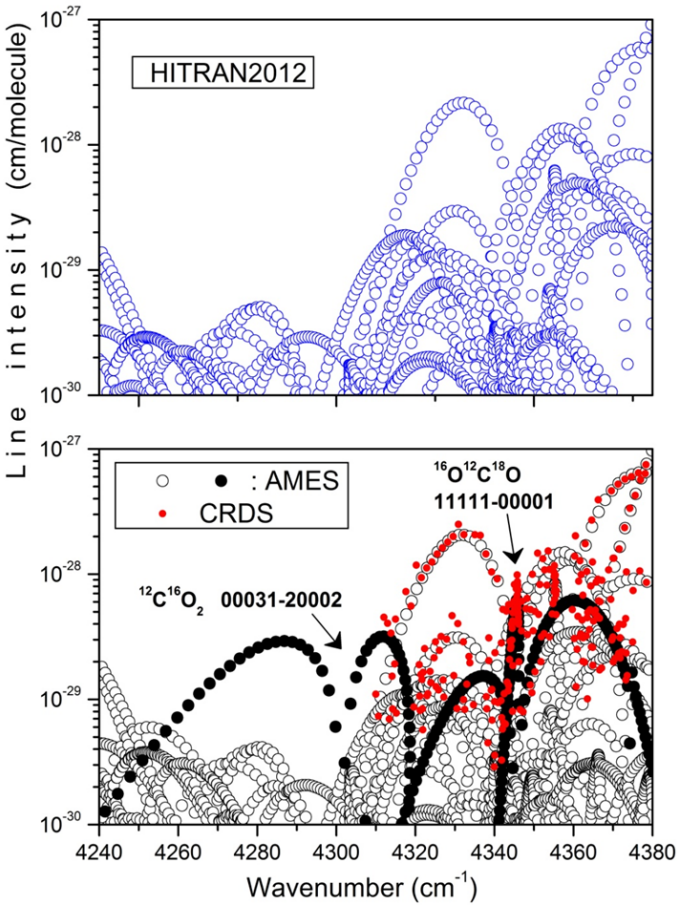

Figure 5.7. Comparison of the HITRAN2012 [2] and Ames variational [216, 217] line lists of carbon dioxide in natural abundance. The 11111-00001 band of $^{16}O^{12}C^{18}O$ and the 00031-20002 hot band of $^{12}C^{16}O_2$ missing in the HITRAN list are highlighted on the lower panel (black full circles) together with the present CRDS measurements (red full circles). Note the four R branch lines of the 00031-20002 hot band observed near 4313 cm^{-1} with intensities on the order of 4×10^{-29} cm/molecule.

values: for 185 lines in common, we obtain an average difference of -0.35×10^{-3} cm^{-1} with an RMS deviation of 2.4×10^{-3} cm^{-1} which is consistent with our experimental accuracy.

The intensity comparison also confirms the quality of the HITRAN line parameters. Considering their uncertainties which range from 10% and 100% according to their weakness and their level of line overlapping, the measured intensities were consistent with HITRAN values and no band was found to deviate systematically from HITRAN intensities.

The main deficiency of the HITRAN CO_2 list in the considered region is the absence of two bands contributing importantly to the absorption: (i) the 11111-00001 band of $^{16}O^{12}C^{18}O$ (in natural abundance) corresponding to a $\Delta P = 6$ variation of the polyad quantum number (see lower panel of Fig. 5.6); (ii) the 00031-20002 hot band of the main isotopologue $\Delta P = 5$ centered near 4301.4 cm^{-1} for which four R branch lines with intensities on the order of 4×10^{-29} cm/molecule could be undoubtedly assigned.

These two bands missing in the HITRAN2012 database were assigned by comparison to the Ames variational line list described bellow [3, 216] (Fig. 5.7).

In fact, while the line positions can be accurately extrapolated independently of

the polyads in the frame of the EH approach, line intensity calculations require the determination of an Effective Dipole Moment (EDM) parameters [212] for each value of the variation, ΔP, of the polyad number. The EDM parameters are adjusted to reproduce measured values of line intensities. In absence of intensity measurements for a given ΔP series, the corresponding transitions are then absent from CDSD and, consequently, HITRAN. This was for instance the case of the $\Delta P = 8$ bands of $^{16}O^{12}C^{18}O$ near 5900 cm^{-1} [218] which are the main contributors to the absorption of carbon dioxide in natural isotopic abundance in the region but were absent in previous versions of the CO_2 spectroscopic databases. In the present study, we face a similar situation with part of the $\Delta P = 6$ bands of $^{16}O^{12}C^{18}O$: The 11111-00001 band and corresponding sub-series are missing in the HITRAN and CDSD databases because no experimental intensities were available to determine the relevant term of the EDM parameter, $M(1\ 1\ 1\ 1)$.

The present CRDS intensities may be useful to determine this parameter and to include not only the 11111-00001 band of $^{16}O^{12}C^{18}O$ but also all the corresponding sub-series, in particular the 11112-00001 band centered at 4201.15 cm^{-1} which has a band intensity similar to that of the 11111-00001 band and then contribute importantly to the CO_2 absorption in the 2.3–μm window.

5.2.4 ^{18}O enriched CO_2 experiment

A major motivation of the CRDS recordings of ^{18}O enriched spectra was to get accurate intensity values for the 11111-00001 band of $^{16}O^{12}C^{18}O$ which had not been observed before. Figure 5.8 illustrates the quality of the recordings in the region of the Q branch of this band.

In this experiment the recording conditions like spectral step, temperature and pressure control, noise level as well as the fitting procedure and the calibration were similar to the previously described experiment dedicated to the natural abundance sample. Here we clarify some details.

Spectra of $^{16}O^{12}C^{18}O$ were recorded at the pressure of 47 Torr in the frequency region from 4297 to 4378 cm^{-1} with a VECSEL source and additionally in the region 4248 to 4257 cm^{-1} by means of a DFB laser diode by Nanoplus. A sample from Sigma-Aldrich with stated chemical purity of 99.9% had the following abundances for the atomic oxygen isotopes: ^{16}O 47.48%, ^{18}O 50.7%, ^{17}O 2.0%. Assuming natural abundance of carbon isotopes (^{12}C= 0.989, ^{13}C= 0.011), a statistical distribution of isotopologue content returns the sample content listed in Table 5.2. These calculated abundance values were validated by the intensity measurements performed in the 5850–7000 cm^{-1} range with the same sample [218–220].

Overall, the line list, derived from the fit of spectrum, includes a total of about

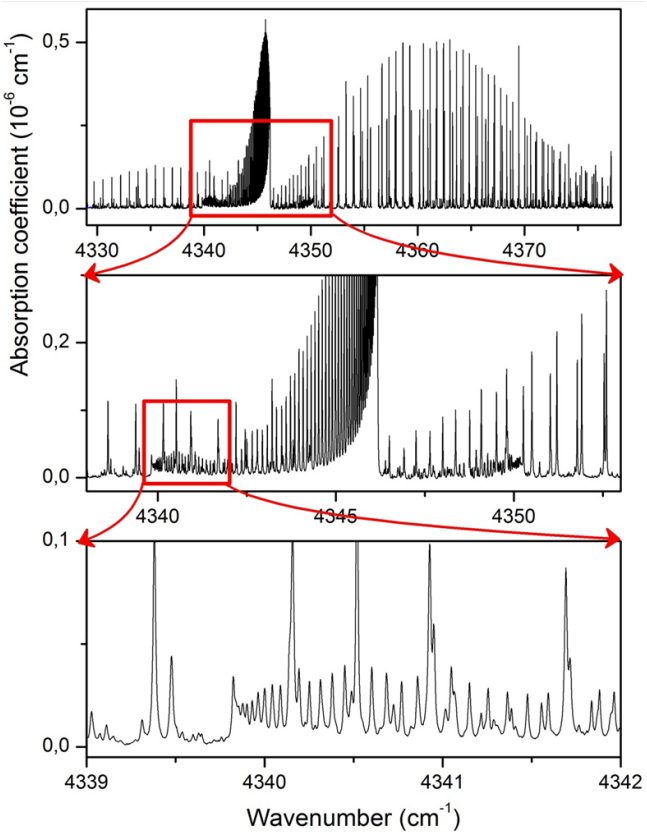

Figure 5.8. CRDS spectrum of carbon dioxide highly enriched in ^{18}O in the region of the newly observed 11111-00001 band of $^{16}O^{12}C^{18}O$ (P = 49 Torr). The enlargements illustrate the high sensitivity and high dynamics of the recordings (noise equivalent absorption on the order of 5×10^{-10} cm^{-1}). The strong Q branch of the 11111-00001 band of $^{16}O^{12}C^{18}O$ near 4346 cm^{-1} is surrounded by the weaker Q branches of the 31104-00001 and 12211-01101 bands of the same isotopologue near 4340 and 4350 cm^{-1}, respectively.

1100 lines in the 4297–4378 cm^{-1} region. About 150 of them were assigned to impurities (mostly CH_4, CO and H_2O) by comparison with the corresponding HITRAN lists [2]. After removal of the impurity lines, about 690 lines were assigned to CO_2 leaving about 230 weak lines unassigned. In the DFB laser diode region 41 lines were assigned to $^{16}O^{12}C^{18}O$ and $^{16}O^{12}C^{17}O$ corresponding to $\Delta P = 5,\ 6$ band series.

Table 5.2. Isotopic abundances of the first eleven CO_2 isotopologues in the sample.

Isotopologue	HITRAN notation	Abundance (%)
$^{12}C^{16}O_2$	626	22.15
$^{13}C^{16}O_2$	636	0.22
$^{16}O^{12}C^{18}O$	628	47.48
$^{16}O^{12}C^{17}O$	627	1.87
$^{16}O^{13}C^{18}O$	638	0.48
$^{16}O^{13}C^{17}O$	637	0.02
$^{12}C^{18}O_2$	828	25.45
$^{17}O^{12}C^{18}O$	728	2.01
$^{12}C^{17}O_2$	727	0.04
$^{13}C^{18}O_2$	838	0.26
$^{17}O^{13}C^{18}O$	738	0.02

As a result of the superposition of the transitions of the various isotopologues, the spectrum is very congested (about 12 lines/cm^{-1}) and the rovibrational assignments were only possible with the accurate predictions performed at IAO Tomsk in the frame of the global effective operator approach [73].

Excluding a few $^{12}C^{16}O_2$ lines, the observed transitions belong to a total of 14 bands of five isotopologues: $^{16}O^{12}C^{18}O$ (7 bands), $^{12}C^{18}O_2$ (4 bands), $^{17}O^{12}C^{18}O$, $^{13}C^{18}O_2$ and $^{16}O^{12}C^{17}O$ (1 band each). Since this work was carried out in collaboration with IAO Tomsk, the EH parameters needed to predict the spectrum of each isotopologue were calculated by V. Perevalov using line parameters taken from the following references: $^{16}O^{12}C^{18}O$ [218], $^{12}C^{18}O_2$ and $^{13}C^{18}O_2$ [219], $^{17}O^{12}C^{18}O$ [220], and $^{16}O^{12}C^{17}O$ [215].

The summary of the assignments is presented in Table 5.3 which also includes our observations in the 4248–4257.3 cm^{-1} interval where a few lines of three bands of $^{16}O^{12}C^{18}O$ and one band of $^{16}O^{12}C^{17}O$ were detected. The different bands of the five carbon dioxide isotopologues correspond to the $\Delta P = 6$ and 7 series of transitions. Line intensity were predicted using the set of $\Delta P = 7$ EDM parameters of the principal isotopologue as explained in Ref. [4]. The $\Delta P = 6$ EDM parameters of $^{16}O^{12}C^{18}O$ were taken from Ref. [215]. The resulting list including rovibrational assignments is attached as supplementary materials of the paper [197]. An overview of the list of the $^{16}O^{12}C^{18}O$ isotopologue is presented in Fig. 5.9 together with the deviations of the line positions from the EH predictions [218]. A very good agreement is noted between the predicted and measured line positions, the deviations being smaller than 0.05 cm^{-1} for all the isotopologues. Some systematic deviations due to a shift of the vibrational term of the upper level are nevertheless observed as for instance for the 31104-00001 band of $^{16}O^{12}C^{18}O$ which deviates by about -0.012 cm^{-1}.

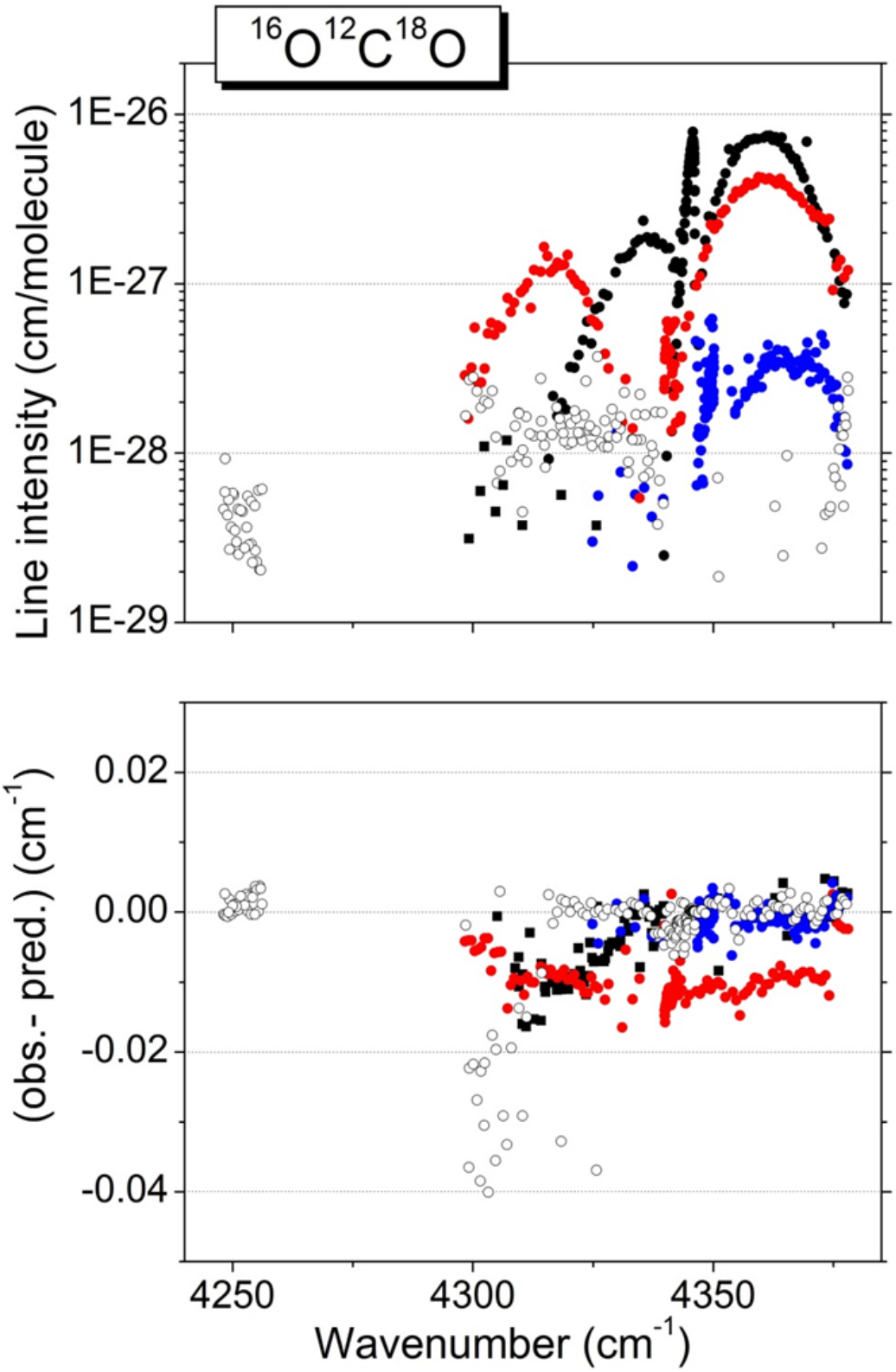

Figure 5.9. *Upper panel:* Overview of the $^{16}O^{12}C^{18}O$ CRDS line list. The black, red and blue symbols correspond to the 11111-00001, 31104-00001 and 12211-01101 bands, respectively. Open circles correspond to the other bands.
Lower panel: Corresponding differences between the measured line positions and those calculated using the EH model [218].

Table 5.3. Summary of the assignments of the ^{18}O enriched CO_2 CRDS spectrum in the two studied spectral intervals.

Isotopologue	Abundance	Band	ΔP	Center (cm^{-1})[1]	Number of lines	J^2 $P/Q/R$
4248−4257.3 cm^{-1}						
$^{16}O^{12}C^{18}O$	0.4748	31101-01101	5	4211.28	14	-/-/45-53
		32201-02201	6	4248.67	5	-/-/5-7
		40001-10001	6	4227.45	10	-/-/26-35
$^{16}O^{12}C^{17}O$	0.0187	31101-01101	6	4239.10	12	-/-/11-21
4297−4378 cm^{-1}						
$^{16}O^{12}C^{18}O$	0.4748	11111-00001	6	4346.18	135	37/64/51
		12211-01101	6	4350.24	129	61/40/41
		20011-01101	6	4382.41	16	8-32/27-48/-
		31104-00001	7	4339.82	124	59/41/49
		32204-01101	7	4302.0	67	-/-/61
		40005-01101	7	4275.25	14	-/-/35-55
		41105-10002	7	4280.93	9	-/-/27-56
$^{12}C^{18}O_2$	0.2545	31103-00001	7	4419.21	12	56-78/-/-
		31104-00001	7	4258.74	11	-/-/56-78
		32203-01101	7	4409.33	17	46-66/-/-
		40004-01101	7	4317.94	35	19-23/6-28/5-53
$^{17}O^{12}C^{18}O$	0.0201	31104-00001	7	4297.48	44	-/19-35/4-61
$^{13}C^{18}O_2$	0.0026	31103-00001	7	4360.13	25	14-58/-/2-24
$^{16}O^{12}C^{17}O$	0.0187	11111-00001	6	4366.79	51	69/89/15

5.2.5 Comparison to the Ames line list

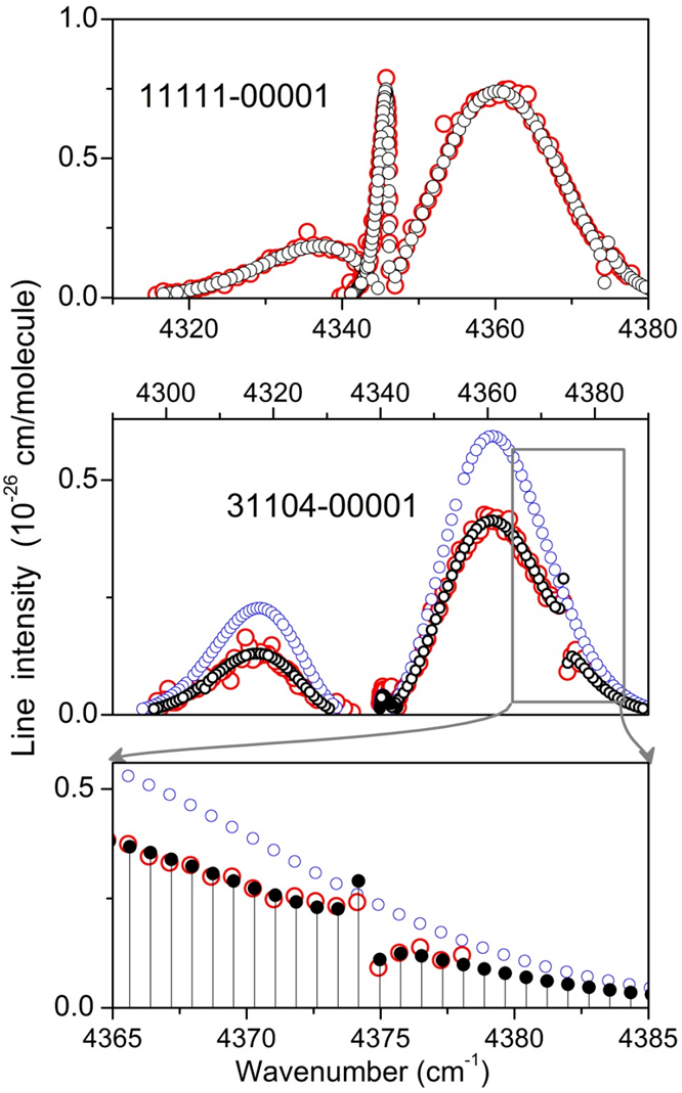

Figure 5.10. Comparison of the Ames [216, 217], CRDS and HITRAN [2] line lists for two bands of $^{16}O^{12}C^{18}O$ (black, red and blue symbols, respectively). (The displayed intensities take into account the 0.4748 relative abundance factor of $^{16}O^{12}C^{18}O$ in our CO_2 sample.) Upper panel: 11111-00001 band (absent in the HITRAN database). Lower panels: 31104-00001 band. The enlargement highlights a perturbation affecting the R branch near $J = 45$ which is fully predicted by the Ames variational calculations. Note that the perturbation is also observed in the R branch of the 11111-00001 band near 4375 cm^{-1}.

Considerable progress has been recently achieved by variational calculations of the CO_2 absorption spectrum [216,217,221]. The Ames-296 K list is a theoretical line list computed using a variational dipole moment surface and an empirically refined potential energy surface. An important advantage of the variational line lists is their completeness as illustrated in Fig. 5.7 by the prediction of the 00031-20002 hot band of the main isotopologue near 4301.4 cm^{-1} which is absent in HITRAN [2] and CDSD [4].

In order to compare our data with the Ames list, it was necessary to assign the Ames list with the spectroscopic nomenclature used for the assignment and adopted in HITRAN and CDSD. In the Ames line list, the V_1, V_2 and V_3 numbers generally differ from the normal V_1, V_2, l_2, V_3 used in CDSD and HITRAN. This issue was resolved by S. Tashkun from the IAO (Tomsk, Russia).

While variational calculations of CO_2 line positions do not reach the experimental accuracy in our region (for instance the positions of the 11111-00001 band of

$^{16}O^{12}C^{18}O$ are calculated about 0.03 cm^{-1} too low compared to the observations and the Ames positions of the 31104-00001 band are overestimated by about 0.06 cm^{-1}), variational line intensities in our spectral range are very accurate. In Fig. 5.10, we present a comparison of the Ames line list for the 11111-00001 and 31104-00001 bands of $^{16}O^{12}C^{18}O$. The overall agreement between the variational and CRDS intensities is impressive for both bands.

The enlargement on the lower panel of Fig. 5.10 shows a line intensity perturbation near $R(44)$ which is very well predicted by the variational calculations. On the basis of the effective Hamiltonian of $^{16}O^{12}C^{18}O$ [218], this perturbation was identified as resulting from an interpolyad resonance anharmonic interaction between the 31104 ($P = 7$) and 11111 ($P = 6$) upper states with an energy level crossing around $J_{up} = 45$. The perturbation is also observed around the R(45) transition of the 11111-00001 band near 4375 cm^{-1} (upper panel of Fig. 5.10). Similar interpolyad intensity perturbations were already evidenced in a spectra analysis of non-symmetric isotopologues of carbon dioxide. [218]. As illustrated by the HITRAN line list included in Fig. 5.10, this kind of interpolyad perturbations cannot be reproduced by the effective Hamiltonian model which is a polyad model. Such local resonance interactions provide crucial tests for variational lists. In this context, the level of agreement achieved by the Ames line list [216, 217] is impressive.

5.2.6 Conclusion

The CO_2 line list, obtained from the CRDS spectra, provides critical tests for the effective operator models because part of the weak transitions contributing importantly to the residual absorption in transparency windows belong to border bands such as very excited hot bands or bands of minor isotopologues. Very high sensitivity of the recordings, made it possible to detect for the first time transitions with intensity values down to 5×10^{-30} cm/molecule providing experimental information valuable for testing and validating calculated line lists provided by the most frequently used spectroscopic databases.

The most significant result is the evidence of bands missing in the HITRAN2012 and CDSD lists like the 11111-00001 band of $^{16}O^{12}C^{18}O$ and the 00031-20002 hot band of $^{12}C^{16}O_2$. These bands are predicted by variational calculations which have the advantage of completeness but variational line positions do not reach the experimental accuracy for line positions which may lead to some inaccuracies in the cases of local resonance interaction. In the particular example found in this study – the anharmonic interaction between the 31104 ($P = 7$) and 11111 (P=6) upper states of $^{16}O^{12}C^{18}O$ the Ames variational calculations were nevertheless able to predict very satisfactorily the observed perturbation. Besides completeness, a considerable advantage of the

most recent variational calculations of CO_2 spectrum is the accuracy of the computed intensities [222]. In the present study, the achieved agreement between the CRDS and Ames intensities of the 11111-00001 and 31104-00001 bands of $^{16}O^{12}C^{18}O$ (Fig. 5.10) confirms this general statement. In those circumstances, the best compromise in terms of completeness and accuracy can be achieved by transferring the experimental accuracy on line positions to the variational line lists using the effective Hamiltonian calculations which reproduce satisfactorily nearly all measured line positions [73]. This approach was recently followed by Zak *et al.* for the main isotopologue up to 8000 cm^{-1} [221].

It is worth mentioning that it is not only the positions and intensities of local lines that we need to reliably simulate transmission of the real Venus' atmosphere. In pressure conditions in atmosphere of Venus, the self- broadening and pressure shift coefficients and their temperature dependence are of significant importance. Moreover, intensities obtained for room temperatures have to be recalculated for real temperature conditions. The high density of the atmospheres implies also the importance of the precise characterization of the continuum absorption due to the far wings of the strong CO_2 absorption bands and broadband collision-induced absorption; the next section of this chapter is dedicated to continuous absorption of CO_2 in the 2.3–μm window.

5.3 The CO_2 continuum absorption

As mentioned in the introduction of this chapter, CO_2 continuum contributes to the total absorption in addition to the monomer local lines. In the rest of this chapter we will describe how we measured and retrieved the contribution of this continuum.

5.3.1 Spectra acquisition

In the present experiment, the spectra were recorded using a gas flow of natural carbon dioxide through the CRDS cell. This flow was regulated with a downstream proportional electro-valve monitored by a Proportional Integral Derivative controller in order to maintain a constant pressure in the CRDS cell. The pressure was measured with a capacitive transducer (model ATM.1ST from STS; 1000 mbar full range; calibration better than 0.04% of the full scale down to 10 mbar). Eight recording pressures between 250 and 750 Torr were selected. The achieved pressure stability was found to be better than 0.3% for all the pressure set-points. The spectra were recorded in the 4324-4336 and 4346-4380 cm^{-1} spectral intervals accessible with our VECSEL. Calibration was proceed as described in previous part. During the calibration, the pressure shift was not taken into account but precise calibration is not critical when

determining broadband continuum absorption.

A key factor in all the measurements of weak broadband continua is the baseline stability. As the absorption continuum is obtained by a difference of the baseline level of spectra recorded with and without the absorber, it is necessary to ensure that the injection of the absorbing gas does not affect the optical alignment of the spectrometer. This is particularly the case in the present measurements where the continuum is weak as a result of the subatmospheric pressures used for the recordings. In general, the background spectrum is recorded with the cell evacuated (for instance, see Refs. [192, 197, 211]) and the continuum absorption manifests itself as an increase in the baseline level when the absorber is injected in the cell. In order to minimize possible biases related to the change in pressure we developed a recording procedure at a constant pressure by using a non-absorbing gas (namely, synthetic air) for the background spectrum.

Starting after the cell is evacuated, the procedure consists of the following steps:

i Injecting a flow of synthetic air into the CRDS cell (Alphagas 2 from Air Liquide, stated purity > 99.9998%) at the chosen pressure and alignment of the high reflectivity mirrors to maximize the ring down time and optimize the mode matching,

ii Recording of the air spectrum,

iii Gradual replacement of air with pure CO_2 (Alphagas 2 from Air Liquide, stated purity of 99.995%) at constant pressure using a switching valve system,

iv Recording of two successive CO_2 spectra.

v Gradual replacement of CO_2 with air keeping the pressure constant,

vi Recording of the air spectrum

The steps from ii to iv of the procedure are illustrated in Fig 5.11. About 25 minutes were needed to record each 12 cm^{-1} wide spectrum displayed on this figure. During the whole procedure two spectra of pure CO_2 and two spectra of pure air are recorded allowing for testing the reproducibility of the measurements. The base line stability during the entire recording procedure was estimated to be better than 5×10^{-10} cm^{-1} from the recording of the air spectra. For comparison, the retrieved continuum absorption coefficient at 750 Torr is on the order of 1.5×10^{-8} cm^{-1} as it will be shown below.

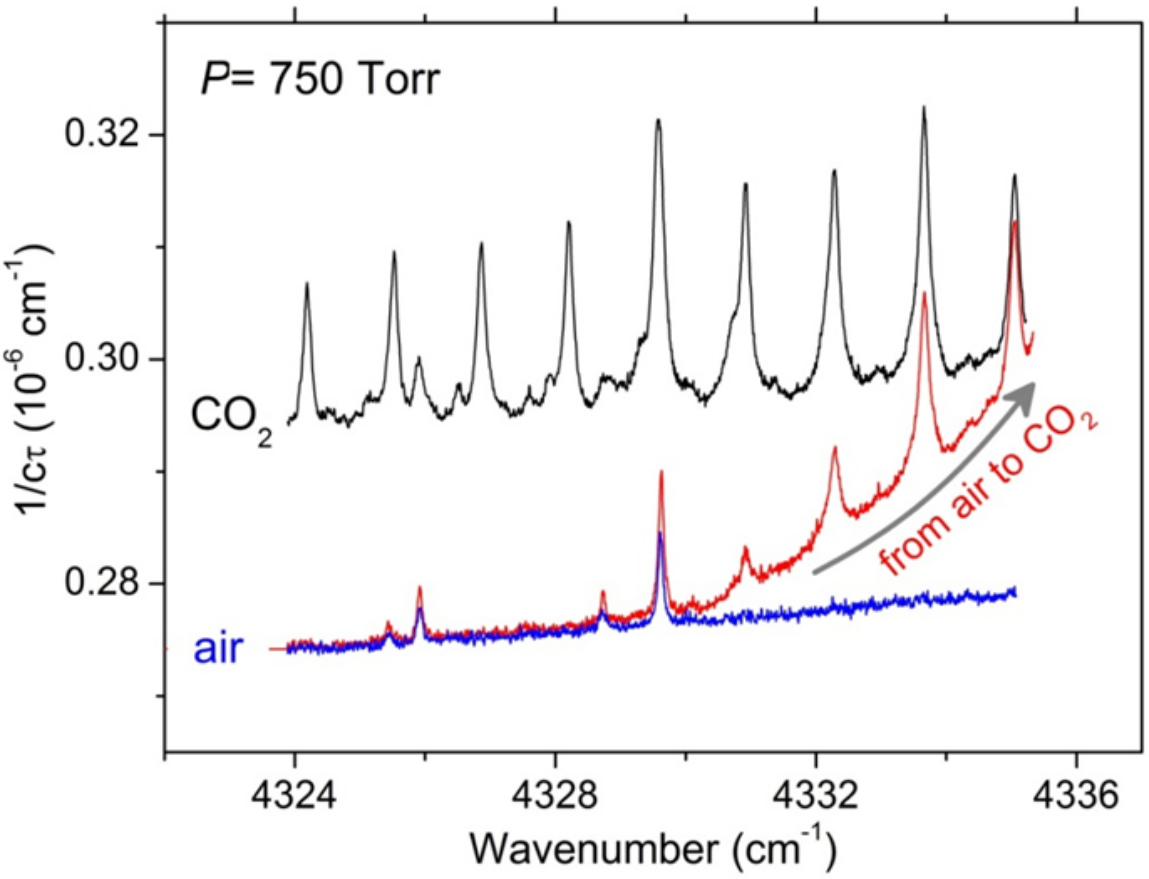

Figure 5.11. Example of a cell flush where synthetic air is progressively replaced by pure CO_2 gas with pressure maintained constant at 750 Torr. The appearance and increase of the CO_2 lines and the progressive increase of the baseline level are observed when air is replaced by CO_2 (red spectrum).

5.3.2 Absorption continuum retrieval

The injection of CO_2 in the CRDS cell results in an increase of the loss rate, $1/c\tau_{CO_2}(\nu)$ (in cm^{-1}) (see Fig. 5.11), in comparison to its baseline value, $1/c\tau_{air}(\nu)$ obtained with the cell filled with air (ν is the wavenumber in cm^{-1}). Neglecting the small differences from unity ($< 10^{-3}$) of the refractive indexes of CO_2 and air, the measured CO_2 extinction coefficient (in cm^{-1}) can be expressed as a sum of three terms:

$$\alpha_{CO_2}(\nu) = \frac{1}{c\tau_{CO_2}(\nu)} - \frac{1}{c\tau_{air}(\nu)} = \alpha_{LL} + \alpha_{CA} + \Delta\alpha_{Ray} \tag{5.1}$$

where α_{LL} and α_{CA} are the contributions due to the CO_2 local lines (LL) and continuum absorption (CA), respectively. $\Delta\alpha_{Ray}$ is the difference between the Rayleigh scattering losses of CO_2 and air.

a. Rayleigh scattering

Similar to Section 4.3.4 following Equation 4.3, the refractive index of CO_2 and

air in our spectral range (4330 cm^{-1}) are 1.000419 and 1.000306 at 1 atm and 296 K, respectively. The absorption due to Rayleigh scattering is obtained by $\sigma N_s \cdot \frac{P}{P_s}\frac{T_s}{T}$. Its amplitude, proportional to the pressure, is small compared to the continuum signal, for instance 5.3×10^{-10} cm^{-1} compared to 1.5×10^{-8} cm^{-1} at 750 Torr.

b. Contribution of CO_2 monomer and trace species local lines

Following the conclusions of the Part 5.2.6, the HITRAN2012 and CDSD line lists are not sufficiently complete in the region. Consequently, we adopted the Ames line list computed by Huang *et al.* [216] using variational calculations [3, 217] as the line list for natural CO_2. The Ames line list has the advantage to be complete (for instance all the needed isotopologues are included) and to provide reliable line intensities based on an *ab initio* dipole moment surface [217] which were validated in Section 5.2.5. In order to achieve experimental accuracy on line positions, the Ames variational line positions were corrected by S.A. Tashkun (IAO Tomsk) using the CDSD line positions which rely on effective Hamiltonian models developed for each CO_2 isotopologue and have experimental accuracy [4].

The line shape parameters (self-broadening coefficient including temperature dependence and shift) were attached to the Ames list [216]. They were calculated theoretically by R. Gamache with the Complex Robert–Bonamy (CRB) method [223,224]. The choice of the line profile is of first importance for the *LL* simulations.

The choice of the profile is another crucial point. It is well known that an untruncated Voigt profile largely overestimates the total gas absorption at high pressure [111]. In order to match simulations with the recorded spectra, sub-Lorentzian profiles are usually used to describe the far wing absorption lines of CO_2. These sub-Lorentzian profiles are generally obtained using an empirical χ-factor that makes the far wings decrease faster than the Lorentzian far wings [111,206,209,225,226]. In Ref [211], it was shown that, near 1.7 μm, absorption continua derived using different χ-factor formulations found in the literature for the Lorentzian part are almost identical to the one obtained with a Voigt profile truncated at ± 25 cm^{-1} away from the line center and corrected from the resulting "pedestal". This ± 25 cm^{-1} truncation which is generally adopted to derive the water continuum, can be seen as a "limit case" of the χ-factor approach. In the present work, we also checked that in the spectral interval under consideration at the pressure of 750 Torr, the truncated Voigt profile and the χ-factor formulations from Refs. [206, 209, 226] lead to negligible differences in the contribution of monomer absorption. In summary, the CO_2 monomer contribution was calculated using the Ames line list corrected with CDSD line positions and a Voigt profile truncated at ± 25 cm^{-1}.

Our choice to use a gas flow instead of a static cell has the advantage to limit the concentration of impurities desorbed from the cell walls such as water. Nevertheless, the achieved sensitivity of the recordings makes detectable absorption lines due to

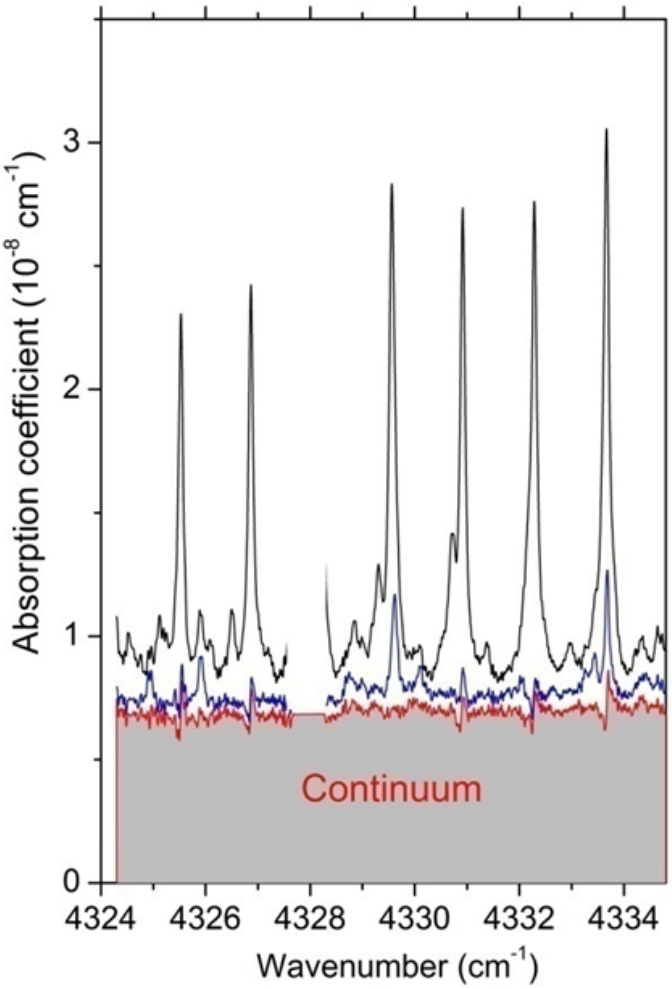

Figure 5.12. Absorption continuum retrieval from the CRDS spectrum of CO_2 recorded at 500 Torr. The spectrum (black line) has been corrected from the Rayleigh scattering contribution and the baseline obtained with synthetic air at the same pressure. The successive results of the subtraction of local line simulations of CO_2 and impurity lines (H_2O, N_2O, CH_4) (blue and red line, respectively) leads to the continuum level (grey).

impurities present in our gas sample at the trace level. These species are H_2O (few tens of ppm), N_2O (<1 ppm) and CH_4 (∼10 ppb). Similarly to the monomer *LL* contribution, their (small) *LL* contributions were subtracted. For this purpose, we used simulations based on the HITRAN2012 database [2] for N_2O and CH_4 and a more complete line list constructed by S. Mikhailenko (IAO Tomsk) for water vapor [4], respectively. When needed, the broadening coefficients were adjusted to better reproduce the spectra and, similarly to CO_2, a Voigt profile truncated at ±25 cm^{-1} was adopted. Note that all calculations of the LL contribution have to take into account absorption lines located 25 cm^{-1} below and above the recording range. Fig. 5.12 illustrates the subtraction of the LL contribution from the CRDS spectrum.

c. Results

The above data treatment was applied to all the spectra recorded at different pressures. For instance, the right panel of Fig. 5.13 shows the frequency dependence of the derived absorption continua at 250 and 500 Torr. The doubling of the pressure is accompanied by a larger variation of the continuum level as expected from the quadratic density dependence of the continuum absorption. This is confirmed in the

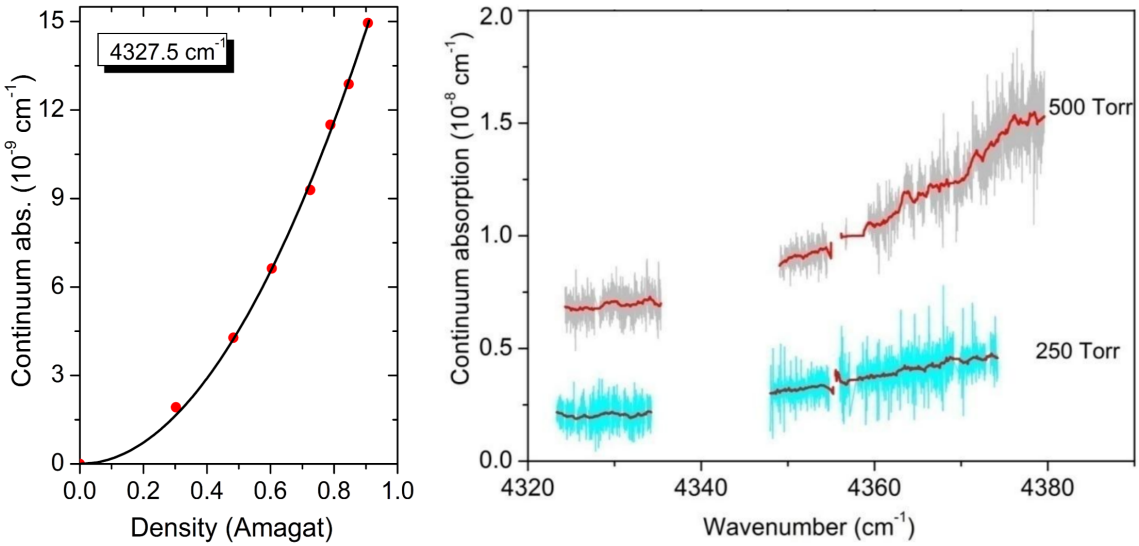

Figure 5.13. *Left panel*: Density dependence of the continuum absorption at 4327.5 cm^{-1}. The solid line represents a purely quadratic fit of the experimental data.
Right panel: Overview of the CO_2 continuum absorption at 250 and 500 Torr. An adjacent averaging was performed (red lines) in order to smooth the high frequency noise related to the subtraction of the local lines contribution

left panel of Fig. 5.13 where a pure quadratic function with fitted quadratic coefficient reproduces satisfactorily the continuum level at 4327.5 cm^{-1}. Note that as the ideal gas law is valid only for low densities, we use in Fig. 5.13 (left panel) the molecular density instead of the pressure value. The CO_2 density values were obtained using a model provided by the National Institute of Standards and Technology (NIST) based on the virial expansion up to the third virial coefficient [227]. For the highest pressure (750 Torr) it leads to a correction limited to 0.5%.

5.3.3 Discussion

The frequency dependence of the retrieved absorption coefficient of the continuum, normalized by the density is shown in Fig. 5.14. Its amplitude is observed to increase from $\sim 2\times10^{-8}$ $cm^{-1}amagat^{-2}$ near 4330 cm^{-1} to 4.5×10^{-8} $cm^{-1}amagat^{-2}$ around 4380 cm^{-1}. According to the results by Tonkov *et al.* [206] discussed hereafter, this increase corresponds to the low energy region of two superimposed collisional–induced absorption (CIA) bands: the 11111-00001 CIA band at 4390 cm^{-1} and the CIA at 4392 cm^{-1} corresponding to the $(10001)^a + (01111)^b$ cooperative excitation of the a and b colliding CO_2 molecules. Note that the present continuum values near 4350 cm^{-1} are typically five times larger than those measured near 5900 cm^{-1} [211].

The only previous work available for comparison to our results is that published by Tonkov *et al.* twenty years ago [206]. These authors used several spectrometers and pressurized absorption cells to measure and empirically model the CO_2 absorption in

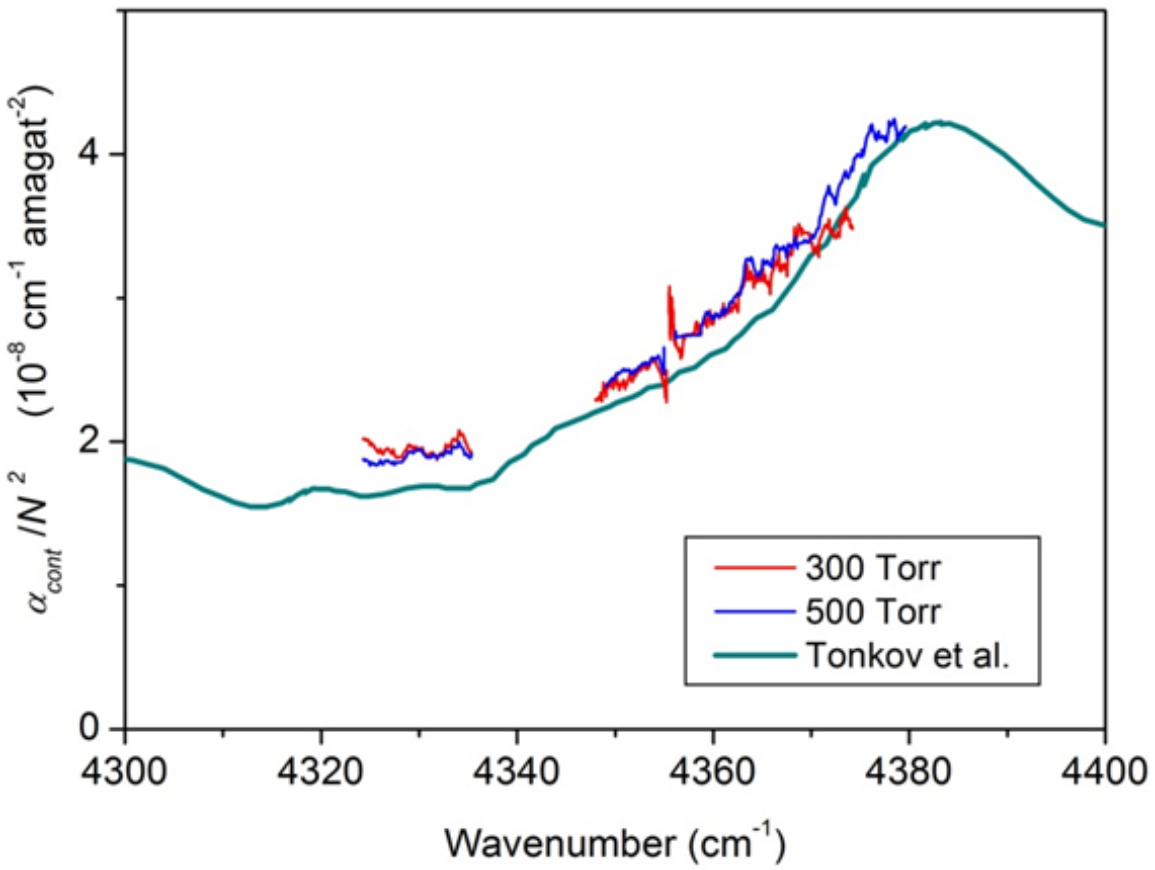

Figure 5.14. Normalized absorption coefficient of CO_2 continuum between 4300 and 4400 cm^{-1}. The CRDS values retrieved from spectra recorded at 300 and 500 Torr (red and blue curves, respectively) are compared to the results reported by Tonkov *et al.* [206] with a density of 20 amagat (black solid line).

the entire 2.3 μm window from 3900 to 4700 cm^{-1}. The weak spectra in our region of interest were recorded with a grating spectrograph at a 3 cm^{-1} resolution and with densities of 20 amagat. Tonkov *et al.* [206] analyzed the different contributions to their spectra: far line wings for which χ-factors were fitted to their experiment, allowed and collision-induced absorption (CIA) bands. An overall good modeling of the spectrum was achieved but the resolution of the spectra at disposal and the very high pressure of the recordings prevented a detailed analysis. In particular the problems of the intensities of the CIA bands and of the completeness of the CO_2 line list were raised [206]. Nowadays the CO_2 line list in the region is much improved and the uncertainty related to the subtraction of the corresponding LL absorption is reduced. In order to compare our results with the measurements by Tonkov *et al.* we have digitalized the spectrum displayed in Fig. 3 of Ref. [206] and subtracted the simulated contribution of the monomer for a density of 20 amagat at 296 K. For this simulation we used the CDSD database [4] from 3000 to 5000 cm^{-1} and the Voigt profile with the χ-factor proposed by Tonkov *et al.* In our region, for a 20 amagat

density, the monomer contribution represents only a few percent of the measured absorption indicating that the monomer absorption is not a major error source of the continuum value at high pressure. In particular, the far wing contribution of the strong $\nu_1 + \nu_3$ band at 3715 cm^{-1} is important below 4200 cm^{-1} but negligible in our region. The resulting normalized absorption coefficient is compared to our results in Fig. 5.14. A systematic underestimation by a few % is noted for the values by Tonkov *et al.* but the overall agreement is particularly convincing in view of the very different experimental conditions of the experimental datasets. Let us underline that with a 20 amagat density, the continuum absorption measured by Tonkov *et al.* is 400 times larger than with 1 amagat, the highest density value that we used for our experiments. In particular, this good agreement indicates that three-body collisions do not play a significant role at 20 amagat.

5.3.4 Conclusion

The CO_2 absorption continuum has been determined by CRDS using a CO_2 gas flow at different pressures between 250 Torr and 750 Torr. To the best of our knowledge, this is the first measurement of the CO_2 continuum at sub-atmospheric pressure, reducing the uncertainty due to the subtraction of the monomer contribution. Pure CO_2 and synthetic air were alternatively injected into the high finesse CRDS cell keeping the pressure constant in order to avoid possible biases due to a change of the optical alignment induced by pressure changes. Following the results of a previous study [211], a CO_2 line list based on Ames variational line parameters [216] with positions with experimental accuracy [4] was used to subtract of the monomer contribution. The Voigt profile truncated at ± 25 cm^{-1} was affected to each line. The sensitivity provided by CRDS allows for the determination of the continuum (on the order of 10^{-8} cm^{-1} at 500 Torr) from spectra recorded at sub-atmospheric pressures. The use of low pressure values is an advantage to properly subtract the monomer local contribution and to avoid three-body collisions effects. The recordings of a series of spectra at different pressures allowed checking the purely quadratic density dependence of the continuum, confirming the binary origin of the measured absorption signal.

Previous measurements by Tonkov *et al.* [206] using much higher densities (20 amagat) and a low resolution grating spectrograph are found in very good agreement with our results. This indicates that three-body collisions do not play a significant role up to 20 amagat and illustrates the fact that the defects of the CO_2 line list used by Tonkov *et al.* for the monomer absorption has a small relative contribution at 20 amagat.

As mentioned in the introduction, the synthetic models of Venus spectra usually used constant absorption continuum in the different windows [14, 203]. In the 2.3 μm

window, Marcq *et al.* [14] adopted a value of 3.5×10^{-8} $cm^{-1}amagat^{-2}$ close to the former estimation by C. de Bergh *et al.* (4×10^{-8} $cm^{-1}amagat^{-2}$) [228]. These values are consistent with the average value in our spectral region (see Fig. 5.14) but neglect the important frequency dependence. In addition, let us note that no temperature dependence of the CO_2 continuum value is included in Venus synthetic models. Considering the high temperatures of Venus lower atmosphere, laboratory validation of this assumption at the temperature conditions met in Venusian troposphere is highly suitable.

Conclusion and perspectives

The 2.3–μm region corresponds to a transparency window for water vapor and carbon dioxide, and is used to sound the Earth's and Venus' atmospheres where water vapor and carbon dioxide represent the main gaseous absorbers in the infrared range, respectively. The lack of high-sensitivity spectroscopic data for these two molecules in that spectral region was the main motivation of the presented PhD work.

In order to improve the spectroscopic knowledge in this region, we developed a cavity ring down spectrometer in the 2.20–2.35 μm spectral range. The developed instrument made it possible to record highly sensitive spectra of molecules of atmospheric and planetologic interest at high spectral resolution with a routine limit of detection from 1×10^{-10} to 3×10^{-10} cm^{-1} and limit sensitivity at the level of 1.2×10^{-11} cm^{-1}. The instrument has unprecedented sensitivity in the region up to date and has two orders of magnitude higher sensitivity compared to the most frequently used FTS spectrometers coupled with long multipass cells.

Within the framework of the thesis, 3 DFB laser diodes and 1 VECSEL were used with the setup, which covered in total 132 cm^{-1} divided in four narrow spectral regions from 4248 to 4516 cm^{-1}. The VECSEL source applied to CRDS for the first time made it possible to cover quasi-continuously 85 cm^{-1} with a sensitivity of up to 2×10^{-10} cm^{-1}. Using this VECSEL–CRDS setup, we recorded a weak S(3) quadrupole electric transition of the HD molecule and its collision-induced absorption for the first time.

The emission bandwidth of 5 MHz of two DFBs purchased from Nanoplus was not suitable for CRDS because of a weak signal transmitted through the cavity. To narrow the laser bandwidth and have more of transmitted intensity we applied the optical feedback from the external cavity. The resulting bandwidth of the locked laser was estimated at the level of 1 MHz for integration time of 1 s. Moreover, to improve the sensitivity of the instrument instead of applying the full amplitude voltage ramp to the PZT of the HFC we adjusted the length of the cavity near resonance to increase both, ring-down voltage threshold leading to better determination of every single ring-down and an increase in ring-down acquisition repetition rate. Using this setup, we achieved the limit sensitivity of the instrument of 1.2×10^{-11} cm^{-1}, and thanks to it realized the first laboratory detection of a highly forbidden O(14) quadrupole

transition of N_2 with an intensity of 1.27×10^{-30} cm/molecule.

The study of water vapor rovibrational transitions in all four accessible spectral regions made it possible to measure and rovibrationally assign about 400 spectral features for 6 most abundant isotopologues, and about half of these lines were detected for the first time. Twelve energy levels were first determined for $H_2{}^{17}O$, $H_2{}^{18}O$ and $HD^{18}O$ minor isotopologues in natural isotopic abundance.

The comparison of the line intensities of very recent FTS measurements at DLR [131] and those obtained in our measurements to the most recent variational line list calculated in collaboration between University College London and the Institute of Applied Physics in Nizhny Novgorod [136–141] evidenced a significant improvement compared to previous variational intensity values by Schwenke and Partridge [126,127] in the region. These intensities will be used as a source for the future HITRAN2017 database and are expected to improve the completeness and accuracy of line intensities in the database, which is among the most frequently used for atmospheric calculations.

We also realized high sensitivity measurements of water vapor self-continuum absorption within the framework of the broad study across several transparency windows [122]. Together with OF–CEAS measurements in the 2.1–μm transparency window [52], we recorded a number of spectral points for four narrow intervals corresponding to the low frequency slope of the window centered at 2.1 μm. Our results align well with the MT_CKD 2.8 self-continuum values. This agreement validates the standard model widely used for the water continuum absorption in atmospheric radiative transfer codes. On the other hand, it seems to indicate that FTS measurements of refs. [149] and [185] largely overestimate the self-continuum cross-section at room temperature in the 2.1–μm window.

Considering further development, it deserves to be mentioned that the significant monomer contribution and uncertainty in the partial pressure of water vapor did not allow us to accurately measure the foreign-continuum absorption. We estimated the resulting uncertainty to be around 30% for measurements carried out in a single spectral region. Despite the high uncertainty of our resulting value in the MT_CKD2.8 model, released in 2016, foreign-continuum cross-sections were modified based on our foreign-continuum measurements together with results obtained by Baranov and Laferty [194]. Up to date, the MT_CKD2.8 foreign-continuum cross-section at 4250 cm^{-1}, which is of 3.9015×10^{-25} $cm^2 molecule^{-1} atm^{-1}$, coincides with our value of 3.91×10^{-25} $cm^2 molecule^{-1} atm^{-1}$. However, in order to improve the accuracy of the foreign-continuum, we need to know precisely the water-air mixing ratio in the cavity. In order to do so, we are developing an instrument which prepares a mixture of water vapor with air at certain partial pressures and maintains them during the measurement.

As for CO_2 absorption spectra, the sensitivity of the recordings made it possible

to detect transitions with intensity values down to 5×10^{-30} cm/molecule for the first time. Our results provide experimental information valuable for testing and validating calculated line lists like Ames [3,216,217] and CDSD [4], which are used as sources in the frequently used HITRAN spectroscopic database. One of the significant results was evidence of bands missing from the HITRAN2012 and CDSD lists such as band 11111-00001 of $^{16}O^{12}C^{18}O$ and hot band 00031-20002 of $^{12}C^{16}O_2$. These bands are predicted by variational calculations which are advantageous because of their completeness, but variational line positions do not reach the experimental accuracy, which may cause some inaccuracies in cases of local resonance interaction. In the particular example found in our study, i.e. the anharmonic interaction between upper states 31104 ($P=7$) and 11111 (P=6) of $^{16}O^{12}C^{18}O$, the Ames variational calculations were able to predict the perturbed intensities very satisfactorily.

The CO_2 continuum absorption in the 4324–4336 and 4346-4380 cm^{-1} spectral intervals was measured for the first time at sub-atmospheric pressures, with a subsequent reduction in the uncertainty achieved by the subtraction of the monomer contribution. The sensitivity and baseline stability provided by CRDS made it possible to determine the continuum which reveals as an increase in the baseline on the order of magnitude of 10^{-8} cm^{-1} at 500 Torr.

So as to ensure the baseline stability, which is critical for continuum recordings, we used synthetic air to record the background spectrum and then replaced it at constant pressure with CO_2 using a flow. Therefore, we did not affect the baseline due to misalignment of the cavity. In so doing, the base line stability during the entire recording procedure was estimated to be better than 5×10^{-10} cm^{-1}. The amplitude of the absorption coefficient normalized by density was observed to be increasIng from $\sim 2 \times 10^{-8}$ $cm^{-1}amagat^{-2}$ near 4330 cm^{-1} to 4.5×10^{-8} $cm^{-1}amagat^{-2}$ around 4380 cm^{-1}. The previous measurements by Tonkov et al. [206] provided at much higher densities of the order of 20 amagat are found in very good agreement with our results, which shows that three-body collisions are of relatively low importance up to 20 amagat.

The values which are used for synthetic models of atmosphere of Venus [14, 228] are consistent with the average value in our spectral region but neglect the important frequency dependence. In addition, let us note that no temperature dependence of the CO_2 continuum value is included in Venus synthetic models. Considering the high temperatures of Venus lower atmosphere, laboratory validation of this assumption at the temperature conditions met in Venusian troposphere is highly suitable.

Our future studies will be concerned to line profile measurements to accurately retrieve such parameters like broadening and narrowing coefficients, speed dependence parameters. This requires the acquisition of line profiles with high quality factors in order to use complex non-Voigt profiles, the quality factor being defined as the

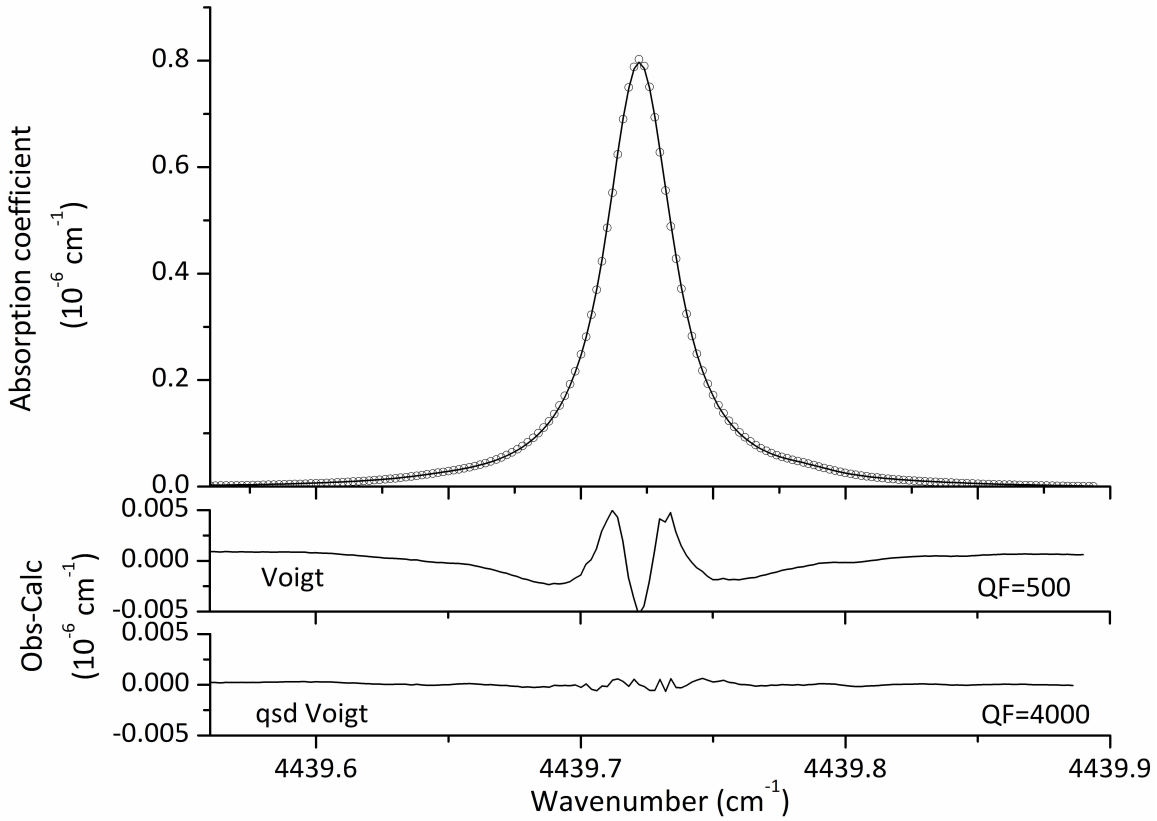

Figure 5.15. Averaged spectrum of an isolated line (black circles) and fit (black solid line). Fit residuals corresponding to Voigt profile fit, and to quadratic speed dependent Voigt profile.

ratio of the absorption at the top of the line over the RMS of the residuals. For that we averaged 108 spectra of a single CO_2 line at the pressure of 120 Torr. The resulting averaged spectrum is plotted in Fig. 5.15. By fitting with profile with a Voigt profile a characteristic residual with a "W" form is observed showing that more complex profiles are required. The same spectrum was fitted with a profile including speed dependence with a quadratic dependence of the parameters (qSD Voigt profile) leading to flat residuals and a quality factor (QF) equal to 4000. In Fig. 5.16 we have plotted the residuals of the averaged spectrum (red line) together with the concatenation of the residuals of the 108 spectra fitted with a Voigt profile (in black). It is clear from this figure that the maximum noise is observed when the first derivative of the profile shows an extremum. This is due to the fact that uncertainty on the measured wavelength on each RD leads to noise amplitude through the local slope of the profile. In our case the amplitude noise of 3×10^{-8} cm^{-1} corresponds to 8 MHz of frequency noise. This value largely exceeds the 1 MHz jitter of the narrowed DFB laser (measured in Chapter 2) and corresponds to the wavelength meter precision.

To go beyond this limit due to the wavelength meter we are developing a new modification of the setup which includes active stabilization of the external cavity

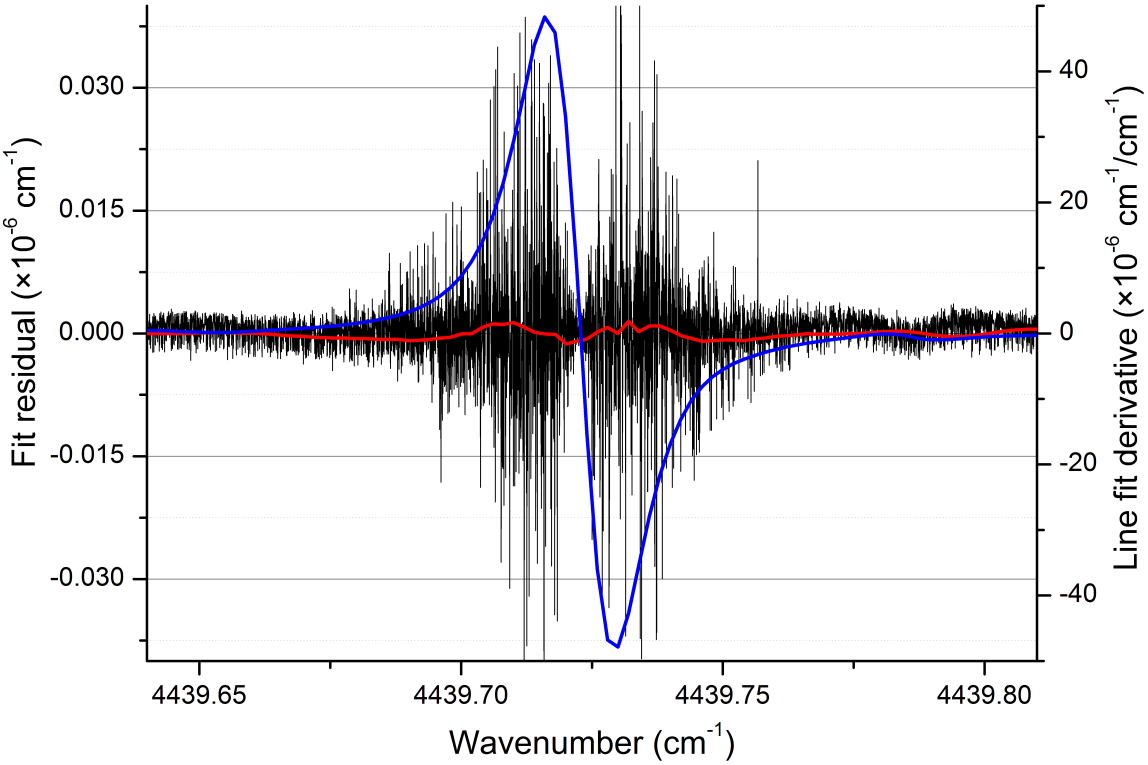

Figure 5.16. Multiple recording of the CO_2 line at pressure of 120 Torr. Residual of fit by Voigt profile of 100 concatenated measurements (black). Residual of fit of the same measurements averaged and fitted with Voigt profile (red). Derivative of fit result (blue solid line)

length using an absolute frequency ultrastable VCOF-laser [229]. With this new setup we should be able to determine the laser frequency during each RD without the need of the wavelength meter but knowing very accurately the FSR and the longitudinal mode number of the external cavity on which the laser diode is lasing.

As a follow-up to the research, together with the development of the instrument, our plan is to extend the accessible spectral range towards the wavelength of 2.0 μm. We have also purchased two DFB lasers and new high reflectivity mirrors, and these are scheduled to be ready for tests and measurements soon.

Bibliography

[1] A. Castrillo, L. Moretti, E. Fasci, M. D. De Vizia, G. Casa, and L. Gianfrani. The Boltzmann constant from the shape of a molecular spectral line. *Journal of Molecular Spectroscopy*, 300:131–138, 2014.

[2] L. S. Rothman, I. E. Gordon, Y. Babikov, A. Barbe, D. Chris Benner, P. F. Bernath, M. Birk, L. Bizzocchi, V. Boudon, L. R. Brown, A. Campargue, K. Chance, E. A. Cohen, L. H. Coudert, V. M. Devi, B. J. Drouin, A. Fayt, J. M. Flaud, R. R. Gamache, J. J. Harrison, J. M. Hartmann, C. Hill, J. T. Hodges, D. Jacquemart, A. Jolly, J. Lamouroux, R. J. Le Roy, G. Li, D. A. Long, O. M. Lyulin, C. J. Mackie, S. T. Massie, S. Mikhailenko, H. S. P. Müller, O. V. Naumenko, A. V. Nikitin, J. Orphal, V. Perevalov, A. Perrin, E. R. Polovtseva, C. Richard, M. A H Smith, E. Starikova, K. Sung, S. Tashkun, J. Tennyson, G. C. Toon, Vl G. Tyuterev, and G. Wagner. The HITRAN2012 molecular spectroscopic database. *Journal of Quantitative Spectroscopy and Radiative Transfer*, 130:4–50, 2013.

[3] X. Huang, D. W Schwenke, S. A Tashkun, and T. J. Lee. An isotopic-independent highly accurate potential energy surface for CO_2 isotopologues and an initial $^{12}C^{16}O_2$ infrared line list. *The Journal of chemical physics*, 136(12):124311, mar 2012.

[4] S.A. Tashkun, V.I. Perevalov, R.R. Gamache, and J. Lamouroux. Cdsd-296, high resolution carbon dioxide spectroscopic databank: Version for atmospheric applications. *Journal of Quantitative Spectroscopy and Radiative Transfer*, 152:45 – 73, 2015.

[5] C. Frankenberg, U. Platt, and T. Wagner. Retrieval of CO from SCIAMACHY onboard ENVISAT: detection of strongly polluted areas and seasonal patterns in global CO abundances. *Atmospheric Chemistry and Physics*, 5(6):1639–1644, jun 2005.

[6] P. Ingmann, B. Veihelmann, J. Langen, D. Lamarre, H. Stark, and G. B. Courrèges-Lacoste. Requirements for the GMES Atmosphere Service and ESA's

implementation concept: Sentinels-4/-5 and -5p. *Remote Sensing of Environment*, 120:58–69, 2012.

[7] A. Butz, A. Galli, O. Hasekamp, J. Landgraf, P. Tol, and I. Aben. TROPOMI aboard Sentinel-5 Precursor: Prospective performance of CH_4 retrievals for aerosol and cirrus loaded atmospheres. *Remote Sensing of Environment*, 120:267–276, 2012.

[8] D. Wunch, G. C Toon, J.-F. L Blavier, R. A. Washenfelder, J. Notholt, B. J. Connor, D. W. T. Griffith, V. Sherlock, and P. O. Wennberg. The Total Carbon Column Observing Network. *Philosophical Transactions of the Royal Society of London A: Mathematical, Physical and Engineering Sciences*, 369(1943):2087–2112, 2011.

[9] D. Fu, T. J. Pongetti, J.-F. L. Blavier, T. J. Crawford, K. S. Manatt, G. C. Toon, K. W. Wong, and S. P. Sander. Near-infrared remote sensing of Los Angeles trace gas distributions from a mountaintop site. *Atmospheric Measurement Techniques*, 7(3):713–729, mar 2014.

[10] E. Marcq, B. Bézard, T. Encrenaz, and M. Birlan. Latitudinal variations of CO and OCS in the lower atmosphere of Venus from near-infrared nightside spectro-imaging. *Icarus*, 179(2):375–386, 2005.

[11] R. A. Rohde. https://commons.wikimedia.org/wiki/File:Atmospheric_ Transmission.png.

[12] A. Galli, A. Butz, R. A. Scheepmaker, O. Hasekamp, J. Landgraf, P. Tol, D. Wunch, N. M. Deutscher, G. C. Toon, P. O. Wennberg, D. W T Griffith, and I. Aben. CH_4, CO, and H_2O spectroscopy for the Sentinel-5 Precursor mission: An assessment with the Total Carbon Column Observing Network measurements. *Atmospheric Measurement Techniques*, 5(6):1387–1398, 2012.

[13] B. Bézard, C. de Bergh, D. Crisp, and J.-P. Maillard. The deep atmosphere of venus revealed by high-resolution nightside spectra. *Nature*, 345(6275):508–511, Jun 1990.

[14] E. Marcq, B. Bézard, P. Drossart, G. Piccioni, J. M. Reess, and F. Henry. A latitudinal survey of CO, OCS, H_2O, and SO_2 in the lower atmosphere of venus: Spectroscopic studies using virtis-h. *J. Geophys. Res.*, 113:E00B07, 2008.

[15] S. A. Clough, M. J. Iacono, and J.-L. Moncet. Line-by-line calculations of atmospheric fluxes and cooling rates: Application to water vapor. *Journal of Geophysical Research*, 97(D14):15761, 1992.

[16] R. R. Gamache, S. Kennedy, R. Hawkins, and L. S. Rothman. Total internal partition sums for molecules in the terrestrial atmosphere. *Journal of Molecular Structure*, 517:407–425, 2000.

[17] A. A. Michelson. Interference phenomena in a new form of refractometer. *Philosophical Magazine*, 13(81):236–242, 1882.

[18] R. J. Bell. CHAPTER ONE – Fourier Transform Spectroscopy. In *Introductory Fourier Transform Spectroscopy*, pages 1–15. 1972.

[19] S. P. Davis, M. C. Abrams, and J. W. (James W.) Brault. *Fourier transform spectrometry*. Academic Press, 2001.

[20] F. Hase, T. Blumenstock, and C. Paton-Walsh. Analysis of the Instrumental Line Shape of High-Resolution Fourier Transform IR Spectrometers with Gas Cell Measurements and New Retrieval Software. *Applied Optics*, 38(15):3417, 1999.

[21] K. Sung, R. A. Toth, L. R. Brown, and T. J. Crawford. Line strength measurements of carbonyl sulfide ($^{16}O^{12}C^{32}S$) in the $2\nu3$, $\nu1+2\nu2+\nu3$, and $4\nu2+\nu3$ bands. *Journal of Quantitative Spectroscopy and Radiative Transfer*, 110(18):2082–2101, 2009.

[22] A. Jenouvrier, L. Daumont, L. Régalia-Jarlot, V. G. Tyuterev, M. Carleer, A. C. Vandaele, S. Mikhailenko, and S. Fally. Fourier transform measurements of water vapor line parameters in the 4200–6600 cm^{-1} region. *Journal of Quantitative Spectroscopy and Radiative Transfer*, 105(2):326–355, 2007.

[23] R. A. Toth. Measurements of positions, strengths and self-broadened widths of H_2O from 2900 to 8000 cm^{-1}: line strength analysis of the 2nd triad bands. *Journal of Quantitative Spectroscopy and Radiative Transfer*, 94(1):51–107, 2005.

[24] J. U. White. Long optical paths of large aperture. *J. Opt. Soc. Am.*, 32(5):285–288, 1942.

[25] Yu.N. Ponomarev, A.A. Solodov, A.M. Solodov, T.M. Petrova, and O.V. Naumenko. FTIR spectrometer with 30 m optical cell and its applications to the sensitive measurements of selective and nonselective absorption spectra. *Journal of Quantitative Spectroscopy and Radiative Transfer*, 177:253–260, 2016.

[26] J. S. Bhosale. High signal-to-noise fourier transform spectroscopy with light emitting diode sources. *Review of Scientific Instruments*, 82(12):129903, 2011.

[27] V.I. Serdyukov, L.N. Sinitsa, and S.S. Vasil'chenko. Highly sensitive Fourier transform spectroscopy with LED sources. *Journal of Molecular Spectroscopy*, 290:13–17, 2013.

[28] X. Chao, J. B. Jeffries, and R. K. Hanson. Absorption sensor for CO in combustion gases using 2.3 μm tunable diode lasers. *Measurement Science and Technology*, 20(11):115201, nov 2009.

[29] C. Wang and P. Sahay. Breath analysis using laser spectroscopic techniques: Breath biomarkers, spectral fingerprints, and detection limits. *Sensors*, 9(10):8230, 2009.

[30] R. Chaux and B. Lavorel. Relative line intensity measurement in absorption spectra using a tunable diode laser at 1.6μm: application to the determination of $^{13}CO_2/^{12}CO_2$ isotope ratio. *Applied Physics B*, 72(2):237–240, 2001.

[31] E. D. Hinkley. High-resolution infrared spectroscopy with a tunable dione laser. *Applied Physics Letters*, 16(9):351, 1970.

[32] V. Zeninari, B. Parvitte, L. Joly, T. Le Barbu, N. Amarouche, and G. Durry. Laboratory spectroscopic calibration of infrared tunable laser spectrometers for the in situ sensing of the Earth and Martian atmospheres. *Applied Physics B: Lasers and Optics*, 85(2-3):265–272, 2006.

[33] D. R. Herriott and H. J. Schulte. Folded optical delay lines. *Appl. Opt.*, 4(8):883–889, 1965.

[34] J. B. McManus, M. S. Zahniser, and D. D. Nelson. Dual quantum cascade laser trace gas instrument with astigmatic Herriott cell at high pass number. *Appl. Opt.*, 50(4):A74—-A85, 2011.

[35] X. Zhu and D. T. Cassidy. Modulation spectroscopy with a semiconductor diode laser by injection-current modulation. *J. Opt. Soc. Am. B*, 14(8):1945–1950, 1997.

[36] J. B. McManus, P. L. Kebabian, and M. S. Zahniser. Astigmatic mirror multipass absorption cells for long-path-length spectroscopy. *Appl. Opt.*, 34(18):3336–3348, 1995.

[37] J. C. Nicolas, A. N. Baranov, Y. Cuminal, Y. Rouillard, and C. Alibert. Tunable diode laser absorption spectroscopy of carbon monoxide around 2.35 microm. *Applied optics*, 37(33):7906–7911, 1998.

[38] O. Svelto. *Principles of lasers*. 2010.

[39] U. W. Hochstrasser. Orthogonal polynomials. In M. Abramowitz and I. A. Stegun, editors, *Handbook of mathematical functions with formulas, graphs, and mathematical tables*, pages 773–792. National Bureau of Standards, 1964.

[40] V. P. Bykov and O. O. Silichev. *Laser Resonators*. Physmathlit, Moscow, 2004.

[41] F. Dominek. A diagram of stability of an optical resonator. https://commons.wikimedia.org/wiki/File:Laser_resonator_stability.svg, 2007.

[42] J. Ye, L. S. Ma, and J. L. Hall. Ultrasensitive detections in atomic and molecular physics: demonstration in molecular overtone spectroscopy. *Journal of the Optical Society of America B*, 15(1):6–15, 1998.

[43] L. A. Pakhomycheva and E. A. Sviridenkov. Line structure of generation spectra of lasers with inhomogeneous broadening of the amplification line. *JETP Letters*, 12(2):60–3, 1970.

[44] D. Romanini. Cavity-Ringdown Spectroscopy versus Intra-Cavity Laser Absorption. In *Cavity-Ringdown Spectroscopy*, chapter 9, pages 125–145. 1999.

[45] V. M. Baev, T. Latz, and P. E. Toschek. Laser intracavity absorption spectroscopy. *Applied Physics B*, 69(3):171–202, 1999.

[46] A. Campargue, F. Stoeckel, and M. Chenevier. High sensitivity intracavity laser spectroscopy: applications to the study of overtone transitions in the visible range. *Spectrochimica Acta Rev.*, 13(1):69–88, 1990.

[47] A. Garnache, A. Liu, L. Cerutti, and A. Campargue. Intracavity laser absorption spectroscopy with a vertical external cavity surface emitting laser at 2.3–μm: Application to water and carbon dioxide. *Chemical Physics Letters*, 416(1):22–27, 2005.

[48] B. J. Orr and Y. He. 6 – Cavity-based absorption spectroscopy techniques. In *Laser Spectroscopy for Sensing*, pages 167–207. 2014.

[49] D. Romanini. *Cavity-Enhanced Spectroscopy and Sensing*, volume 179. 2014.

[50] Ph. Laurent, A. Clairon, and Ch. Breant. Frequency noise analysis of optically self-locked diode lasers. *IEEE Journal of Quantum Electronics*, 25(6):1131–1142, 1989.

[51] P. Čermák. *Spectroscopie optique de haute sensibliité dans les plasmas et les gazes*. Phd, Thèse de Doctorat, Université de Grenoble, 2010.

[52] I. Ventrillard, D. Romanini, D. Mondelain, and A. Campargue. Accurate measurements and temperature dependence of the water vapor self-continuum absorption in the 2.1 μm atmospheric window. *Journal of Chemical Physics*, 143(13):1–10, 2015.

[53] D. Romanini, M. Chenevier, S. Kassi, M. Schmidt, C. Valant, M. Ramonet, J. Lopez, and H. J. Jost. Optical-feedback cavity-enhanced absorption: A compact spectrometer for real-time measurement of atmospheric methane. *Applied Physics B: Lasers and Optics*, 83(4):659–667, 2006.

[54] A. O'Keefe and D. A. G. Deacon. Cavity ring-down optical spectrometer for absorption measurements using pulsed laser sources. *Review of Scientific Instruments*, 59(12):2544, 1988.

[55] D. Romanini, A. A. Kachanov, N. Sadeghi, and F. Stoeckel. CW cavity ring down spectroscopy. *Chemical Physics Letters*, 264(3):316–322, 1997.

[56] D. Romanini, A. A. Kachanov, and F. Stoeckel. Diode laser cavity ring down spectroscopy. *Chemical Physics Letters*, 270(5):538–545, 1997.

[57] D. Romanini, A.A. Kachanov, and F. Stoeckel. Cavity ringdown spectroscopy: broad band absolute absorption measurements. *Chemical Physics Letters*, 270(5):546–550, 1997.

[58] G. Berden and R. Engeln, editors. *Cavity ring-down spectroscopy: Techniques and Applications*. 2009.

[59] S. Kassi and A. Campargue. Cavity ring down spectroscopy with 5×10^{-13} cm^{-1} sensitivity. *Journal of Chemical Physics*, 137(23), 2012.

[60] C. Bray, A. Pailloux, and S. Plumeri. Tritiated water detection in the 2.17 μm spectral region by cavity ring down spectroscopy. *Nuclear Instruments and Methods in Physics Research Section A: Accelerators, Spectrometers, Detectors and Associated Equipment*, 789:43–49, 2015.

[61] S. Kassi, M. Chenevier, L. Gianfrani, A. Salhi, Y. Rouillard, A. Ouvrard, and D. Romanini. Looking into the volcano with a Mid-IR DFB diode laser and Cavity Enhanced Absorption Spectroscopy. *Optics Express*, 14(23):11442–11452, 2006.

[62] D. Zhao, J. Guss, A. J. Walsh, and H. Linnartz. Mid-infrared continuous wave cavity ring-down spectroscopy of a pulsed hydrocarbon plasma. *Chemical Physics Letters*, 565:132–137, 2013.

[63] K. Iga and F. Koyama. Surface emitting lasers. *Semiconductor Lasers II: Materials and Structures*, 82(10):70–82, 1999.

[64] A. Ouvrard, A. Garnache, L. Cerutti, F. Genty, and D. Romanini. Single-frequency tunable Sb-based VCSELs emitting at 2.3 μm. *IEEE Photonics Technology Letters*, 17(10):2020–2022, 2005.

[65] L. Cerutti, A. Garnache, A. Ouvrard, and F. Genty. High temperature continuous wave operation of Sb-based vertical external cavity surface emitting laser near 2.3μm. *Journal of Crystal Growth*, 268(1):128–134, 2004.

[66] A. Garnache, A. Ouvrard, and D. Romanini. Single-Frequency operation of External-Cavity VCSELs: Non-linear multimode temporal dynamics and quantumlimit. *Optics Express*, 15(15):9403–9417, 2007.

[67] M. Triki, P. Čermák, L. Cerutti, A. Garnache, and D. Romanini. Extended continuous tuning of a single-frequency diode-pumped vertical-external-cavity surface-emitting laser at 2.3 μm. *IEEE Photonics Technology Letters*, 20(23):1947–1949, Dec 2008.

[68] K. Petermann. *Laser Diode Modulation and Noise*. Kluwer Academic Publishers, 1988.

[69] P. Čermák, B. Chomet, L. Ferrieres, S. Vasilchenko, D. Mondelain, S. Kassi, A. Campargue, S. Denet, V. Lecocq, M. Myara, L. Cerutti, and A. Garnache. CRDS with a VECSEL for broad-band high sensitivity spectroscopy in the 2.3 μm window. *Review of Scientific Instruments*, 87(8):083109, aug 2016.

[70] A. Salhi, D. Barat, D. Romanini, Y. Rouillard, A. Ouvrard, R. Werner, J. Seufert, J. Koeth, A. Vicet, and A. Garnache. Single-frequency Sb-based distributed-feedback lasers emitting at 2.3 μm above room temperature for application in tunable diode laser absorption spectroscopy. *Appl. Opt.*, 45(20):4957–4965, 2006.

[71] G. D. Domenico, S. Schilt, and P. Thomann. Simple approach to the relation between laser frequency noise and laser line shape. *Appl. Opt.*, 49(25):4801–4807, sep 2010.

[72] J.-L. Teffo, O.N. Sulakshina, and V.I. Perevalov. Effective Hamiltonian for rovibrational energies and line intensities of carbon dioxide. *Journal of Molecular Spectroscopy*, 156(1):48–64, 1992.

[73] S.A. Tashkun, V.I. Perevalov, J.L. Teffo, L.S. Rothman, and Vl.G. Tyuterev. Global fitting of $^{12}C^{16}O_2$ vibrational-rotational line positions using the effective Hamiltonian approach. *Journal of Quantitative Spectroscopy and Radiative Transfer*, 60(5):785–801, 1998.

[74] Q. Lin, M. A. Van Camp, H. Zhang, B. Jelenković, and V. Vuletić. Long-external-cavity distributed bragg reflector laser with subkilohertz intrinsic linewidth. *Opt. Lett.*, 37(11):1989–1991, Jun 2012.

[75] G. C. Wick. The spectrum of rotation–vibration of the molecule HD. *Atti della Accademia Nazionale dei Lincei, Classe di Scienze Fisiche, Matematiche e Naturali, Rendiconti*, 21:708–14, 1935.

[76] G. Herzberg. Rotation–Vibration Spectrum of the HD Molecule. *Nature*, (166):563, 1950.

[77] R. A. Durie and G. Herzberg. Forbidden transitions in diatomic molecules: V. The rotation–vibration spectrum of the hydrogen–deuteride (HD) molecule. *Canadian Journal of Physics*, 38(6):806–818, jun 1960.

[78] L. Wolniewicz. Nonadiabatic energies of the ground state of the hydrogen molecule. *The Journal of Chemical Physics*, 103(5):1792–1799, aug 1995.

[79] K. Pachucki and J. Komasa. Electric dipole rovibrational transitions in the HD molecule. *Physical Review A*, 78(5):052503, nov 2008.

[80] K. Pachucki and J. Komasa. Rovibrational levels of HD. *Physical Chemistry Chemical Physics*, 12(32):9188–9196, 2010.

[81] K. Pachucki. Born-Oppenheimer potential for H 2. *Physical Review A*, 82(3):032509, sep 2010.

[82] A. Campargue, S. Kassi, K. Pachucki, and J. Komasa. The absorption spectrum ofH_2: CRDS measurements of the (2–0) band, review of the literature data and accurate ab initio line list up to 35 000 cm^{-1}. *Physical Chemistry Chemical Physics*, 14(2):802–815, 2012.

[83] S.-M. Hu, H. Pan, C.-F. Cheng, Y. R. Sun, X.-F. Li, J. Wang, A. Campargue, and A.-W. Liu. The $\nu = 3 \leftarrow 0$ S(0)–S(3) Electric Quadrupole Transitions ofH_2 near 0.8 μm. *The Astrophysical Journal*, 749(1):76, 2012.

[84] E. J. Salumbides, G. D. Dickenson, T. I. Ivanov, and W. Ubachs. QED effects in molecules: test on rotational quantum states ofH_2. *Physical review letters*, 107(4):043005, jul 2011.

[85] G. D. Dickenson, M. L. Niu, E. J. Salumbides, J. Komasa, K. S. E. Eikema, K. Pachucki, and W. Ubachs. Fundamental vibration of molecular hydrogen. *Physical review letters*, 110(19):193601, may 2013.

[86] C.-F. Cheng, Y. R. Sun, H. Pan, J. Wang, A.-W. Liu, A. Campargue, and S.-M. Hu. Electric–quadrupole transition of H2 determined to 10^{-9} precision. *Physical Review A*, 85(2):024501, feb 2012.

[87] S. Kassi and A. Campargue. Electric quadrupole transitions and collision-induced absorption in the region of the first overtone band ofH_2 near 1.25 μm. *Journal of Molecular Spectroscopy*, 300:55–59, 2014.

[88] D. Mondelain, S. Kassi, T. Sala, D. Romanini, D. Gatti, and A. Campargue. Sub-MHz accuracy measurement of the S(2) 2–0 transition frequency of D_2 by Comb-Assisted Cavity Ring Down spectroscopy. *Journal of Molecular Spectroscopy*, 326:5–8, 2016.

[89] P. Wcisło, H. Tran, S. Kassi, A. Campargue, F. Thibault, and R. Ciuryło. Velocity-changing collisions in pure H_2 and H_2-Ar mixture. *The Journal of Chemical Physics*, 141(7):74301, aug 2014.

[90] P. Wcisło, I. E. Gordon, H. Tran, Y. Tan, S.-M. Hu, A. Campargue, S. Kassi, D. Romanini, C. Hill, R. V. Kochanov, and L. S. Rothman. The implementation of non-Voigt line profiles in the HITRAN database: H_2 case study. *Journal of Quantitative Spectroscopy and Radiative Transfer*, 177:75–91, 2016.

[91] M. Abel, L. Frommhold, X. Li, and K. L. C. Hunt. Collision-induced absorption by H_2 pairs: From hundreds to thousands of Kelvin. *The Journal of Physical Chemistry A*, 115(25):6805–6812, jun 2011.

[92] A. R. W. McKellar. The collision-induced first-overtone band of hydrogen at low temperature. *Canadian Journal of Physics*, 66(2):155–158, feb 1988.

[93] Y. Tan, J. Wang, C.-F. Cheng, X.-Q. Zhao, A.-W. Liu, and S.-M. Hu. Cavity ring-down spectroscopy of the electric quadrupole transitions of H_2 in the 784–852 nm region. *Journal of Molecular Spectroscopy*, 300:60–64, 2014.

[94] N. H. Rich, J. W. C. Johns, and A. R. W. McKellar. Frequency and intensity measurements in the fundamental infrared band of HD. *Journal of Molecular Spectroscopy*, 95(2):432–438, 1982.

[95] A. R. W. McKellar. Intensities of the dipole and quadrupole rotation-vibration spectra of HD. *Canadian Journal of Physics*, 52(13):1144–1151, jul 1974.

[96] A. R. W. McKellar. Interference effects in the spectrum of HD: VI: HD–HD, and HD–Kr at room temperature. *Canadian Journal of Physics*, 72(5-6):215–224, may 1994.

[97] A. R. W. McKellar, W. Goetz, and D.A. Ramsay. The rotation-vibration spectrum of HD – Wavelength and intensity measurements of the 3–0, 4–0, 5–0, and 6-0 electric dipole bands. *Astrophysical Journal*, 207:663–670, July 1976.

[98] L. Ulivi, P. de Natale, and M. Inguscio. Pure rotational spectrum of hydrogen deuteride by far-infrared Fourier transform spectroscopy. *Astrophysical Journal, Part 2 – Letters*, 378:L29–L31, September 1991.

[99] B. J. Drouin, S. Yu, J. C. Pearson, and H. Gupta. Terahertz spectroscopy for space applications: 2.5–2.7 thz spectra of hd, H_2O and NH_3. *Journal of Molecular Structure*, 1006(1):2–12, 2011.

[100] S. Vasilchenko, D. Mondelain, S. Kassi, P. Čermák, B. Chomet, A. Garnache, S. Denet, V. Lecocq, and A. Campargue. The HD spectrum near 2.3 μm by CRDS-VECSEL: Electric quadrupole transition and collision-induced absorption, 2016.

[101] S. Kassi and A. Campargue. Electric quadrupole and dipole transitions of the first overtone band of HD by CRDS between 1.45 and 1.33 μm. *Journal of Molecular Spectroscopy*, 267(1):36–42, 2011.

[102] T. Lin, C.-C. Chou, D.-J. Lwo, and J.-T. Shy. Absorption spectrum of the P(5) transition of the first overtone band of HD. *Physical Review A*, 61(6):064502, may 2000.

[103] A. Watanabe, J. L. Hunt, and H. L. Welsh. Structure of the pressure-induced infrared spectrum of hydrogen in the first overtone region. *Canadian Journal of Physics*, 49(7):860–863, apr 1971.

[104] C. Brodbeck, J.-P. Bouanich, Nguyen V.-T., Y. Fu, and A. Borysow. Collision-induced absorption by H_2 pairs in the second overtone band at 298 and 77.5 K: Comparison between experimental and theoretical results. *The Journal of Chemical Physics*, 110(10):4750–4756, feb 1999.

[105] A. Borysow, J. Borysow, and Y. Fu. Semi–empirical model of collision–induced absorption spectra of H_2–H_2 complexes in the second overtone band of hydrogen at temperatures from 50 to 500 K. *Icarus*, 145(2):601–608, 2000.

[106] A. Borysow, U. G. Jørgensen, and Y. Fu. High-temperature (1000–7000 K) collision-induced absorption of H_2 pairs computed from the first principles, with

application to cool and dense stellar atmospheres. *Journal of Quantitative Spectroscopy and Radiative Transfer*, 68(3):235–255, 2001.

[107] A. S. Pine and T. Gabard. Multispectrum fits for line mixing in the ν_3 band Q branch of methane. *Journal of Molecular Spectroscopy*, 217(1):105–114, 2003.

[108] H. Tran, J.-M. Hartmann, F. Chaussard, and M. Gupta. An isolated line–shape model based on the Keilson–Storer function for velocity changes. II. Molecular dynamics simulations and the Q(1) lines for pure H_2. *The Journal of Chemical Physics*, 131(15):154303, oct 2009.

[109] M. Wojdyr. Fityk: a general–purpose peak fitting program. *Journal of Applied Crystallography*, 43(5):1126–1128, sep 2010.

[110] M. Nelkin and A. Ghatak. Simple binary collision model for van hove's $G_s(r,t)$. *Phys. Rev.*, 135:A4–A9, Jul 1964.

[111] J. M. Hartmann, C. Boulet, and D. Robert. *Collisional Effects on Molecular Spectra: Laboratory experiments and models, consequences for applications.* Elsevier, 2008.

[112] L. Wolniewicz A. Dalgarno and I. Simbotin. Quadrupole Transition Probabilities for the Excited Rovibrational States of H_2. *The Astrophysical Journal Supplement Series*, 115(2):293, 1998.

[113] R. J. Le Roy, Y. Huang, and C. Jary. An accurate analytic potential function for ground-state N_2 from a direct-potential–fit analysis of spectroscopic data. *The Journal of Chemical Physics*, 125(16):164310, oct 2006.

[114] H. Li and R. J. Le Roy. Quadrupole moment function and absolute infrared quadrupolar intensities for N_2. *The Journal of Chemical Physics*, 126(22):224301, jun 2007.

[115] D. Reuter, D. E. Jennings, and J. W. Brault. The $\nu = 1 \leftarrow 0$ quadrupole spectrum of N_2. *Journal of Molecular Spectroscopy*, 115(2):294–304, 1986.

[116] S. Kassi, I. E. Gordon, and A. Campargue. First detection of transitions in the second quadrupole overtone band of nitrogen near 1.44 μm by CW-CRDS with 6×10^{-13} cm^{-1} sensitivity. *Chemical Physics Letters*, 582:6–9, 2013.

[117] A. Goldman, J. Reid, and L. S. Rothman. Identification of electric quadrupole O_2 and N_2 lines in the infrared atmospheric absorption spectrum due to the vibration-rotation fundamentals. *Geophysical Research Letters*, 8(1):77–78, jan 1981.

[118] C. Camy-Peyret, J.-M. Flaud, L. Delbouille, G. Roland, J. W. Brault, and L. Testerman. Quadrupole transitions of the $1 \leftarrow 0$ band of N_2 observed in a high resolution atmospheric spectrum. *Journal de Physique Lettres*, 42(13):279–283, 1981.

[119] C. P. Rinsland, R. Zander, A. Goldman, F. J. Murcray, D. G. Murcray, M. R. Gunson, and C. B. Farmer. The fundamental quadrupole band of $^{14}N_2$: Line positions from high-resolution stratospheric solar absorption spectra. 148(1):274–279, 1991.

[120] J. Tennyson, P. F. Bernath, A. Campargue, A. G. Császár, L. Daumont, R. R. Gamache, J. T. Hodges, D. Lisak, O. V. Naumenko, L. S. Rothman, H. Tran, J.-M. Hartmann, N. F. Zobov, J. Buldyreva, C. D. Boone, M.-D. De Vizia, L. Gianfrani, R. McPheat, D. Weidmann, J. Murray, N. H. Ngo, and O. L. Polyansky. Recommended isolated-line profile for representing high-resolution spectroscopic transitions (IUPAC technical report). *Pure and Applied Chemistry*, 86(12):1931–1943, 2014.

[121] D. Mondelain, S. Vasilchenko, P. Čermák, S. Kassi, and a. Campargue. The self- and foreign-absorption continua of water vapor by cavity ring-down spectroscopy near 2.35 μm. *Phys. Chem. Chem. Phys.*, pages 1–18, 2015.

[122] A. Campargue, S. Kassi, D. Mondelain, S. Vasilchenko, and D. Romanini. Accurate laboratory determination of the near-infrared water vapor self-continuum: A test of the MT_CKD model. *Journal of Geophysical Research: Atmospheres*, 121(21):13,180–13,203, 2016.

[123] A. Campargue, S. N. Mikhailenko, S. Vasilchenko, C. Reynaud, S. Béguier, P. Čermák, D. Mondelain, S. Kassi, and D. Romanini. The absorption spectrum of water vapor in the 2.2–μm transparency window: High sensitivity measurements and spectroscopic database. *Journal of Quantitative Spectroscopy and Radiative Transfer*, 189:407–416, 2017.

[124] J. Cihelka, I. Matulková, and S. Civiš. Laser diode photoacoustic and FTIR laser spectroscopy of formaldehyde in the 2.3 μm and 3.5 μm spectral range. *Journal of Molecular Spectroscopy*, 256(1):68–74, 2009.

[125] J.-M. Flaud, W. J. Lafferty, R. L. Sams, and S. W. Sharpe. High resolution spectroscopy of $H^{12}_2C^{16}O$ in the 1.9 to 2.56 μm spectral range. *Molecular Physics*, 104(12):1891–1903, 2006.

[126] D. W. Schwenke and H. Partridge. Convergence testing of the analytic representation of an ab initio dipole moment function for water: Improved fitting

yields improved intensities. *The Journal of Chemical Physics*, 113(16):6592–6597, 2000.

[127] H. Partridge and D. W. Schwenke. The determination of an accurate isotope dependent potential energy surface for water from extensive ab initio calculations and experimental data. *The Journal of Chemical Physics*, 106(11):4618–4639, 1997.

[128] J. Tennyson, P. F. Bernath, L. R. Brown, A. Campargue, M. R. Carleer, A. G Császár, R. R Gamache, J. T. Hodges, A. Jenouvrier, O. V. Naumenko, O. L. Polyansky, L. S. Rothman, R. A. Toth, A. C. Vandaele, N. F. Zobov, L. Daumont, A. Z. Fazliev, T. Furtenbacher, I. E. Gordon, S. N. Mikhailenko, and S. V. Shirin. IUPAC critical evaluation of the rotational-vibrational spectra of water vapor. Part I – Energy levels and transition wavenumbers for $H_2{}^{17}O$ and $H_2{}^{18}O$. *Journal of Quantitative Spectroscopy and Radiative Transfer*, 110(9–10):573–596, 2009.

[129] J. Tennyson, P. F. Bernath, L. R. Brown, A. Campargue, A. G. Császár, L. Daumont, R. R. Gamache, J. T. Hodges, O. V. Naumenko, O. L. Polyansky, L. S. Rothman, R. A. Toth, A. C. Vandaele, N. F. Zobov, S. Fally, A. Z. Fazliev, T. Furtenbacher, I. E Gordon, S.-M. Hu, S. N Mikhailenko, and B. A. Voronin. IUPAC critical evaluation of the rotational-vibrational spectra of water vapor. Part II: Energy levels and transition wavenumbers for $HD^{16}O$, $HD^{17}O$, and $HD^{18}O$. *Journal of Quantitative Spectroscopy and Radiative Transfer*, 111(15):2160–2184, 2010.

[130] J. Tennyson, P. F. Bernath, L. R. Brown, A. Campargue, A. G. Császár, L. Daumont, R. R. Gamache, J. T. Hodges, O. V. Naumenko, O. L. Polyansky, L. S. Rothman, A. C. Vandaele, N. F. Zobov, A. R. A. Derzi, C. Fábri, A. Z. Fazliev, T. Furtenbacher, I. E. Gordon, L. Lodi, and I. I. Mizus. IUPAC critical evaluation of the rotational-vibrational spectra of water vapor, Part III: Energy levels and transition wavenumbers for $H_2{}^{16}O$. *Journal of Quantitative Spectroscopy and Radiative Transfer*, 117:29–58, 2013.

[131] J. Loos, M. Birk, and G. Wagner.

[132] S. N. Mikhailenko, Vl. G. Tyuterev, V. I. Starikov, K. K. Albert, B. P. Winnewisser, M. Winnewisser, G. Mellau, C. Camy-Peyret, R. Lanquetin, J.-M. Flaud, and J. W. Brault. Water Spectra in the Region 42006250 cm^{-1}, Extended Analysis of $\nu_1+\nu_2$, $\nu_2+\nu_3$, and $3\nu_2$ Bands and Confirmation of Highly Excited States from Flame Spectra and from Atmospheric Long-Path Observations. *Journal of Molecular Spectroscopy*, 213(2):91–121, 2002.

[133] R. A. Toth. Line list of water vapor parameters from 500 to 8000 cm^{-1}.

[134] I. I. Bubukina, N. F. Zobov, O. L. Polyansky, S. V. Shirin, and S. N. Yurchenko. Optimized semiempirical potential energy surface for $H_2{}^{16}O$ up to 26000 cm^{-1}. *Optics and Spectroscopy*, 110(2):160–166, 2011.

[135] S. N. Mikhailenko, A. Keppler Albert, G. Mellau, S. Klee, B. P. Winnewisser, M. Winnewisser, and Vl. G. Tyuterev. Water vapor absorption line intensities in the 1900–6600 cm^{-1} region. *Journal of Quantitative Spectroscopy and Radiative Transfer*, 109(16):2687–2696, 2008.

[136] L. Lodi, J. Tennyson, and O. L. Polyansky. A global, high accuracy ab initio dipole moment surface for the electronic ground state of the water molecule. *The Journal of Chemical Physics*, 135(3):34113, 2011.

[137] L. Lodi and J. Tennyson. Line lists for $H_2{}^{18}O$ and $H_2{}^{17}O$ based on empirical line positions and ab initio intensities. *Journal of Quantitative Spectroscopy and Radiative Transfer*, 113(11):850–858, 2012.

[138] R. J. Barber, J. Tennyson, G. J. Harris, and R. N. Tolchenov. A high-accuracy computed water line list. *Monthly Notices of the Royal Astronomical Society*, 368(3):1087, 2006.

[139] B. A. Voronin, J. Tennyson, R. N. Tolchenov, A. A. Lugovskoy, and S. N. Yurchenko. A high accuracy computed line list for the HDO molecule. *Monthly Notices of the Royal Astronomical Society*, 402(1):492, 2010.

[140] S. V. Shirin, N. F. Zobov, R. I. Ovsyannikov, O. L. Polyansky, and J. Tennyson. Water line lists close to experimental accuracy using a spectroscopically determined potential energy surface for $H_2{}^{16}O$, $H_2{}^{17}O$, and $H_2{}^{18}O$. *The Journal of Chemical Physics*, 128(22):224306, 2008.

[141] O. L. Polyansky, R. I. Ovsyannikov, A. A. Kyuberis, L. Lodi, J. Tennyson, and N. F. Zobov. Calculation of rotation-ribration energy levels of the water molecule with near-experimental accuracy based on an ab initio potential energy surface. *The Journal of Physical Chemistry A*, 117(39):9633–9643, 2013.

[142] I.E. Gordon. Private comunication.

[143] O. Leshchishina, S. N. Mikhailenko, D. Mondelain, S. Kassi, and A. Campargue. An improved line list for water vapor in the 1.5 μm transparency window by highly sensitive CRDS between 5852 and 6607 cm^{-1}. *Journal of Quantitative Spectroscopy and Radiative Transfer*, 130:69–80, 2013.

[144] A.-W. Liu, J.-H. Du, K.-F. Song, L. Wang, L. Wan, and S.-M. Hu. High-resolution Fourier-transform spectroscopy of ^{18}O-enriched water molecule in the 1080–7800 cm^{-1} region. *Journal of Molecular Spectroscopy*, 237(2):149–162, 2006.

[145] S. Mikhailenko, S. Kassi, L. Wang, and A. Campargue. The absorption spectrum of water in the 1.25 μm transparency window (7408–7920 cm^{-1}). *Journal of Molecular Spectroscopy*, 269(1):92–103, 2011.

[146] A. Campargue, S. N. Mikhailenko, B. G. Lohan, E. V. Karlovets, D. Mondelain, and S. Kassi. The absorption spectrum of water vapor in the 1.25 μm atmospheric window (7911–8337 cm^{-1}). *Journal of Quantitative Spectroscopy and Radiative Transfer*, 157:135–152, 2015.

[147] S. N. Mikhailenko, S. Kassi, D. Mondelain, R. R. Gamache, and A. Campargue. A spectroscopic database for water vapor between 5850 and 8340 cm^{-1}. *Journal of Quantitative Spectroscopy and Radiative Transfer*, 179:198–216, 2016.

[148] T. Nakajima and M. D. King. Determination of the optical thickness and effective particle radius of clouds from reflected solar radiation measurements. Part I: Theory. *Journal of the Atmospheric Sciences*, 47(15):1878–1893, aug 1990.

[149] I. V. Ptashnik, R. A. McPheat, K. P. Shine, K. M. Smith, and R. G. Williams. Water vapor self-continuum absorption in near-infrared windows derived from laboratory measurements. *Journal of Geophysical Research Atmospheres*, 116(16):1–16, 2011.

[150] D. Paynter and V. Ramaswamy. Variations in water vapor continuum radiative transfer with atmospheric conditions. *Journal of Geophysical Research: Atmospheres*, 117(D16):n/a–n/a, aug 2012.

[151] H. Rubens and E. Aschkinass. Beobachtungen über Absorption und Emission von Wasserdampf und Kohlensäure im ultrarothen Spectrum. *Annalen der Physik*, 300(3):584–601, 1898.

[152] G. Hettner. Über das ultrarote Absorptionsspektrum des Wasserdampfes. *Annalen der Physik*, 360(6):476–496, 1918.

[153] J. T. Kiehl and K. E. Trenberth. Earth's annual global mean energy budget. *Bulletin of the American Meteorological Society*, 78(2):197–208, feb 1997.

[154] I. M Held and B. J. Soden. Water vapor feedback and global warming. *Annu. Rev. Energy Environ.*, 25:441–75, 2000.

[155] I. V. Ptashnik, R. A McPheat, K. P. Shine, K. M. Smith, and R. G. Williams. Water vapour foreign-continuum absorption in near-infrared windows from laboratory measurements. *Philosophical Transactions of the Royal Society A: Mathematical, Physical and Engineering Sciences*, 370(1968):2557 LP – 2577, apr 2012.

[156] D. J. Paynter and V. Ramaswamy. An assessment of recent water vapor continuum measurements upon longwave and shortwave radiative transfer. *Journal of Geophysical Research*, 116(D20):D20302, oct 2011.

[157] D. Paynter and V. Ramaswamy. Investigating the impact of the shortwave water vapor continuum upon climate simulations using GFDL global models. *Journal of Geophysical Research: Atmospheres*, 119(18):10,720–10,737, sep 2014.

[158] R. K. Kopparapu, R. Ramirez, J. F. Kasting, V. Eymet, T. D. Robinson, S. Mahadevan, R. C. Terrien, S. Domagal-Goldman, V. Meadows, and R. Deshpande. Habitable zones around main-sequence stars: New estimates. *The Astrophysical Journal*, 765(2):131, mar 2013.

[159] J. Leconte, F. Forget, B. Charnay, R. Wordsworth, F. Selsis, E. Millour, and A. Spiga. 3D climate modeling of close-in land planets: Circulation patterns, climate moist bistability, and habitability. *Astronomy & Astrophysics*, 554:A69, jun 2013.

[160] J. Leconte, F. Forget, B. Charnay, R. Wordsworth, and A. Pottier. Increased insolation threshold for runaway greenhouse processes on Earth-like planets. *Nature*, 504(7479):268–71, dec 2013.

[161] K. P Shine, I. V Ptashnik, and G. Rädel. The water vapour continuum: Brief history and recent developments. *Surveys in Geophysics*, 33(3):535–555, 2012.

[162] I.V. Ptashnik. *Continuum absorption of water vaporin band centers of near-infrared region. (In Russian).* PhD thesis, Insitute of Atmospheric optics, 2007.

[163] W. M. Elsasser. Mean absorption and equivalent absorption coefficient of a band spectrum. *Physical Review*, 54(2):126–129, jul 1938.

[164] K. Bignell, F. Saiedy, and P. A. Sheppard. On the atmospheric infrared continuum. *J. Opt. Soc. Am.*, 53(4):466–479, 1963.

[165] S. S. Penner and P. Varanasi. Spectral absorption coefficients in the pure rotation spectrum of water vapor. *Journal of Quantitative Spectroscopy and Radiative Transfer*, 7(4):687–690, jul 1967.

[166] P. Varanasi, S. Chou, and S. S. Penner. Absorption coefficients for water vapor in the 600–1000 cm^{-1} region. *Journal of Quantitative Spectroscopy and Radiative Transfer*, 8(8):1537–1541, aug 1968.

[167] J. H. McCoy, D. B. Rensch, and R. K. Long. Water vapor continuum absorption of carbon dioxide laser radiation near 10 μm. *Appl. Opt.*, 8(7):1471–1478, 1969.

[168] K. J. Bignell. The water-vapour infra-red continuum. *Quarterly Journal of the Royal Meteorological Society*, 96(409):390–403, jul 1970.

[169] Q. Ma and R. H. Tipping. A far wing line shape theory and its application to the water continuum absorption in the infrared region. I. *The Journal of Chemical Physics*, 95(9):6290–6301, 1991.

[170] S. D. Tvorogov and O. B. Rodimova. Spectral line shape. I. Kinetic equation for arbitrary frequency detunings. *The Journal of Chemical Physics*, 102(22):8736–8745, 1995.

[171] Q. Ma, R. H. Tipping, and C. Leforestier. Temperature dependences of mechanisms responsible for the water-vapor continuum absorption. I. Far wings of allowed lines. *The Journal of Chemical Physics*, 128(12):124313, 2008.

[172] E. J. Mlawer, V. H. Payne, J.-L. Moncet, J. S. Delamere, M. J. Alvarado, and D. C. Tobin. Development and recent evaluation of the MT_CKD model of continuum absorption. *Philosophical transactions. Series A, Mathematical, physical, and engineering sciences*, 370(1968):2520–56, jun 2012.

[173] D. E. Burch and R. L. Alt. Continuum absorption by H_2O in the 700–1200 cm^{-1} and 2400–2800 cm^{-1} windows. Technical report, May 1984.

[174] S. A. Clough, F. X. Kneizys, and R. W. Davies. Line shape and the water vapor continuum. *Atmospheric Research*, 23:229–241, 1989.

[175] D. E. Burch. Continuum absorption by H_2O.Technical report AFGL-TR-81-0300. Air Force Geophysical Laboratory. Technical report, May 1982.

[176] K. P. Shine, A. Campargue, D. Mondelain, R. A. McPheat, I. V. Ptashnik, and D. Weidmann. The water vapour continuum in near-infrared windows – Current understanding and prospects for its inclusion in spectroscopic databases. *Journal of Molecular Spectroscopy*, 327:193–208, 2016.

[177] J. G. Cormier, R. Ciurylo, and J. R. Drummond. Cavity ring-down spectroscopy measurements of the infrared water vapor continuum. *The Journal of Chemical Physics*, 116(3):1030–1034, 2002.

[178] S. M. Newman, P. D. Green, I. V. Ptashnik, T. D. Gardiner, M. D. Coleman, R. A McPheat, and K. M. Smith. Airborne and satellite remote sensing of the mid-infrared water vapour continuum. *Philosophical Transactions of the Royal Society of London A: Mathematical, Physical and Engineering Sciences*, 370(1968):2611–2636, 2012.

[179] S. M. S. Costa and K. P. Shine. Outgoing Longwave Radiation due to Directly Transmitted Surface Emission. *Journal of the Atmospheric Sciences*, 69(6):1865–1870, 2012.

[180] D. D. Turner, D. C. Tobin, S. A. Clough, P. D. Brown, R. G. Ellingson, E. J. Mlawer, R. O. Knuteson, H. E. Revercomb, T. R. Shippert, W. L. Smith, and M. W. Shephard. The QME AERI LBLRTM: A Closure Experiment for Downwelling High Spectral Resolution Infrared Radiance. *Journal of the Atmospheric Sciences*, 61(22):2657–2675, 2004.

[181] M. J. Alvarado, V. H. Payne, E. J. Mlawer, G. Uymin, M. W. Shephard, K. E. Cady-Pereira, J. S. Delamere, and J.-L. Moncet. Performance of the Line-By-Line Radiative Transfer Model (LBLRTM) for temperature, water vapor, and trace gas retrievals: recent updates evaluated with IASI case studies. *Atmospheric Chemistry and Physics*, 13(14):6687–6711, jul 2013.

[182] Yu. I. Baranov and W. J. Lafferty. The water-vapor continuum and selective absorption in the 3–5μm spectral region at temperatures from 311 to 363K. *Journal of Quantitative Spectroscopy and Radiative Transfer*, 112(8):1304–1313, 2011.

[183] W. E. Bicknell, S. DiCecca, M. K. Griffin, S. D. Swartz, and A. Flusberg. Search for Low-Absorption Regions in the 1.6- and 2.1-μm Atmospheric Windows. *J. Direct Energy*, 2:151–61, 2006.

[184] S. F. Fulghum and M. M. Tilleman. Interferometric calorimeter for the measurement of water-vapor absorption. *J. Opt. Soc. Am. B*, 8(12):2401–2413, 1991.

[185] I. V. Ptashnik, T. M. Petrova, Yu. N. Ponomarev, K. P. Shine, A. A. Solodov, and A. M. Solodov. Near-infrared water vapour self-continuum at close to room temperature. *Journal of Quantitative Spectroscopy and Radiative Transfer*, 120:23–35, 2013.

[186] I. V. Ptashnik, T. M. Petrova, Yu. N. Ponomarev, A. A. Solodov, and A. M. Solodov. Water vapor continuum absorption in near-IR atmospheric windows. *Atmospheric and Oceanic Optics*, 28(2):115–120, 2015.

[187] D. L. Hartmann, A. M. G. Klein Tank, M. Rusticucci, L. V. Alexander, S. Brönnimann, Y. Charabi, F. J. Dentener, E. J. Dlugokencky, D. R. Easterling, A. Kaplan, B. J. Soden, P. W. Thorne, M. Wild, and P.M. Zhai. Observations: Atmosphere and Surface. In *Climate Change 2013 – The Physical Science Basis: Working Group I Contribution to the Fifth Assessment Report of the Intergovernmental Panel on Climate Change*, pages 159–254. Cambridge University Press, Cambridge, 2014.

[188] J. S. Yoon and S. S. Lee. Calorimetric interferometry using pulsed Ndglass laser for measurement of small absorption coefficient at 1.06 μm. *Applied Physics Letters*, 46(10):913–914, 1985.

[189] R. Thalman, K. J. Zarzana, M. A. Tolbert, and R. Volkamer. Rayleigh scattering cross-section measurements of nitrogen, argon, oxygen and air. *Journal of Quantitative Spectroscopy and Radiative Transfer*, 147:171–177, 2014.

[190] P. Schiebener, J. Straub, J. M. H. Levelt Sengers, and J. S. Gallagher. Refractive index of water and steam as function of wavelength, temperature and density. *Journal of Physical and Chemical Reference Data*, 19(3):677–717, 1990.

[191] V. I. Serdyukov, L. N. Sinitsa, and A. A. Lugovskoi. Influence of gas humidity on the reflection coefficient of multilayer dielectric mirrors. *Appl. Opt.*, 55(17):4763–4768, 2016.

[192] D. Mondelain, A. Aradj, S. Kassi, and A. Campargue. The water vapour self-continuum by CRDS at room temperature in the 1.6 μm transparency window. *Journal of Quantitative Spectroscopy and Radiative Transfer*, 130:381–391, 2013.

[193] D. Mondelain, S. Manigand, S. Kassi, and A. Campargue. Temperature dependence of the water vapor self-continuum by cavity ring-down spectroscopy in the 1.6μm transparency window. *Journal of Geophysical Research: Atmospheres*, 119(9):5625–5639, may 2014.

[194] Yu. I. Baranov and W. J. Lafferty. The water vapour self- and water-nitrogen continuum absorption in the 1000 and 2500 cm^{-1} atmospheric windows. *Philosophical Transactions of the Royal Society of London A: Mathematical, Physical and Engineering Sciences*, 370(1968):2578–2589, 2012.

[195] B. E. Rocher-Casterline, L. C. Ch'ng, A. K. Mollner, and H. Reisler. Communication: Determination of the bond dissociation energy (D_0) of the water dimer, $(H_2O)_2$, by velocity map imaging. *The Journal of Chemical Physics*, 134(21):211101, 2011.

[196] D. Mondelain, S. Vasilchenko, P. Čermák, and A. Campargue S. Kassi. The CO_2 absorption spectrum in the 2.3 μm transparency window by high sensitivity CRDS: (ii) self absorption continuum. *Journal of Quantitative Spectroscopy and Radiative Transfer*, 2016.

[197] S. Vasilchenko, M. Konefal, D. Mondelain, S. Kassi, P. Čermák, S.A. Tashkun, V.I. Perevalov, and A. Campargue. The CO_2 absorption spectrum in the 2.3 μm transparency window by high sensitivity CRDS: (I) Rovibrational lines. *Journal of Quantitative Spectroscopy and Radiative Transfer*, 184:233–240, 2016.

[198] D. V. Titov, H. Svedhem, and F. W. Taylor. The Atmosphere of Venus: Current Knowledge and Future Investigations. *Solar System Update*, pages 87–110, 2006.

[199] Venus and Mars. https://studylib.net/doc/17697401/venus-and-mars-%C2%A9-2011-pearson-education–inc., 2010.

[200] F. W. Taylor, D. Crisp, and B. Bézard. *Near-infrared sounding of the lower atmosphere of Venus. In: Venus II: Geology, Geophysics, Atmosphere, and Solar Wind Environment*. Univ. of Arizona Press, 1997.

[201] C. C. Tsang, C. F. Wilson, J. K. Barstow, P. G. J. Irwin, F. W. Taylor, K. McGouldrick, G. Piccioni, P. Drossart, and H. Svedhem. Correlations between cloud thickness and sub-cloud water abundance on venus. *Geophis. Res. Lett.*, 37:L02202, 2010.

[202] E. Marcq, B. Bézard, P. Drossart, G. Piccioni, J. M. Reess, and F. Henry. Remote sensing of venus lower atmosphere from ground-based ir spectroscopy: Latitudinal and vertical distribution of minor species. *Planet. Space Sci.*, 54:1360–1370, 2006.

[203] J. B. Pollack, J. B. Dalton, D. Grinspoon, R. B. Wattson, R. Freedman, D. Crisp, D. A. Allen, B. Bezard, C. DeBergh, L. P. Giver, Q. Ma, and R. Tipping. Near-Infrared Light from Venus' Nightside: A Spectroscopic Analysis. *Icarus*, 103(1):1–42, 1993.

[204] C. Brodbeck, N. Van-Thanh, J.-P. Bouanich, C. Boulet, A. Jean-Louis, B. Bezard, and C. de Bergh. Measurements of pure CO_2 absorption at high densities near 2.3 μm. *Journal of Geophysical Research*, 96(E2):17497, 1991.

[205] N. I. Moskalenko, Y. A. Ilin, S. N. Parzhin, and L. V. Rodinovon. Pressure-induced ir radiation absorption in atmospheres. *Bull Acad Sci USSR, Atmos Oceanic Phys*, 15:632–7, 1979.

[206] M. V. Tonkov, N. N. Filippov, V. V. Bertsev, J. P. Bouanich, Nguyen Van-Thanh, C. Brodbeck, J. M. Hartmann, C. Boulet, F. Thibault, and R. Le Doucen. Measurements and empirical modeling of pure CO_2 absorption in the 2.3-μm region at room temperature: far wings, allowed and collision-induced bands. *Appl. Opt.*, 35(24):4863–4870, Aug 1996.

[207] J. F. Moore. *Infrared absorption of carbon dioxide at high densities with application to the atmosphere of Venus*. PhD thesis, Goddard Institut for Space Studies, Columbia University, 1971.

[208] M. Snels, S. Stefani, G. Piccioni, and B. Bèzard. Carbon dioxide absorption at high densities in the 1.18 μm nightside transparency window of venus. *Journal of Quantitative Spectroscopy and Radiative Transfer*, 133:464–471, 2014.

[209] H. Tran, C. Boulet, S. Stefani, M. Snels, and G. Piccioni. Measurements and modelling of high pressure pure CO_2 spectra from 750 to 8500 cm^{-1}. Icentral and wing regions of the allowed vibrational bands. *Journal of Quantitative Spectroscopy and Radiative Transfer*, 112(6):925–936, 2011.

[210] S. Stefani, G. Piccioni, M. Snels, D. Grassi, and A. Adriani. Experimental CO_2 absorption coefficients at high pressure and high temperature. *Journal of Quantitative Spectroscopy and Radiative Transfer*, 117:21–28, 2013.

[211] S. Kassi, A. Campargue, D. Mondelain, and H. Tran. High pressure Cavity Ring Down Spectroscopy: Application to the absorption continuum of CO_2 near 1.7 μm. *Journal of Quantitative Spectroscopy and Radiative Transfer*, 167:97–104, 2015.

[212] S. A. Tashkun, V. I. Perevalov, J-l. Te, and Vl. G. Tyuterev. Global fitt of $^{12}C^{16}O_2$ vibrational–rotational line intensities using the effective operator approach. *Journal of Quantitative Spectroscopy and Radiative Transfer*, 62:571–598, 1999.

[213] J.-Y. Mandin. Interpretation of the CO2 absorption bands observed in the Venus infrared spectrum between 1 and 2.5 μm. *Journal of Molecular Spectroscopy*, 67(1):304–321, 1977.

[214] L.P. Giver and C. Chackerian. Rovibrational intensities for the $(31\,^10)_{\,\mathrm{IV}} \leftarrow (00\,^00)$ band of $^{12}C^{16}O_2$ at 4416 cm^{-1}. *Journal of Molecular Spectroscopy*, 148(1):80–85, 1991.

[215] Yu. G. Borkov, D. Jacquemart, O.M. Lyulin, S.A. Tashkun, and V.I. Perevalov. Infrared spectroscopy of ^{17}O- and ^{18}O-enriched carbon dioxide: Line positions

and intensities in the 3200–4700 cm^{-1} region. Global modeling of the line positions of $^{16}O^{12}C^{17}O$ and $^{17}O^{12}C^{17}O$. *Journal of Quantitative Spectroscopy and Radiative Transfer*, 137:57–76, 2014.

[216] X. Huang, R. S. Freedman, S. A. Tashkun, D. W. Schwenke, and T. J. Lee. Semi-empirical $^{12}C^{16}O_2$ IR line lists for simulations up to 1500K and 20,000 cm^{-1}. *Journal of Quantitative Spectroscopy and Radiative Transfer*, 130:134–146, 2013.

[217] X. Huang, R. R. Gamache, R. S. Freedman, D. W. Schwenke, and T. J. Lee. Reliable infrared line lists for $^{13}C^{16}O_2$ isotopologues up to E'=18,000 cm^{-1} and 1500K, with line shape parameters. *Journal of Quantitative Spectroscopy and Radiative Transfer*, 147:134–144, 2014.

[218] E.V. Karlovets, A. Campargue, D. Mondelain, S. Béguier, S. Kassi, S.A. Tashkun, and V.I. Perevalov. High sensitivity Cavity Ring Down spectroscopy of ^{18}O enriched carbon dioxide between 5850 and 7000 cm^{-1}: I. Analysis and theoretical modeling of the $^{16}O^{12}C^{18}O$ spectrum. *Journal of Quantitative Spectroscopy and Radiative Transfer*, 130:116–133, 2013.

[219] E.V. Karlovets, A. Campargue, D. Mondelain, S. Kassi, S.A. Tashkun, and V.I. Perevalov. High sensitivity Cavity Ring Down spectroscopy of ^{18}O enriched carbon dioxide between 5850 and 7000 cm^{-1}: Part II — Analysis and theoretical modeling of the $^{12}C^{18}O_2$, $^{13}C^{18}O_2$ and $^{16}O^{13}C^{18}O$ spectra. *Journal of Quantitative Spectroscopy and Radiative Transfer*, 136:71–88, 2014.

[220] E.V. Karlovets, A. Campargue, D. Mondelain, S. Kassi, S.A. Tashkun, and V.I. Perevalov. High sensitivity Cavity Ring Down spectroscopy of ^{18}O enriched carbon dioxide between 5850 and 7000 cm^{-1}: Part III — Analysis and theoretical modeling of the $^{12}C^{17}O_2$, $^{16}O^{12}C^{17}O$, $^{17}O^{12}C^{18}O$, $^{16}O^{13}C^{17}O$ and $^{17}O^{13}C^{18}O$ spectra. *Journal of Quantitative Spectroscopy and Radiative Transfer*, 136:89–107, 2014.

[221] E. Zak, J. Tennyson, O. L. Polyansky, L. Lodi, N. F. Zobov, and S. A. Tashkun. A room temperature CO_2 line list with ab initio computed intensities. *Journal of Quantitative Spectroscopy and Radiative Transfer*, 177:31–42, 2016.

[222] O. L. Polyansky, K. Bielska, M. Ghysels, L. Lodi, N. F. Zobov, J. T. Hodges, and J. Tennyson. High-accuracy co_2 line intensities determined from theory and experiment. *Phys. Rev. Lett.*, 114:243001, Jun 2015.

[223] J. Lamouroux, R. R. Gamache, A. L. Laraia, J.-M. Hartmann, and C. Boulet. Semiclassical calculations of half-widths and line shifts for transitions in the

30012 ← 00001 and 30013 ← 00001 bands of CO_2. III: Self collisions. *Journal of Quantitative Spectroscopy and Radiative Transfer*, 113(12):1536–1546, 2012.

[224] R. R. Gamache and J. Lamouroux. The vibrational dependence of half-widths of co2 transitions broadened by N_2, O_2, air, and CO_2. *Journal of Quantitative Spectroscopy and Radiative Transfer*, 117:93–103, 2013.

[225] M. Y. Perrin and J. M. Hartmann. Temperature-dependent measurements and modeling of absorption by CO_2-N_2 mixtures in the far line-wings of the 4.3μm CO_2 band. *Journal of Quantitative Spectroscopy and Radiative Transfer*, 42(4):311–317, 1989.

[226] B. Bézard, A. Fedorova, J.-L. Bertaux, A. Rodin, and O. Korablev. The 1.10- and 1.18-μm nightside windows of venus observed by spicav-ir aboard venus express. *Icarus*, 216(1):173–183, 2011.

[227] E. Lemmon, M. McLinden, and D. Friend. Thermophysical properties of fluid systems. In *NIST chemistry webbook, NIST standard reference database number 69*. National Bureau of Standards and Technology, Gaithersburg, MD, 2012.

[228] C. de Bergh, B. Bézard, D. Crisp, J.P. Maillard, T. Owen, J. Pollack, and D. Grinspoon. Water in the deep atmosphere of Venus from high-resolution spectra of the night side. *Advances in Space Research*, 15(4):79–88, 1995.

[229] J. Burkart. *Optical feedback stabilized cavity ring-down spectroscopy Highly coherent near-infrared laser sources*. Phd, 2015.

[230] J. M. Hollas. *Moder Spectroscopy*. John Wiley & Sons, Chichester, England, 1992.

Appendix A

Vibrational modes of H_2O and spectroscopic notation

The water molecule is an asymmetric top molecule belonging to the C_{2v} point group. The molecule has three normal vibrational modes: two stretch modes denoted ν_1 for the symmetric one and ν_3 for the antisymmetric one, and one bending mode ν_2 (Fig. 5.17).

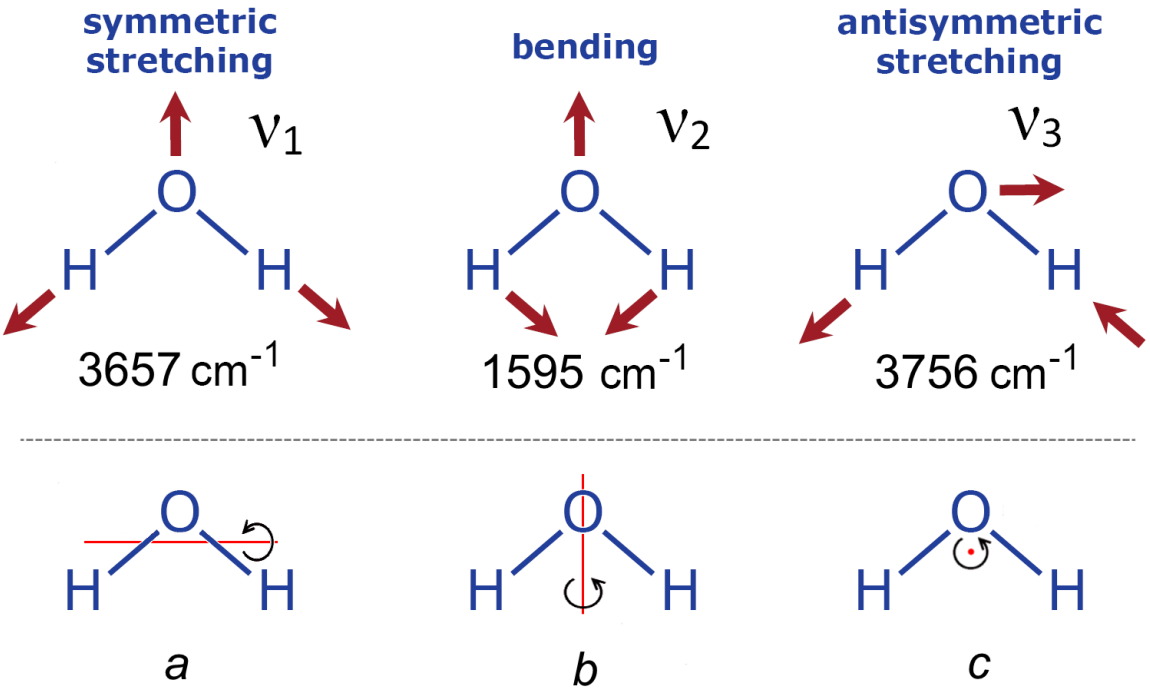

Figure 5.17. Normal modes and fundamental frequencies of H_2O molecule. a, b and c denote rotational axis of water molecule ordered as follows with increasing of the moment of inertia $I_a < I_b < I_c$.

Rotational quantum numbers J, K_a and K_c denote the total angular momentum and the projection of this momentum on axis a and c, respectively. Here a, b and c denote the directions of the three principal axes of inertia (fixed in the molecule) and the labeling of the axes is chosen so that $I_a < I_b < I_c$ (Fig. 5.17).

In the case of the water molecule, only J represents a good rotational quantum number. As water molecule is an asymmetric top molecule with a large degree of asymmetry neither K_a and K_c are not good quantum numbers. Nevertheless, K_a and K_c provide a convenient and unambiguous label for the energy levels.

For each quantum number J, there are $2J+1$ rotational energy levels which are shown in Table 5.4 and ordered as follows with increasing energy.

Table 5.4. Rotational energy levels of H_2O molecule in the order of energy increasing.

J	K_a	K_c	Example for $J=3$
J	0	J	3 0 3
J	1	J	3 1 3
J	1	$J-1$	3 1 2
J	2	$J-1$	3 2 2
J	2	$J-2$	3 2 1
...	...	...	3 3 1
J	J	0	3 3 0

Thus, to label each rotational-vibrational transition, 12 quantum numbers are used as this adopted in the HITRAN database [2]:

$$\nu_1'\nu_2'\nu_3'\ J'K_a'K_c' \leftarrow \nu_1''\,\nu_2''\,\nu_3''\ \ J''\,K_a''\,K_c'',$$

where $'$ and $''$ denote the upper and lower rovibrational states respectively.

Not all the transitions are possible and their number is limited due to selection rules. Ttransitions are allowed if:

$$\begin{aligned} \Delta J = \pm 1 \quad &\text{and} \quad \Delta p = 0 \\ \Delta J = 0 \quad &\text{and} \quad \Delta p = 1 \end{aligned}$$

with

$$\begin{aligned} p = 0 \quad &\text{for} \quad e \quad \text{state}, \\ p = 1 \quad &\text{for} \quad f \quad \text{state}. \end{aligned}$$

As explained in Ref. [230] "Vibrational transition moments are confined to the a, b or c axis and the rotational selection rules are characteristic". They are called "type A, type B and type C selection rules corresponding to a transition moment along the a, b or c axis respectively". In the case of water water only type A (parallel

bands) and type B (perpendicular bands) are present giving the following selection rules:

Parallel bands:

$$\begin{aligned} \nu_3 \quad &- \quad \text{even}, \\ K_a'' - K_a' \quad &- \quad \text{odd}, \\ K_c'' - K_c' \quad &- \quad \text{odd}, \end{aligned}$$

i.e. changes of K_a and K_c of a transition have to be odd;

Perpendicular bands:

$$\begin{aligned} \nu_3 \quad &- \quad \text{odd}, \\ K_a'' - K_a' \quad &- \quad \text{even}, \\ K_c'' - K_c' \quad &- \quad \text{odd}, \end{aligned}$$

i.e. change of K_a has to be even, change of K_c has to be odd. For example, the band (010)-(000) is parallel, the band (003)-(000) - perpendicular.

Appendix B

Vibrational modes of CO_2 and spectroscopic notation

Carbon dioxide is a linear triatomic molecule which has four normal vibrational modes. For the $^{12}C^{16}O_2$ isotologue these modes are: symmetric stretch, doubly degenerated bending mode, and asymmetric stretch (see Fig. 5.18). The vibrational

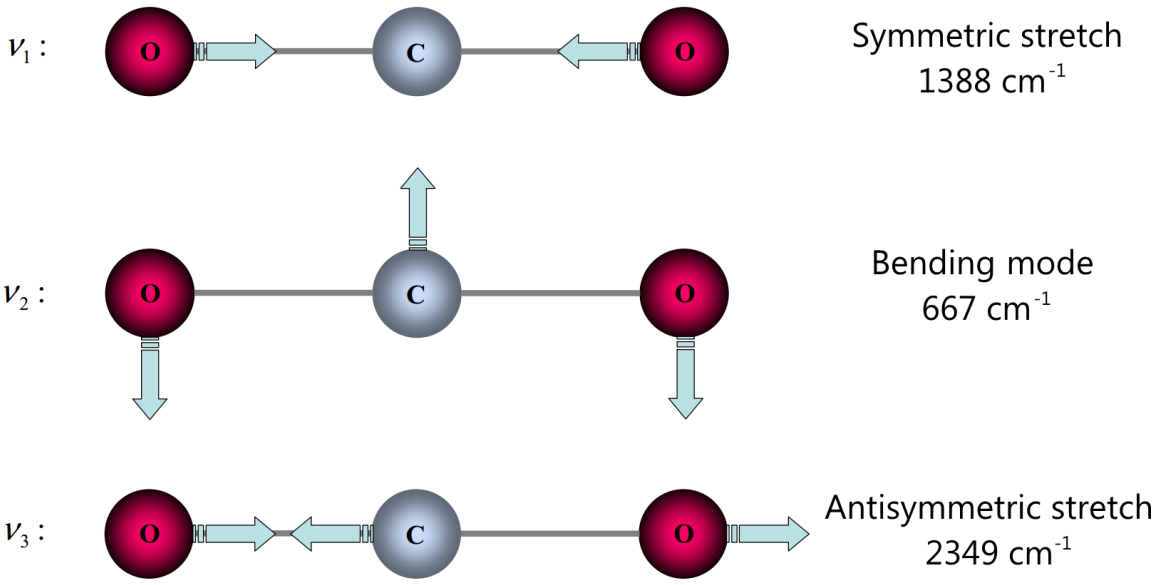

Figure 5.18. Normal modes of carbon dioxide and frequencies

energy state of the molecule is defined by 3 vibrational quantum numbers V_1, V_2, V_3 corresponding to the degree of excitation of normal these vibrational modes. Due to approximate relations between the harmonic frequencies

$$\omega_1 \approx 2\omega_2 \qquad \omega_3 \approx 3\omega_2 \tag{5.2}$$

of the CO_2 molecule and hence strong Fermi resonance, normal mode labeling fails. In the HITRAN type labeling ($V_1V_2l_2V_3r$), vibrational states are grouped into polyads, which have the same polyad quantum number P satisfying the following equation:

$$P = 2V_1 + V_2 + 3V_3, \tag{5.3}$$

l_2 is the quantum number of the vibrational angular momentum which depends on the quantum number of the doubly degenerated normal mode: $l_2 = 0, 2, ...V_2$ if V_2 is even and $l_2 = 1, 3, ..V_2 - 1$ if V_2 is odd but in the labeling of the polyad and state labeling in spectroscopic notation l_2 is always equal to V_2. The ranking number r of the states takes values from 1 to V_1+1 in order of decreasing energy values. For each P there is series of Fermi polyads, which consist of vibrational states with the same values of P, l_2 and V_3. Table 5.5 represents an example of Fermi polyads, corresponding basis states and labeling for $P = 4$.

Table 5.5. Example of Fermi polyads and corresponding basis states for $P = 4$.

Fermi polyad	Number of states	Basis state, $\|V_1\, V_2\, l_2\, V_3\rangle$	Eigenstate, $V_1\, V_2\, l_2\, V_3 r$
(2000)	3	$\|20^00\rangle$	20001
		$\|12^00\rangle$	20002
		$\|04^00\rangle$	20003
(1220)	2	$\|12^20\rangle$	12201
		$\|04^20\rangle$	12202
(0440)	1	$\|04^40\rangle$	04401
(0111)	1	$\|01^11\rangle$	01111

To complete the state labeling with rotational assignment two quantum numbers have to be added. C and J are parity (e or f) and the quantum number of total angular momentum respectively. The former relates to the sign $\varepsilon = \pm 1$ of the Wang combination of the basis functions

$$|V_1\, V_2\, l_2\, V_3\, J\, \varepsilon\rangle = \frac{1}{\sqrt{2}} \left(|V_1\, V_2\, l_2\, V_3\rangle |JK = l_2\rangle + \varepsilon |V_1\, V_2\, (-l_2)\, V_3\rangle |JK = -l_2\rangle \right), \quad (5.4)$$

$$|V_1\, V_2\, 0\, V_3\, J\, \varepsilon = 1\rangle = |V_1\, V_2\, 0\, V_3\rangle |J0\rangle \quad (5.5)$$

as follows: $e \to \varepsilon = 1, f \to \varepsilon = 1$. HITRAN labeling also assumes that states with different V_3 and l_2 quantum number values are weakly mixed. However, HITRAN labeling comes up short in highly excited states, where Coriolis and Fermi + l–type resonance interactions cause mixing between some states of different Fermi polyads with different l_2 quantum numbers. Therefore, along with HITRAN labeling (spectroscopic nomenclature), the CDSD uses the generalized nomenclature for energy level labeling (P, J, C, N) [4]. Herein, P is a polyad number, J is total angular momentum quantum number, $C = 1$ or 2 for e and f levels, respectively, and $N =$ is the eigenvalue index of the J–P–C block in the Hamiltonian matrix in the ascending order of the eigenvalues.